

Current Sheet Canting in Pulsed Electromagnetic Accelerators

Thomas Edward Markusic

A DISSERTATION
PRESENTED TO THE FACULTY
OF PRINCETON UNIVERSITY
IN CANDIDACY FOR THE DEGREE
OF DOCTOR OF PHILOSOPHY IN ENGINEERING

RECOMMENDED FOR ACCEPTANCE
BY THE DEPARTMENT OF
MECHANICAL AND AEROSPACE ENGINEERING

June, 2002

Current Sheet Canting in Pulsed Electromagnetic Accelerators

Prepared by:

Thomas Edward Markusic

Approved by:

Professor Edgar Y. Choueiri
Dissertation Advisor

Professor Robert G. Jahn
Dissertation Reader

Professor Dennis R. Keefer
Dissertation Reader

© Copyright by Thomas E. Markusic, 2002. All rights reserved.

Acknowledgments

The completion of this Ph.D. thesis owes not only to my own effort, but to the invaluable support of many individuals, most notably:

My wife, Christa, whose irresistible charms led to the birth of our second child, Nathaniel, in Princeton, during my General's semester. Thank you.

Prof. Choueiri, who worked tirelessly to provide me with every experimental resource that I requested, taught me to communicate scientific information more accurately and effectively, and always encouraged me to strive, in my work, for a higher level of excellence. I am a much better scientist from having been your student. Thank you.

Prof. Jahn, who inspired me with his spirited enjoyment of life and learning, and who greatly expanded my inventory of big words. Thank you.

Kamesh, who became a dear friend and late-night companion. Thank you.

Bob, who transferred more knowledge to me than any other individual at Princeton. Thank you.

Finally, to the One who calls Himself "I Am", who stirred His matter to create me, and stirred in me a creative spirit to undertake this task, thank you for showing me "the Way."

This research has been supported by the Air Force Office of Scientific Research (Grant #F49620-98-1-0119). I gratefully acknowledge the support of the Air Force under this grant, as well as the Air Force Palace Knight program for providing the fellowship which enabled me to pursue my Ph.D..

This dissertation carries the designation 3102T in the records of the Department of Mechanical and Aerospace Engineering.

Abstract

The phenomenon of current sheet canting in pulsed electromagnetic accelerators is the departure of the plasma sheet that carries the current from a plane that is perpendicular to the electrodes to one that is skewed, or tipped. Review of pulsed electromagnetic accelerator literature reveals that current sheet canting is a ubiquitous phenomenon – occurring in all of the standard accelerator geometries. Developing an understanding of current sheet canting is important because it can detract from the propellant sweeping capabilities of current sheets and, hence, negatively impact the overall efficiency of pulsed electromagnetic accelerators. In the present study, photographic, magnetic, and laser-interferometric diagnostics were implemented to measure the current sheet canting angle in an experimental pulsed electromagnetic accelerator. Eight different propellants (hydrogen, deuterium, helium, neon, argon, krypton, xenon, and methane) were tested in a rectangular-geometry accelerator, at pressure levels ranging from 75-400 mTorr. The photographic, magnetic, and interferometric diagnostics were used to infer the spatial configuration of the current sheet by measuring its optical emission, current density, and electron density, respectively. The three techniques showed quantitative agreement. Additionally, emission spectroscopy was used to measure the electron temperature in the current sheet plasma. The canting angle was found to increase with the atomic mass of the propellant and the current sheet was always found to tilt such that the anode current attachment leads the cathode attachment. Lighter atoms were observed to yield less canting (the measured angles ranged from approximately 10° for hydrogen to 70° for xenon). Hydrogen, deuterium, and methane were found to exhibit the peculiar, and possibly beneficial, property of having reduced current sheet canting at the highest pressure level. The experimental results also motivated further analysis of the data, and led to the conclusion that current sheet canting is a natural consequence of the manner in which current is conducted in pulsed electromagnetic accelerators. It is postulated that depletion of plasma near the anode, which results from axial density gradient induced diamagnetic drift, occurs during the early stages of the discharge, creating a density gradient normal to the anode, with characteristic length on the order of the ion skin depth. Rapid penetration of the magnetic field through this region ensues, due to Hall effect, leading to a canted current front ahead of the initial current conduction channel. In this model, once the current sheet reaches appreciable speeds, entrainment of stationary propellant replenishes plasma in the anode region, inhibiting further Hall-convective transport of the magnetic field; however, the previously established tilted current sheet remains at a fairly constant canting angle for the remainder of the discharge cycle, exerting a transverse $\mathbf{J} \times \mathbf{B}$ force which drives plasma toward the cathode and accumulates it there. This proposed sequence of events has been incorporated into a phenomenological model. The model is shown to give quantitative agreement with the experimentally measured canting angle mass dependence trends.

Nomenclature

\mathbf{J}	average current density in current sheet
\mathbf{B}	average magnetic inductance in current sheet
\mathbf{E}	average electric field in current sheet
\mathbf{F}	Lorentz force
\mathbf{j}	local current density
\mathbf{v}	current sheet velocity
\mathbf{u}	current sheet plasma velocity
\mathbf{u}_\perp	current sheet transverse velocity
\mathbf{u}_E	$\mathbf{E} \times \mathbf{B}$ drift velocity
\mathbf{u}_d	diamagnetic drift velocity
c	speed of light in vacuum
v	current sheet propagation speed
v_A	Alfvén speed
v_A^c	canting-corrected Alfvén speed
v_D	characteristic speed for resistive field diffusion
v_C	characteristic speed for convective skin effect field transport
L	characteristic length of density gradient in current sheet
v_{BA}	branch-anode(BA) interface propagation speed
v_{BT}	branch-trunk(BT) interface propagation speed
s	axial separation distance between BA and BT
R_C	convective skin effect Reynolds number
θ	current sheet canting angle
ν_{ee}	electron-electron collision frequency
ν_{ii}	ion-ion collision frequency
V_L	inductive voltage drop
L_o	initial circuit inductance
t	time
I	total circuit current
I_{max}	maximum circuit current
\bar{I}	average circuit current
V_o	initial bank voltage
$c(\omega)$	B-dot probe calibration constant
ω	field variation frequency
Δx	axial probe separation
Δy	vertical probe separation
\mathcal{N}_o	free space index of refraction
\mathcal{N}	local index of refraction

Nomenclature (cont.)

n	plasma number density
n_e	electron number density
n_i	ion number density
p	hydrostatic pressure
m_i	ion atomic mass
Z	degree of ionization
N	total number of neutral atoms in current sheet
N_e	total number of electrons in current sheet
q	electrostatic charge
η	plasma resistivity
η_H	Hall resistivity
r	radial coordinate in cylindrical geometry
λ_D	Debye length
δ_e	electron skin depth
δ_i	ion skin depth
η_{\perp}	transverse Spitzer resistivity
β	plasma “beta”
Ω_e	electron Hall parameter
Ω_i	ion Hall parameter
$I_{nm}(\omega)$	spectral emission line intensity profile
i_{nm}	spectrally integrated emission line intensity
\hbar	Planck’s constant
ω_{nm}	radiative transition frequency
A_{nm}	Einstein A coefficient
E_m	energy of m^{th} energy level
N_m	population of m^{th} energy level
g_m	degeneracy of m^{th} energy level
Z_a	electronic partition function of species “a”
l	depth of plasma
y	normalized radiative intensity
a	slope of temperature line
b	y-intercept of temperature line
λ_s	current sheet thickness
τ_s	characteristic time for onset of anode starvation
j_d	diamagnetic drift induced current density
I_d	total diamagnetic drift induced current

Contents

Acknowledgments	ii
Abstract	iii
Nomenclature	v
1 Introduction	1
1.1 The pulsed plasma thruster	2
1.2 History of the Pulsed Plasma Thruster	4
1.3 Definition of the Problem	5
1.4 Importance of the Problem	7
1.5 Organization	8
2 Review of the Problem	10
2.1 Review by Research Group	11
2.1.1 Los Alamos Scientific Laboratory (1961-1962)	11
2.1.2 Princeton University (1962-1968)	12
2.1.3 Avco-Everett Research Laboratory (1962-64)	14
2.1.4 Stevens Institute of Technology (1963)	22
2.1.5 Institut fur Plasmaphysik Garching bei Munchen (1963)	23
2.1.6 General Atomic Division of General Dynamics Corporation (1964- 66)	24

2.1.7	The University of Strathclyde (1966)	27
2.1.8	ONRA (France) (1968)	30
2.2	Summary and Discussion	31
3	Apparatus	33
3.1	General experimental layout	33
3.2	Accelerator	34
3.3	Pulse forming networks	36
3.3.1	PFN I	37
3.3.2	PFN II	38
3.4	Vacuum facility	39
3.5	Data Acquisition Equipment and Noise Suppression	39
4	Diagnostics	41
4.1	Circuit current measurement	41
4.2	Voltage measurement	42
4.3	High-speed photography	43
4.4	Schlieren imaging	43
4.4.1	Light source	45
4.4.2	Camera	45
4.4.3	Schlieren optical arrangements	45
4.4.4	Experimental timing	48
4.5	Magnetic field probes	49
4.6	Laser interferometry	51
4.7	Emission spectroscopy	55
4.7.1	Apparatus	56

4.7.2	Plasma Spectroscopy	59
5	Experimental Results	60
5.1	Circuit Current and Voltage Measurements	61
5.1.1	Circuit Current	61
5.1.2	Terminal voltage measurements	64
5.2	High-speed photography	68
5.2.1	Evolution of the discharge	69
5.2.2	Speed and canting-angle measurements	72
5.2.3	Discussion	73
5.3	Schlieren imaging	75
5.3.1	Schlieren photography configuration	75
5.3.2	Shadowgraph configuration	75
5.3.3	Modified shadowgraph configurations	76
5.3.4	Discussion	77
5.4	Magnetic field probes	78
5.4.1	Database of canting angles	78
5.4.2	Evolution of the canting angle	80
5.4.3	Discussion	81
5.5	Laser interferometry	84
5.5.1	Discussion	86
5.6	Emission spectroscopy	88
5.6.1	Survey of spectral lines	88
5.6.2	Time-resolved spectra and temperature determination	90
5.7	Summary of experimental results	91

6	Analysis and Modelling	93
6.1	Further analysis of the experimental data	94
6.1.1	Characteristic plasma parameters	94
6.2	Modelling	97
6.2.1	Heuristic model of current sheet structure	98
6.2.2	Canting model preliminary description	101
6.2.3	Anode starvation phase	105
6.2.4	Branching phase	112
6.2.5	Snowplow phase	119
6.3	Correlations with earlier research	122
6.4	Concluding remarks on the analysis	124
7	Conclusion	128
7.1	Summary of findings	128
7.2	Future work	130
7.3	How to build a better thruster	131
A	DESIGN and CONSTRUCTION DETAILS	134
A.1	Pulse forming networks	134
A.1.1	Design principles	134
A.1.2	Analytical design	137
A.1.3	Numerical simulations	137
A.1.4	Physical construction	140
A.2	Accelerator electrical schematic	142
A.3	Optically isolated trigger box	144
A.4	Differential high-voltage Probe	145

A.5	Helmholtz coil	146
B	CALIBRATION	147
B.1	High-voltage probe calibration	147
B.2	Spectroscopy calibration	148
B.2.1	Spectroscopic system ultimate resolution	148
B.2.2	Spectrometer input slit	149
B.2.3	Wavelength calibration	151
B.2.4	Intensity calibration	151
B.3	Magnetic field probe calibration	153
C	ADDITIONAL DATA	155
C.1	Circuit Current	155
C.2	High-speed photography	157
C.2.1	Influence of Polarity	157
C.2.2	Influence of Contaminated Electrodes	158
C.2.3	Breech Photographs	159
C.2.4	Mid-section Photographs	159
C.3	Magnetic field probes	162
C.4	Laser interferometry	167
C.5	Emission Spectroscopy	176
D	THEORY DETAILS	181
D.1	Emission spectroscopy electron temperature calculation	181
D.2	Laser interferometry electron density calculation	183
D.2.1	Analysis of experimental waveforms	184

E	UNCERTAINTY ANALYSIS	189
E.1	Definitions	190
E.2	Uncertainty Analysis for a Measured Value	191
E.2.1	Random Uncertainty	191
E.2.2	Systematic Uncertainty	191
E.2.3	Total Uncertainty	193
E.3	Uncertainty Analysis for a Calculated Value	193
F	EQUIPMENT SPECIFICATIONS	196
F.1	Pearson 301X Current Monitor[1]	196
F.2	Tektronix P6015A High Voltage Probe[2]	196

Chapter 1

Introduction

Pulsed electromagnetic accelerators are devices which use intense bursts of electrical current ($\mathcal{O}(10^4 - 10^6)$ A) to create high speed ($\mathcal{O}(10^3 - 10^5)$ m/s) jets of plasma. They find application as plasma sources in many basic plasma science experiments[3] as well as in a specific genre of electric space propulsion device called the pulsed plasma thruster (PPT)[4]. The present work is motivated by the desire to improve the performance of pulsed electromagnetic accelerators in the context of plasma propulsion.

Understanding the performance of PPTs requires a detailed knowledge of the physics of the current conduction channel (the so-called current sheet) within the gas. When one begins to study the physics of current sheets, it becomes readily apparent that there are a multitude of interesting physical phenomena at play. Since current sheets are transient, inherently unstable structures, any rigorous theoretical treatment of current sheet physics would involve a complete, time-dependent, magnetoplasmadynamic model coupled with sheath and electrical circuit models. Similarly, experimental measurements of current sheet properties requires the use of specialized instruments capable of resolving rapidly evolving plasma structures. With these realities in mind, attempting to completely understand the physics of current sheets in a single study appears to be a rather daunting task. Rather than

seeking a paragon, a more manageable approach is to develop simplified theoretical models and specialized experimental tools which expose a particular facet of current sheet behavior, and later assemble a more panoramic view of the overall physics through a succession of studies. This is the spirit of the present work, which focuses on understanding the spatial configuration of the current sheet in an experimental accelerator (the accelerator used was of the *gas-fed* variety, where electromagnetic acceleration is the dominant mode of acceleration; the results of this study may not be directly relevant to the *ablative* thrusters, where electrothermal acceleration may be significant[5]). More specifically, experimental measurements were obtained which show that current sheets tilt (or cant) relative to the electrodes as they propagate. The degree of canting was measured under a variety of experimental conditions and theoretical models were employed to explain the observed behavior. The sections which follow more completely define the background, scope, and general relevance of this thesis.

1.1 The pulsed plasma thruster

The motivation of this thesis is to gain a better understanding of the acceleration mechanism in pulsed plasma thrusters. Let us first, then, place the present problem in context by defining the general operation of a PPT. Figure 1.1 shows the basic components of a PPT. The schematic shows a rectangular, parallel plate geometry, for illustrative purposes. PPTs come in many other geometries (e.g., coaxial, linear pinch, etc).; however, the discussion which follows for the rectangular geometry describes the general operation of any PPT operating in the electromagnetic acceleration mode. The plasma discharge in a PPT progresses as follows. First, the volume between two electrodes, separated at the breech by an insulator, is filled with a working gas. High voltage (typically 1-15 kV) is then applied between the electrodes (typically a capacitor bank is connected to the electrodes with a

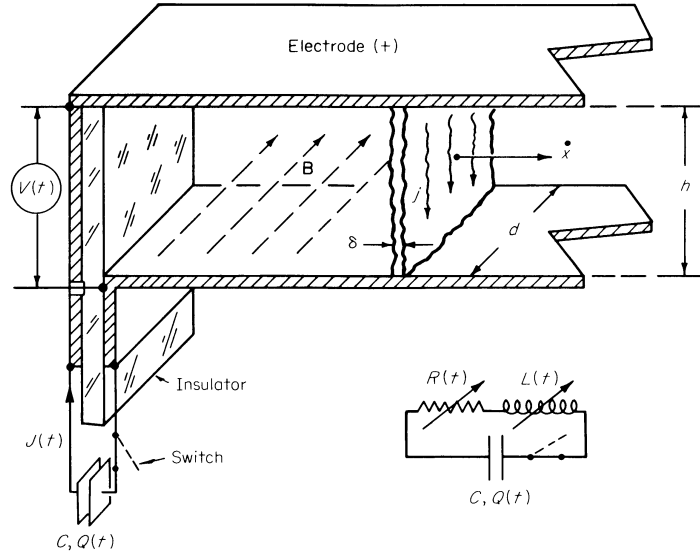


Figure 1.1: Schematic of pulsed plasma thruster components and circuit model[4].

high speed switch such as an ignitron). The gas between the electrodes then breaks down and current begins to flow. The initial current distribution is in the form of a planar current sheet along the face of the insulator at the breach. The current sheet forms at the breach because it is the path of least impedance available to the circuit; in a circuit with rapidly rising current, the inductive voltage drop, $V_L = L_o dI/dt$ (where, L_o is the initial inductance and I is the total circuit current (typically 10-100 kA)), dominates the impedance of the system and, hence, the circuit seeks the path of least initial inductance, which is at the breach. As the current rises, a transverse magnetic self-field (\mathbf{B}) forms behind current sheet; this magnetic field interacts with the current sheet to create an axially directed electromagnetic self-force, $\mathbf{F} = \int \mathbf{j} \times \mathbf{B} d^3x$. This force causes the current sheet to accelerate axially, away from the breach – sweeping up gas along the way (the current sheet is often referred to, figuratively, as an electromagnetic “snowplow”). At the end of the electrodes, the gas entrained in the current sheet is ejected (typically with a speed of 10-100 km/s) and thrust is derived (typically a 0.1-1 mN-s impulse bit).

1.2 History of the Pulsed Plasma Thruster

PPTs have the potential for fulfilling the attitude control requirements on a satellite at greatly reduced mass and cost. They are also being considered for constellation maintenance for missions such as interferometric imaging of the Earth from space or deep space from an Earth orbit (c.f., Polzin *et al*[6]). The benefits of PPTs are their simplicity, very small impulse bits for precise control of satellite motion, reliability, and high specific impulse. Two classifications of PPTs exist, corresponding to the form of propellant used: gas-fed (GFPPT) or ablative propellant (APPT). The gas-fed variety has the advantages of a “clean” exhaust plume and high specific impulse. The ablative version of the PPT uses a solid propellant, such as Teflon, to provide other advantages such as compactness and overall ease of system integration; however, plume contamination and lower specific impulse may limit the application of APPTs for some missions.

From about 1960 to 1968 PPT research focused on the gas-fed variant (GFPPT). The GFPPT was envisioned as a potential “primary” propulsion system, where the GFPPT would process large amounts of power (> 100 kW) and provide enough average thrust (> 1 N) to perform large Δv maneuvers, such as interplanetary missions. By the late sixties it was realized that a steady-flow electromagnetic accelerator, the MPD thruster[7], was better suited for this type of mission. A “secondary” propulsion niche, i.e., small Δv attitude control maneuvers, still existed for the GFPPT. However, at about the same time, the ablative variety of PPT (APPT) was gaining favor, mainly due to its mechanical simplicity. The GFPPT requires the storage of gaseous propellant under high pressure and a fast-acting valve to meter puffs of propellant into the discharge chamber. Further, the propellant feed system in the GFPPT is required to operate in a leak-free manner for many ($> 10^6$) shots. A qualified system capable of performing this demanding task was not available at the time and, hence, only APPTs were flown[8].

This state of affairs remained until the mid-90's, when the negative issues related to propellant feeding in the GFPPT were ameliorated by the availability of flight-qualified valves and the development of high-speed solid-state electrical switching technology. The former development addressed the reliability issue, while the latter showed promise for substantially increasing the propellant utilization efficiency. These technologies were implemented in the thrusters of Ziemer *et al.*[9, 10, 11]. Still, with the addition of these new technologies, PPTs remain one of the least efficient electric propulsion systems ($\eta_t \sim 10\%$). However, the possibility of large incremental gains in performance make PPTs one of the most interesting devices, from a research perspective.

With the renewed interest in GFPPTs it is fitting and natural that there is a revitalized interest in understanding the physical principles which underlie PPT operation, in order to improve their performance. Careful review of the work of earlier researchers[12] shows that our understanding of the acceleration mechanism in PPTs is deficient in several areas. This thesis aims to help clear up one such area of ambiguity – current sheet canting.

1.3 Definition of the Problem

The phenomenon of current sheet canting is the departure of the current sheet from perpendicular attachment to the electrodes to a skewed, or tipped, attachment. It is best illustrated by an example. Figure 1.2 shows the evolution of two discharges near the breech of a rectangular-geometry pulsed electromagnetic accelerator; outlines of the electrodes (the cathode is the bottom electrode) have been added for clarity. Ideally, we would like the current sheet to initiate at the breech, perpendicular to the electrodes, and remain so as it propagates axially (as illustrated on the left-hand side of the figure). In contrast, the right-hand side of the figure shows the experimentally observed evolution of a discharge[13]. As expected, the current sheet is seen to initiate at the breech; however, as time progresses, the

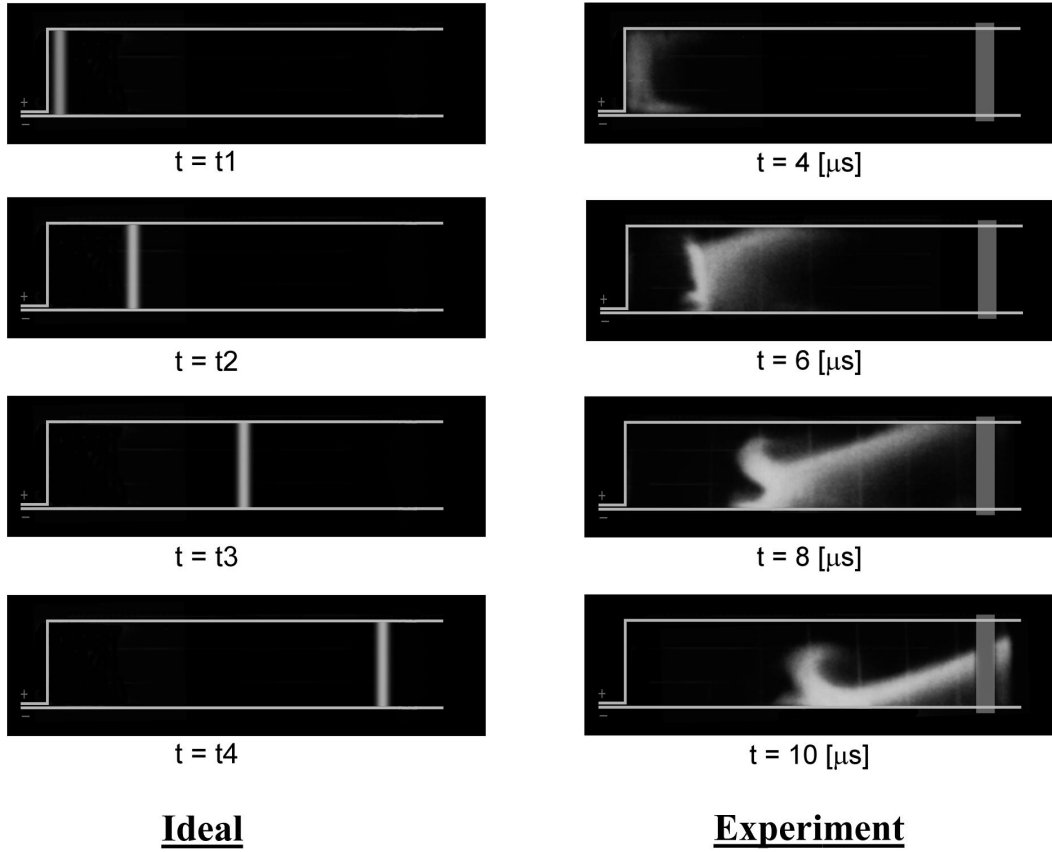


Figure 1.2: Comparison of ideal and experimentally observed current sheet propagation. In the ideal case, it is implied that time $t_1 < t_2 < t_3 < t_4$. The experimental photographs are from an argon (100 mTorr, uniform fill) discharge with peak current about 60 kA. Outlines of the electrodes have been added for clarity; the vertical rectangular element on the right-hand side of the pictures is a structural element that obstructed optical access.

current sheet is seen to severely tilt, or cant, as it propagates.

The photographs shown in Fig. 1.2 were some of the earliest observations in an experiment designed to understand the basic macroscopic stability of current sheets under a variety of experimental conditions. The observed severity of the current sheet canting warranted further investigation and, hence, provided the topic for this thesis.

1.4 Importance of the Problem

Since the overall goal is to improve PPT performance, it is first important to identify why understanding current sheet canting will help us to build better thrusters. While direct measurements of the impact of canting on overall thruster performance remain to be carried out, we can make arguments which suggest that it may have adverse implications.

Canting creates off-axis components of thrust, which constitute a profile loss. Consider the $t = 8 \mu\text{s}$ photograph on the right-hand side of Fig. 1.2. Assuming that the magnetic field is uniform behind the current sheet, the force on the top electrode (which is found by integrating the magnetic pressure on the electrode surface) will be greater than on the bottom electrode, because the top electrode has more surface area exposed to the magnetic field. This transverse force imbalance may result in an undesirable torque on a spacecraft which uses a PPT. Also, considering the work done by the current sheet, it is clear that a canted current sheet will apply a force to the propellant transverse to the thrust axis and thus expend energy which is not converted into useful thrust.

In addition to causing an off-axis component of thrust, current sheet canting may undermine the effective sweeping up of propellant as the current sheet propagates. The effect of canting may be to force the plasma entrained by the current sheet into the cathode where it stagnates and is then left behind. Indeed, canted current sheets may act, undesirably, like *real* snowplows – never accumulating but, rather, throwing their load to the side as they pass by.

Again, while direct studies of performance degradation due to current sheet canting are needed, the potentially adverse effects envisaged above provide reasonable justification for pursuing a detailed study of the phenomenon. By developing an understanding of the physical processes which drive current sheet canting, we can develop prescriptions for how to reduce the effect, and ultimately provide guidance for the design of better pulsed plasma

thrusters.

1.5 Organization

This thesis is primarily experimental in nature and, as such, the bulk of what follows will describe the details of experimental setups and data analysis techniques. In particular, the implementation of photographic, magnetic, and laser-interferometric diagnostics, which were used to measure the canting angle and thermodynamic properties of current sheets in a pulsed electromagnetic accelerator, will be described. A later chapter, Analysis and Modelling, attempts to use the experimental data to make a compelling theoretical argument for processes which can cause current sheet canting.

The organization of the remaining chapters is given below.

Chapter 2: Review of the Problem. A review of past literature relevant to the subject is presented. In particular, any articles which report observations of current sheet canting or offer opinions as to its origin, however cursory, are critiqued.

Chapter 3: Apparatus. The general layout and properties of the major components of the experiment are described.

Chapter 4: Diagnostics. Details are given about the implementation of and the relevant theory behind for all of the plasma diagnostics.

Chapter 5: Experimental Results. The data collected in all of the experiments are summarized.

Chapter 6: Analysis and Modelling. Drawing on further analysis of the experimental data, a model is proposed to describe the mechanisms which drive current sheet canting.

Chapter 7: Discussion and Conclusions. The major results of the study are reiterated. Recommendations for further experiments and design guidelines for the development of future pulsed plasma thrusters are suggested.

In an effort to maintain a continuous, readable presentation, many details (e.g., calibration procedures, design details, etc.), while essential to the completeness of the thesis, are relegated to the appendices.

Chapter 2

Review of the Problem

This chapter reviews past research on the subject of pulsed electromagnetic accelerators; in particular, the scope of this review is limited to articles in which current sheet canting was either observed or commented upon. The information which is available indicates that the phenomenon was ubiquitous – occurring in a variety of different electrode geometries and experimental conditions. However, detailed treatment of the subject is limited, with most references to the phenomenon being anecdotal in nature – with the exception of work carried out by researchers at Avco-Everett Research Laboratory during the mid-sixties. Their work is particularly relevant and, as such, will be considered in the most detail in the review which follows.

This review is arranged by research group (chronologically). Within each section, the major findings of each group are first summarized. These findings are then critiqued and contrasted with the findings of other research groups. The final section summarizes all of the literature and describes the approach that will be taken in the present study to build on the work of the previous researchers.

2.1 Review by Research Group

2.1.1 Los Alamos Scientific Laboratory (1961-1962)

Burkhardt and Lovberg produced the seminal work in the experimental study of current sheets in pulsed electromagnetic accelerators[14]. Electric and magnetic field probes were used to map the trajectory and propellant sweeping characteristics of the current sheet in a conventional Marshall gun geometry (coaxial). The center electrode (the cathode) was charged to -16 kV (relative to the anode) by a 15 μ F capacitor bank. Deuterium was injected into the discharge chamber after which an ignitron switched the capacitor bank into the accelerator resulting in a peak current of about 110 kA.

Two major conclusions resulted from this study: the current sheet was found to be planar (no canting was observed) and the current sheet plasma density was found to be approximately the same as the initial gas injection density – indicating that very little propellant sweeping was taking place.

Comments: The observation that the current sheet did not tilt was somewhat surprising since one would expect that the $1/r^2$ variation in magnetic pressure would result in a bullet shaped current sheet with the cathode arc attachment (center electrode) leading that of the anode. The authors reasoned that the observed current distribution could be realized if the current sheet became “leakier” with increasing radius, thus offsetting the effect of reduced magnetic pressure with increasing radius. A later experiment by Lovberg (which is described in section 2.1.6) used a uniform gas fill, as opposed to the propellant injection technique used in this study. We will revisit the lack of canting in the Los Alamos experiments when we discuss Lovberg’s later work.

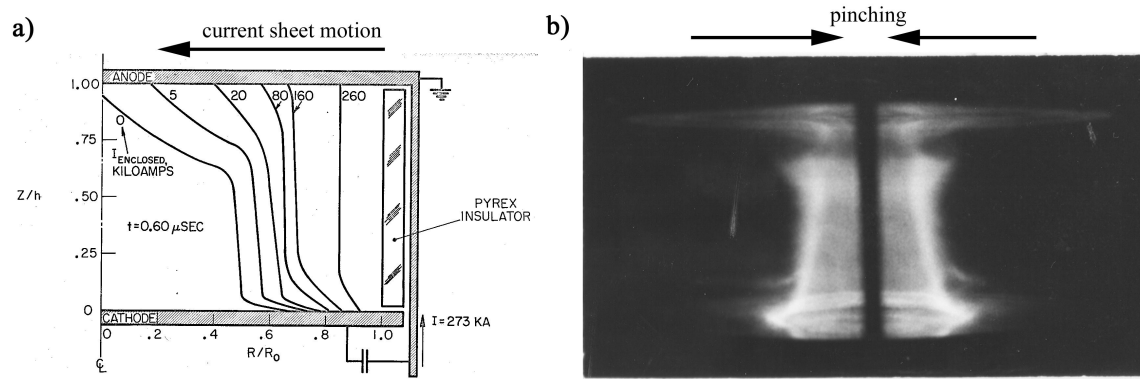


Figure 2.1: Figures from Burton[15]: a) Accelerator schematic and measured contours of constant current, b) Kerr-cell photograph of discharge (argon (120 mTorr)).

2.1.2 Princeton University (1962-1968)

Researchers at Princeton, led by Jahn, undertook the longest lasting and most comprehensive effort to study the physics of current sheets (see, for example, [16]-[18].) Two publications from this study have information directly relevant to current sheet canting.

Burton studied the evolution of the current sheet in a coaxial z-pinch geometry (height = 2 in. , radius = 5 in.) accelerator[15]. Experiments were conducted using 15 $1 \mu\text{F}$ capacitors in parallel charged to 10 kV with argon propellant (ambient fill, 120 mTorr) which yielded peak currents of about 300 kA. Figure 2.1a shows typical measured current contours superimposed on a schematic illustration of the experimental apparatus; figure 2.1b shows a Kerr-cell photograph of a typical discharge. It is clear in both figures that a pronounced canting of the current sheet occurs on the anode side of the device; for $z/h \leq 0.5$ (as defined in Fig. 2.1a) the current sheet appeared to be normal to the electrodes, except very close to the cathode. Using the Kerr-cell photographs, Burton attempted to quantify the canting angle at $z/h = 0.5$. He found that the canting angle increased as the current sheet propagated toward the center of the chamber ($\theta \approx 0.5^\circ$ at $R/R_0 = 0.8$, $\theta \approx 4^\circ$ at $R/R_0 = 0.2$). Burton postulated that the increased canting with time may be related to the onset of the “sausage” instability. Although no further quantitative canting angle

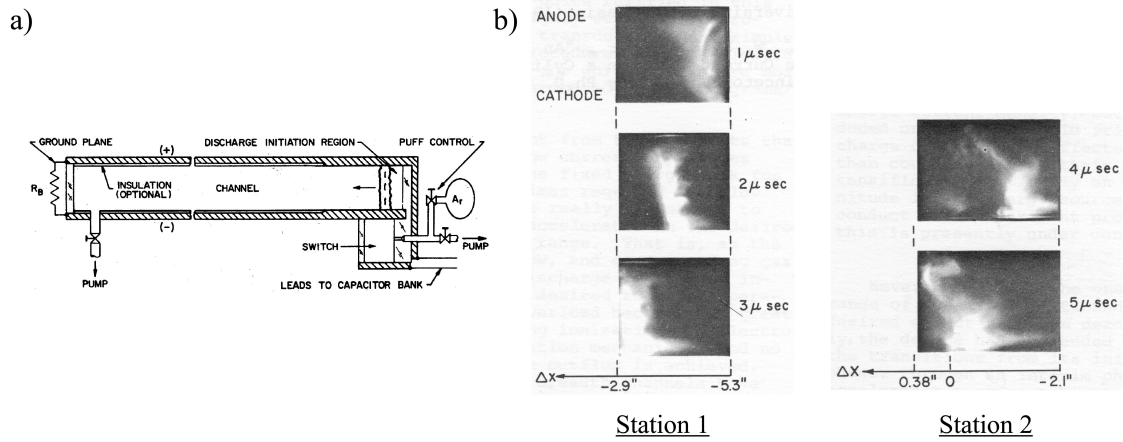


Figure 2.2: Figures from Eckbreth[19]: a) Accelerator schematic, b) Kerr-cell photographs of discharges at two axial locations (argon (100 mTorr), motion is to the left.)

measurements were tabulated, the figures clearly suggest much larger canting angles for $z/h > 0.5$.

The second relevant study from Princeton was conducted by Eckbreth[19]. His work focused on understanding current pattern stabilization when the current sheet reached the end of the electrodes in a rectangular geometry accelerator. While Eckbreth was interested in the steady-state phase of the discharge that occurs after the current sheet reaches the end of the electrodes, and was not concerned with studying the propagation phase of the discharge, he did obtain Kerr-cell photographs of both the steady and unsteady phase of the current sheet evolution; the photographs of the early stages of the discharges reveal the development of a canted current sheet. Figure 2.2a shows a schematic of the experimental apparatus. The aluminum electrodes were 6 in. wide and separated by 2 in. . Axially, the first 5 in. of the electrodes were aluminum; the remainder of the electrode surfaces were covered with nylon. Energy storage consisted of 40 $3.2 \mu\text{F}$ capacitors charged to 10 kV; the peak current was about 120 kA when discharged into a 100 mTorr argon ambient propellant fill. Figure 2.2b shows a series of photographs taken in $1 \mu\text{sec}$ intervals at two different axial locations. In the $t = 1 \mu\text{sec}$ picture we see the current sheet just after initiation, at the breech

of the accelerator. The successive frames show that as the current sheet propagates, by $t = 4 \mu\text{sec}$, a canted luminous structure begins to protrude from the initially planar current sheet. The last frame shows the current sheet approaching the nonconductive portion of the channel ($\Delta x = 0$). Eckbreth did not attempt to explain the physical origin of the anode-leading canted current sheet; rather, he noted, by referencing Burton's work, that it seemed to be a geometry invariant feature which the Princeton group referred to as the "anode foot". The anode foot is most visible (albeit weakly) in the $4 \mu\text{s}$ image in Fig. 2.2b. The "foot" is upside down, with the "toes" pointing to the left, touching the anode. The small hook on the upper right side of the image is the "heel". The features are actually much more visible in the $8 \mu\text{s}$ frame of Fig. 1.2, in the Introduction.

Comments: Despite the different geometries, time-scales, and current levels, the structure of the current sheets in both Princeton experiments showed common features: tilting of the current sheet along the anode and an "anode foot". Also mentioned in both studies was the appearance of a "hook-like" feature behind the current sheet. These similarities are encouraging because conclusions, such as those put forth in the present study, may have general validity for a wide variety of accelerators.

2.1.3 Avco-Everett Research Laboratory (1962-64)

Three articles relevant to the current sheet canting problem were published by researchers at Avco-Everett. While their interest was not in PPTs but, rather, in the development of shock tubes, the physical configuration of their devices were very similar to coaxial PPTs. Keck[20] constructed and tested a magnetic annular shock tube; Fishman and Petschek[21] attempted to explain Keck's experimental results with analytical models. Johansson[22] built a radial magnetic shock tube specifically to resolve the polarity dependence question which surfaced in Keck's experiment. Each of these studies will be described, in turn,

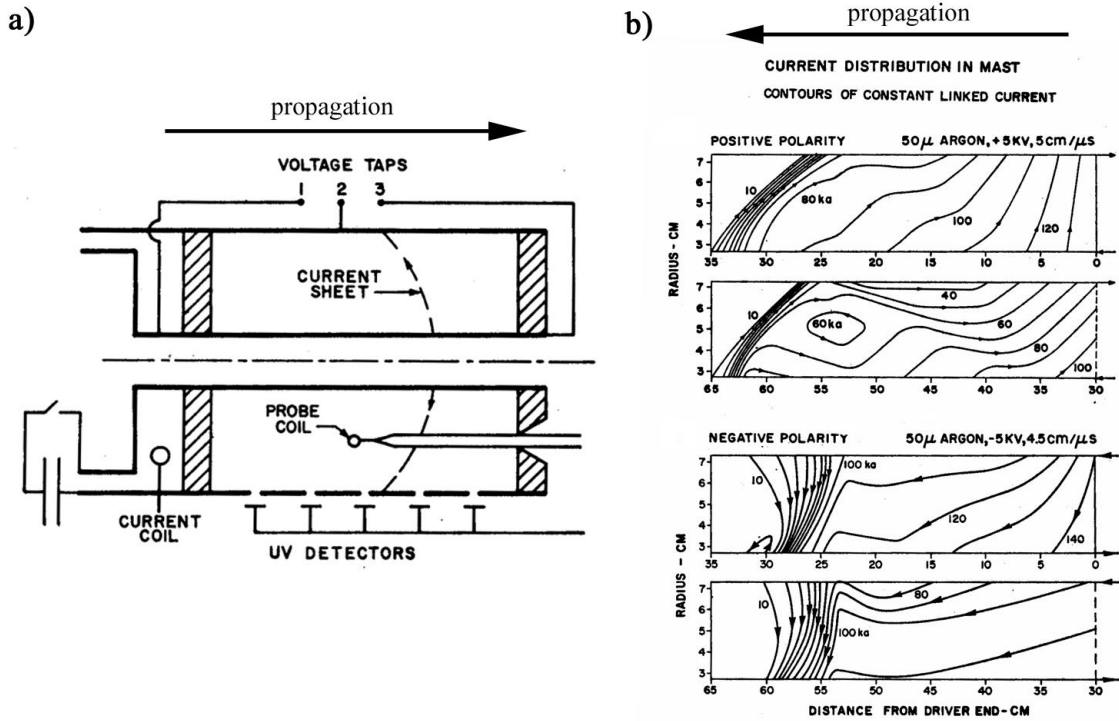


Figure 2.3: Figures from Keck[20]: a) Accelerator schematic, b) Current distribution for positive and negative center electrode at two different times (argon, 50 mTorr, motion is to the left.)

below.

Figure 2.3a shows a schematic of Keck's device[20], which was essentially a coaxial accelerator. Both the inner and outer electrodes were 36 inches long, with radii of 1 and 3 in., respectively. A 365 μ F capacitor bank provided an essentially flat 12 μ s, 165 kA pulse. The working gas was argon (50 mTorr, ambient fill). Diagnostics included several axially spaced uv detectors and magnetic field probes.

Keck observed an unexpected polarity dependence both in current sheet propagation speed and overall current pattern. Figure 2.3b shows current contours which he inferred from magnetic field probe data. Data is displayed for two cases: anode (positive) center electrode and cathode (negative) center electrode. The two plots (for each polarity) illustrate the current pattern at two different times. It is immediately apparent that the current

pattern is dependent on the polarity of the electrodes. For positive operation, the current sheet is canted, with the inner attachment (anode) leading the outer attachment by about 8 cm. For negative operation, the sheet, although not as well defined, is more or less perpendicular to the walls.

There are other noteworthy features in the plots. First, it is apparent that the current is much more concentrated near the front of the current sheet in the positive polarity case; the current channel appears to be broader in the negative polarity case. Also, for the positive polarity case, the current distribution suggests the growth of a plasma “bubble” along the cathode, behind the current sheet.

Fishman and Petschek[21] attempted to explain Keck’s results using a simple force balance model in which the gas pressure on one side of the current sheet was balanced by the magnetic pressure on the other face. With reference to Fig. 2.4a, and applying suitable boundary conditions, they arrive at an analytical solution for the current sheet propagation speed, $u_s = B_o(8\pi\rho_1)^{-1/2}$, where B_o is the magnetic field at the inner electrode radius and ρ_1 is the ambient gas density ahead of the shock. They also derived an expression for the shape of the current sheet; a plot of the resulting relation and experimental data from Keck is shown in 2.4b. Both the estimate of the sheet speed and shape are found to be in qualitative agreement with the experimental results (positive polarity).

Nothing in the model, however, addresses the observed differences in Keck’s experimental results with negative polarity. The authors speculate that the difference between positive and negative operation is caused by the fact that there is insufficient electron emission from the cathode and that this tends to force the flow towards a configuration which allows the current to be carried by ions. To support this conclusion, for positive operation, they note that their model predicts radially outward mass flow from the anode (and a concomitant positive ion current) sufficient to account for almost all of the conduction current.

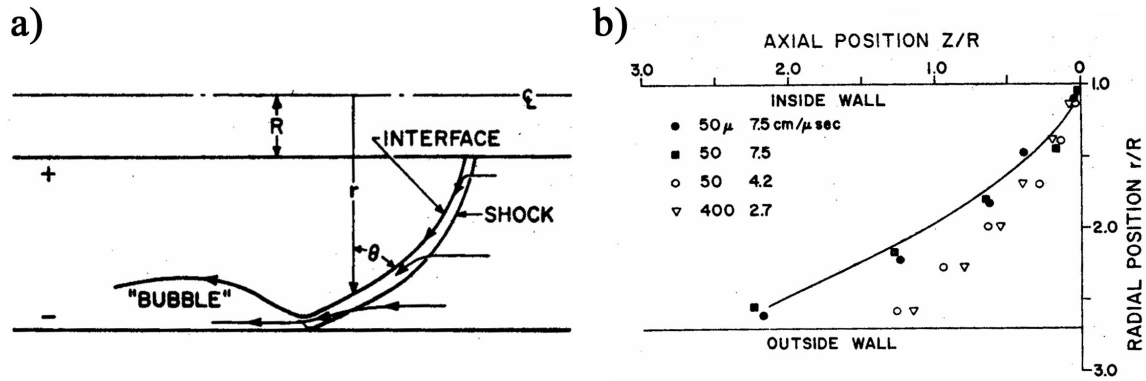


Figure 2.4: Figures from Fishman and Petschek [21]: a) flow model for Keck accelerator[20], b) comparison of the shape of the current sheet observed by Keck with the analytical model.

They note that the “bubble” of plasma that Keck observed along the outer electrode may be the result of the stagnation of this radial mass pumping. In the negative configuration, the mass pumping would be in the opposite direction of the current flow; therefore, they conjecture, the current sheet adjusts its physical orientation to pump ions toward the cathode, which results in a planar, non-canted current sheet.

Johansson[22] attempted to resolve the question of current sheet canting experimentally using a radial magnetic shock tube, which is essentially an inverse z-pinch accelerator. This geometry (illustrated at the top of Fig. 2.5) provides a uniform magnetic field along the back of the current sheet, eliminating the radial dependence which complicated the analysis of Fishman and Petschek. The accelerator consisted of two disk-shaped electrodes mounted on a coaxial structure. Hydrogen and argon were tested in the 50-800 mTorr pressure range (ambient fill). A 1 mF capacitor bank, charged to 5 kV, delivered a sinusoidal current waveform with 500 kA peak current and 64 μs period. Johansson found that uniform discharge initiation was erratic under some experimental conditions. To rectify this problem, trigger electrodes and an inductive high-frequency coil were placed at the center of the discharge cavity. These pre-discharge circuits facilitated uniform, repeatable

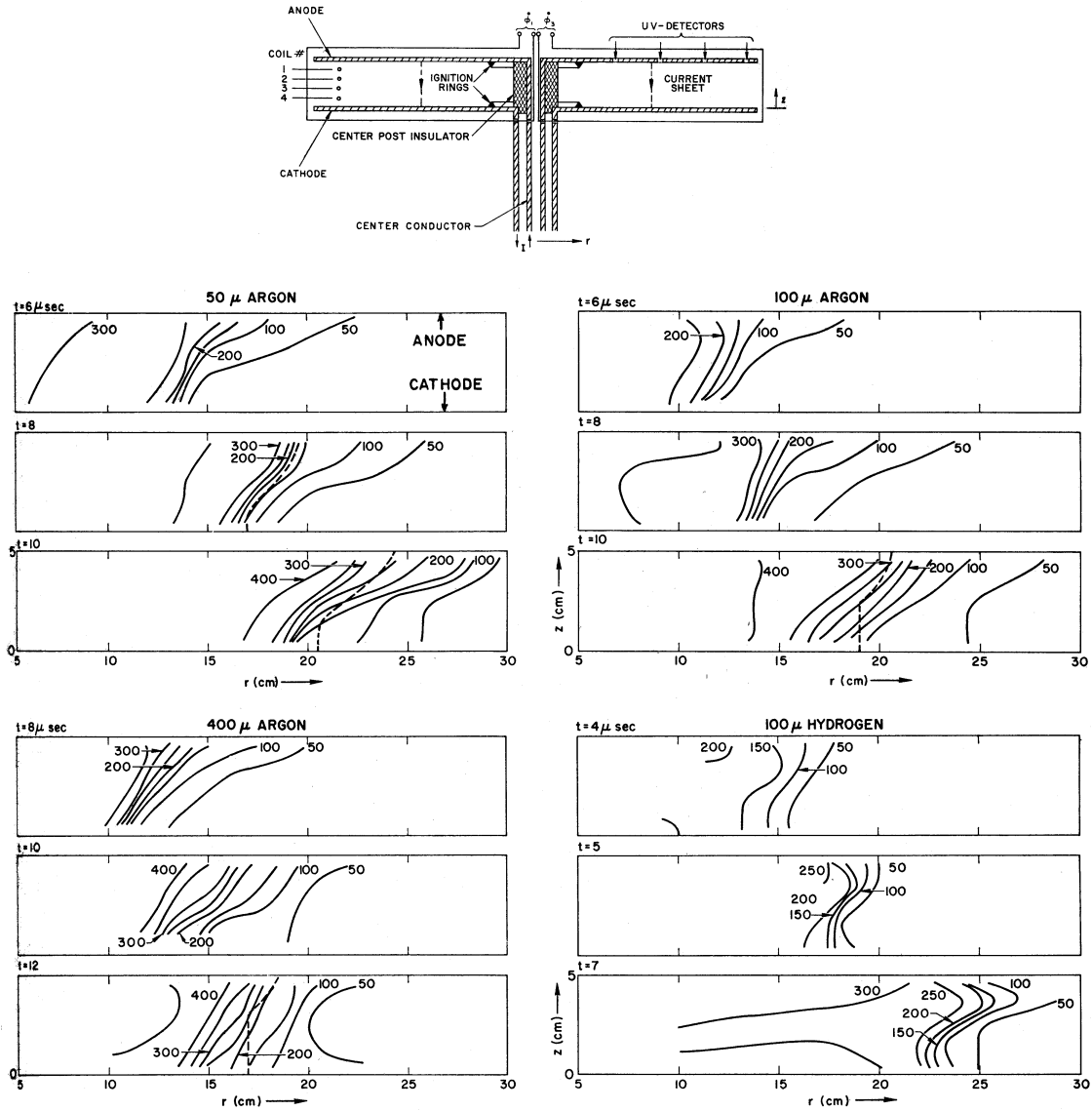


Figure 2.5: Schematic of radial magnetic shock tube and current contours (from Johansson[22]).

breakdown at the center of the discharge chamber. Experimental diagnostics included UV-detectors, magnetic field probes, and a framing camera.

Figure 2.5 shows current contours, inferred from magnetic field measurements, for several different experimental conditions. Johansson drew several conclusions from these plots. He noted that the tilt of the current sheet varied between 30° and 50° (such that

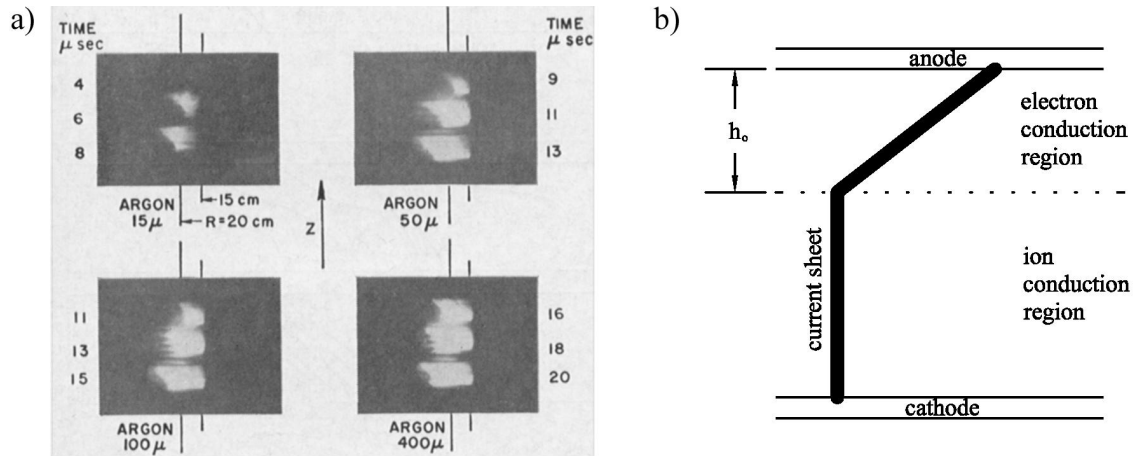


Figure 2.6: More figures from Johansson[22]: a) framing camera images of accelerating current sheets (motion is to the left), b) schematic of current conduction regions (present author's interpretation of the discussion in the paper).

the cathode side lags the anode side) for argon in the 50-400 mTorr pressure range. The thickness of these current sheets was approximately 5 cm at a radius of 15-20 cm. During the first part of the motion the maximum current density at the cathode was 3-5 times greater than at the anode; the cathode current density diminished as the sheet moved out. At the axial midpoint, the canting angle of the current sheets for hydrogen and argon were about the same. The hydrogen current sheet thickness exhibited a different behavior than that found in argon; the sheet was thick at both electrode interfaces and thinnest at the mid-plane. The tilt angle for both propellants exhibited no systematic variation with pressure.

Similarly, framing camera images (see Fig. 2.6a) of the discharge showed that a strongly luminous band developed close to the cathode, from which a canted luminous front emanated; the canting angle was estimated to be about 45° .

Johansson concludes his paper by postulating a physical model for current sheet canting and developing a simple analytical expression for its spatial extent. As pictured in Fig. 2.6b (which is our interpretation of his discussion), Johansson envisioned that the current sheet may be divided into two phenomenologically different regions: a region where electron

current dominates and a region where ion current is predominate. The ion conduction region is normal to the cathode (while the electron region is canted, that is, only *part* of the current sheet is tilted); in this region, almost all of the conduction current is assumed to be carried by the ions. He makes the assumption that everywhere in the current sheet the electron Hall parameter is large, while the ion Hall parameter is negligible. Therefore, he concludes that the electron trajectories are determined by $\mathbf{E} \times \mathbf{B}$ drift, while the ion movement is governed by hydromagnetic pressure exerted on the ion fluid. In order for the ions to develop the requisite component of velocity directed toward the cathode, a canted section of the current sheet is necessary; this canted section exerts a cathode-directed force on the ions – propelling them into the ion current region. The height, h_0 , of the canted, electron current dominated region is estimated by calculating the distance within which the ion flow into the current sheet is equal to the total current flowing between the electrodes. Using an expression for the total ion flux into the current sheet and a momentum balance Johansson arrives at an expression for the height of the canted section:

$$h_o = \frac{1}{q} \left(\frac{2M}{\mu_o n} \right)^{1/2}, \quad (2.1)$$

where, μ_o is the magnetic permeability of free space, and q , M , and n are the charge, mass, and number density of the ions, respectively.

Johansson goes on to tabulate h_o for various gas species and pressures used in his and others' experiments – showing, for the most part, that the calculated values agree with the experimentally observed features. It should be reemphasized that Johansson does not attempt to calculate the canting angle but, rather, the spatial extent over which canting is expected to exist.

Comments: Keck's paper was the first to introduce the issue of current sheet canting by way of noting the polarity-dependent current configuration in his accelerators. Johansson went on to show that current sheet canting was related to factors other than the non-uniform

magnetic pressure found in coaxial accelerators, through experiments with a geometry which presented a uniform magnetic field to the current sheet.

The theoretical arguments, in regard to current sheet canting, presented by all of the authors from Avco, require all of the current to be carried by ions without making any compelling arguments for the necessity of ion current in the first place. Furthermore, the proposed notion that ion current can be carried by driving propellant toward the cathode seems to contradict the fact that current is only carried by motion of the electron fluid *relative* to the ion fluid; no net current results from the motion of the fluid as a whole. This notion can be reconciled, perhaps, by considering the neutralization process that takes place when an ion impacts the cathode. To extend the discussion further would amount to “putting words in their mouth”, from which we shall refrain. The work of the Avco group was unique, and will provide a model with which to contrast the results of the present study. In later discussions we will refer to their model for canting as the “ion conduction current canting model”.

Some of the other implications of their models are interesting to consider. The value of the current sheet propagation speed that Fishman and Petschek derived is approximately the same as the Alfvén speed (by a multiplicative factor of $1/\sqrt{2}$). This seems reasonable since, for the coaxial geometry, the magnetosonic speed is the same as the Alfvén speed. The model of Johansson implies that the ion fluid will transport a large amount of its momentum to the cathode, where it stagnates and is neutralized. As a consequence, a large part of the propellant will not be accelerated axially but, rather, will “slip under” the current sheet as it passes by. This picture is supported by their experimental observations of a plasma “bubble” which trailed behind the current sheets along the cathode.

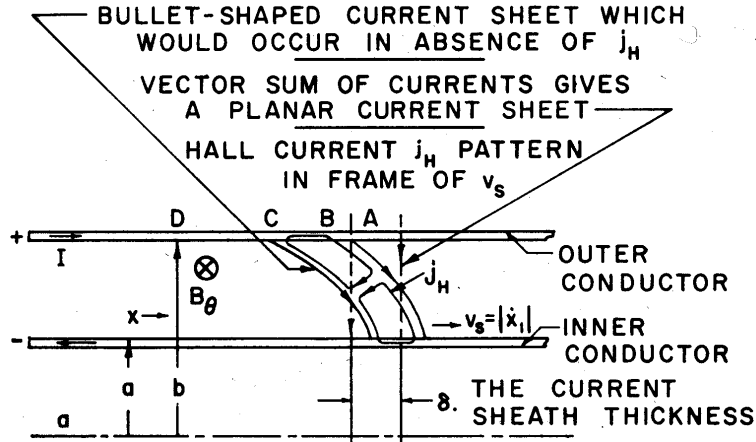


Figure 2.7: Bostick's suggested Hall current pattern which is used to explain the planar current sheet observed by Keck[20] with negative polarity.

2.1.4 Stevens Institute of Technology (1963)

Bostick[23] attempted to explain the polarity dependence in the current patterns observed by Keck[20]; he hypothesized that the variation in current sheet shape was a result of Hall currents within the sheet. The Hall currents which he described are not the Hall currents which would arise from $\mathbf{E}_{\text{applied}} \times \mathbf{B}$ drift but, rather, drifts associated with the back emf from the motion of the current sheet encroaching on a stationary plasma (in front of the current sheet), $\mathbf{E}_{\text{emf}} \times \mathbf{B}$.

Figure 2.7 illustrates Bostick's theory of how a planar current sheet is realized in a coaxial accelerator. In the absence of any other effects, the current sheet would be expected to accelerate more rapidly along the center electrode due to the radially (outward) decreasing magnetic pressure. However, as plasma is entrained in the current sheet, an electric field, tangential to the current sheet, arises (i.e., the back emf associated with bringing the plasma from rest up to the sheet propagation speed). This field, \mathbf{E}_{emf} , when crossed with the self field \mathbf{B} , leads to a Hall current directed perpendicular to the current sheet. The vector sum of this Hall current and the conduction current yields a planar current sheet.

Bostick further notes that, due to the $1/r$ variation in the magnetic field, there will exist a radial shear in the electric field. This will lead to current vortices and mass circulation within the current sheet. He adds that this theory is supported by the experimentally measured electric field profiles of Burkhardt *et al.*[14], which exhibit a dip that is characteristic of plasma vortices in a magnetic field.

Comments: Bostick’s paper is the only one that postulates the existence of such structures; however, the hook-like features observed in the Princeton studies could possibly be related. Following the phenomenological model presented in Bostick’s paper, it is unclear what the current sheet would look like if more than the two illustrated “plasma vortices” are present.

2.1.5 Institut für Plasmaphysik Garching bei München (1963)

A single paper from this group by Liebing[24] presented data that clearly showed the presence of current sheet canting. A parallel plate accelerator (two copper electrodes 8 cm wide, 80 cm long and 5 cm apart) with argon propellant at various pressures (20 mTorr to 3 Torr, ambient fill) was used. A 10 capacitor PFN produced an approximately square 60 kA current pulse of 35 μ s duration. Diagnostics included a streak camera, magnetic field probes, and a fast-framing camera.

Figure 2.8 shows a schematic of Liebing’s accelerator and current contours that he interpreted from magnetic field probe data. The current streamlines clearly indicate the presence of tilting of the current sheet, roughly 45° , with the anode attachment leading the cathode attachment. Also, the anode arc attachment appears more diffuse than on the cathode side. Liebing reports that after switching the polarization of the electrodes, the current distribution shown in the figure was inverted, but no theoretical explanation was offered.

Comments: Unfortunately, Liebing’s article does not contain many experimental details

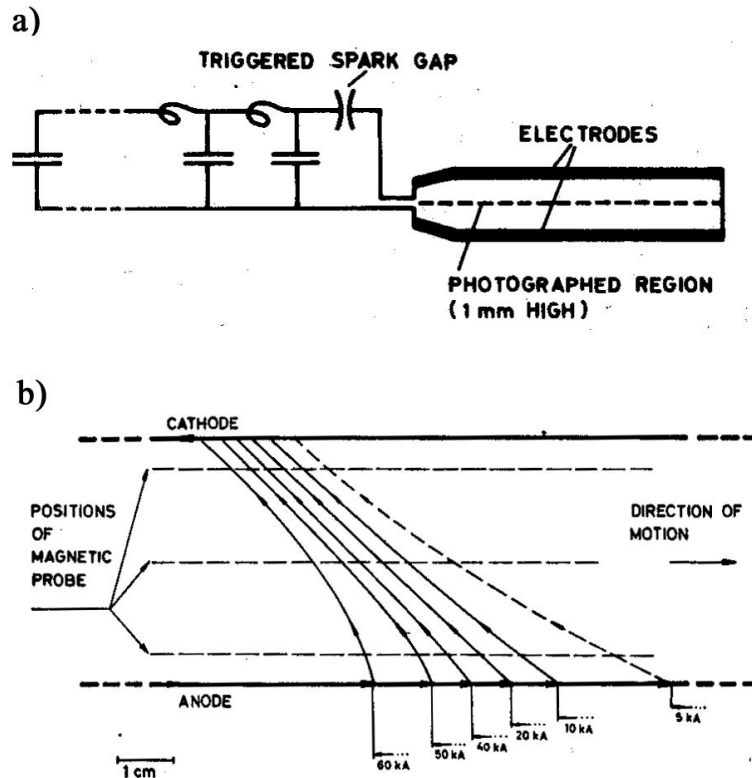


Figure 2.8: Figures from Liebing[24]: a) accelerator schematic, b) current distribution in plasma (argon, 130 mTorr.)

or technical discussion (even the axial position at which the current profile data was taken is not specified.) He notes the tilting of the current sheet but does not suggest what causes it.

2.1.6 General Atomic Division of General Dynamics Corporation (1964-66)

Lovberg continued his research into current sheet physics by carrying out schlieren photography experiments in both rectangular and coaxial geometry accelerators. Several of the published images from these studies are shown in Fig. 2.9.

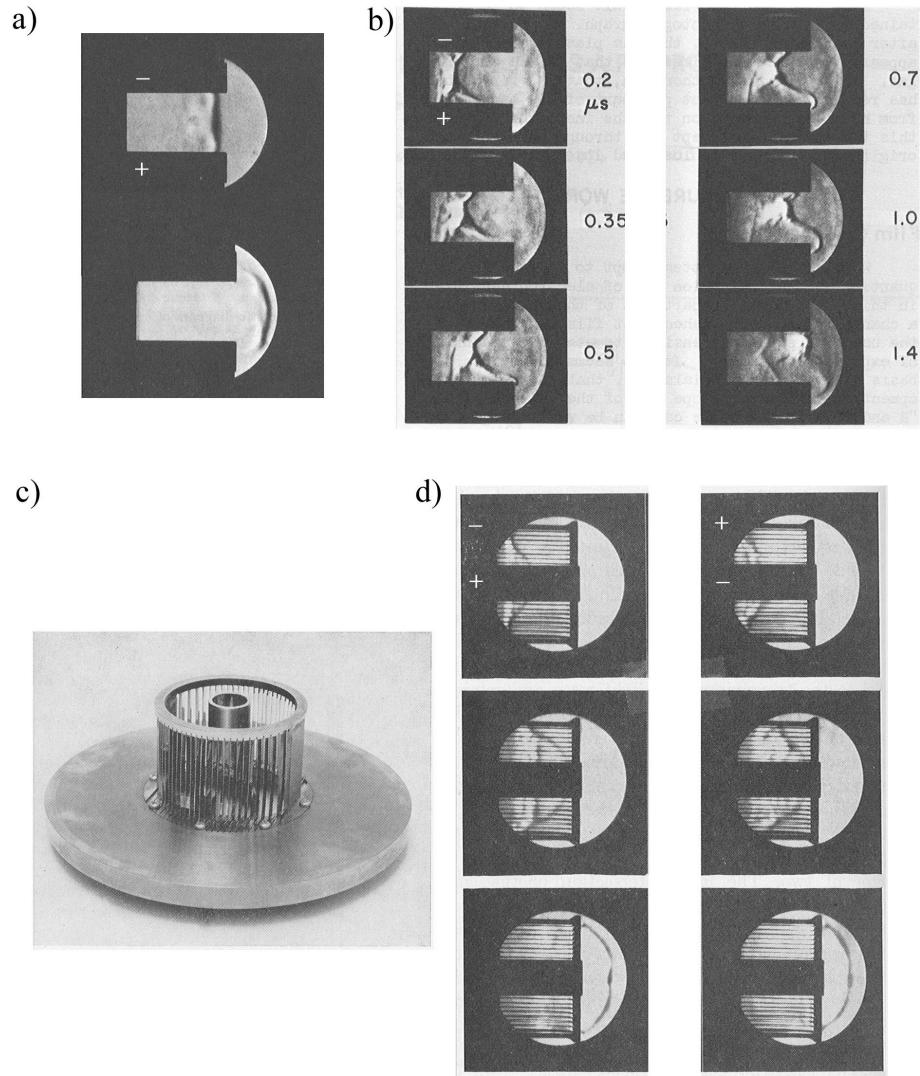


Figure 2.9: Figures from Lovberg[25][26]: a) schlieren photographs of rectangular geometry accelerator (Hydrogen (300 mTorr)), b) schlieren photographs of rectangular geometry accelerator (Nitrogen (120 mTorr)), c) photograph of slotted-anode coaxial accelerator, d) schlieren photographs of coaxial geometry accelerator (Hydrogen (300 mTorr)).

Figures 2.9a and 2.9b show images from the rectangular geometry study[25]. The dimensions of the accelerator channel were $6(L) \times 8(W) \times 3.8(H)$ cm. A single $3 \mu\text{F}$ capacitor charged to 16 kV yielded 100 KA peak current in hydrogen (300 mTorr, ambient fill).

Figure 2.9a shows two images from hydrogen discharges (the top electrode is the cathode.) The top image shows the current sheet just as it reaches the end of the electrodes; the

bottom image shows the ejected current sheet. In the top image, it is clear that the current sheet is planar and perpendicular to both electrodes. This ideal orientation of the current sheet is starkly contrasted by the current configuration realized in a nitrogen discharge, as shown in Fig. 2.9b. These photographs show that as the discharge evolves, canted structures develop along both electrodes – with the anode canting being most pronounced (the bottom electrode in the photographs). Lovberg also saw these asymmetric features in hydrogen discharges in which contamination of the electrodes was suspected; cleaning of the electrodes resulted in a return to the planar behavior illustrated in Fig. 2.9a. The structure of the nitrogen discharge, however, remained invariant, regardless of the electrode preparation procedures.

In an attempt to clarify the results of his earlier work with a coaxial accelerator[14], and to explore the polarity effects observed by Keck[20], Lovberg conducted schlieren photography experiments on a coaxial geometry accelerator[26]. The same imaging system and power supply that was used in the rectangular geometry experiment was utilized in this experiment as well, but the parallel plates were replaced with the slotted wall coaxial accelerator shown in Fig. 2.9c. All experiments used hydrogen (500 mTorr). Figure 2.9d shows sequences of photographs typical of those obtained in the study. The three figures on the left were obtained with positive polarity (anode center electrode) while the three photographs on the right of the figure were taken with negative electrode polarity. The top, middle, and bottom photographs were taken at 0.45, 0.75, and 1.05 μsec after initiation, respectively.

Consider first the the positive polarity case. The current sheet is seen to form a bullet shape, as one would expect for the $1/r^2$ force distribution in a coaxial accelerator. What is unexpected in the photos is the formation of a second planar sheet behind the first, curved sheet. Subsequent experiments with magnetic field probes showed that the second sheet,

while clearly having substantial plasma density, carries little to no current. The first current sheet in the negative polarity case looks very similar to the current sheet observed with positive polarity. However, the second planar current sheet is not seen to form with negative electrode polarity.

Comments. Lovberg’s first paper[14] (rectangular geometry) was the first to show that current sheet canting is a species-dependent phenomenon. What Lovberg called “unstable” operation in Hydrogen could have been the result of the presence of other gas species in his propellant which, for example, could have come from “dirty” electrodes. When he eliminated these contaminants, the current sheet returned to its planar, “stable” configuration.

The results of Lovberg’s coaxial accelerator study are at variance with both Keck’s work and his own earlier study. The polarity dependence observed by Keck was not observed; also, the planar current sheet that was observed in Lovberg’s earlier study was not repeated in this later experiment. One possible explanation is the difference in the gas loading: the earlier experiment used gas injectors whereas the later study used an ambient pre-fill. Also, the use of a slotted outer electrode may have influenced the evolution of the current sheet in the second study. We will return this issue later in the thesis, where it is proposed that the current sheet canting is tied to the plasma conditions near the anode.

2.1.7 The University of Strathclyde (1966)

MacLelland[27] published one paper showing schlieren and framing camera images from a parallel plate accelerator using hydrogen, nitrogen and argon propellants (ambient fill). The accelerator electrodes (brass) were $30(\text{L}) \times 5(\text{W})$ cm and separated by 5 cm. Detachable, transparent, sidewalls ran the length of the accelerator (the type of sidewall material was not specified). A 20 μF capacitor bank delivered 600 J of energy with a damped sinusoidal (10 μs period) current waveform (no current magnitudes are given). The light source for

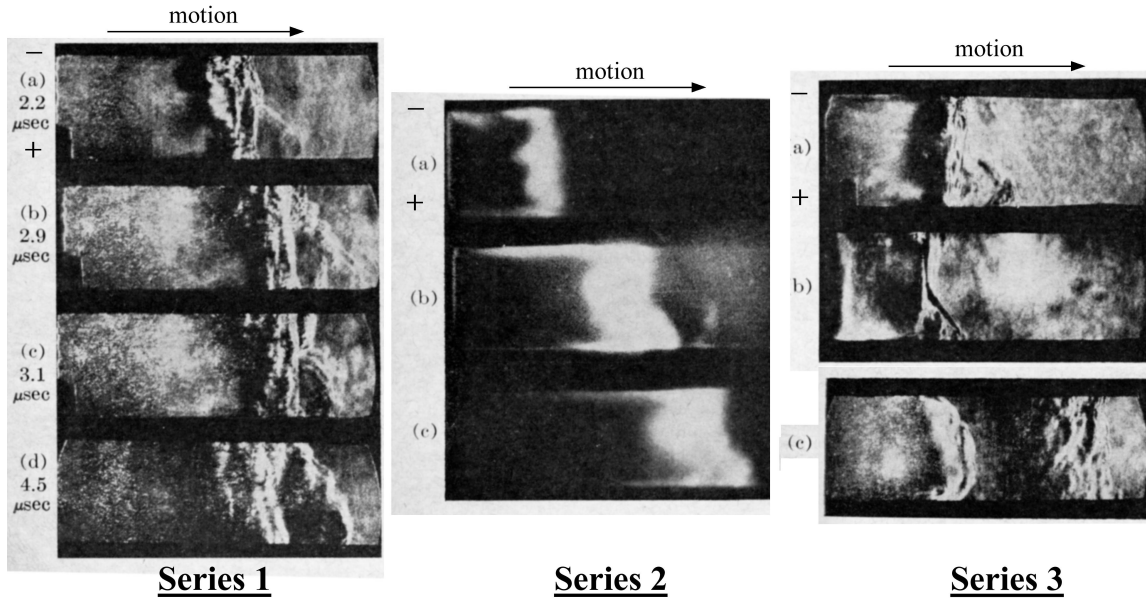


Figure 2.10: Figures from MacLelland[27]. **Series 1:** series of schlieren photographs (hydrogen, 750 mTorr) taken at various times; the anode is on the bottom and the plasma travels from left to right. **Series 2:** series of framing camera pictures (hydrogen, 750 mTorr). **Series 3:** schlieren photographs of a) nitrogen discharge (500 mTorr, $2.2 \mu s$), b) argon discharge (500 mTorr, $2.2 \mu s$) and c) argon discharge (500 mTorr) showing presence of both first and second half-cycle current sheets.

the schlieren images was a pulsed ruby laser.

Figure 2.10 shows some of the more revealing images from the study; with the exception of series 3c, the anode was the bottom electrode. In series 1, schlieren photographs of a hydrogen discharge at several times are shown. These pictures show that initially the main current front is at right angles to the electrodes; however, later in the discharge a new, inclined current filament is seen to emanate from the main current sheet. Series 2 shows a set of framing camera pictures taken under the same conditions; the inclined front seen in the schlieren photographs is only faintly visible in series 2b. The authors suggested that the relatively long exposure time of the camera (150 ns) smeared out the evolution of the second current front. Series 3a shows a schlieren photograph taken with nitrogen propellant; features similar to those observed in the hydrogen discharge are apparent. The argon

discharge illustrated in series 3b shows some features not seen in hydrogen or nitrogen. First, the current sheet is much more defined (thinner). Also, the current front is normal to the electrodes on the cathode side, but is inclined on the anode side. Series 3c shows a schlieren photograph of an argon discharge after the circuit current has reversed (the anode is the top electrode in the photo.) The original current sheet plasma is near the right hand side of the photograph, while a new current sheet is seen to have formed to its left. It is interesting to note that the second current sheet does not have an anode-leading canted, profile but, rather, the anode attachment appears to tilt backward toward the breech.

MacLelland makes some other observations about his photographs. In the framing camera images (and in some of the schlieren images that had an appropriately aligned knife edge) a dense plasma layer was observed along the cathode, behind the current sheet. Also, he found that the “texture” of the schlieren images varied with pressure. At low pressures the schlieren images had a smooth uniform appearance, whereas the images appeared granular at higher pressures. He offers no physical explanation for either of these observations.

Comments. MacLelland’s observations are generally consistent with those of Lovberg’s rectangular geometry accelerator study(section 2.1.6)[25]. The nitrogen schlieren images in both studies look very similar, while the hydrogen images in MacLelland’s paper resemble the “unstable” current sheet images reported by Lovberg; MacLelland may have been operating with “dirty” electrodes or, possibly, the longer duration of the current pulse in MacLelland’s experiment may have allowed sufficient time for ablated electrode products to diffuse into the current sheet and influence the canting angle.

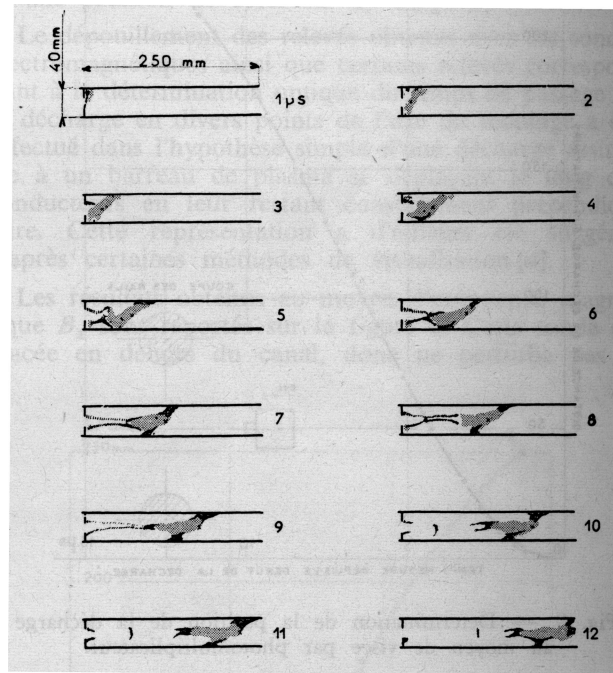


Figure 2.11: Evolution of a pulsed discharge between two parallel rods (argon (100 mTorr)) (from Robert and Redding[28].)

2.1.8 ONRA (France) (1968)

Robert and Redding studied the evolution of a pulsed discharge between two parallel rods[28]. This short ONRA internal technical report gives few technical details; however, it does provide sketches of the evolution of an argon discharge (ambient fill) in their device (see Fig. 2.11). The figure shows a series of snapshots in $1 \mu\text{sec}$ increments. Two sharp pins were placed at the breech of the accelerator to encourage initial breakdown in that area; the pictures indicate that the current continues to attach to these pins long after the main current channel has moved away from the breech. Also, it is clear that the arc cants as it progresses along the rods, with the top electrode (anode) current attachment leading. The authors suggest that this canting is due to the Hall effect, with no further elaboration.

2.2 Summary and Discussion

This review has attempted to be a comprehensive summary of the current sheet accelerator literature in which current sheet canting was noted. Other pertinent areas of research may include plasma armature railguns, dense plasma focus, and plasma erosion opening switches. These sources of information were not exhaustively surveyed because the operating conditions in these devices are generally much different than those encountered in pulsed plasma thrusters, which is the application of primary interest in the present study. For example, railguns generally operate at significantly higher plasma densities and plasma focus experiments and opening switches typically conduct mega-amp currents. Therefore, conclusions reached in those studies may have little relevance to the significantly lower density and current devices which we are concerned with here.

Let us summarize the conclusions that can be drawn from the literature reviewed in the previous section:

- Current sheets are always observed to cant with nitrogen and argon propellant – irrespective of geometry (rectangular, coaxial, z-pinch, inverse z-pinch, and parallel rod), gas pressure, or current level.
- Current sheet canting always occurs in an orientation such that the anode current attachment leads the cathode current attachment.
- Uncanted hydrogen and deuterium current sheets have been observed but only with specially prepared electrodes.
- Ion current conduction is believed to play an important role in establishing the overall current pattern.
- Current sheets appear to exhibit invariant features (e. g. anode foot, cathode hook,

and canting) over a wide range of geometries, propellant species, gas pressures, and current levels.

- Conflicting experimental results exist with regard to the influence of polarity in coaxial accelerators, but variations in the construction (e.g., slotted electrodes) may account for the different observations.

The conclusions enumerated above show that current sheet canting has been observed in many studies. However, there was no unanimity of opinion as to its origin. Furthermore, no study has accurately quantified canting angles. The remainder of this thesis attempts to address these deficiencies through targeted experiments and theoretical analysis. To isolate the current sheet canting effect we have followed the lead of Lovberg in using a rectangular geometry accelerator. This geometry eliminates the radial field variation found in the coaxial geometry, provides ease of diagnostic access, and is amenable to analytical studies. One significant difference in the present study is the use of a pulse forming network; almost all of the experimental results described in the review above used sinusoidal waveforms. In doing so, the intent was to eliminate any phenomena that result from current transients and also make the analytical studies more tractable.

Chapter 3

Apparatus

This chapter describes the components of the CSCX (Current Sheet Canting Experiment) experimental apparatus. The design rationale and performance of the accelerator, pulse forming networks, vacuum facility, and data acquisition equipment are described in detail.

3.1 General experimental layout

The basic components of the CSCX experimental apparatus are the accelerator, pulse forming network, vacuum facility, and data acquisition equipment. The general layout of these components is illustrated in Fig. 3.1.

Tables inside the vacuum chamber support the accelerator and provide mounting surfaces for optics and diagnostic probes. A $4' \times 6'$ optics table, positioned next to the tank, was used to lay out optical diagnostics. Glass windows on the sides of the vacuum chamber provided optical access to the accelerator discharge. Two Faraday cages were used to house the data acquisition equipment.

The overriding design rationale was to create an accelerator configuration which provided convenient access to optical and probe diagnostics. Furthermore, it was desired that

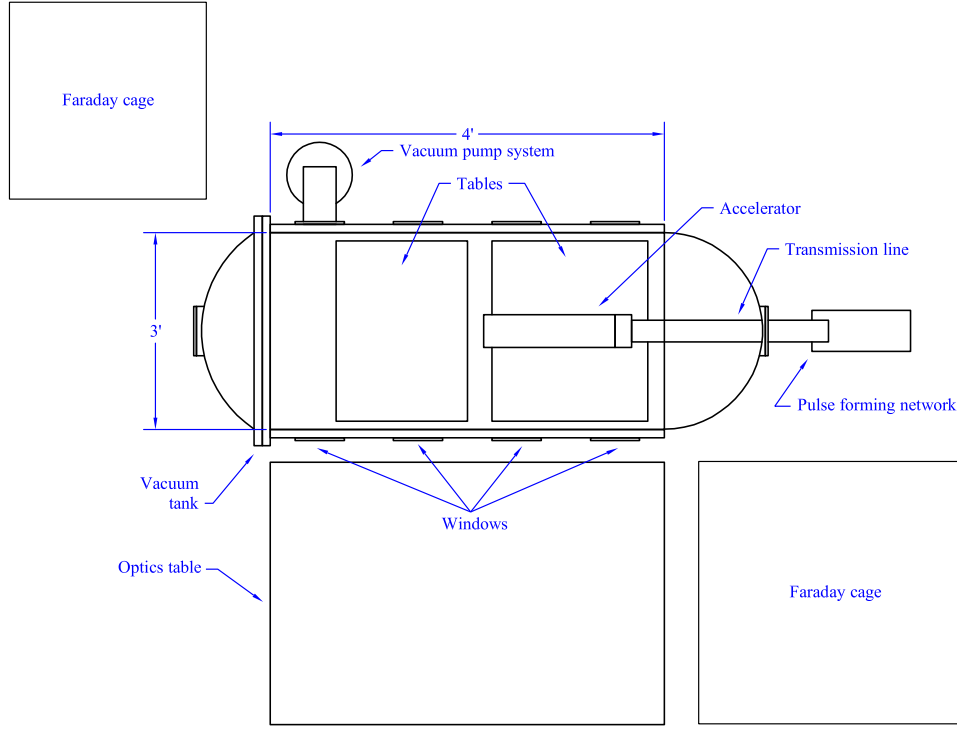


Figure 3.1: Top-view schematic of the general experimental layout.

the configuration would be amenable to analytic modelling (e.g., one-dimensional electromagnetic fields, constant current, etc.). Details about each of the major components of the apparatus are given in the remaining sections.

3.2 Accelerator

The CSCX Accelerator is a parallel-plate pulsed plasma accelerator with glass sidewalls (a schematic illustration with relevant dimensions is shown in Fig. 3.2). The dimensions of the discharge chamber were chosen to be similar to those found to “work” by earlier researchers (see, for example, Eckbreth[19]). The electrodes are made of copper and the sidewalls are made of Pyrex. The sidewalls reduce the region accessible to the discharge to 10 cm (width), whereas the electrodes themselves are 15 cm wide. The motivation for using

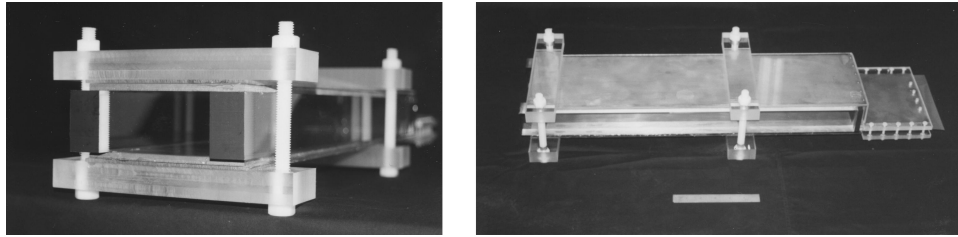
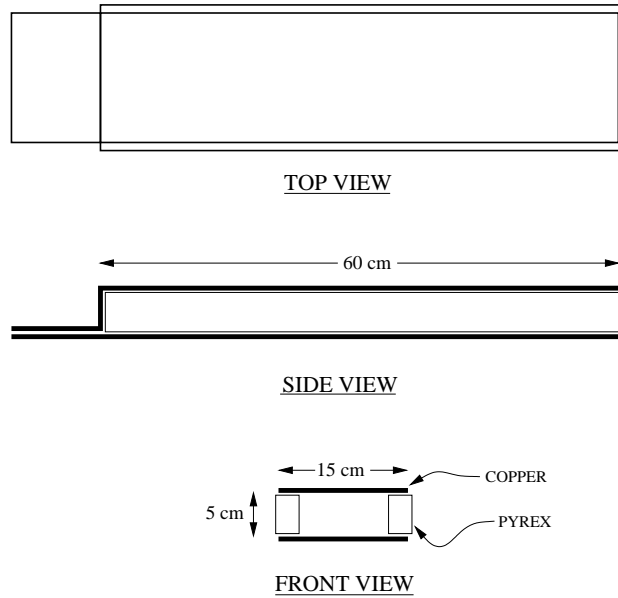


Figure 3.2: Schematic and photographs of the CSCX accelerator.

Pyrex sidewalls is several-fold: first, they provide an excellent optical view of the discharge, second, they isolate the current sheet to a well-defined spatial region, third, they isolate the discharge from electric field singularities which are associated with the sharp edges of the electrodes, and last, they isolate the discharge from the rapidly fringing magnetic field at the edges of the electrodes. The two latter benefits tend to make the discharge environment more conducive to the formation of spatially uniform current sheets.

Propellant loading was accomplished using the ambient fill technique. After the vacuum tank was pumped down to its base pressure (1×10^{-5} Torr), the entire tank was brought to the desired operating pressure with the chosen propellant (hydrogen, deuterium, helium,

neon, argon, krypton, xenon, and methane were used in the present study). This resulted in a uniform gas distribution within the accelerator prior to discharge initiation. Approximately ten pulses at full capacitor bank voltage were executed before taking data in an attempt to remove adsorbed gases from the electrodes. It is uncertain whether or not this preparation technique was sufficient to remove contaminants from the electrodes.

In general, the accelerator performed very well; current sheets were generated in the expected manner (i.e., formation at the breech and propagation to the exit) and the experiments were very repeatable. High speed photographs (see section 5.2) taken of different discharges (with the same initial conditions and same camera time delay) were practically indistinguishable.

3.3 Pulse forming networks

The accelerator was powered by a pulse forming network (PFN). Two different PFNs were used in the experiments; this was necessitated by a failure of two of the capacitors in the original capacitor bank. This section describes the basic design of the two PFNs; details about the designs (e.g., calculation of component values, numerical circuit simulations, etc.) are given in Appendix A.1.

The values of the electrical components at each stage of the PFNs were chosen to give a nearly flat current profile with a pulse width that corresponds to the time it takes the current sheet to traverse the length of the accelerator. Assuming a sheet propagation speed of 2-3 cm/ μ s (which is typical of gas-fed pulsed plasma accelerators found in the literature), a pulse width of approximately 20-30 μ s is required to allow the current sheet to traverse the (60 cm) length of the electrodes. With a given set of capacitors, electrical design of each PFN entailed determining the proper stage inductance to give the desired pulse length.

As described in Chapter 1, it is desirable for the current rise rate (dI/dt) to be as large

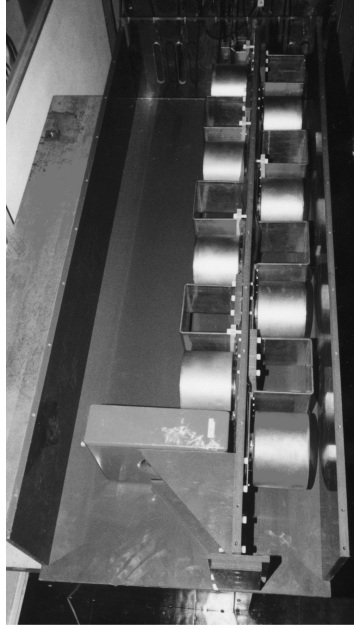
as possible. Since $dI/dt \propto V_o/L_o$ (L_o is the initial, or parasitic, inductance, V_o is the initial capacitor bank voltage), special care was taken to configure the conductors which connect the PFN to the accelerator in a low inductance geometry.

The final designs of PFN I and II are described below. Detailed electrical, electromagnetic, and mechanical design notes are given in Appendix A.1. A complete electrical schematic of the CSCX power supply is shown in Fig. A.5.

3.3.1 PFN I

Eight capacitors from the LES 8/9 series of ablative PPTs[29] were available to be used for PFN I. These cylindrical capacitors have a capacitance of about $18 \mu\text{F}$ and are rated at 3 kV. In the experimental configuration, each stage of PFN I was composed of an $18 \mu\text{F}$ capacitor in series with a 60 nH inductor. The bank voltage was generally set to 5 kV, yielding a total discharge energy of about 2 kJ. The PFN was switched into the accelerator using an ignitron. The peak current was approximately 60 kA (with 5 kV bank voltage), with an initial rise rate on the order of 10^{10} A/s. The duration of each pulse was about 20 μs , which was followed by one cycle of damped ringing. The experimentally measured current waveform closely followed the design waveform, up to the point of voltage reversal. Examples, and more detailed analysis, of these waveforms are given in Chapter 6: Experimental Results.

PFN I experienced a catastrophic short-circuit which destroyed two of its capacitors, after having successfully generated about three thousand pulses over a period of about two years. The failure was most likely due to continually charging the capacitors above their rated voltage.



PFN I



PFN II

Figure 3.3: Photographs of complete PFN assemblies.

3.3.2 PFN II

PFN II was designed to replace PFN I. Custom-made capacitors were obtained from Maxwell Technologies, Inc.. These rectangular capacitors have a capacitance of $10\ \mu\text{F}$ and are rated at 10 kV. Higher voltage capacitors (compared with PFN I) were chosen in order to generate higher dI/dt and peak currents – which leads to better defined current sheets. Dual-ended capacitors were selected for ease of mechanical assembly. PFN II used ten stages; each stage was composed of a $10\ \mu\text{F}$ capacitor in series with a $100\ \text{nH}$ inductor. The bank voltage was generally set to 10 kV, yielding a total discharge energy of 5 kJ. The PFN was switched into the accelerator using an ignitron. The peak current was approximately 75 kA, with an initial rise rate on the order of $10^{11}\ \text{A/s}$. The duration of each pulse was about

20 μ s, which was followed by one cycle of damped ringing. The experimentally measured current waveform followed the design waveform, up to the point of voltage reversal. Examples, and more detailed analysis, of these waveforms are given in Chapter 6: Experimental Results.

3.4 Vacuum facility

The vacuum facility used in this experiment (see figure 3.1) is described in detail by Jahn [16]. The vacuum vessel is a 3' diameter, 6' long cylindrical tank made entirely of Plexiglass (which has been shown to eliminate the electromagnetic interactions sometimes found in metallic vessels), with glass optical access windows. Gases are introduced into the tank using a regulated feed-through. The tank uses a diffusion pump with a freon-cooled trap to achieve a base pressure of 1×10^{-5} Torr. Sub-milliTorr pressures were measured with a CVC cold cathode gauge. All pressures above one milliTorr were monitored using a MKS Baratron vacuum gauge; this gauge gave a gas-species-independent reading which allowed an accurate measurement of the initial propellant pressure in the accelerator.

3.5 Data Acquisition Equipment and Noise Suppression

The data recording equipment used in the experiments consisted of a digital oscilloscope, a high-speed film camera, two CCD cameras, and a personal computer. The oscilloscope, a Tektronix TDS 460A, is capable of sampling signals at up to 200 MHz – much faster than any time-varying phenomena which were observed in the present work. A Dell XP200 computer was used to record oscilloscope waveforms, via a GPIB connection and Labview software. The oscilloscope and computer were housed in a Faraday cage to suppress RF noise pickup. Specifications for the cameras are given in Chapter 5: Diagnostics.

Pulsed power experiments can suffer from undesirable electromagnetic coupling of the various experimental and diagnostic equipment components. These interactions can introduce noise, cause components to trigger out of the desired sequence, or even destroy some sensitive electronic equipment. To avoid these negative effects, in addition to the use of Faraday cages, two measures were taken: a single point ground and optical isolation of all trigger circuits.

In order to maintain a constant potential reference (ground) in the lab space, almost all of the lab floor was covered with copper sheet (200 square feet). A large diameter copper ground wire (size 00), which is connected to a large copper plate buried outside the building, was connected to this sheet. All equipment (charging circuitry, Faraday cage, oscilloscope, etc.) used this copper sheet as their ground reference. This helped to eliminate ground-loops, which can cause high voltage transients in equipment when the accelerator is fired.

Many of the diagnostic experiments relied on the accurate sequential triggering of several components of the experiment. For example, the schlieren photography experiment required that the camera, accelerator, oscilloscope, and laser to be triggered in the given order and with specific time delays between each trigger. It was observed that because all of the components were connected, RF noise, reflections, etc., created in one device could travel through interconnecting BNC cables and cause another device to trigger prematurely. To eliminate this effect, an optical isolation scheme was implemented. A six channel box in which the input and output signals are optically coupled via optocouplers and TTL line drivers was constructed. This box only allows signals to travel from the input BNC to the output BNC. Spurious signals that enter from the output side are not communicated back through the input; thus, cross-talk between the components is eliminated. The electronic details of this box are given in Appendix A.3.

Chapter 4

Diagnostics

This chapter gives detailed descriptions of the diagnostics which were applied to obtain both qualitative and quantitative information about the current sheet plasma in the CSCX accelerator. Details regarding calibration of the diagnostic devices are given in appendix B.

4.1 Circuit current measurement

The total current delivered to the CSCX accelerator was measured using a commercial current transformer. Both PFN I and II used a Pearson Model 301X current transformer located between the final capacitor/inductor stage and the accelerator (see figure 3.3.) No calibration procedure was carried out to verify that the published characteristics were accurate; however, the simplicity and ruggedness of the device make it unlikely for it to fall out of calibration. The published specifications for the current monitor are given in appendix F. The output of the transformer (with two calibrated 50Ω 10X attenuators in series) was recorded using a Tektronix model TDS-460A digital oscilloscope.

4.2 Voltage measurement

The terminal or “muzzle” voltage in a pulsed electromagnetic accelerator represents the contribution of the plasma resistive voltage drop and the sheath potential; since little to no magnetic flux exists in front of the current sheet, a terminal voltage probe does not detect the (very large) inductive voltage drop that occurs behind the current sheet. Therefore, by measuring the terminal voltage drop, a rough estimate of the plasma resistivity can be calculated[14].

The development of a specialized voltage probe was necessitated by the wide range of voltages to which the probe is exposed. Just before the discharge initiation, the probe is exposed to the full bank voltage (~ 10 kV). As the current sheet propagates the probe sees only the resistive and sheath voltage drop (~ 100 V). Finally, when the current sheet reaches the end of the electrodes, the probe measures both the resistive and inductive voltage drop (~ 1 kV). Furthermore, because of the highly transient nature of the discharge, both accelerator electrodes may float up to high voltage relative to the ground potential. This latter situation poses a serious threat to any data acquisition equipment (e.g., an oscilloscope) connected to the voltage probe. Two measures were taken to enable an accurate and safe measurement of the terminal voltage in the present study: a differential high voltage probe was constructed, and a battery powered, floating oscilloscope was used to record the probe output. A differential voltage probe measures the potential difference between two electrodes directly without reference to an external reference potential, that is, it is insensitive to the electrodes instantaneous potential relative to the ground potential.

The voltage probe used in the present study was a differential probe with 100:1 attenuation and both DC and AC compensation elements. The construction details are given in appendix A.4 and the calibration procedure is outlined in appendix B.1. The output of the probe was recorded on a Tektronix model 3032 battery powered digital oscilloscope.

4.3 High-speed photography

The camera used in this study, a Hadland Photonics Imacon 792LC, is capable of taking pictures at a rate of up to 20 MHz and provides up to sixteen images printed on Polaroid film. In the experiments presented here, the framing rate was set to 500 kHz; the exposure time for each image was 400 ns. This camera was useful for creating movies which show how the discharge evolves spatially during the entire pulse.

The layout of the photography experiment is shown in Fig. 4.1. The camera was placed at one of two positions. Position 1 was used to photograph the breech section of the accelerator; position 2 was used to photograph the mid-section. In order to more easily visualize the spatial position of the current sheets and to estimate the size and orientation of current sheet features, a black screen with white gridding (1 cm spacing) was placed on the outside of one side of the accelerator. The propagation speed of the current sheet was estimated by comparing successive frames in a single shot (with known inter-frame time delay). The canting angle was estimated graphically, using the photographs, by drawing two lines, one parallel to the cathode and one parallel to the luminous front, and measuring the angle between them.

4.4 Schlieren imaging

Since the photographs obtained in the present study relied on monitoring optical emission, they may not necessarily show the position of the current sheet. A more direct method is to visualize the current sheet through light refraction as it passes through its steep electron gradients.

The term “schlieren techniques” refers to the broad class of optical diagnostics which exploit the fact that light from a source external to a test object (a flowing gas, for example),

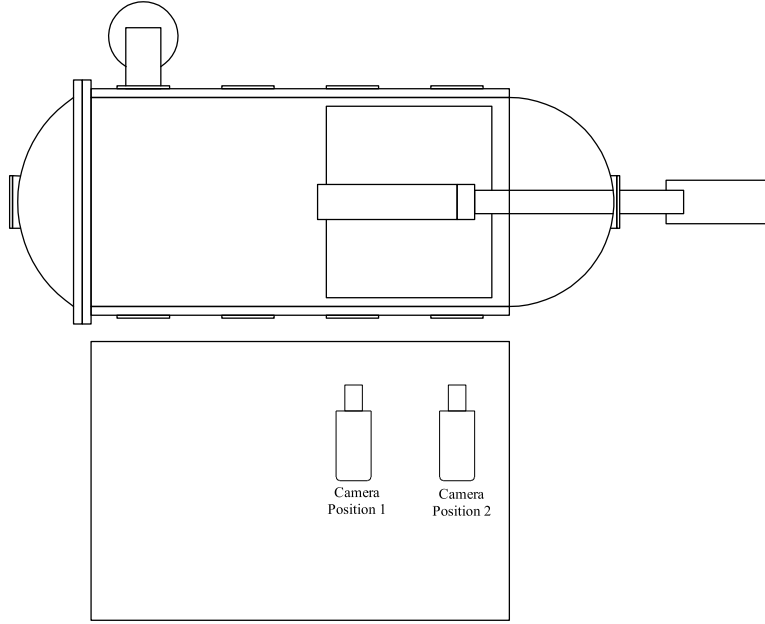


Figure 4.1: Schematic of high speed photography experimental layout.

when made to pass through it, will be refracted by any density gradients which exist in the flow. After passing through the flow, with appropriate optical arrangements, the refracted and un-refracted light can be separated to yield an image with dark and light areas which correspond to disturbed (i.e., areas where density gradients exist) and undisturbed regions of the flow, respectively. So, in the case of visualizing current sheets, the high electron density gradient associated with a thin, propagating current sheet should produce an image with high contrast in the areas which correspond to the spatial extent of the sheet. It was hoped that visualization of the current sheet using schlieren techniques would give better spatial and temporal resolution of the position of the current sheet, since these techniques rely upon directly imaging electron density gradients. This would allow for more accurate calculation of properties such as canting angle and sheet sweeping speed.

Schlieren techniques have been used by earlier researchers to visualize current sheets. Notably, both Lovberg *et al.*[25] and MacLelland *et al.*[27] used schlieren photography with parallel plate accelerators similar to the device used in the present work. We have

implemented a wide variety of optical arrangements, which are described below, in an attempt to obtain similar results.

4.4.1 Light source

Pulsed Nd:YAG lasers were used in all of the schlieren experiments. The first, a Continuum Minilite II, was capable of generating a 5 ns burst of radiation (532 nm, 25 mJ). The second, a Continuum NY61-20, was rated at up to 100 mJ at 532 nm. In both cases, the output energy was not measured, so it is uncertain if the lasers were operating at their peak capability.

4.4.2 Camera

The camera used to acquire images was a Kodak DCS 460 digital camera. This camera has a mechanical shutter and a six million pixel color CCD array. A 532 nm laser line filter was placed over the camera lens in order to discriminate laser light from the accelerator plasma emission. Acquired images were downloaded directly to the data acquisition computer.

4.4.3 Schlieren optical arrangements

Schlieren techniques are well developed and have been used to visualize many different types of flows. The basic principles of the method can be found in the standard references[30]. Four optical arrangements were used in the present experiments – the conventional schlieren and three variations of the shadowgraph configuration.

Conventional schlieren layout

The most complicated of the optical arrangements used was the schlieren photography arrangement. Figure 4.2 shows the schlieren photography experimental configuration used

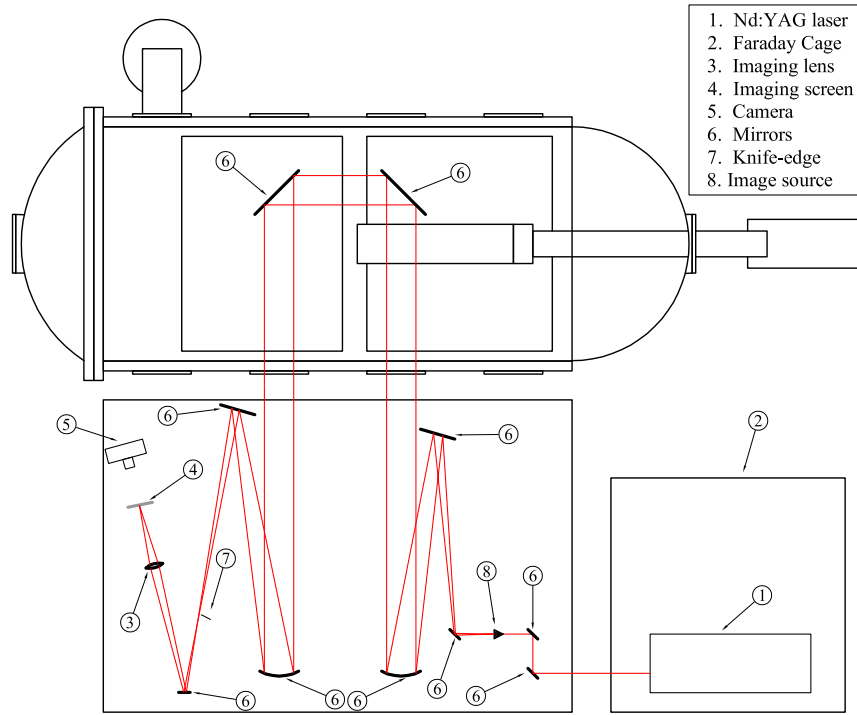


Figure 4.2: Schematic of schlieren photography optical arrangement.

in the present study.

Schlieren photography involves imaging a light source through a system of optical elements. The criteria for a useful schlieren photography light source are that it have a *finite size* and that it *radiates isotropically*. A laser, which has a very small cross-section and is highly collimated, violates both of the criteria. In order to use our lasers as a light source, the beams were expanded with a microscope objective and diffused through a masked opal glass slit (2 mm x 10 mm). Six inch diameter mirrors were used for both the collimating and focussing lenses. A razor was used as a knife edge and the centerline of the accelerator electrodes was imaged onto a ground glass screen using a 3" lens.

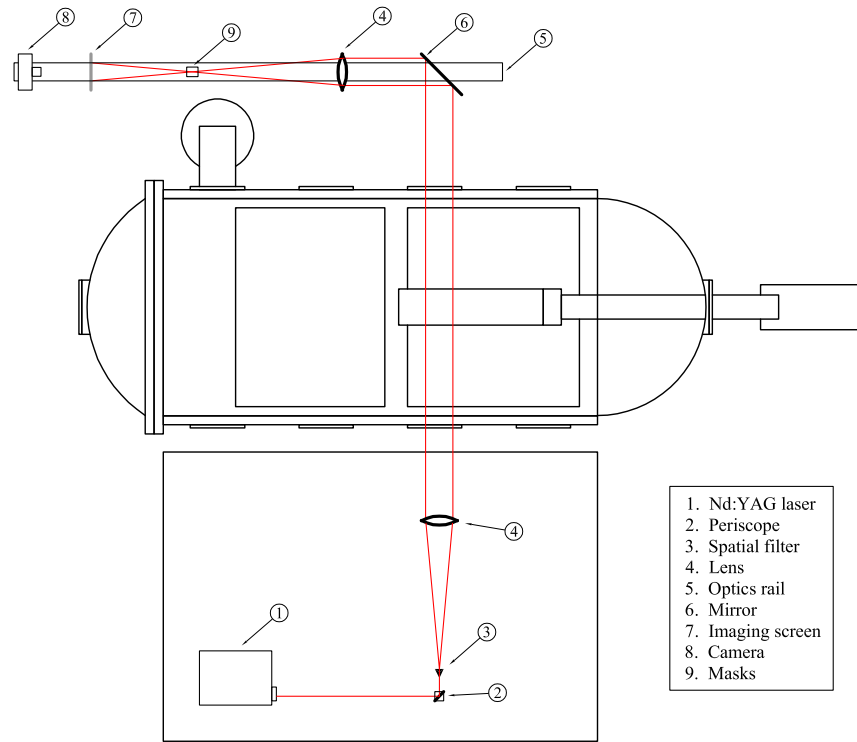


Figure 4.3: Schematic of shadowgraph optical arrangement.

Shadowgraph configuration

The shadowgraph configuration is the simplest of the optical arrangements used. The source and collection optics for this configuration are shown in figure 4.3. Unlike in the schlieren photography arrangement, in the shadowgraph configuration it is desirable to have the smallest source size possible; in our experiments the laser was passed through a spatial filter with a $25\text{ }\mu\text{m}$ pinhole to provide a small source as well as to expand the beam to the desired diameter ($\sim 4\text{ in.}$). Six-inch diameter lenses were used for both the collimating and focusing lenses. The collection optics consisted of only a focusing lens and a ground glass plate.

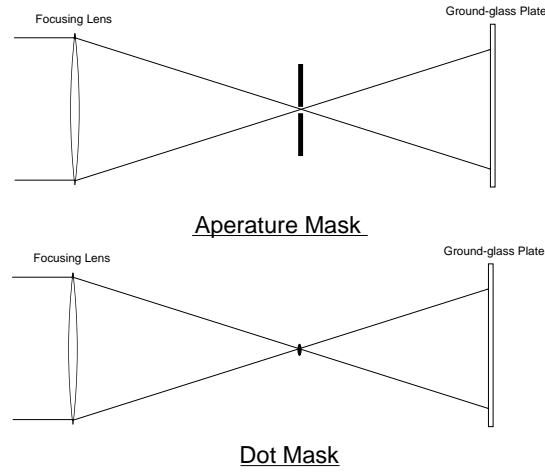


Figure 4.4: Schematic of modified shadowgraph collection optics.

Modified Shadowgraph Configurations

In the modified shadowgraph scheme the source optics are the same as in the standard shadowgraph configuration. The difference lies in the collection optics, which use masks at the focal plane of the focusing lens to intercept (or pass) refracted rays. The masks allow the modified shadowgraph technique to have (theoretically) near-infinite contrast. Two different types of masks were used in the present study: a pinhole aperture and a “dot” mask (see Fig. 4.4). The pinhole aperture allows all of the un-refracted light to pass, resulting in a shadowgraph image with an illuminated background and dark striations, while the dot mask produces the opposite effect – illuminated striations on a dark background.

4.4.4 Experimental timing

The component trigger timing requirements in the schlieren photography experiments were especially stringent because the timing of three instruments had to be carefully coordinated. A Stanford Research digital delay generator (model DG535) and the optically isolated trigger box (see section 3.5) were used to: 1) open the shutter on the camera, 2) fire the accelerator, and 3) fire the laser when the current sheet had reached the imaging location.

The accelerator current waveform and laser q-switch timing signal were monitored on an oscilloscope to assure that the laser was firing at the desired time in the current pulse.

4.5 Magnetic field probes

Magnetic field probes were used to determine the current sheet canting angle by monitoring the response of two probes at different spatial locations and inferring the spatial configuration of the current sheet through a time-of-flight analysis.

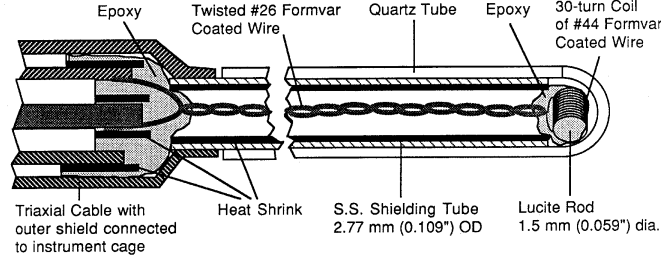
The magnetic field probes used in this study were magnetic induction coils, commonly referred to as B-dot probes. These probes are simply linear coils of wire that generate an emf proportional to the time variation of the magnetic flux through the coil. So, experimentally, we determine the local magnetic field by evaluating the expression

$$B(t') = \int_0^{t'} c(\omega)V(t)dt \quad , \quad (4.1)$$

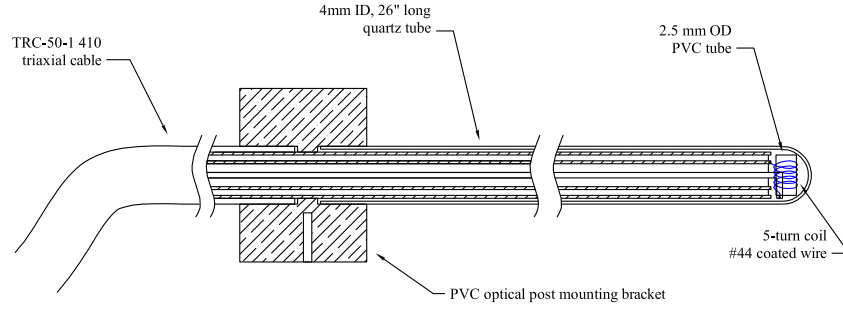
where V is the measured probe voltage and $c(\omega)$ is a (frequency-dependent) parameter determined through calibration.

Two sets of B-dot probes were used in the present study. Probe set I was acquired from an earlier experiment[31] (the details of the probe set I construction are shown in Fig. 4.5a). Construction of probe set II was necessitated by the destruction of one of the probe set I probes, which resulted from spurious arcing from the main discharge to the probes shielding (the details of the probe set II construction are shown in Fig. 4.5b). The probes were calibrated by placing them in the uniform-field region of a Helmholtz coil; pulses of known current and frequency were driven through the Helmholtz coil and the probe response was recorded (see appendix B.3). The probes' frequency response is expected to be linear in dB/dt (i.e., $c(\omega) = c$, a constant) through $\omega \leq 100$ MHz, due to the probes' low inductance; however, we verified the linearity only up to approximately 2 MHz, which

a)



b)



c)

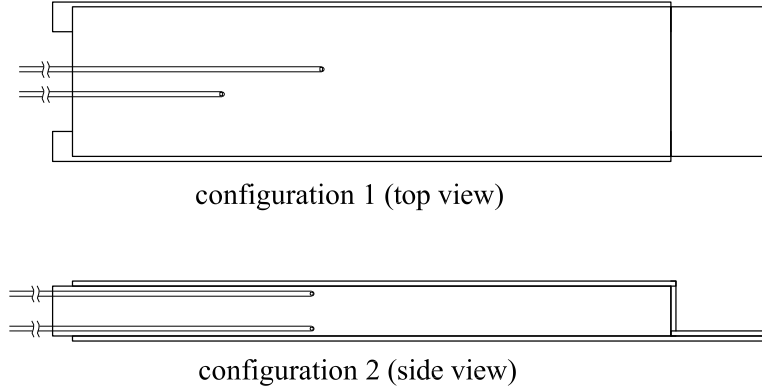


Figure 4.5: Magnetic field probe schematics: a) probe set I construction details (from Hoskins[31]), b) probe set II construction details, c) probe placement for speed (configuration 1) and canting angle (configuration 2) determination.

was sufficient for our purposes. No analog integration was used; instead, the probe voltage was measured directly and integrated numerically to determine $B(t')$.

The probes were used in two different configurations, as illustrated in Fig. 4.5b and Fig. 4.5c. In configuration 1, the probes were placed inside the accelerator in the same horizontal plane (separated by approximately 2.5 cm), and separated axially by approximately $\Delta x_1 = 20$ cm. During a discharge the two probe responses were simultaneously

monitored. By dividing the known axial probe separation by the difference in the arrival time of the current sheet to each probe (Δt_1), the average current sheet propagation speed ($v = \Delta x_1 / \Delta t_1$) was determined. In configuration 2 the probes were placed at the same axial position, but vertically displaced by approximately $\Delta y = 3$ cm. By measuring the time delay between the arrival times of the current sheet to each probe (Δt_2), and multiplying by the previously determined value of v , we can determine the axial displacement of the current channel ($\Delta x = v \Delta t_2$) and, hence, the current sheet canting angle ($\tan \theta = \Delta x / \Delta y$) relative to the electrode normal.

Probe set I was used in fixed locations near the axial center of the accelerator. Probe set II was used to map the axial evolution of the magnetic field. The probes were mounted on an electrically actuated translation stage which allowed their position to be continuously adjusted from the breech to the exhaust.

4.6 Laser interferometry

A two-chord heterodyne laser interferometer with electronic quadrature phase detection was constructed. The system is very similar to the single-chord system implemented by Spanjers *et al.*[32] in APPT research. A schematic of the experimental layout is shown in Fig. 4.6. The interferometer was used to determine the current sheet speed and canting angle by monitoring the phase variations of two laser beams at different spatial locations within the accelerator and inferring the spatial configuration of the current sheet through a time-of-flight analysis in a completely analogous manner to that used in the analysis of the magnetic field waveforms. The response from two horizontally separated beams (approximately 10 cm axial separation) were used to determine the propagation speed (the orientation of the optics for this experiment is illustrated in Fig. 4.6). The beams were retro-reflected back through the plasma to give twice the phase shift of a single pass. For

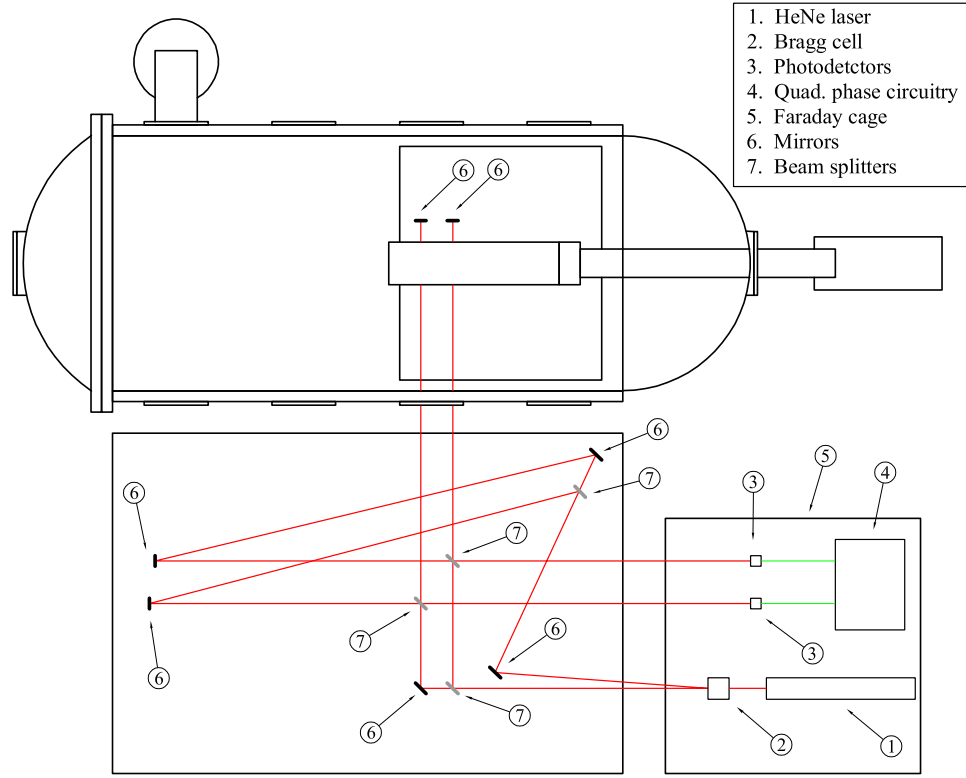


Figure 4.6: Schematic of laser interferometry layout (configuration 1).

canting angle determination, two beams at the same axial location but vertically separated by about 3.5 cm were used. Additionally, accurate quantitative measurements of the current sheet electron density were obtained from the measured phase shift in each beam.

The system functionally consists of two interferometers in the Mach-Zehnder configuration. This type of interferometer detects phase differences between the “scene” and “reference” beams. When these two beams are recombined at the detector, any phase mismatches between the beams causes amplitude variations in the detector output due to constructive or destructive interference. In our experiment, phase differences between the two paths arise when the current sheet plasma passes through the scene beam; the plasma index of refraction (\mathcal{N}) is different than that of free space (\mathcal{N}_o) and, hence, the scene beam optical path changes as the current sheet passes by. By measuring the phase change of the scene

beam we can determine the change in optical path length and, in turn, the effective index of refraction of the plasma. Finally, through a suitable theoretical model of the interaction of the laser beam's electromagnetic wave with the plasma, the electron density of the plasma can be determined.

The simplest model of the plasma-EM wave interaction assumes a weak magnetic field and isotropic plasma – the plasma is essentially considered to be a dielectric. Within this framework, analysis (see appendix D.2) leads to an expression for the electron density as a function of the instantaneously measured phase shift which, in our particular implementation reduces to

$$n_e = 2.78 \times 10^{15} \Delta\phi [\text{cm}^{-3}] . \quad (4.2)$$

Two problems arise in the interpretation of data obtained with a conventional Mach-Zehnder interferometer: amplitude variations in the detected signal which arise from attenuation or refractive bending in the plasma must be distinguished from phase variations, and, in general, it is not possible to determine the direction of the phase change (i.e., positive phase changes cannot be distinguished from negative ones). These problems can be eliminated by using a heterodyne light source and quadrature phase detection. In a heterodyne system, either the scene or reference beam is phase modulated at the source; when the beams are recombined at the detector the amplitude of the detected signal will oscillate at the modulation frequency; the task of detecting the phase changes due to the plasma becomes that of measuring the phase of the oscillation at the detector relative to the driving modulation at the source. The technology for this type of measurement, which is essentially one of homodyne detection, has been well developed by the radio reception community. Drawing on this knowledge, we have developed a two-channel quadrature phase detector. Each channel uses two double balanced mixers to produce output signals proportional to the sine and cosine of the instantaneous phase and, hence, unambiguously determines the

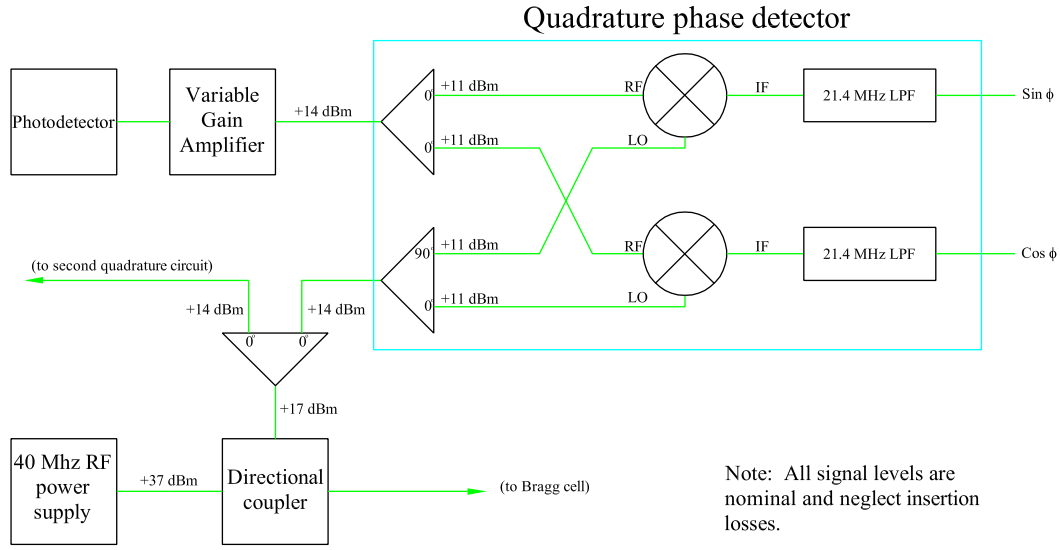


Figure 4.7: Schematic of one channel of the interferometer quadrature phase detection circuitry.

quadrant of the phase angle. A schematic of one channel of the phase detection circuitry is shown in Fig. 4.7.

The specific components used in the interferometer were as follows. The light source was a Coherent model 31-2108 17 mW HeNe laser. The beam splitting into the scene and reference beams, along with modulation of the reference beam, was accomplished using an IntraAction model AOM-405 acousto-optic cell driven by a 40 Mhz, 5 W RF power source. Two Thor Labs model PDA155 photo detectors were used. These amplified (1×10^4 V/A) Si detectors have a 50 Mhz bandwidth. It was found that, because of the large amount of electromagnetic noise created by the firing of the accelerator, all electronics, including the laser, had to be housed in a Faraday cage. Standard optical components (aluminized mirrors, dielectric beam splitters, and anti-reflection windows) were used to steer the beams.

No direct calibration of the instrument was carried out (i.e., the response of the system to a known change in optical path length was not attempted). It is difficult to conceive

of how such a procedure could be accomplished. The phase variations measured by the detector due to room vibrations and atmospheric fluctuations alone reduce the useful time scale of the device to experiments which last less than $100 \mu\text{sec}$. It is unclear how one would introduce an object of known optical path length into the scene beam on such a short time scale. We have, however, based simply on signal-to-noise ratio considerations, estimated the minimal resolvable variation in electron density in our device to be on the order of $1 \times 10^{14} \text{ cm}^{-3}$. On the high frequency end, the Nyquist criterion limits the frequency response to about 10 MHz. From Eq. D.9, this implies that the maximum resolvable temporal variation in electron density was about $10^{17} \text{ cm}^{-3} \mu\text{s}^{-1}$. As will be shown later, this limit was exceeded in some measurements near cathode; the complications which resulted are described in appendix D.2.1. The spatial resolution of the interferometry system, which was limited by the laser beam diameter, was about 3 mm.

4.7 Emission spectroscopy

Interpretation of spectral emission lines requires theory to predict both the wavelength and intensity of emitted radiation. The wavelength of the acquired lines is readily correlated with atomic species using standard tables [33]. The intensity of the emitted lines is related to the thermodynamic state of the plasma. This opens up a diagnostic avenue – by measuring the intensity of the radiation emitted by a plasma, we can infer bulk thermodynamic properties, such as temperature.

One such technique uses the ratio of spectral line intensities to yield a measure of the electron temperature. The principle of this technique is as follows. If the electrons in a plasma are in equilibrium (i.e., have a Maxwellian distribution of speeds), then the atomic species with which they are collisionally coupled will be in excitation equilibrium, that is, the bound electrons will be in a Boltzmann energy distribution. The actual distribution of

excited states in a plasma is revealed when electrons in excited states relax to lower energy states and radiate light. By measuring the intensity of this light, we can infer the population of a particular upper state. Carrying out this procedure for many different transitions, we can determine the energy distribution of the bound electrons. Knowing this distribution, we can calculate the temperature of the free electrons needed to achieve the measured distribution of excited states.

Emission spectroscopy was used in the present experiment to obtain information about the atomic species present in the current sheets as well as to determine the electron temperature. In this section the general layout of the spectroscopy apparatus, calibration techniques, and the underlying principles used to interpret the spectral data are described.

4.7.1 Apparatus

Spectral data was recorded by imaging the CSSX accelerator plasma in two different orientations (see Fig. 4.8). Configuration 1 was used to construct a time-integrated survey of all of the radiation emitted between 3500-8500 Å. In configuration 2, a few selected lines were interrogated to provide a measurement of the electron temperature. In both cases, a point on the centerline of the accelerator was imaged onto the input slit of the spectrometer. Configuration 2 was used in the quantitative work because it was easier to verify that the current sheet was in the same spatial location from shot to shot. If configuration 1 had been used, differences in the spatial position of the current sheet from shot to shot would have caused the current sheet to be intermittently out of focus and, consequently, these variations would have been indistinguishable from differences in plasma optical emission intensity. In configuration 2, the plasma had no component of velocity perpendicular to the imaging plane and thus decoupled the measured intensity from the propagation of the current sheet.

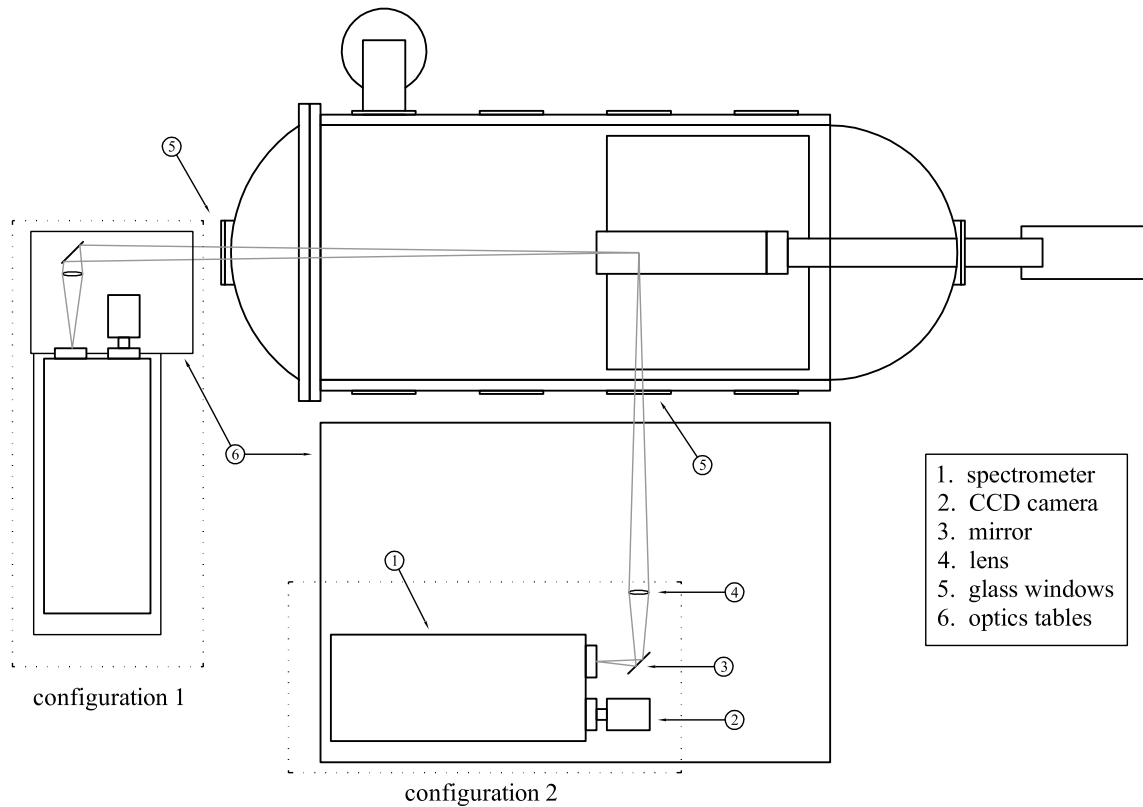


Figure 4.8: Schematic of emission spectroscopy optical layouts.

Light collection optics

The light collection optics consisted of a vacuum chamber window, a periscope, and a focusing lens. The window, an 8 inch diameter, 1/2 inch thick soda lime glass disk, allowed the entire front view of the accelerator to be imaged. The periscope, which used two 3 inch diameter first surface mirrors, allowed the vertical position of the accelerator image to be adjusted to the level of the input slit of the spectrometer. Also, the periscope rotated the image ninety degrees, so that the horizontal plane of the accelerator was aligned with the (vertical) spectrometer slit. The image plane of the spectrometer was aligned with the centerline of the accelerator. The spectral data presented in this thesis result from the integration of all light emitted by the plasma in this plane.

Spectrometer

The spectrometer used in this study was a Spex 1269 grating spectrometer. The slit-to-mirror length is 1 m and the grating has 1200 groove/mm; the grating blaze angle is optimized for optical wavelengths. This configuration results in an exit plane linear dispersion of $D = 9.08 \times 10^{-3} \text{ \AA}/\mu\text{m}$ at 4000 \AA (D varies slightly with wavelength.) The grating angle (wavelength position) of the spectrometer was adjusted using a Spex Compudrive spectrometer controller.

Camera

The detector used in this study was a Princeton Instruments ICCD 576 CCD camera. The camera has an array of 576×384 square $22 \mu\text{m}$ pixels. The quantum efficiency of the pixels is optimized for optical wavelengths. The array is both intensified and temporally gated. Photoelectron amplification of up to 1000:1 is continuously adjustable. A microchannel plate allows the CCD array exposure time to be adjusted from 10 ns to continuous exposure. The camera was gated using a Princeton Instruments PG-200 pulse generator. Camera images were acquired using a Princeton Instruments ST-138 controller and downloaded to a computer.

Calibration and data reduction

In order to determine plasma species and make quantitative estimates of electron temperature, it was necessary to calibrate the spectroscopic system for wavelength and intensity. The details of the procedure used in the present study are given in Appendix B.2.

Computer code was written to automate the process of data reduction. The code takes raw CCD intensity information and interprets a curve of intensity versus wavelength – applying both wavelength and intensity calibration.

4.7.2 Plasma Spectroscopy

The primary motivation for implementing the emission spectroscopy diagnostic was to measure the electron temperature of the current sheet plasmas. The methodology for correlating the measured plasma optical emission with electron temperature is well developed[34]. In particular, we plotted the weighted optical emission versus photon energy (for several spectral lines of a given species) and inferred electron temperature from the slope of a straight-line curve fit through these points. A complete description of this technique, as applied to our particular problem, is given in appendix D.1.

Chapter 5

Experimental Results

This chapter presents all of the experimental data that were collected in the CSCX study. The chapter is organized in sections which correspond to the diagnostic technique used to acquire the data. The primary goal of the experiments was to accurately measure the canting angle of the current sheet under a variety of initial conditions. Some of the diagnostics gave additional information about the thermodynamic state of the current sheet plasma (e.g., number density, temperature, etc.).

Each diagnostic was applied to eight different working propellants: hydrogen, deuterium, helium, neon, argon, krypton, xenon, and methane; three different initial gas pressures were used: 75, 200, and 400 mTorr. The pressure range was chosen to correspond to that of propulsive interest, that is, pressure levels which give propellant exhaust speeds in range of 10-100 km/s. To allow for direct comparisons between the various diagnostics, all quantitative work was done with PFN II charged to 9 kV.

In this chapter all measured quantities are plotted as functions of propellant species and pressure only. Undoubtedly, plotting the measurements as a function of other physical quantities would be more likely to expose parametric trends (e.g., plotting the current as a function of propellant atomic mass might give some insight as to how mass loading in

the current sheet influences the current). However, such analysis is deferred to Chapter 6: Analysis and Modelling, since such interrogations of the data will be more meaningful if they are guided by trends suggested in the theoretical models. Limiting the scope of the analysis in this chapter allows it to serve as a more concise database of current sheet canting data. Furthermore, rather than cluttering the presentation with page-after-page of data, this chapter summarizes the results of each diagnostic in a few figures; support data are accumulated in Appendix C: Additional Data, where it may serve as a useful resource for other current sheet studies.

The uncertainty reported for all quantitative results includes the influence of both systematic and random errors. The confidence level for all graphical error bars and explicitly stated error values is 90%. Details of the procedures used to calculate the uncertainty in the experimental results are presented in Appendix E.

5.1 Circuit Current and Voltage Measurements

Before presenting the current sheet canting measurements, the two sections which follow describe the measured PFN/accelerator electrical circuit behavior.

5.1.1 Circuit Current

General circuit performance

The total current delivered to the accelerator was measured using a current transformer positioned between the accelerator and the last stage of the PFN. Details about the transformer are given in section 4.1. Typical current waveforms are shown in figure 5.1. In both cases the current pulse was followed by about two cycles of damped sinusoidal ringing.

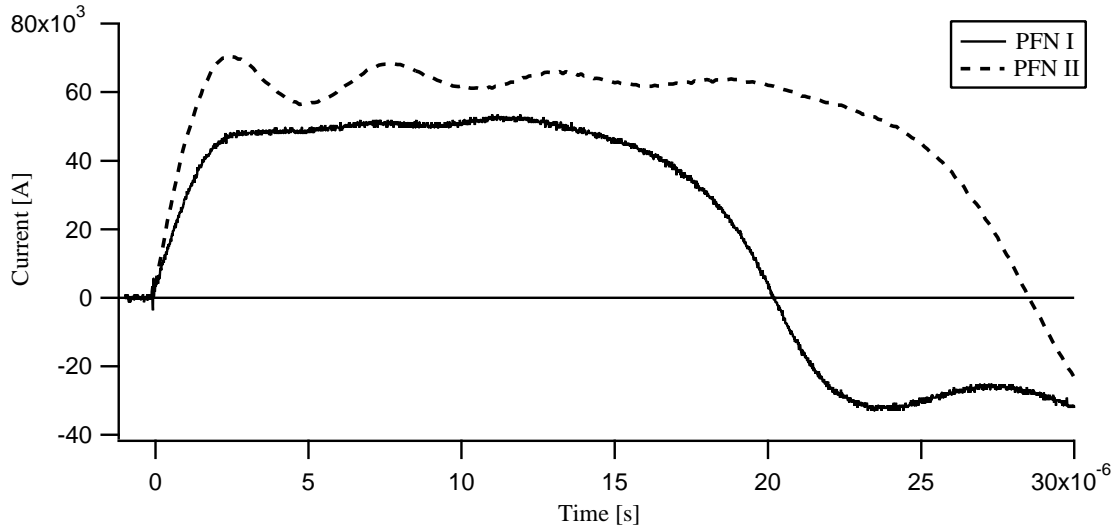


Figure 5.1: Experimental current waveforms (PFN I: 4.5 kV, Argon (100 mTorr), PFN II: 9.0 kV, Argon (200 mTorr).)

Influence of gas species and pressure

Figure C.1 shows the peak current, I_{\max} , and average current, \bar{I} (the average is taken over the 15 μsec which follow the peak current), attained for each propellant at initial pressures of approximately 75, 200, and 400 mTorr. The plotted points represent averages over about twenty tests.

Discussion

Comparison of figures 5.1 and A.3 (the PFN numerical design simulations) indicates that both PFNs gave performance in qualitative agreement with their design (note that the simulations were for maximum design voltage whereas the experimental waveforms were recorded at slightly lower voltages). Differentiating the PFN II waveform yields an initial current rise-rate of approximately 10^{11} A/sec – in agreement with the design estimates.

PFN I's peak current and pulse-width showed closer agreement to its design waveform than did PFN II's. As is evident in figure 5.1, the PFN II current waveform seems to

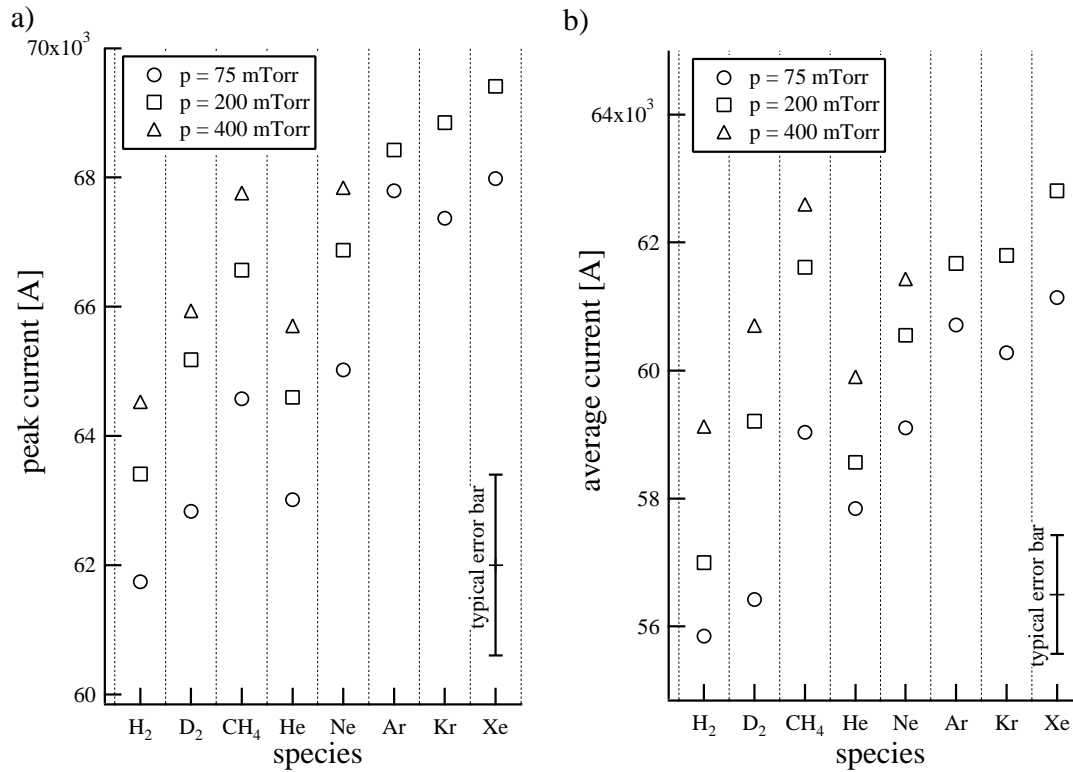


Figure 5.2: Influence of propellant species and pressure on a) peak current and b) average current.

initially “overshoot” the desired “flat-top” current level; this overshoot leads to a damped oscillation that persists for most of the pulse. The overshoot most likely results from the use of a reduced-size initial stage inductor; the first-stage inductor was reduced in size in order to achieve the highest possible dL/dt . In PFN I, all of the inductors were identical. Again, comparing the calculated and experimental waveforms, the peak current attained by PFN II was slightly less than expected and the pulse width was slightly longer than predicted. These three factors combined suggest that the actual PFN II inter-stage inductance was higher than the design value. Reflecting back on the physical construction (see figure A.4), it is most likely that the extra inductance originates from the capacitor mounting scheme. The analysis called for 100 nH of inter-stage inductance; for the given copper plate width and separation (capacitor height), approximately four inches of inter-stage spacing was

required to give 100 nH. PFN II was constructed with four inches of space between the capacitor cases, whereas the the capacitor mounting terminals were spaced eight inches apart. The (unaccounted for) volume of the capacitor bodies is most likely the source of the extra inductance. In any event, the actual waveform, while somewhat different from the design, was adequate for the present study. Compared to PFN I, PFN II had a higher rise-rate, peak current, and pulse width – enabling tests to be run at higher pressure levels. The current sheet structures observed using PFN I were the same as those observed using PFN II, indicating that the slight ripple in the PFN II current waveform did not give rise to new phenomena.

The current measurements shown in figure 5.2 show two general trends: both peak and average currents increase with increasing pressure and atomic mass of the accelerated propellant. It should be noted that the molecular propellants experience a rapid increase in pressure (above the initial ambient fill) when they enter the current sheet – due to dissociation. It is more revealing to plot the current as a function of total propellant mass (total mass of propellant contained within the discharge chamber prior to firing), in which case we find that the current increases monotonically with increasing total propellant mass. This trend is shown in Fig. C.1 and the associated discussion, in the appendix, concludes that the current variation with propellant mass is due to variation of the dynamic impedance.

5.1.2 Terminal voltage measurements

The terminal (muzzle) voltage was measured using the voltage divider described in section 4.2. The probe was attached at the center of the end of the electrodes (i.e., approximately 24 in. from the breech, and 3 in. from the outer edges of the electrodes). The goal of this experiment was to gain an estimate of the inter-electrode voltage drop associated with the plasma resistivity. Figure 5.3 shows the results from the measurements. The measurements

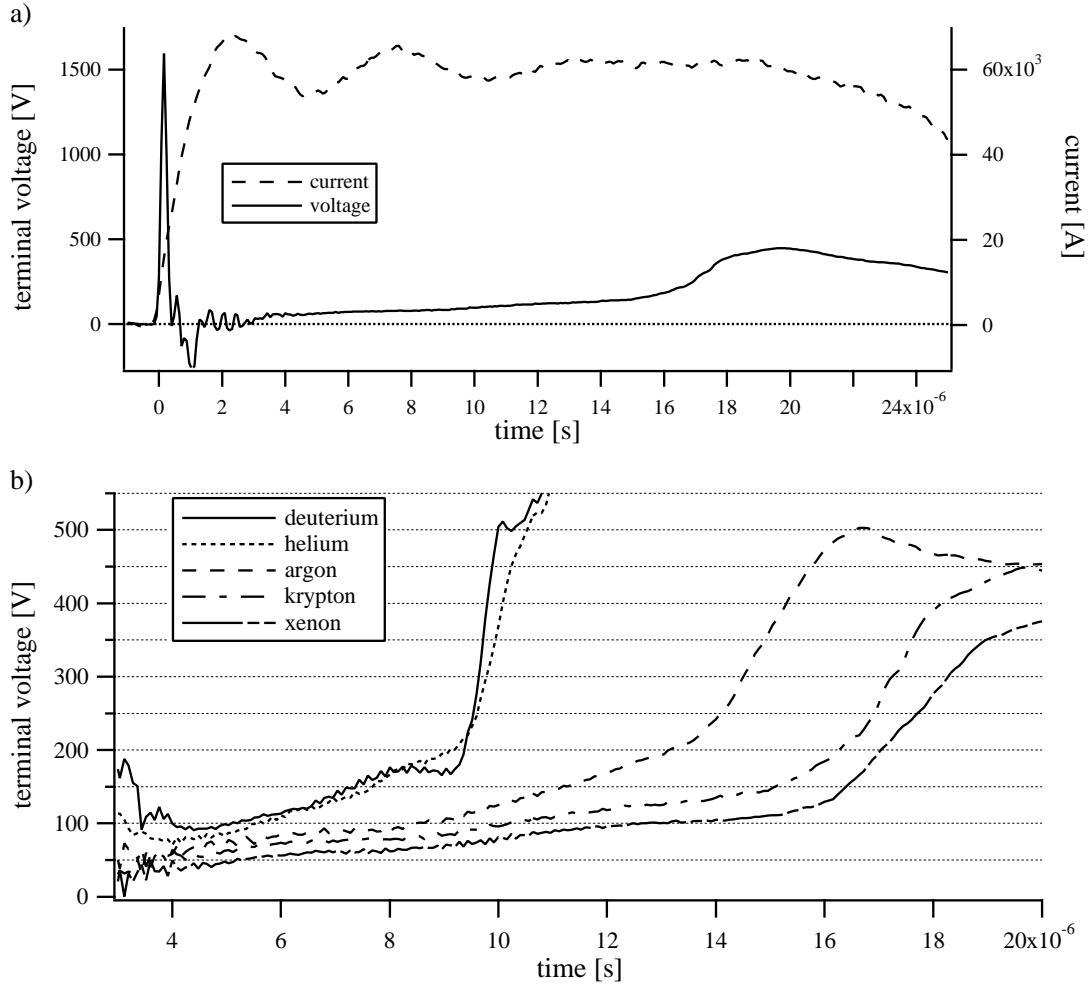


Figure 5.3: Terminal voltage measurements: a) terminal voltage and current from a krypton discharge, b) terminal voltage for several different propellants.

were made with an initial background gas pressure of 75 mTorr. The plots represent the oscilloscope-averaged waveforms from five shots.

In Fig. 5.3a the voltage history for an entire discharge event in krypton is illustrated; the associated current waveform is included for reference. The figure shows that there is, as expected, an initial high voltage spike associated with the gas breakdown process, after which there are somewhat erratic oscillations (for about the first $3 \mu\text{s}$) including an excursion into negative voltage. After this initial transient region, the voltage monotonically

cally increases (fairly linearly) up to about $t = 15 \mu\text{s}$, after which the voltage increases more rapidly, reaches a maximum, and then falls off. Figure 5.3b shows similar plots for other propellants; however, only the post-transient region is plotted so that the scale of the vertical axis could be adjusted to provide greater resolution of the regions of most interest.

Discussion

The voltage waveforms can be divided into three regions: initial transient, current sheet propagation, and blowing regions.

The transient region extends from about $t = 0 - 3 \mu\text{s}$. Any interpretation of this portion of the waveform is dubious because the high dI/dt associated with the initial transient can induce (inductive) voltages in the probe circuitry which are not associated with the plasma resistivity. For example, since the magnetic field extends in front of the current sheet in the present experiment, although the magnetic field itself is expected to be fairly weak ($< 10^{-2}$ T), dB/dt may be quite large. Since the flux surface defined by the probe, electrode, and current sheet loop is large, it is possible for non-ohmic voltage drops to be induced during times of high dI/dt .

The propagation region is defined by the time it takes for the current sheet to traverse the length of the electrodes, which of course varies from propellant to propellant. The time of arrival of the current sheet to the end of the electrodes is indicated in the figures by the time at which the voltage begins to rapidly increase. At this point in time, the voltage probe not only is exposed to the resistive voltage drop, but also the inductive voltage drop, which is confined behind the current sheet. In the deuterium and helium discharges, this transition is most abrupt – occurring at approximately $9.5 \mu\text{s}$. For argon the transition occurs at approximately $14 \mu\text{s}$ and at approximately $16 \mu\text{s}$ for both krypton and xenon. Within the propagation region the voltage drop is found to vary from about 50-250 V, depending on

the propellant. Using the current data from the previous section, the total plasma Ohmic resistance is estimated to be 1-5 m Ω .

There are several interesting features observed in the propagation region. First, a rough estimate of the current sheet propagation speed can be found by dividing the length of the electrodes (60 cm) by the time for the current sheet to reach the propagation-blowing transition. For deuterium and helium this analysis yields a speed of about 6.3 cm/ μ s; similarly, for argon, 4.3 cm/ μ s, and 3.8 cm/ μ s for both krypton and xenon. These values will be seen to agree well with results obtained using more advanced speed measurement techniques, as presented in subsequent sections of this chapter.

Next, it is apparent that the inter-electrode voltage increases, for all of the propellants, as the current sheet propagates. For example, the terminal voltage in the xenon current sheet increases from about 50 to 100 V during propagation. Recall, again, that the muzzle voltage should have no contribution from the inductive voltage drop associated with the propagation of the current sheet[14]. One possible explanation for the progressively increasing voltage is that the current sheet cools as it propagates, causing the plasma resistivity to increase. Another possible explanation for this trend is acceleration of the current sheet; in other words, the rate at which conduction electrons experience inelastic collisions (e.g. ionization) may be related to the instantaneous speed of the current sheet. As the speed increases, the current sheet must ingest and ionize neutral atoms at a progressively increasing rate; this would be reflected in a requisite increase in the total energy budget (voltage drop).

Along the same line of reasoning, another trend in the data might be explained. It is seen in Fig. 5.3b that the voltage drop at any instant of time increases as the atomic mass of the propellant decreases (note that helium and deuterium have about the same mass). Again, this could be explained by the fact that the current sheet moves faster in the lighter

propellants, and thus has a higher internal rate of inelastic collisions. This reasoning is complicated by variations in ionization potential amongst the various propellants. However, this explanation is supported by the helium and D_2 . In addition to having the same mass, helium and D_2 require about the same total amount of energy to singly ionize. The plots show that their voltage histories track very closely.

The terminal voltage data also show possible evidence of current sheet canting. With a canted current sheet one of the electrode current sheet attachments would arrive at the end of the accelerator before the other electrode attachment; consequently, we might expect that an uncanted current sheet current sheet would produce a sharp propagation-blowing region transition in the terminal voltage measurement whereas the transition would appear more gradual with a canted current sheet. In this framework, the data in Fig. 5.3b would indicate that the helium and deuterium current sheets are less canted than the heavier propellant current sheets. Alternatively, the differences in the voltage increase rate could be related to differences, from propellant to propellant, in the current pattern transformation from propagation to blowing mode (see Eckbreth[19]).

After the current sheet reaches the end of the electrodes (both the anode and cathode attachments), the arc is expected to go into a "blowing" mode; the arc will balloon out into the chamber with attachments anchored to the ends of the electrodes. As the current begins to fall off, a "crowbar" arc is expected to form at the breech and short-circuit the initial current sheet, leaving its plasma to dissipate.

5.2 High-speed photography

High-speed photography (see section 4.3) was initially used to obtain images of the macroscopic evolution of the discharge. This diagnostic was especially important because it established that the accelerator was functioning as a conventional pulsed plasma accel-

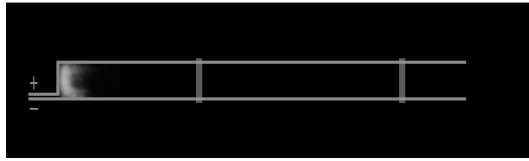
ator – a current sheet was seen to form at the breech and propagate between the plates and eject from the end of the electrodes. Later, the diagnostic was used to provide a first, rough, quantitative estimate of the current sheet propagation speed and canting angle. The two sections which follow present a photographic survey of the discharge evolution and canting. Other pertinent photographs which show, for example, the influence of electrode polarity and contamination, are given in Appendix C.2.

5.2.1 Evolution of the discharge

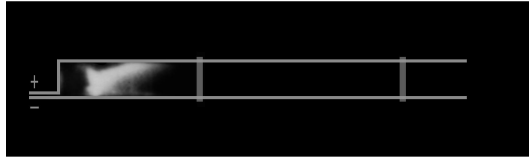
The Imacon camera was used to obtain spatially and temporally resolved images of a single discharge event; the interframe delay of the Imacon was set to $2\ \mu\text{s}$ (500 ns exposure). When the camera trigger was offset from the initiation of the discharge by $1\ \mu\text{s}$, the good reproducibility of the discharge structure allowed two separate runs to be interleaved to give a succession of images that show the complete discharge event in $1\ \mu\text{s}$ intervals.

Figure 5.4 (series I) shows photographs of a discharge for several successive times during a single pulse (the times shown correspond to those in the current waveform of Fig. 5.1 (PFN I). The Polaroid images were scanned into a computer and processed with photo-editing software. Lines were drawn to indicate the position of the electrodes. The two vertical rectangles on the electrodes represent bolts that are used to hold the accelerator together; they caused an optical obstruction between the plasma and the camera. The top electrode is the anode. The propellant used was argon at 100 mTorr and the capacitor bank voltage was set to 4 kV. A narrow-pass line filter (488 nm, 10 nm FWHM) was used to allow only the light emitted by argon ions to enter the camera; this was done to exclude the more spatially diffuse glow of the neutrals, and enhance the contrast in the regions where current was flowing. The photographs show that the discharge forms at the breech, accelerates down the electrodes, and is ejected from the exit. Immediately after the current

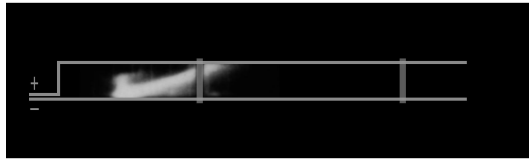
sheet leaves the breech it begins to tilt — with the anode attachment leading that of the cathode. The sheet then stabilizes to a fairly fixed angle, leaving a trail of plasma along the cathode in its wake, while it propagates down the rest of the discharge channel. Since the anode arc attachment reaches the end of the accelerator first, the ejection of the plasma is quite asymmetric; the current sheet is forced to curl back on itself to re-attach at the anode. The discharge propagates 60 cm in approximately $15\ \mu\text{s}$ implying an average sheet speed of about $4\ \text{cm}/\mu\text{s}$.



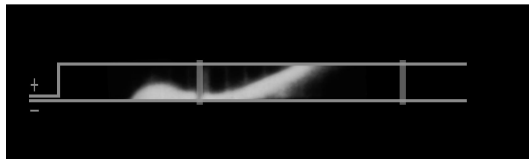
$t = 0 \text{ } [\mu\text{s}]$



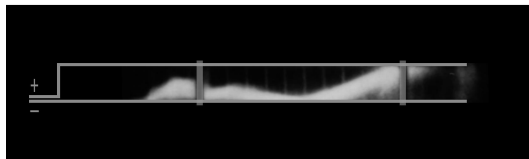
$t = 3 \text{ } [\mu\text{s}]$



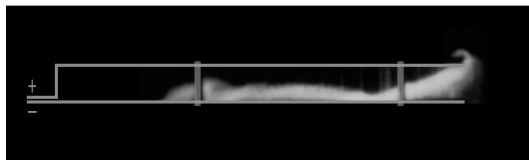
$t = 6 \text{ } [\mu\text{s}]$



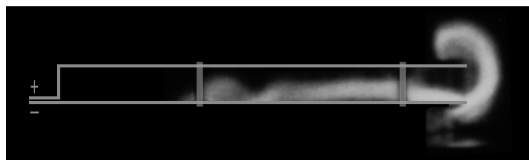
$t = 9 \text{ } [\mu\text{s}]$



$t = 12 \text{ } [\mu\text{s}]$



$t = 15 \text{ } [\mu\text{s}]$

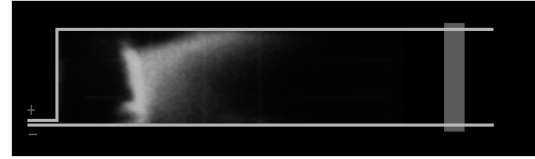


$t = 18 \text{ } [\mu\text{s}]$

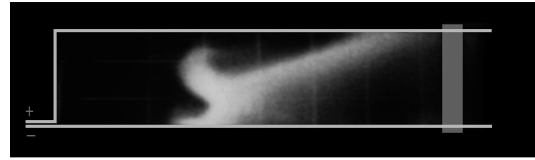
Series I



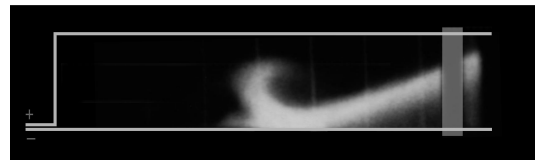
$t = 0 \text{ } [\mu\text{s}]$



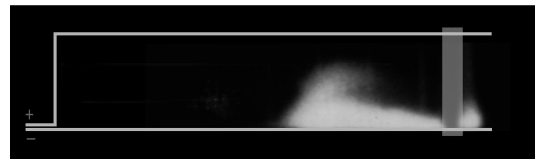
$t = 2 \text{ } [\mu\text{s}]$



$t = 4 \text{ } [\mu\text{s}]$



$t = 6 \text{ } [\mu\text{s}]$



$t = 8 \text{ } [\mu\text{s}]$

Series II

Figure 5.4: **Series I:** Series of photographs showing the evolution of the discharge in a single pulse ($p=100 \text{ mTorr}$ (argon), $V = 4 \text{ kV}$). **Series II:** Series of photographs showing the evolution of the discharge near the breech ($p=100 \text{ mTorr}$ (Argon), $V=5 \text{ kV}$).

Figure 5.4 (series II) shows a close-up of the breech region of the accelerator. The initial conditions for the accelerator in this set of photographs were the same as those used in series I, with the exception that the bank voltage was 5 kV instead of 4 kV. This figure more clearly shows the transition of the arc from its planar initial state, to the fully canted current sheet. As the current sheet leaves the back of the accelerator, it immediately begins to bifurcate. The initial anode attachment point recedes from the electrode, and a diagonal sheet forms. Within several microseconds the sheet attains the canted structure that it maintains for the remainder of its propagation. The base of the arc (cathode attachment) forms a hook-like structure which has been previously reported in earlier studies (see Chapter 2).

Additional accelerator breech and midsection photographs (in which different propellants were used) are given in appendices C.2.3 and C.2.4.

5.2.2 Speed and canting-angle measurements

Photographs were taken of the mid-section of the accelerator (using PFN II), with the camera in position 2 (see Fig. 4.1). Seven different propellants were tested at up to three pressure levels (75, 200, and 400 mTorr). Higher atomic mass propellants (e.g., xenon) were not photographed at 400 mTorr because the current pulse was not of sufficient duration to drive the discharge into the viewing region at higher propellant mass loadings. The goal of this set of photographic experiments was to get a rough idea of the current sheet propagation speed and canting angle.

Figure 5.5 shows examples of the photographs obtained in the study. For clarity, lines representing the position of the electrodes (anode on top) have been drawn on the images. Also, a gridded background outside of the accelerator is visible (the grid spacing was 1 cm). In the pictures the current sheet is moving from left to right. The right-most visible feature, which spans the entire gap between the electrodes, is assumed to be the current sheet. Also,

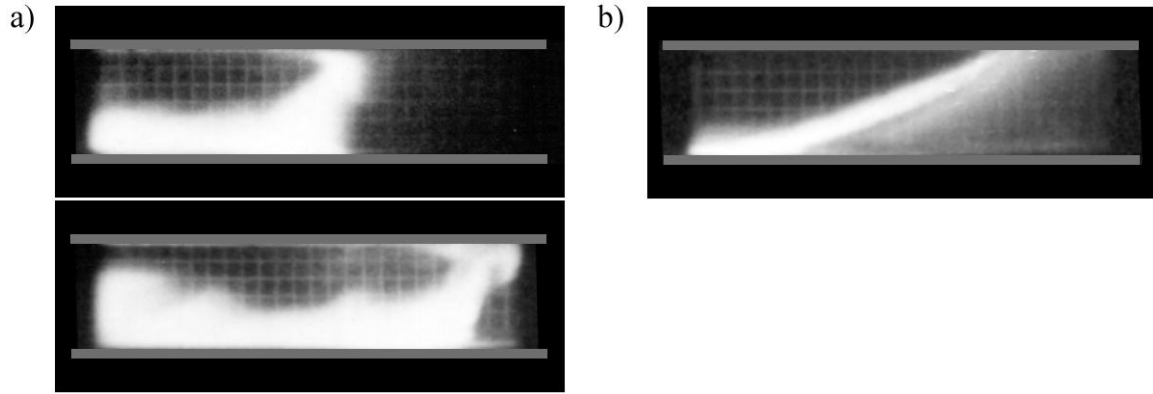


Figure 5.5: High-speed photographs of current sheets at the midsection of the CSCX accelerator: a) example of two successive photographs used in the determination of propagation speed (helium (400 mTorr), $\Delta t = 2 \mu\text{sec}$ between frames), b) example of a photograph used to determine canting angle (xenon (75 mTorr)).

a luminous cloud is seen to trail behind the current sheet; we assume that this is not part of the current conduction zone but, rather, gas that has been heated by the current sheet. Figure 5.5a shows two images from a helium discharge, taken $2 \mu\text{sec}$ apart. By measuring the change in spatial position of the sheet between the two frames, the propagation speed was estimated. Figure 5.5b shows a single frame from a xenon discharge. By measuring the slope of the luminous front, the canting angle was estimated. Figure 5.6 summarizes the measurements obtained from all of the photographs (additional photographs that were used to create Fig. 5.6 are given in Appendix C.2.4).

5.2.3 Discussion

Each point in Fig. 5.6 was distilled from two photographs. In some cases the images were difficult to interpret (for example, the high speed of the hydrogen current sheets caused the images to be blurred); those cases are not included in the graphs. The diagnostic technique is not well suited for precise measurements because interpretation of the photographs relies on the assumption that the luminosity patterns correspond to the spatial location of the

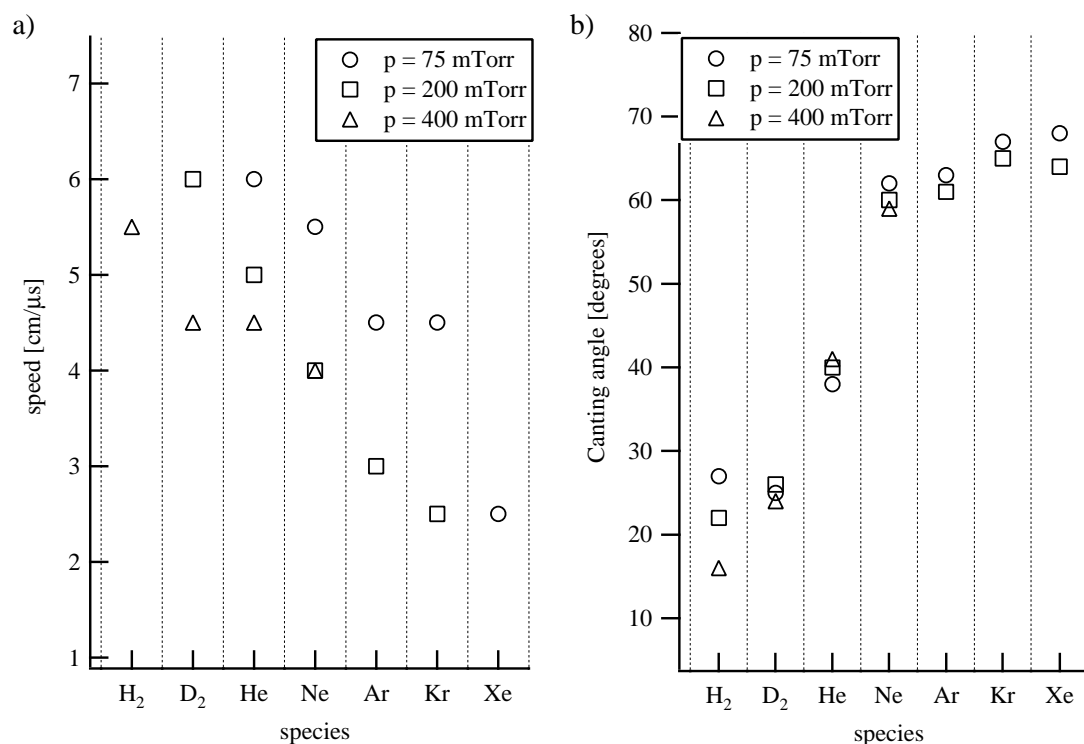


Figure 5.6: Current sheet a) propagation speed and b) canting angle, interpreted from high-speed photographs (no error bar is included because of the inherent subjectivity in the measurement technique).

current. This assumption may not be valid if the luminous regions are caused by other phenomena, such as shock waves. No meaningful error analysis can be carried out on the plotted values because of the small number of samples as well as the inherent subjectivity in the interpretation of the luminosity patterns.

In any event, some qualitative trends can be gleaned from the results. First, the higher atomic weight propellant cases had slower moving current sheets, which is what one would expect from mass loading considerations. Second, it is apparent that the higher atomic mass propellants had a higher degree of current sheet canting – with xenon having almost 40° more tilt than hydrogen. Hydrogen at high pressure exhibited the lowest canting angle; no correlation between canting angle and pressure can be made for the other propellants,

since the uncertainty in this measurement technique is large.

The luminous region which trails behind the current sheet, along the cathode, was present in all of the photographs obtained in this study. This observation, along with additional data presented in subsequent sections of this chapter, will later be used to support conclusions reached in the CSCX study about current conduction and the effectiveness of current sheets in sweeping up propellant.

5.3 Schlieren imaging

Despite the implementation of several different optical configurations and lasers, only a very limited amount of data was obtained using schlieren imaging. The suspected problem with our systems will be discussed after a brief summary of the results from each optical arrangement.

5.3.1 Schlieren photography configuration

Schlieren photographs were acquired near the breech and center of the accelerator using the apparatus described in section 4.4.3. However, after repeated attempts, the schlieren photography configuration yielded no resolvable features in the discharges.

5.3.2 Shadowgraph configuration

Slightly better results were obtained using the shadowgraph configuration. Figure 5.7a shows an image obtained near the midsection of the accelerator. A faint image of the current sheet is visible along the bottom electrode (cathode). The direction of current sheet motion was from left to right. As was observed in the photographic study, the shadowgraph image indicates that the current sheet is highly canted, and a trailing plasma tail can be seen in

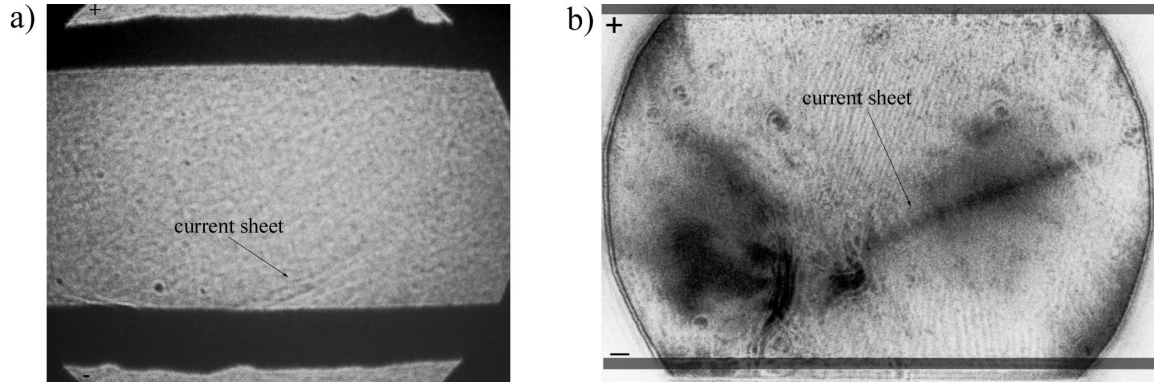


Figure 5.7: a) Shadowgraph image of current sheet near bottom electrode and b) modified shadowgraph image of current sheet near the breech (Argon, 100mTorr, $V = 4\text{kV}$).

the lower left corner. However, this image is too faint and small in spatial extent to provide any useful quantitative information.

5.3.3 Modified shadowgraph configurations

Both modified shadowgraph configurations illustrated in Fig. 4.4 were implemented. Use of the aperture mask yielded an image very similar to the image in Fig. 5.7a but much darker (better contrast). The spatial extent of the image, however, was no greater than that obtained using the standard shadowgraph technique.

Figure 5.7b shows a modified shadowgraph image that was acquired using the dot mask. The contrast of the image has been reversed to better clarify the structure. In this image we begin to see features reminiscent of the photographic survey. In particular, the image was acquired near the same spatial position and at about the same time as the image in Fig. 5.5 (series II) labelled $t = 4 \mu\text{s}$. In both of these images we see that a sharp, linear structure emanates from a more diffuse, blob-like structure near the cathode. The canting angle in the modified shadowgraph image is severe – approximately sixty degrees. This agrees with the data in Fig. 5.6 from the high-speed photography experiment.

5.3.4 Discussion

It still remains to discuss the reason why schlieren imaging was not fruitful in this experiment. The most likely culprit was the “smearing out” of the images by light emitted from the plasma. In the shadowgraph configuration, maximum contrast is obtained when the imaging screen is placed near the refractive medium[30] (the current sheet, in the present case). However, when the screen was placed near the CSCX accelerator, the optical emission from the plasma was sufficient to saturate the CCD camera. This was quite remarkable considering that the camera lens was covered with a 532 nm laser line filter, and no line radiation was expected to be emitted within the bandpass of the filter. This implies that the camera saturation occurred due to time-integrated (the slow mechanical shutter allowed light to be collected during the entire current pulse) exposure to broadband radiation. When the imaging screen was moved far away from the accelerator, the exposure due to plasma emission was significantly reduced, however, the contrast due to the shadow effect was lost.

On the other hand, the contrast of the conventional schlieren system is actually enhanced when the imaging plane is far from the refractive medium. Unfortunately, most of the laser light is lost in the preparation of the schlieren image source (see section 4.4.3); also, the optical system is set up to image the discharge chamber and, consequently, the optics efficiently transmit the plasma emission to the imaging plane. These two factors combined to, again, create a situation where the total amount of laser light and plasma radiation collected were comparable.

The most likely solution to the problems detailed above would be to use an electro-optically gated CCD camera. Such a camera could be gated to about 10 ns and, hence, would collect all of the laser light and only a very small fraction of the light emitted by the plasma.

5.4 Magnetic field probes

5.4.1 Database of canting angles

In order to obtain a more accurate measurement of the current sheet speed and canting angle, two magnetic field probes were introduced into the accelerator channel as illustrated in Fig. 4.5c. Probe set I was used and all measurements were obtained near the midpoint (30 cm) of the accelerator. The same propellants and pressure levels that were used in the photographic study were tested.

Figure 5.8 shows a typical set of data with hydrogen as a propellant. A more extensive set of data for all of the propellants is given in appendix C.3. The data plotted in Fig. 5.8a were acquired with the B-dot probes aligned in configuration 1 (see Fig. 4.5); the probes were axially (note: the axial direction is the direction of the thrust axis, or the $+\hat{x}$ direction, as illustrated in Fig. 6.2.1) separated by 21 cm. We see that, as the current sheet approaches a probe, the magnetic field in front of the sheet is gradually detected; then, as the probe enters the current sheet, the magnetic field quickly reverses direction. When the current sheet has passed the probe, the magnetic field reaches its peak value and remains fairly constant (~ 0.35 Tesla) until the current reverses. The peak value of the magnetic field near the mid-section of the accelerator for all of the propellants tested is shown in Fig. 5.8c.

Data, such as that shown in Fig. 5.8a, was used to estimate (using the time-of-flight technique) the current sheet propagation speed by measuring the time delay between a common feature on each waveform (the point at which the magnetic field reached 0.1 T on each waveform was used as the reference point throughout this study). Similarly, Fig. 5.8b shows data from B-dot probes aligned in configuration 2; the probes were vertically separated by 3 cm. By measuring the time delay between the arrival time of the current sheet

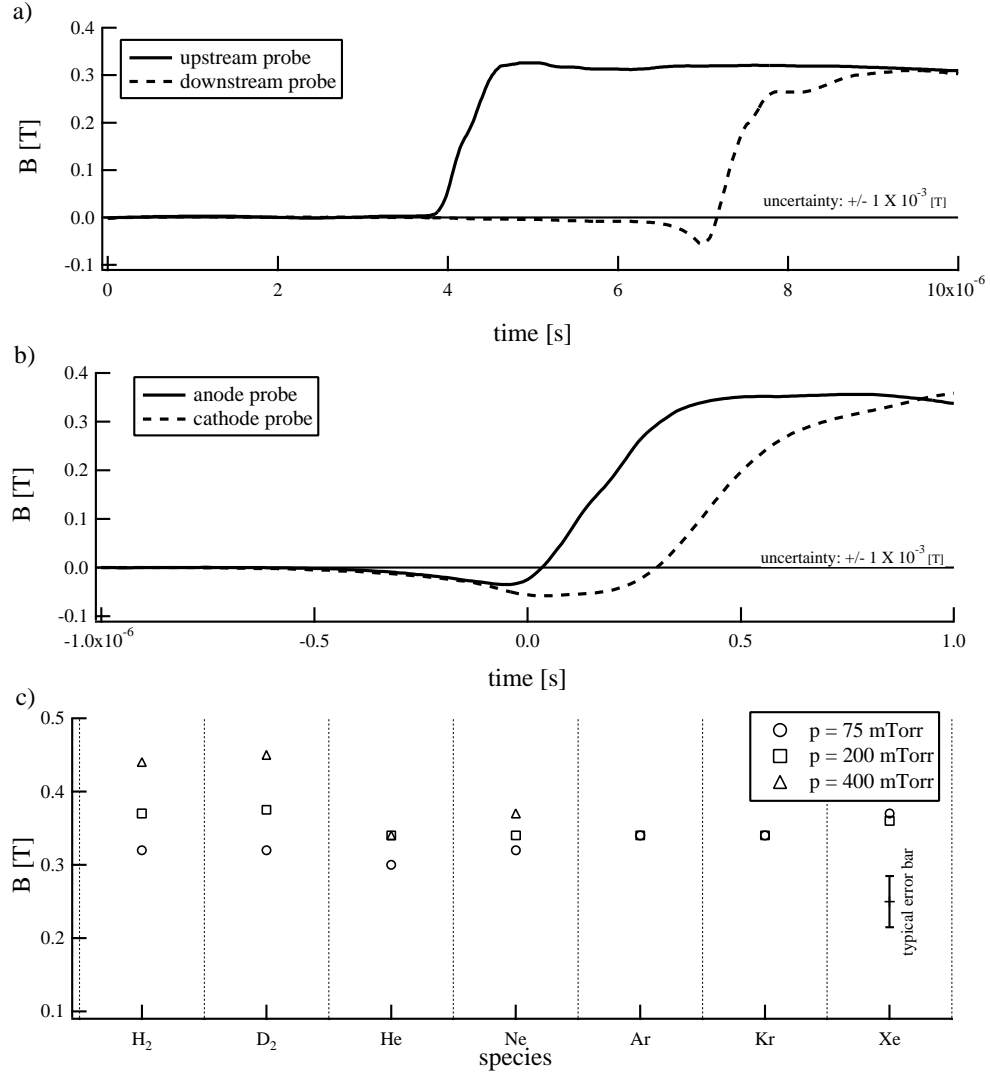


Figure 5.8: Magnetic field measurements using B-dot probes for time-of-flight canting angle analysis in a) configuration 1 and b) configuration 2 (Hydrogen, 75 mTorr.) In c) the peak magnetic field at the accelerator mid-section is plotted.

to each probe and, knowing the propagation speed of the current sheet, the canting angle was estimated. Figure 5.9 summarizes all of the speed and canting angle measurements obtained using the magnetic field probes and time-of-flight analysis. Each datum point represents the average of two experimental measurements. The random error associated with having only two samples is large, and is reflected in the large error bars.

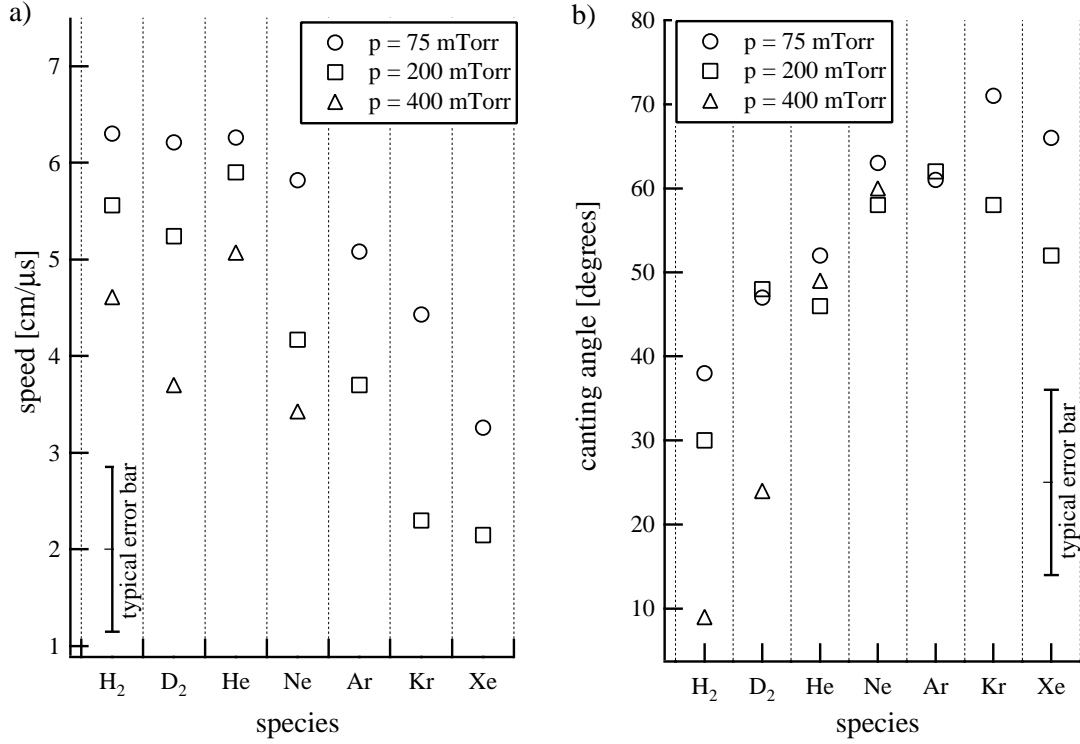


Figure 5.9: Current sheet a) propagation speed and b) canting angle, interpreted from magnetic field probe data.

5.4.2 Evolution of the canting angle

In addition to quantifying the canting angle at one axial location, a magnetic field probe study was conducted to reveal how the canting angle evolved as the current sheet propagated down the electrodes. Probe set II was used in configuration II with the probes vertically displaced by 4 cm (see Fig. 4.5). Data were acquired at about forty different axial locations. Only argon propellant (75 mTorr) was used in this study.

Figure 5.10a shows the measured current sheet arrival time at each of the axial probe locations for both the anode and cathode probes. Each datum point represents the average of four shots. Polynomial curve fits (fifth order) to the datum are also shown. By taking the average of the of the anode and cathode curves, the trajectory of the geometric center of the current sheet can be constructed. Taking the time-derivative of the trajectory yields

the current sheet speed profile, as illustrated in Fig. 5.10b. Similarly, the evolution of the canting angle can be constructed by comparing the anode probe position curve with the cathode probe position at fixed times; figure 5.10c shows the results of such an analysis.

Figure 5.11 shows the evolution of the magnetic field at several axial locations, for both the anode and cathode probe. Each waveform is the record from a single shot.

5.4.3 Discussion

The expected peak value of the magnetic field may be estimated using the parallel plate transmission line inductance formulas given in appendix A.1. Since the surface area of the flux loop increases as the current sheet propagates, the magnetic field is expected to decrease with axial distance from the breech. At the center of the accelerator (30 cm), using $L=90$ nH, $I=60$ kA, the dimensions of the accelerator and the definition of inductance, the magnetic field is estimated to be 0.36 T, which is consistent with the data plotted in Fig. 5.8c. The magnetic field in the immediate vicinity of the breech was measured to be about 0.7 T.

The trends found in the photographic data are also evident in the magnetic field data: the speed of the current sheet decreases with increased mass loading and, in general, the current sheet canting is more severe for the higher atomic mass propellants. Comparison of the numerical values in both plots show sporadic quantitative agreement. The canting angles for hydrogen and deuterium (at 75 and 200 mTorr) and helium were found to be substantially larger than those measured in the photographic study – which underpins the comments made earlier about the difficulty of interpreting photographic data. The magnetic field data did reinforce, however, that the lowest canting angles are achieved with hydrogen and deuterium at 400 mTorr.

The canting evolution data show that current sheet canting is not a continuously evol-

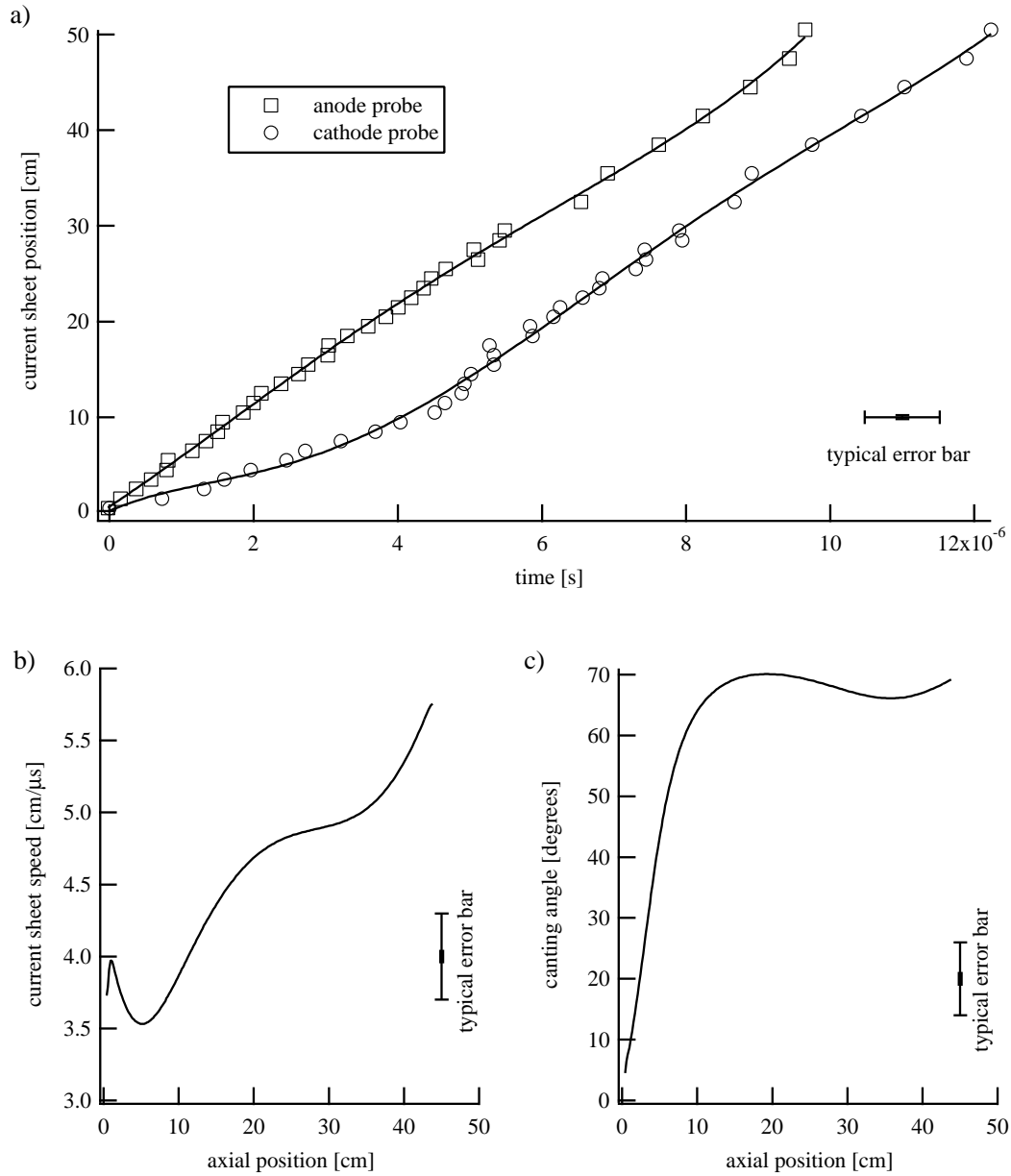


Figure 5.10: Evolution of current sheet canting interpreted from magnetic field probe data (argon, 75 mTorr): a) trajectory of anode and cathode current sheet attachment, b) current sheet speed as a function of axial position, c) current sheet canting angle as a function of axial position.

ing phenomenon but, rather, the degree of canting is set up in about the first ten centimeters, after which the current sheet maintains a fairly constant canting angle. The plot in Fig. 5.10c indicates a canting angle of about 60° - 70° near the midsection of the accelerator (30

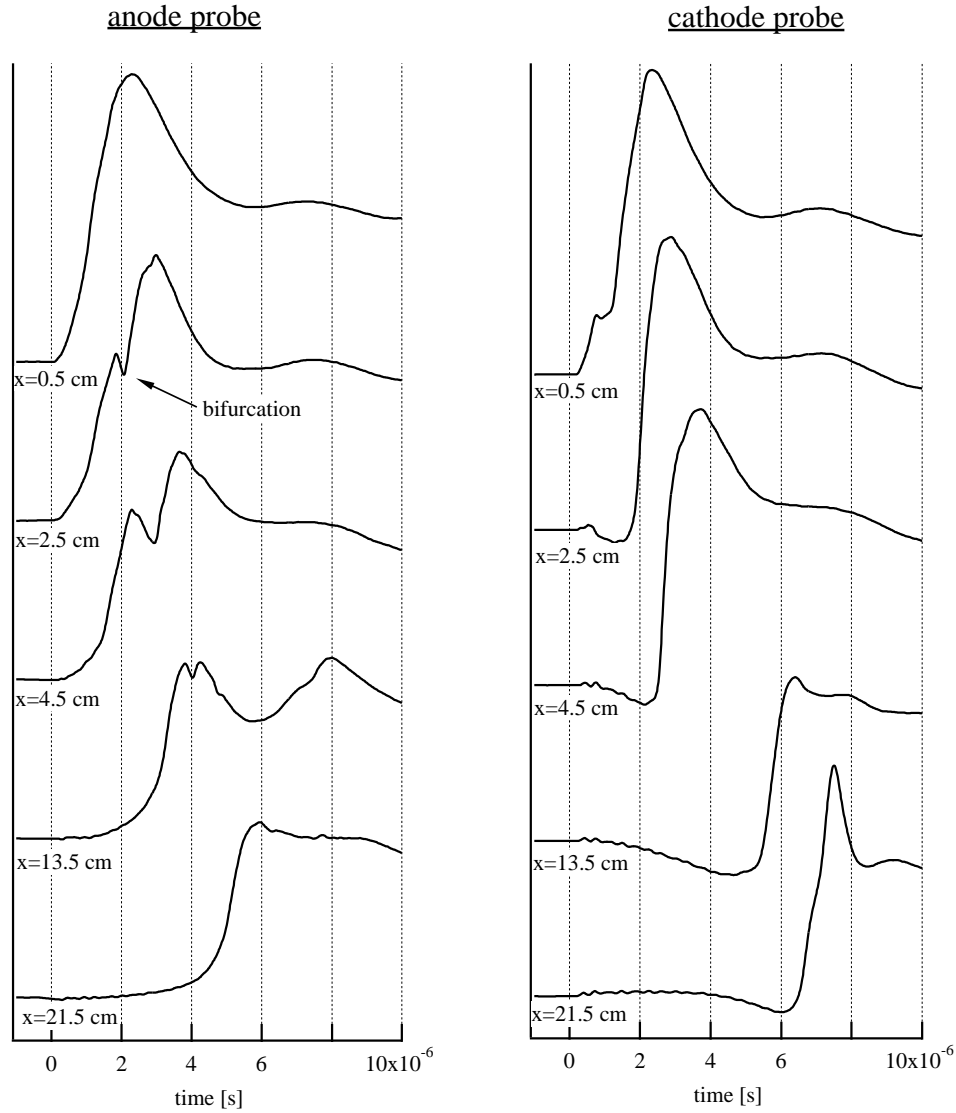


Figure 5.11: Magnetic field histories at selected axial locations (argon, $p=75$ mTorr). For reference, the peak value of the magnetic field for both the anode and cathode probes were measured to be about 0.7 T at the $x=0.5$ cm location.

cm), which agrees with the data presented in Fig. 5.8b. Also, Fig. 5.10b indicates a current sheet speed of about $4.5\text{--}5.0$ cm/ μs at the midsection, in agreement with the data presented earlier. Figure 5.10b also shows that the current sheet slows during the early stages of the discharge, but then accelerates as it propagates down the electrodes.

The data in Fig. 5.11 provide some insight into the sequence of events which cause

the current sheet to cant during the early stages of the discharge. The plots show very different behavior for the anode current conduction as compared to the cathode attachment. The $x=0.5$ cm curves look very similar; however, a double-peaked structure is evident in the $x=2.5$ cm anode waveform which is not present in the corresponding cathode trace. The two peaks in the anode data imply the presence of two current conduction paths – bifurcation of the initial current sheet. In the $x=4.5$ cm data the bifurcation is seen to be more pronounced. As the current sheet continues to propagate, the two current attachments spread apart and the leading sheet becomes the dominant current conduction channel (as illustrated by the $x=13.5$ cm data). By the time the current sheet reaches the 21.5 cm location the trailing (initial) current sheet is seen to have disappeared altogether, and the discharge returns to a single current conduction channel mode of operation. The important point here is that no comparable (bifurcation) features are present in the cathode magnetic field waveforms. An interpretation of this experimental observation will be given in section 6.2, where it is proposed that bifurcation is the beginning of a process that leads to a canted current sheet.

5.5 Laser interferometry

The final diagnostic technique implemented to measure the current sheet speed and canting angle was a two-chord laser interferometer (see Fig. 4.6). In addition to the propellants described in the preceding sections, methane was tested. The interferometry experiment was carried out in a manner completely analogous to the magnetic field measurement experiment: two axially separated laser beams (configuration 1) were used to measure the current sheet speed and two vertically separated beams (configuration 2) were used to measure the canting angle.

Figure 5.12 shows examples of electron density measurements acquired with the interferometer using argon propellant. A more extensive set of data for all of the propellants is

given in appendix C.4. Figure 5.12a shows a typical result using the interferometer in configuration 1. In this case the laser beams were axially separated by about 11 cm. It is seen that the time delay between the two signals was about $2.5 \mu\text{s}$ – indicating a propagation speed of about $4.5 \text{ cm}/\mu\text{s}$. Also, this figure indicates that the electron density decreased as the current sheet propagated between the upstream and downstream beams.

Figure 5.12b shows a typical result using the interferometer in configuration 2 (4 cm vertical beam separation), with the same initial propellant loading as in Fig. 5.12a. The anode signal is seen to arrive about $1.5 \mu\text{s}$ before the cathode signal, in agreement with our previous observations that the anode current sheet attachment leads the cathode attachment. Multiplying the anode-cathode time delay by $11 \text{ cm}/\mu\text{s}$ (the sheet propagation speed), yields an axial anode-cathode arc attachment separation of about 7 cm, so that the canting angle may be estimated to be about 60° . Another readily apparent feature in Fig. 5.12b is the large disparity in electron density near the cathode as compared to near the anode. Also, the cathode trace indicates that a layer of plasma persists along the cathode long after the current sheet has passed by.

Figure 5.12c shows a summary of the peak electron density at the accelerator midsection for all of the propellants tested. The plotted values were compiled from data obtained using the upstream probe in configuration 1. For reference, horizontal lines have been added to indicate the initial propellant fill number density for the specified initial pressure levels. Additional data for the current sheet widths and electron density gradients are given in appendix C.4 (Fig. C.17): typical values are 1 cm and $5 \times 10^{16} \text{ cm}^{-4}$, respectively.

Figure 5.13 summarizes the speed and canting angle measurements from the interferometric diagnostic and time-of-flight analysis. Each datum point is the result of ten experimental measurements and, hence, has a smaller error bar than in the magnetic field experiment.

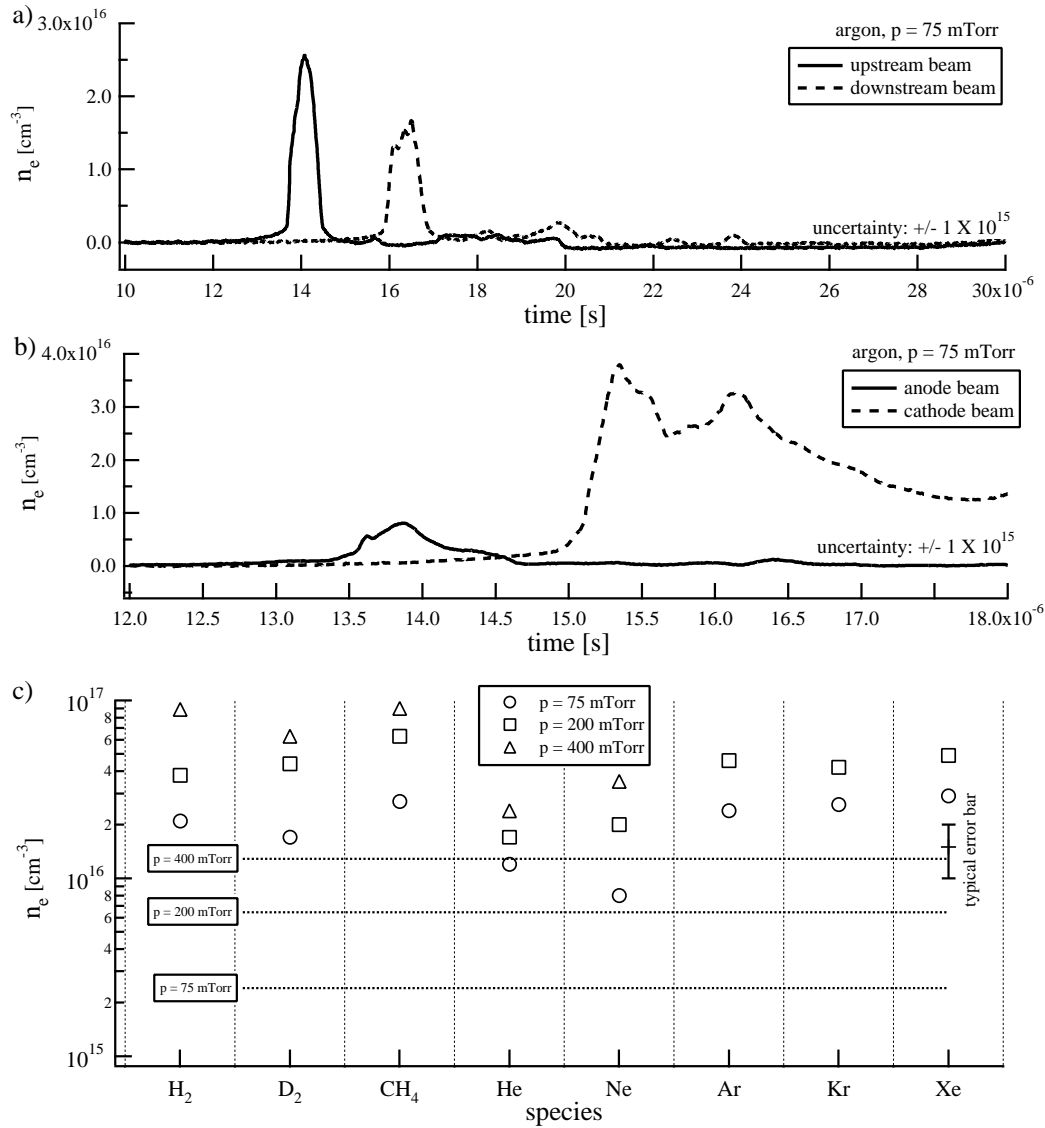


Figure 5.12: Example electron density profiles for laser beams aligned in a) configuration 1 and b) configuration 2 (argon, $p = 75$ mTorr). The peak electron density at the accelerator midsection, for each of the propellants tested, is plotted in c).

5.5.1 Discussion

The interferometry diagnostic was very successful in providing quantitative measurements of the current sheet electron density, speed and canting angle. The measured electron densities were up to an order of magnitude higher than the initial fill density indicating ei-

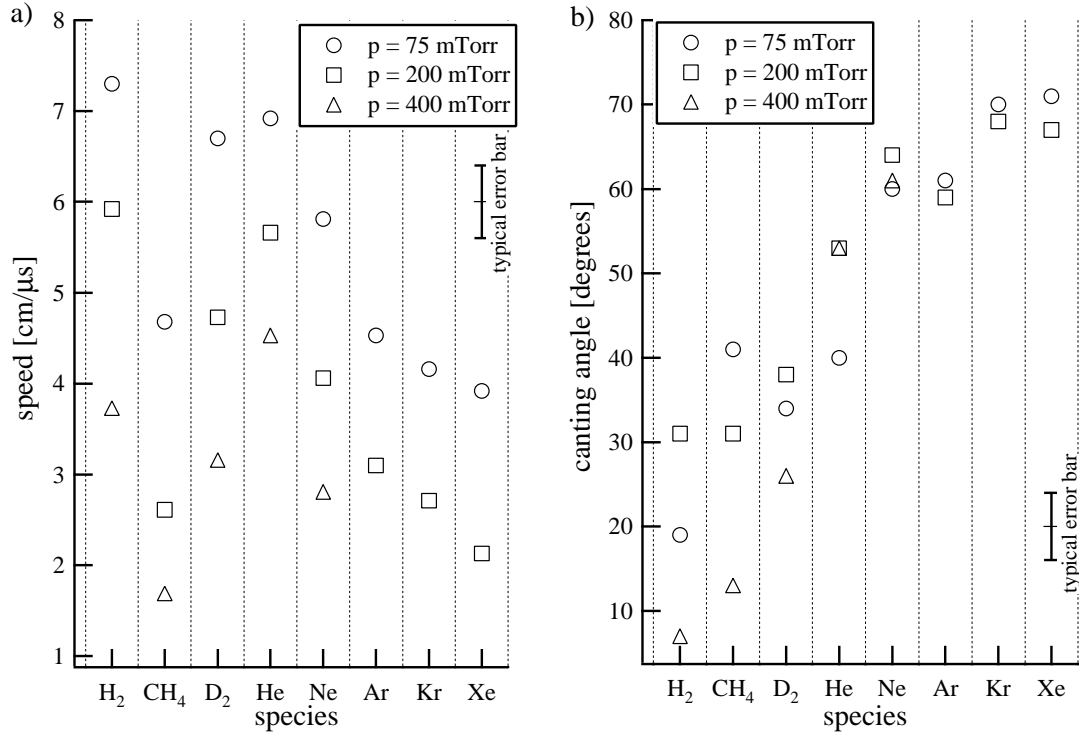


Figure 5.13: Current sheet a) propagation speed and b) canting angle, interpreted from interferometric data.

ther local compression of the propellant, entrainment of propellant in the current sheet, or higher level ($Z > 1$) ionization. The latter possibility is excluded in the next section (which presents the spectroscopic results) where it is shown that singly ionized species are the most prevalent ions.

In many cases the high electron density near the cathode caused phase variations which exceeded the frequency response of the interferometric system. While this did not effect the calculation of the current sheet speed and canting angle, it did make an accurate measurement of the electron density near the cathode impossible in some situations. These cases are more completely discussed in appendix D.2.1.

Comparison of the data in Figs. 5.9 and 5.13 shows, within the bounds of the given error bars, that all of the major trends discussed in the interpretation of the magnetic field

data are also borne out by the interferometric data. Also, methane (which is largely composed of hydrogen (CH_4)) exhibits the same peculiar tendency as hydrogen and deuterium – reduced canting at higher pressure. The analysis of the photographic data, however, gave significantly different estimates of the canting angle for the lower molecular mass propellants. Evidently, some of the luminous regions in the photographs are not zones of current flow but originate from other processes.

5.6 Emission spectroscopy

Both time-integrated and time-resolved spectral data were acquired. The time-integrated surveys were intended to determine the species present in the CSCX arc discharges, while the time-resolved data were aimed at providing an estimate of the electron temperature in the current sheet.

5.6.1 Survey of spectral lines

The acquisition of time-integrated data yielded a broad (wavelength) spectral survey of the plasma optical emission in order to identify candidate lines for the more detailed time-resolved experiments. The emission was surveyed by scanning the spectrometer between 350-850 nm (in 10 nm increments) with the spectrometer aligned in configuration 1 (see Fig. 4.8.) The camera was gated for about 1 ms exposure; therefore, emission from the entire duration of each discharge event was recorded. The capacitor bank was charged to 3 kV before each shot; this reduced voltage was used in the survey study in order to reduce, in light of the large number of required shots, the “wear and tear” on PFN II.

The sequences of about fifty frames of spectral data (for each propellant) were “pasted” together and calibrated using the software described in section 4.7.1. An example of a

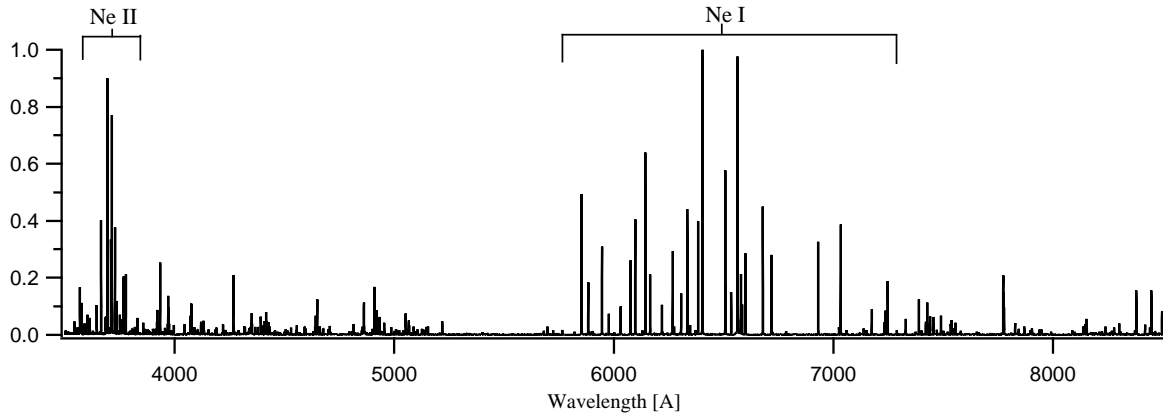


Figure 5.14: Normalized intensity of time-integrated optical emission from a neon arc discharge in the CSCX accelerator ($p=75$ mTorr).

complete data set, using neon propellant, is shown in Fig. 5.14; the concentration of lines around 6000 \AA reflects the characteristic red glow of low pressure neon discharges. In addition to plots of data for the other propellants, appendix C.5 presents tabular data which identifies the atomic species associated with each emission line. The table shows that the emission spectra from all of the propellants can be characterized as line radiation of neutral and singly ionized species.

Another noteworthy result from the spectral survey was that no copper emission lines were observed (there are many tabulated copper neutral and ion transitions in the region surveyed[33]). This is most evident in the hydrogen survey graph (see Fig. C.18a), where only the H_α and H_β lines were observed. This implies that there was no appreciable contamination of the propellant (at least in the central region of the accelerator) due to electrode erosion. We make this assertion cautiously, though. Other researchers[35] have observed that significant concentrations of copper electrode material can migrate into arc discharges without producing significant *optical* emission. The low ionization potential of copper allows ablated electrode material to rapidly reach high levels of ionization, where bound-bound electronic transitions result in the production of radiation in the *vacuum ultraviolet*,

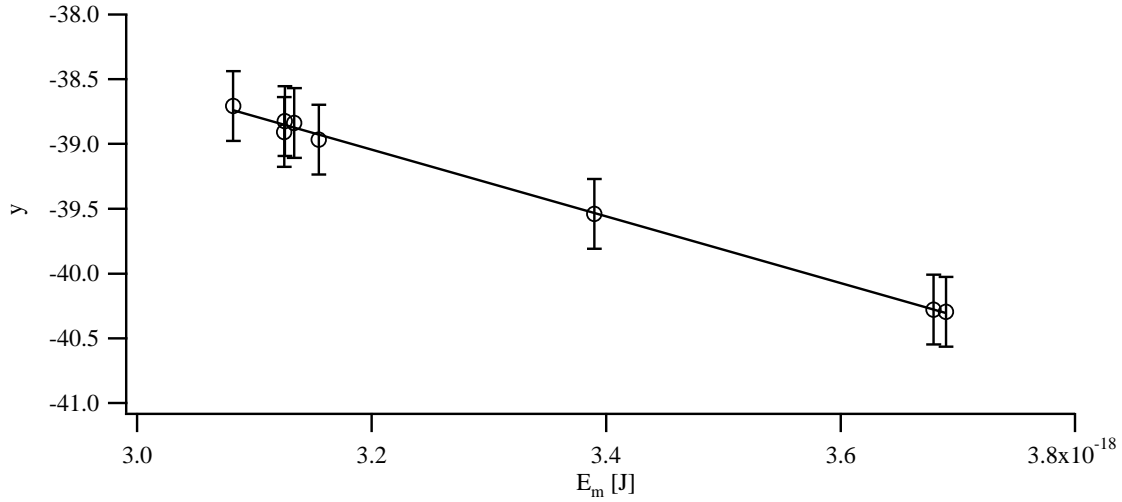


Figure 5.15: Temperature data: weighted dimensionless spectral emission intensity (y) versus energy of upper state (E_m) (argon, $p = 75$ mTorr).

which cannot be detected with our instrument. Therefore, we cannot completely rule out the presence of electrode material in our discharges.

5.6.2 Time-resolved spectra and temperature determination

Argon was chosen for more detailed, time-resolved analysis. Eight lines were acquired with the spectrometer in configuration 2 (see Fig. 4.8). The camera was gated to 50 ns exposure-time. The spatial position of the light collection was chosen to roughly correspond to the position where the previous magnetic and interferometric data were acquired. Based on the current sheet speed measurements observed in those previous experiments, current sheet motion was expected to be restricted to less than a few millimeters during the CCD array exposure. The PFN II voltage was set to 9 kV and the propellant pressure was 75 mTorr for all shots.

The procedure for determining the electron temperature involved the construction of a “Boltzmann plot” and fitting a straight line to the experimental datum points; this procedure

is described in detail in appendix D.1. Figure 5.15a shows the argon emission data and a linear fit through the points; each of the plotted points is the average of data collected from five different shots. It is apparent that the experimental data do indeed follow a linear trend. This is especially important because it implies that the free electrons in the arc plasma were indeed in a Maxwellian distribution of speeds, which is essential if we are to use the relative line ratio technique to infer electron temperature. The uncertainty indicated by the error bar for each point is primarily due to random uncertainty in the intensity data. In the case illustrated above, the calculated electron temperature was found to be 2.4 ± 0.2 eV.

Time-resolved data for several other propellants were also acquired (hydrogen, helium, krypton, and xenon); however, the results of the analysis of that data is not reported here for the following reasons. In the hydrogen and helium data, too few lines were available to make a statistically meaning linear fit (only two lines were available for hydrogen, and three for helium). On the other hand, many well defined lines were recorded with krypton and xenon. However, we were not able to locate the atomic energy level data necessary for temperature analysis of these plasmas. For analysis purposes in the next chapter, the electron temperature will be assumed to be the measured argon value of 2.4 eV for all of the propellants. This value of temperature will be used to to calculate some characteristic plasma parameters in CSCX plasmas but the main focus of the chapter, which is to develop an analytical expression for the canting angle dependence on propellant molecular mass, will be shown to independent of temperature.

5.7 Summary of experimental results

The results of this chapter show that the experimental apparatus performed as designed; current sheets were formed and stably accelerated in a repeatable manner. For the most part, the diagnostics also proved to be well-suited for measuring the canting angle and

thermodynamic state of the current sheet plasmas.

The first data presented in this chapter showed how the accelerator behaved as a circuit element. The data showed that the accelerator very weakly loaded the PFN: the current reversal was large ($\sim 80\%$), indicating small dissipation in the load. Also, large changes (factors of 3 to 4) in the dynamic impedance (i.e., dL/dt) produce only a small variation ($\sim 10\%$) in the current, providing further evidence that most of the reactance in the circuit resides outside of the accelerator.

The photographic, magnetic and interferometric diagnostics present systematic, quantitative measurements of current sheet canting in a pulsed electromagnetic accelerator. The picture that emerges, from all of the diagnostics, is that, after breakdown, the current sheet bifurcates and evolves into a highly canted, propagating structure.

A few issues regarding the validity of the canting angle measurements at higher pressure levels need to be addressed. The propellant that is overrun at the cathode may form a plasma “bubble” which, in time, stretches across the entire discharge channel and, hence, provides an alternative current path – effectively short circuiting the initial current sheet. The presence of these structures is evident in most of the higher pressure level electron density data shown in appendix C.4. Also, the corresponding magnetic field data in appendix C.3 show fluctuations suggestive of the passing of multiple current conduction zones. The influence of these “re-strikes” on the canting angle of the leading current sheet is uncertain. The phenomenon may possibly be beneficial in pulsed plasma thrusters, as the propellant will experience a multi-stage acceleration of sorts.

The next chapter, Analysis and Modelling, attempts to develop an explanation for why current sheets cant. The observations reported above, as well as the historical review presented earlier, will be drawn upon heavily to guide this conceptualization of the mechanisms which drive canting.

Chapter 6

Analysis and Modelling

Having reported all of the experimental results in a rather fast-paced manner in the last chapter, we now turn to trying to better understand what the data as a whole mean. This chapter aims to explain, through further analysis of the experimental data and phenomenological modelling, why current sheets cant.

The first section of this chapter tabulates some relevant derived physical quantities which are calculated using the measurements from the last chapter. The next section draws on “conspicuous” features, noted in the analysis of the data, to develop a model for current sheet canting. Let us state from the outset that a complete theoretical model of the current sheet accelerator discharge is not something which can be easily grasped. This owes not only to the fact that all facets of the problem are highly unsteady, but also that many of the physical processes which constitute boundary conditions for the problem are poorly understood. Nevertheless, it will be shown that a simplified model of the canting process provides qualitative agreement with the trends in the data and, hence, gives us insight into the physical processes which drive canting. The last section looks back to the work of earlier researchers (see Chapter 2) and evaluates how well the proposed model agrees with their observations.

6.1 Further analysis of the experimental data

Before modelling the canting problem it is useful first to collect in one place, and in a general sense, a description of the plasmas that we are dealing with – that is, to define their physical characteristics. This is especially important because in the absence of a holistic model, such as in the present case, it is often fruitful to identify some of the more conspicuous physical traits of the object under study and then use simple models to check the influence of each of these traits on the phenomenon of interest.

6.1.1 Characteristic plasma parameters

Figure 6.1 shows some calculated fundamental quantities which characterize CSCX current sheet plasmas. These plots were constructed using the magnetic field, electron density, and temperature data from Figs. 5.8, 5.12, and 5.15 (p=200 mTorr data was used in all of the calculations); these values are the peak measured values as the current sheet propagated through the measurement region near the center of the accelerator. The temperature measurement from argon current sheets (i.e., $T_e = 2.4 \pm 0.2$ eV) was used in all calculations. The parameters were calculated using their standard definitions[36]. Some additional characteristic parameter values are tabulated in Table 6.1. Throughout the calculations it was assumed that: $n_i = n_e$, $T_i = T_e$, and $Z = 1$.

Let us consider first some characteristic lengths in the CSCX current sheet plasmas. Figure 6.1a shows that the electron and ion gyroradii are small relative to the device dimensions (~ 5 cm), which shows that particle orbital motion is, for the most part, not interrupted by the proximity of the electrodes. This figure also shows that the mean free path (Coulomb collisions) is small compared to the current sheet dimensions (~ 1 cm), implying that the plasma is collisional for both electrons and ions. Using the approximate dimensions of the current sheet ($1 \text{ cm} \times 10 \text{ cm} \times 5 \text{ cm}$) and the calculated value of the transverse

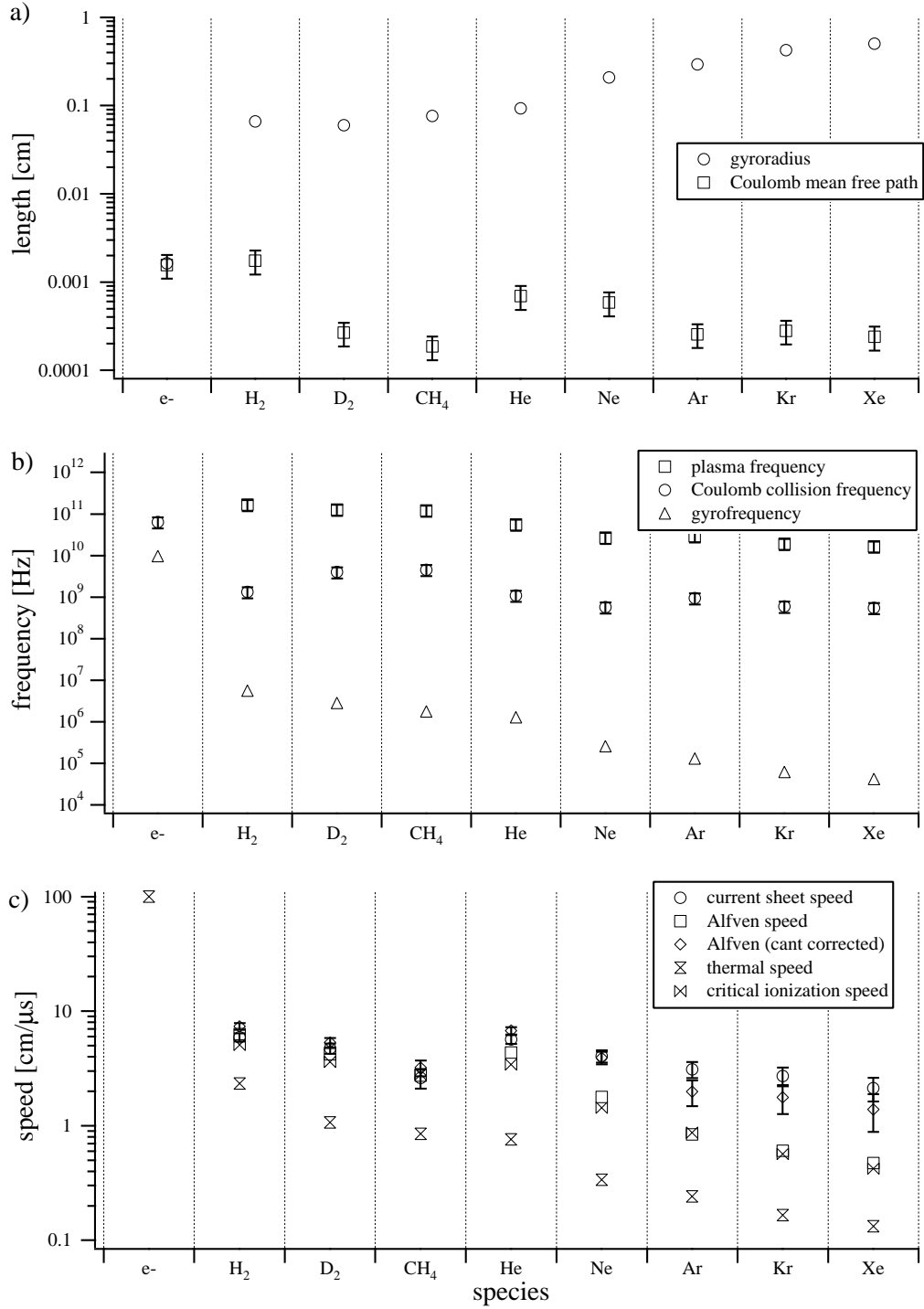


Figure 6.1: Characteristic values of a) length, b) frequency, and c) speed in CSCX current sheets (error bars not illustrated are comparable to marker size).

Spitzer resistivity (η_{\perp}), the Ohmic resistance of the current sheet is estimated to be $5 \text{ m}\Omega$, which is the same order of magnitude as the measured value (see section 5.1.2). For the ions, the mean free paths are also seen to be much smaller than the corresponding gyroradii, whereas the electron mean free path and electron gyroradius are seen to be comparable in magnitude. Table 6.1 lists two other characteristic lengths: the Debye length (λ_D), and the electron skin depth (δ_e). The Debye length is seen to be small compared to the device dimensions, so non-quasineutral electrode sheaths are expected to be small. The small value of the skin depth implies that the plasma is well suited for containing magnetic fields via surface currents, that is, forming current sheets.

Figure 6.1b shows some calculated characteristics frequencies in the CSCX plasmas. Of particular interest is the ratio of the gyrofrequency to the collision frequency (Coulomb) – the so-called Hall parameter. Table 6.1 shows that the Hall parameter is expected to be small for both electrons (Ω_e) and ions (Ω_i). This implies that minimal Hall Effect-induced transverse (i.e., perpendicular to both the magnetic field and the applied electric field) components of current are expected to arise. It should be emphasized that these statements only apply to the Hall Parameter calculated using the average measured current sheet properties near the midsection of the accelerator – where the canting angle has stabilized. The Hall Effect may, as will be shown later in this chapter, play a very important role in causing the current sheet to cant, during the early stages of the discharge.

Figure 6.1c shows some characteristics speeds in the CSCX plasmas. The measured current sheet speed is seen to track close to the Alfvén (v_A) and critical ionization (v_{ci}) speeds for the lower atomic mass propellants, but diverges at higher atomic masses. (Note:

$$v_A = \frac{B}{\sqrt{4\pi n_i m_i}} , \quad (6.1)$$

$$v_{ci} = \sqrt{\frac{2\phi_i}{m_i}} , \quad (6.2)$$

Table 6.1: Order of magnitude estimates of characteristic parameter values for CSCX current sheets (representative values used: $T = 2.4$ eV, $n = 3 \times 10^{16} \text{ cm}^{-3}$, $B = 0.35$ T).

parameter	value	parameter	value
λ_D [cm]	1×10^{-5}	β	1×10^{-1}
δ_e [cm]	1×10^{-3}	Ω_e	1×10^{-1}
η_{\perp} [Ω cm]	1×10^{-2}	Ω_i	1×10^{-3}

where B is the magnetic inductance, n_i is the ion number density, m_i is the ion atomic mass, and ϕ_i is the first ionization potential of the neutral gas.) This divergence may, in part, be due to the fact that $Z = 1$ was assumed in the calculations, whereas higher levels of ionization may have existed in the heavier propellants; this would lead to a lower calculated Alfvén speed, since n_i would actually be lower than n_e (which was measured and used in the calculations) in the plasma. However, even if $Z = 2$ is used in the calculation, multiplying the plotted Alfvén speeds by the corresponding factor of $\sqrt{2}$ would be insufficient to bring the Alfvén speeds for the heavier propellants into parity with the measured values. Figure 6.1c shows a canting-corrected Alfvén speed, v_A^c , which more closely tracks the measured current sheet speed. The calculation of v_A^c is described in section 6.2.5.

6.2 Modelling

In this section we develop phenomenological models of the current sheet which describe the evolution of its structure into sheet with a canted current front.

6.2.1 Heuristic model of current sheet structure

In preparation for postulating the complete current sheet canting model, it is useful to first set the stage by bringing together the experimental results and the calculated parameters above into a working, heuristic model of the current sheet. Since, as shown in chapter 2, there is no unanimity of opinion as to what goes on inside a current sheet, it is important for us to define first the palette from which we will draw and develop ideas.

Figure 6.2 shows a graphical conceptualization of the spatial configuration of the current channel, magnetic field, electron density and electron density gradient in an idealized current sheet. The breech is to the left and the current sheet accelerates to the right under the action of the $\mathbf{J} \times \mathbf{B}$ force. The calculations in the previous section show that the CSCX current sheets were collisional and the Hall parameter was calculated to be small; therefore, current conduction is expected to occur in a narrow channel orthogonal to the electrodes, as pictured. The experimental data (see Fig. C.17) indicate that the CSCX current sheet width was on the order of 1 cm.

In theory, the idealized current sheet entrains the neutral gas that it overruns, leaving a vacuum region in its wake. The exact physical mechanism through which the gas entrainment takes place is not completely understood; Rosenbluth[37] described the process as collisionless, specular reflection while Lovberg[38] pointed to an accelerating electric field originating from an inertially-induced separation of electrons from their parent ions. Reflecting on the analysis of the data in the previous section, it appears that the entrainment process in CSCX current sheets can be explained more simply. The calculations in the previous section showed that in CSCX current sheets both the electron-electron and electron-ion collision frequencies are adequately large to characterize the plasma as a fluid. The current channel accelerates under the influence of the $\mathbf{J} \times \mathbf{B}$ force wherein the current carriers transfer the force to the bulk fluid through their tight collisional coupling. Now, on

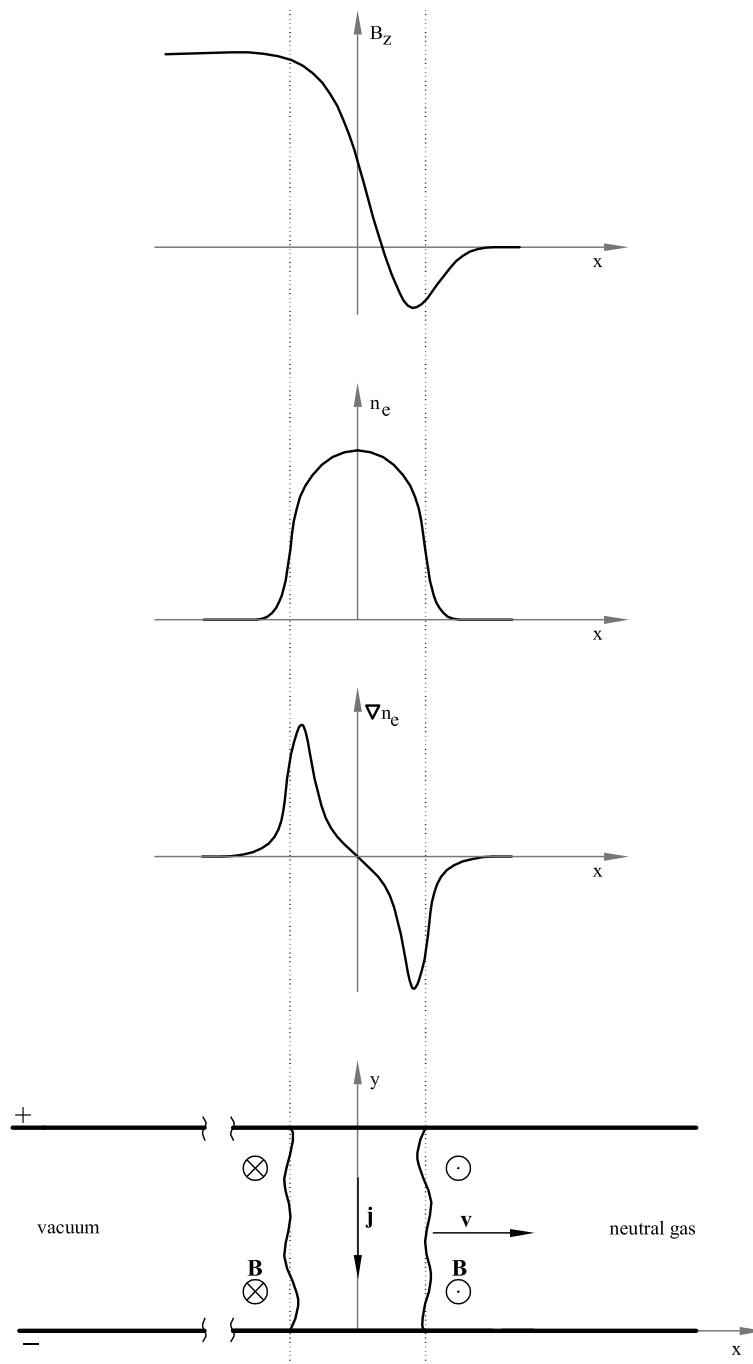


Figure 6.2: Heuristic model of a current sheet.

the front face of the current sheet, each of the incident neutral (test) particles with streaming speed v (relative to the current sheet) undergoes a “slowing down” relaxation process through collisions with the background current sheet (field) particles described by [36]

$$\frac{dv}{dt} = -\nu_{ii}v, \quad (6.3)$$

where ν_{ii} is the ion-ion collision frequency (it is assumed that the incident neutral particle is immediately ionized as it enters the current sheet). The incident particle will become stationary relative to the current sheet in a characteristic slowing time $\tau_s = 1/\nu_{ii}$ and a characteristic slowing distance $\lambda_s = v\tau_s$. From Fig. 6.1 we find typical values for ν_{ii} ($\mathcal{O}(10^9)$ Hz) and v ($\mathcal{O}(10^6)$ cm/s). This implies that λ_s is $\mathcal{O}(10^{-3})$ cm. Since the current sheet thickness is $\mathcal{O}(10^0)$ cm (see Fig. C.17), the incident neutral flux is expected to be subsumed into the current sheet plasma before penetrating very deeply. Again, this analysis assumes that the heavy particles enter the current sheet as ions; we have not addressed the ionization process. It may be possible for neutral atoms to pass through the current sheet without being ionized, yet still experience some acceleration through ion neutral collisions. Calculations of the relevant parameters (the ionization length and the ion-neutral collision frequency) are not carried out here, but remain a very relevant research question.

The current sheet propagation speed is theoretically limited to the so-called magnetosonic speed. In magnetized plasmas, the magnetosonic speed is the analogue of the sound, or acoustic speed in ordinary fluids. It is the characteristic rate at which disturbances are propagated through a plasma, transverse to an imbedded magnetic field. When the magnetic field is one-dimensional (as is approximately the case in the CSCX experiment), the magnetosonic speed can be shown to be numerically equal to the Alfvén speed[39].

The expected distribution of the magnetic field strength in the ideal current sheet shown in Fig. 6.2 is suggested by the experimental data shown in appendix C.3. Because of the solenoidal nature of magnetic fields, the lines of force must wrap around the current sheet,

resulting in a field with reversed direction in front of the current sheet. By solving the full boundary value problem with the conductors configured as illustrated, it can be shown that the magnetic field in front of (upstream side) the current sheet is much smaller than inside (downstream side) the current loop[40]. Nevertheless, there will be a region of finite width inside the current sheet where the magnetic field is reversed; this is interesting because it implies that the plasma near the leading edge of the current sheet will be accelerated opposite to the sheet velocity vector, \mathbf{v} . The magnetic field reverses at some point inside the current sheet – eventually reaching its peak value at the back edge of the current sheet. The magnetic field is expected to be constant between the back edge of the current sheet and the breech; figure 5.8 shows that this peak value was measured to be about 0.35 T (at the accelerator midsection) in the present experiment.

The simple electron density distribution sketched in Fig. 6.2 mirrors the general structure seen in many of the experimental profiles (see appendix C.4), where the typical peak electron density was found to be about $5 \times 10^{16} \text{ cm}^{-3}$. Near the edges of the current sheet, the typical electron density gradient was large (typically about $5 \times 10^{16} \text{ cm}^{-4}$, as shown in Fig. C.17). The magnitude of this electron density gradient is large enough to characterize it as a “conspicuous” feature; it will be shown below that steep electron density gradients may be a catalyst for initiating the rapid evolution of current sheet canting.

Above we have outlined the expected behavior of an ideal current sheet. Below we propose a model for how current sheets in real accelerators may deviate from this idealized behavior.

6.2.2 Canting model preliminary description

One of the most distinguishing characteristics of the CSCX experiment, as compared to the majority of the earlier studies reported in chapter 2, was the use of a protracted, non-

sinusoidal current pulse. As will be shown below, allowing the current to stabilize enables remnants of early, transient processes to be distinguished from the stable propagation phase and provides insight into the cause of current sheet canting. Below, a phenomenological model for the evolution of a canted current sheet is proposed. The model draws on the parametric description of the current sheet plasma given in the previous section, as well as qualitative features from data in the previous chapter and from similar data in chapter 2.

It is instructive to first present a qualitative description of the entire model and then analyze the components individually (note: it is most expedient to describe the facets of the model as if they were facts rather than to repetitively state comments such as “this may happen” or “it is probable”, etc.. With this noted caveat in mind, let us consider a potential sequence of events that could lead to current sheet canting).

Figure 6.3 shows a sequence of events which could culminate in a canted current sheet. The grey objects are meant to illustrate the spatial extents of the current sheet plasma. The solid lines behind the current sheet are meant to represent magnetic flux tubes (i.e., the amount of magnetic flux contained between consecutive pairs of lines is constant from frame-to-frame).

The first illustration in Fig. 6.3 shows the initiation of the current sheet at the breech of the accelerator. In illustration 2 the current sheet is shown shortly after initiation. The plasma in the region near the anode becomes severely depleted due to mass motion of the fluid toward the cathode (for reasons to be explained later). This first phase is termed the “starvation phase”, borrowing terminology from a phenomenon observed in MPD thrusters called “anode starvation”[41] (which probably originates from an altogether different physical mechanism).

Between illustrations 2 and 3 the plasma near the anode becomes so tenuous that it can no longer contain the magnetic field behind it. In a sense the current sheet can be thought of

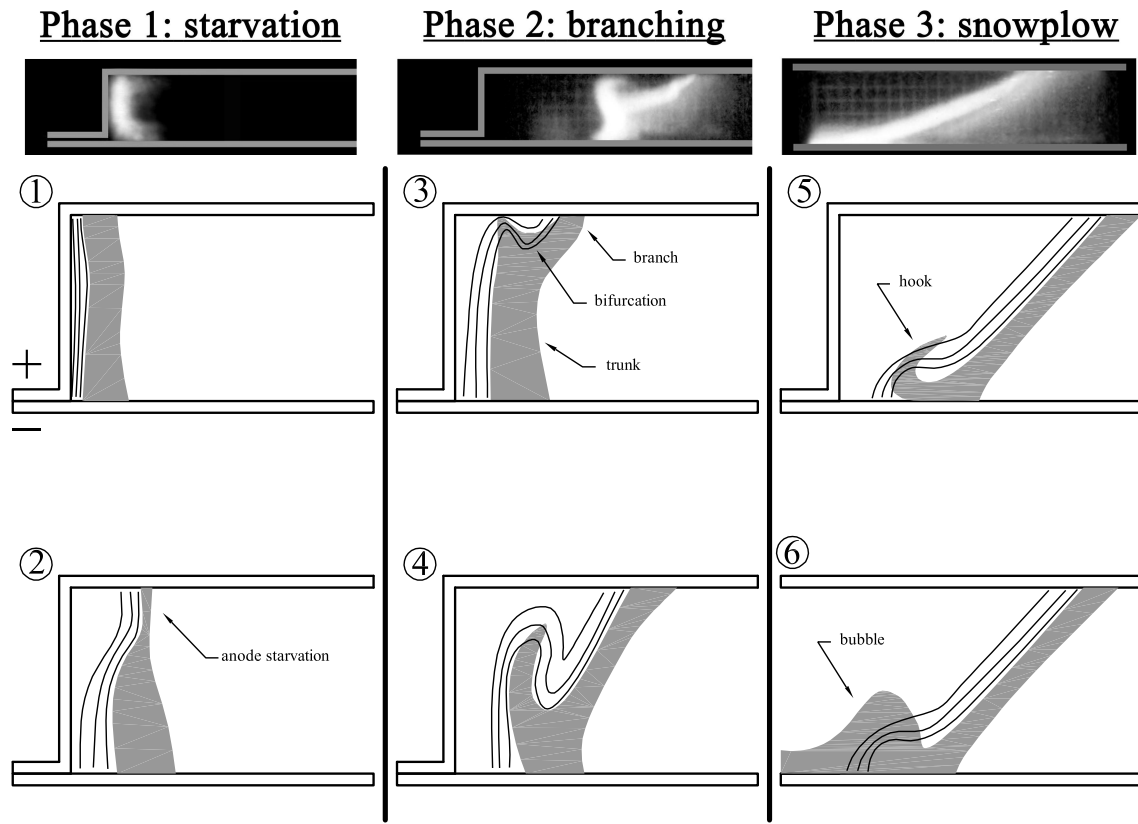


Figure 6.3: Illustration of a phenomenological model showing current conduction phases which may lead to a canted current sheet.

as a thin membrane (like a balloon) that contains a high pressure “magnetic fluid”. When the plasma near the the anode becomes sufficiently “thin”, the membrane quickly expands, or ruptures, allowing the contained magnetic flux to rapidly stream through. The initial current channel (henceforth referred to as the “trunk”) becomes bifurcated along the anode, as the streaming magnetic flux (and associated surface current) propagate ahead of the original current attachment point; this interface forms a new conduction path for the current sheet which connects the trunk to the anode (this new conduction path will be referred to as the “branch”). The newly formed branch and trunk form what was referred to by earlier

researchers as the “anode foot”. Eventually the trunk becomes magnetically insulated (as the magnetic field wraps around the top of the trunk, transport from the top of the trunk to the anode is impeded by the transverse magnetic field) from the anode whereupon all of the current flows through the branch.

The branch propagates, borrowing from shock-tube parlance, as a contact discontinuity, with the anode as one wall and the trunk as the other. The magnetic pressure drives the contact point down along the branch-trunk interface and forward along the branch-anode interface, resulting in a canted current sheet. Anode starvation occurs to a lesser extent in the branch because it continually propagates into a fresh supply of propellant (the branch-anode interface is replenished with propellant from the *dynamic* pressure associated with its substantial axial speed). On the other hand, the initial current sheet (the trunk), is unable to avoid anode starvation because of its slow initial speed. As a final note on the branching phase, the magnetic pressure between the branch and the trunk causes the trunk to deform into the hook-like structure reported in many studies; the hook is simply a vestige of the initial current sheet.

The branching phase ends when the bottom of the branch reaches the cathode and the final phase (as shown in illustration 5), the snowplow phase, begins. The magnetic pressure is uniformly distributed on the back face of the canted current sheet and the current sheet is sufficiently dense in all areas to prevent further field leakage. The current sheet thus remains at a fairly constant canting angle during the remainder of its propagation. The tilt of the current sheet causes it to exert a cathode-directed component of the $\mathbf{J} \times \mathbf{B}$ force density on all of the propellant which is subsequently swept up. As a result, the propellant is preferentially directed toward cathode, where it accumulates. This “mass-funnelling” to the cathode may cause elevated plasma pressure along the cathode – leading to expansion of the propellant into the region *behind* the current sheet. A structure in the form of a

plasma “bubble” behind the current sheet could form and, over time, grow large enough to span the entire gap between the anode and cathode and cause a “restrike”, which effectively short circuits the initial current sheet.

In the sections which follow, each of the phases described above are analyzed in more quantitative detail in order to attempt to bridge the chasm between the conjectured model and the experimental facts.

6.2.3 Anode starvation phase

In the phenomenological model proposed above the sequence of events that lead to a canted current sheet is initiated by depletion of the conducting plasma in the vicinity of the anode. It is shown below that, in CSCX current sheets, diamagnetic drift induced fluid motion is of sufficient magnitude to cause the onset of anode starvation in the first few microseconds of the discharge.

Diamagnetic drift

In section 6.2.1 we noted that one of the most conspicuous physical traits of current sheets are the large gradients in both the field strengths and thermodynamic state variables. It is therefore natural to first check the influence of these abrupt transitions on the phenomenon of interest. In current sheets the gasdynamic pressure and magnetic field gradients are generally quite large. Below we will analyze the influence of these gradients on the macroscopic evolution of the current sheet.

It is generally instructive to consider the trajectory of a single particle under the influence of the prescribed electromagnetic field of interest (the so-called guiding center theory) in order to gain a qualitative feel for how a plasma, which is a collection of particles executing similar trajectories, will behave. This work has been done for us: the presence of

a pressure gradient transverse to a magnetic field is said to give rise to “diamagnetic drift” and, similarly, magnetic field gradients cause “grad B” drift[42]. Unfortunately, both of these phenomena have been the subject of widespread confusion and contradiction. The fundamental question is “do all guiding center theory trajectories manifest themselves in real fluids and, the corollary, do all mass motions predicted by fluid theory have an associated guiding center description?” The pursuit of answering to these questions has led to artifices such as “reflecting boundaries”[42] to ameliorate apparent paradoxes. The resolution of these issues has been handled best in the rigorous treatment of Woods[43]; in his own words:

The preference for mathematical formalism over physical mechanism is due in part to the misconception that in a tenuous gas the equations of fluid dynamics and thermodynamics can be *derived* from kinetic theory alone. By leaving the physical nature of pressure obscure, the formal approach fosters two misbeliefs that have afflicted plasma theory, namely that pressure gradients can exist without particle collisions, and that individual particles are not subject to pressure gradient forces. (pg. v)

The collisional force has a systematic, or non-random component that tends to drive the particles down the pressure gradient, and a random component that scatters the particles. In a neutral gas the pressure and scattering forces are transmitted impulsively by abrupt collisions, whereas in a plasma the range of the Coulomb force results in a continuum of ‘soft’ or grazing collisions. Hence individual particles in a plasma experience a continuous pressure gradient force and are progressively scattered through a sequence of small angles. (pg. vi)

An obvious requirement relating particle and fluid dynamics is as follows: since a fluid motion is merely the average motion of an assembly of particles, then (i) individual particles are subject to *all* the forces acting on the fluid, and (ii) upon summation, forces known to act on the particles, but not on the fluid, must cancel. Despite (i) and (ii) it is widely believed that pressure gradients act on the fluid but not upon the particles, and that the forces responsible for the guiding center motions in magnetic gradients do not vanish on summation. (pg. vi)

So we are led to understand that diamagnetic drift is a real, observable effect whereas grad B drift does not affect fluid motion. Let us look at diamagnetic drift in more detail,

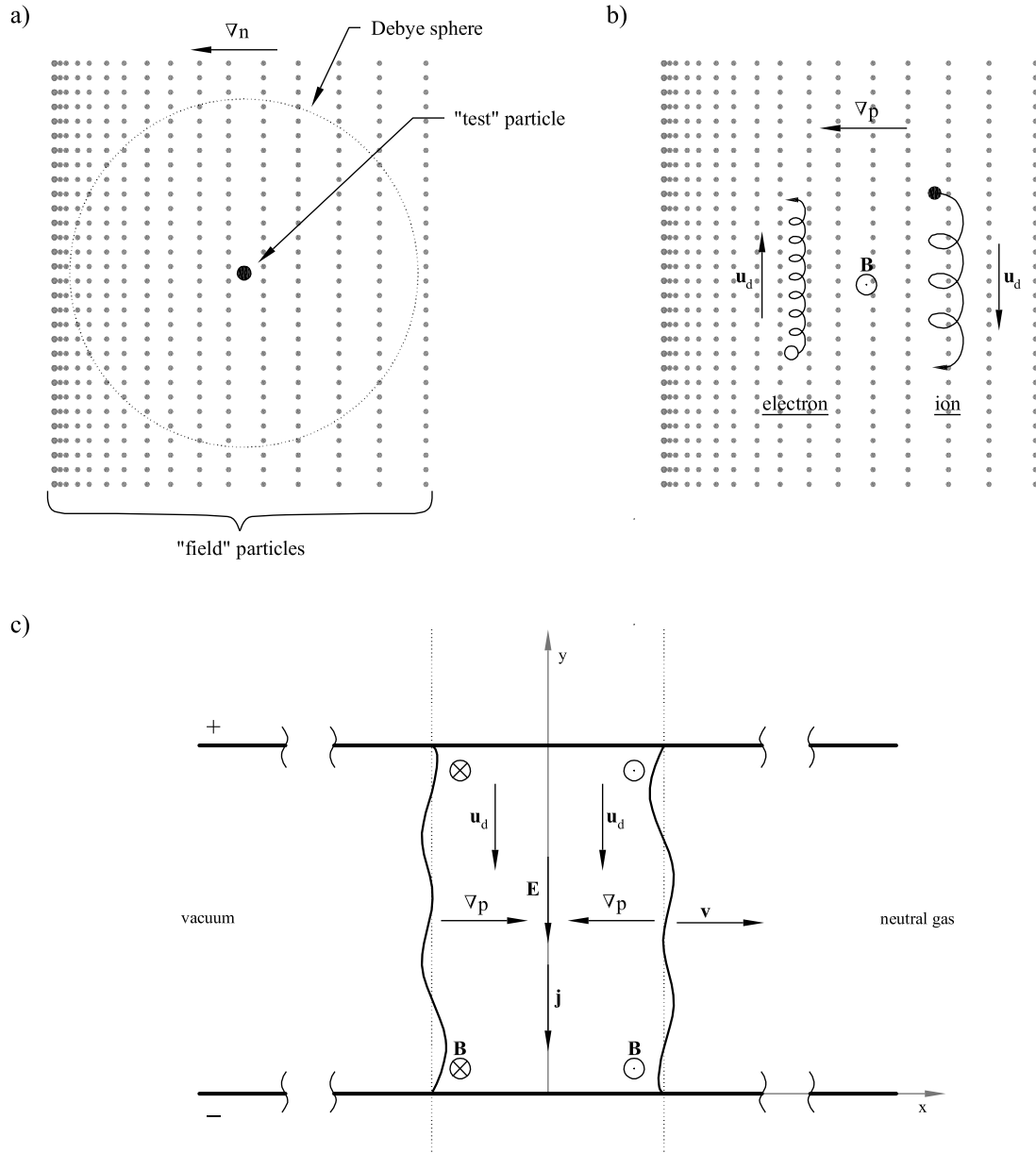


Figure 6.4: Schematics illustrating diamagnetic drift: a) test particle in a pressure gradient field, b) particle orbits in a pressure gradient field with crossed magnetic field, c) schematic of current sheet with vectors related to diamagnetic drift.

from both particle and fluid perspectives.

Figure 6.4a shows a hypothetical situation in which we consider the forces on a single “test” particle immersed in a sea of many “field” particles (both types of particles are non-neutral). A density gradient in the field particles is indicated by progressive “bunching up” of the particles toward the left-hand side of the figure. The test particle is circumscribed by sphere of radius λ_D , the Debye length. Field particles within the Debye sphere undergo Coulomb collisions with the test particle. Since these collisions are not abrupt or impulsive but, rather, the long range nature of the Coulomb force causes an averaging over all of the individual particles forces, which results in a net continuous, averaged force. Since, as shown in the figure, there are more particles in the left hemisphere of the Debye sphere than in the right hemisphere, the net force on the test particle is to the right, and the test particle is expected to drift in that direction. The particle can be thought of as being under the influence of of quasi-continuous “pressure gradient force field”.

Now, if we add a transverse magnetic field, as shown in Fig. 6.4b, the test particles are expected to execute guiding-center trajectories as illustrated (more specifically, the particles execute the illustrated trajectories in the absence of *large-angle* collisions). Ions and electrons move in opposite directions because the sense of their gyro-motions are opposite. Also note that if both the direction of the magnetic field and the density gradient are simultaneously reversed, the particle trajectories remain the same. Upon summation over all particles, a diamagnetic current will arise because of the relative motion of the ions and electrons, and a net mass motion of the plasma will occur in the direction of the ion drift (the plasma moves with the ions because of their predominant inertia).

A more useful description of diamagnetic drift (one from which we can make representative calculations) can be derived from the fluid model. The high electron density and high collisionality of the CSCX current sheet plasmas allow it to be characterized as a fluid.

Consider the motion of the current sheet plasma illustrated in Fig. 6.4c. Within the fluid framework the ions and electrons each obey a momentum equation of the form (neglecting viscous interactions with other species)[42]

$$m_j n_j \frac{d\mathbf{u}_j}{dt} = q_j n_j (\mathbf{E} + \mathbf{u}_j \times \mathbf{B}) - \nabla p_j \quad j = i, e \quad , \quad (6.4)$$

where m_j is the mass, n_j is the number density, q_j is the charge, \mathbf{u}_j is the fluid velocity in the laboratory reference frame, \mathbf{E} is the electric field, \mathbf{B} is the magnetic inductance, and p_j is the hydrostatic pressure.

If we consider the constant-speed propagation phase of current sheet motion, and consider only the velocity components transverse to the magnetic field then Eqn. 6.4 becomes

$$\mathbf{u}_{\perp j} \times \mathbf{B} = q_j n_j \mathbf{E} - \nabla p_j \quad . \quad (6.5)$$

Taking the cross product of Eqn. 6.5 with \mathbf{B} yields

$$\mathbf{u}_{\perp j} = \underbrace{\frac{\mathbf{E} \times \mathbf{B}}{B^2}}_{\mathbf{u}_E} - \underbrace{\frac{\nabla p_j \times \mathbf{B}}{q_j n_j B^2}}_{\mathbf{u}_d} \quad . \quad (6.6)$$

The first term in Eqn. 6.6 is the $\mathbf{E} \times \mathbf{B}$ drift (\mathbf{u}_E) and the second term is the diamagnetic drift (\mathbf{u}_d). The direction of \mathbf{u}_E is the same for both ions and electrons but, as in the particle model, the diamagnetic drift direction is seen to be charge dependent. As shown in both Figs. 6.2 and 6.4, \mathbf{E} is directed in the $-\hat{y}$ direction, and \mathbf{B} (for the most part) is directed in $-\hat{z}$ direction so that \mathbf{u}_E is directed in the $+\hat{x}$ direction. Similarly, the figures indicate that, for ions, \mathbf{u}_d is directed in the $-\hat{y}$ direction, or away from the anode throughout the current sheet.

Let us now consider the relative magnitude of each term in Eqn. 6.6. The magnitude of the electric field can be approximated using the measured voltage reported in section 5.1.2, typical values of \mathbf{B} are given in section 5.4, the temperature measurement is given

in section 5.6.2, and the measured electron density gradients are given in Fig. C.17. Thus (taking $n_i = n_j = n$, $q_j = q_i = e$),

$$|\mathbf{u}_E| = \frac{|\mathbf{E}||\mathbf{B}|}{|\mathbf{B}|^2} \sim \frac{\mathcal{O}(10^3)\mathcal{O}(10^{-1})}{[\mathcal{O}(10^{-1})]^2} = \mathcal{O}(10^4) \text{ m/s} \quad (6.7)$$

and

$$|\mathbf{u}_d| = \frac{kT|\nabla n||\mathbf{B}|}{en|\mathbf{B}|^2} \sim \frac{\mathcal{O}(10^{-23})\mathcal{O}(10^4)\mathcal{O}(10^{24})\mathcal{O}(10^{-1})}{\mathcal{O}(10^{-19})\mathcal{O}(10^{22})[\mathcal{O}(10^{-1})]^2} = \mathcal{O}(10^3) \text{ m/s}. \quad (6.8)$$

The $\mathbf{E} \times \mathbf{B}$ drift speed is of the same order of magnitude as the measured current sheet propagation speeds; this is as it should be since it is in fact the microscopic $\mathbf{E} \times \mathbf{B}$ particle drifts which cause the current sheet to accelerate. What is somewhat surprising is that equation 6.8 shows that the calculated diamagnetic drift in CSCX current sheets is sufficient in magnitude to induce ion fluid motion toward the cathode at appreciable speeds; in fact, the data in Fig. C.17 indicates that ∇n approaches 10^{25} m^{-4} in some cases, implying that \mathbf{u}_d may be comparable in magnitude to \mathbf{u}_E in some cases.

We can also estimate the amount of current induced by diamagnetic drift. According to Eqn. 6.6 electrons will experience diamagnetic drift in the opposite directions of ions, so that the net current will be twice that due to the ion drift alone:

$$j_d = |n_i q_i \mathbf{u}_{di} - n_e q_e \mathbf{u}_{de}| = |2ne\mathbf{u}_d| \sim \mathcal{O}(10^{22})\mathcal{O}(10^{-19})\mathcal{O}(10^3) = \mathcal{O}(10^6) \text{ A/m}^2. \quad (6.9)$$

Since the cross sectional area of the current sheet is $A \sim \mathcal{O}(10^{-3})$ (1 cm thick by 10 cm wide), the total diamagnetic current can be estimated as

$$I_d \sim j_d A \sim \mathcal{O}(10^6)\mathcal{O}(10^{-3}) = \mathcal{O}(10^3) \text{ A}. \quad (6.10)$$

Referring back to section 5.1.1, we find that the predicted diamagnetic current may contribute on the order of ten percent of the total measured current. This conclusion is potentially related to the assertion put forth (although not in a formal manner) by the earlier

researchers (see Chapter 2) that ion current contributes significantly to the total discharge current.

Since we are considering the potential for diamagnetic drift to cause anode starvation, it is useful to describe the relevant characteristic time and length scales for diamagnetic drift-induced anode starvation. To start, it seems logical to first define what we mean by the term “anode starvation”, that is, how much of the initial plasma must be transported away from the anode before we label it “starved”? This is a relative question which, fortunately, we do not have to answer directly. Instead, our approach will be to obtain the characteristic time for the canting process (τ_c) from the experimental data, and then calculate the plasma displacement (L_d) that diamagnetic drift is capable of inducing on that timescale. This characteristic length will then be used as an input parameter in a phenomenological model for the canting process, and the relevance of diamagnetic drift will be (albeit indirectly) revealed by the model’s ability to follow the trends in the measured current sheet canting angle data.

The characteristic time for the canting process can be gleaned from the experimental data; in particular, the magnetic field data in Fig. 5.10 shows that the time for the current sheet to reach a (fairly) constant canting angle is several microseconds, so we take

$$\tau_c = \mathcal{O}(10^{-6}) \text{ s} . \quad (6.11)$$

Therefore, the characteristic length for diamagnetic drift-induced plasma displacement normal to the anode (on the canting-process timescale) is (using equation 6.8)

$$L_d \sim |\mathbf{u}_d \tau_c| \sim \mathcal{O}(10^3) \mathcal{O}(10^{-6}) = \mathcal{O}(10^{-3}) \text{ m} = \mathcal{O}(1) \text{ mm} . \quad (6.12)$$

The magnitude of this characteristic length is perhaps not surprising, since the experimental measurements yield a comparable estimate for the *axial* (note: the axial direction is the direction of the thrust axis, or the $+\hat{x}$ direction, as illustrated in Fig. 6.2.1) characteristic

length, $n/\nabla n$. Using the data from Figs. 5.12 and C.17 we find that $n/\nabla n \sim 5$ mm for all cases, which is the same order of magnitude as the *normal* characteristic length value calculated in Eqn. 6.12.

Note that we are not trying to prove here that diamagnetic drift is the only mechanism that can cause anode starvation; there may in fact be alternative processes at play in the CSCX current sheets that lead to anode starvation. Our aim was to show that at least one process has been identified which can cause the current sheet plasma to be pulled away from the anode, on the timescale of the canting evolution. In the next section, we describe how anode plasma depletion can lead to current sheet canting, through a sequence of events that we term “branching”.

6.2.4 Branching phase

The argument that is put forth in this thesis suggests that current sheet canting is caused by rapid penetration of the magnetic field through a narrow region of the current sheet along the anode. This perspective on the problem is adopted based on the experimental data. In particular,

- The photographic data (see, for example, Fig. 5.4) clearly show the projection of a luminous canted structure ahead of the initial current which initiates near the anode.
- The magnetic field data in Fig. 5.10c show that canting occurs rapidly in the early stages of the discharge, after which a fairly constant canting angle propagation phase takes place.
- The magnetic field data in Fig. 5.11 show that the current sheet bifurcates along the anode early in the discharge. No similar phenomenon is seen in the cathode magnetic field traces.

We now turn to explaining how the branching process takes place. We are therefore led to consider theories relevant to the penetration and expulsion of magnetic fields in plasmas. A recent series of seminal articles by Fruchtman[44, 45, 46] appears to have direct relevance to the present study and, as such, will be drawn upon heavily. Fruchtman's major contribution in this area has been to formalize the description of the role that the Hall effect plays in accelerating the penetration of magnetic fields through plasmas. The Hall effect may be relevant to the current sheet canting problem because the anode starvation process described in the previous section may create a region in the current sheet where the Hall parameter becomes appreciable in magnitude.

In the next section the process of rapid magnetic field penetration is discussed. The results of the analysis are used in the succeeding section to calculate predicted canting angles in the CSCX accelerator.

Rapid penetration of magnetic fields into plasmas

We are concerned here with understanding the penetration of magnetic fields into plasmas that are being pushed by those selfsame fields. Classically, two extreme cases can be distinguished. If the plasma is highly conductive, the penetration of the fields is confined to a thin layer of thickness on the order of the electron skin depth and the plasma is pushed by the magnetic pressure (snowplowed) with a characteristic speed (the Alfvén speed)[47]

$$v_A \equiv \frac{B}{\sqrt{4\pi n_i m_i}} , \quad (6.13)$$

where B is the magnetic inductance, n_i is the ion density, and m_i is the atomic mass of the ions. If, on the other hand, the plasma is highly resistive, the magnetic field simply diffuses through the plasma (without imparting significant momentum to the plasma) with characteristic speed[47]

$$v_D \equiv \frac{c^2 \eta}{4\pi L_D} , \quad (6.14)$$

where c is the speed of light in vacuum, η is the plasma resistivity, and L_D is the characteristic diffusion length.

Fruchtman *et al*[44, 45, 46] describes a mechanism for fast magnetic field penetration into a plasma which is *independent* of the resistivity, which he calls the “convective skin effect” (the relevant results are reported here, the interested reader is directed to the references where the detailed derivations are shown). The mechanism results from the Hall electric field, which allows the magnetic field to penetrate the plasma with characteristic speed

$$v_C \equiv \frac{c^2(B/n_e e c)}{4\pi L_C}, \quad (6.15)$$

where $-e$ is the electron charge and L_C is the characteristic length of a density gradient in the plasma. The term $\eta_H = B/n_e e c$ can be thought of as a “Hall resistivity”. As with conventional plasma resistivity, the Hall resistivity allows the magnetic field to rapidly propagate through a plasma without imparting significant momentum to the ions (the Hall resistivity is, however, non-dissipative).

In the course of his derivations Fruchtman defines the circumstances under which the convective skin effect is “activated”. He shows that Hall effect-enhanced magnetic field penetration will occur when a density gradient occurs in the (pushed) plasma with characteristic dimension of the order of the ion skin depth,

$$\delta_i \equiv \sqrt{\frac{m_i c^2}{4\pi n_i e^2}}. \quad (6.16)$$

Also, a parameter equivalent to the magnetic Reynolds number can be defined, which is the ratio of the plasma pushing speed (v_A) to the field penetration speed (v_C):

$$R_C \equiv \frac{v_A}{v_C} = \frac{\frac{B}{\sqrt{4\pi n m_i}}}{\frac{c^2(B/n_e e c)}{4\pi L}} = \frac{L_C}{\delta_i}. \quad (6.17)$$

Equation 6.17 shows us that when L_C is less than the ion skin depth, field penetration dominates over pushing.

Let us consider some typical CSCX current sheet parameter values to demonstrate the relevance of the Hall effect on the current sheet canting problem. From Fig. 6.1 we see that the ion plasma frequency (ω_{pi}) is $\mathcal{O}(10^{11})$ rad/s so that

$$|\delta_i| = \left| \frac{c}{\omega_{pi}} \right| \sim \frac{\mathcal{O}(10^8)}{\mathcal{O}(10^{11})} = 1 \text{ mm} . \quad (6.18)$$

Now, in section 6.2.3 we found that, on the timescale of the canting process, the diamagnetic drift in CSCX current sheets was capable of inducing a density gradient of characteristic length $L_d = 1\text{mm}$. The influence of the convective Hall effect is found by considering the effect of such a gradient within the framework of Fruchtman’s model, that is, setting $L_C = L_d$. From equation 6.17 we find that $R_c \sim 1$, indicating that Hall effect-induced magnetic field penetration may significantly affect the evolution of CSCX current sheets, near the anode, during the early stages of the discharge.

Predicted terminal canting angle

We now attempt to calculate the canting angles that will result from the competing processes of plasma pushing and Hall effect-induced magnetic field penetration, in the CSCX accelerator. The model is simply an attempt quantify the statements given in section 6.2.2, where the evolution of the canting angle was described in a general sense.

The approach will be to track the trajectories of two points on the branch: the branch-trunk interface point (point BT) and the branch-anode interface point (point BA). The elements of the model are schematically illustrated in Fig. 6.5. The figure shows “snapshots” of the current sheet at several different times. The branch comes into existence at some time t_o ; the points BA and BT are assumed to initially be separated by the distance L_C – the characteristic length of the anode density gradient. The motion of the point BA is assumed to be governed by the convective skin effect; the point BA is assumed to propagate with constant velocity $\mathbf{v}_{BA} = v_C \hat{x}$. The motion of the trunk and the point BT is assumed to

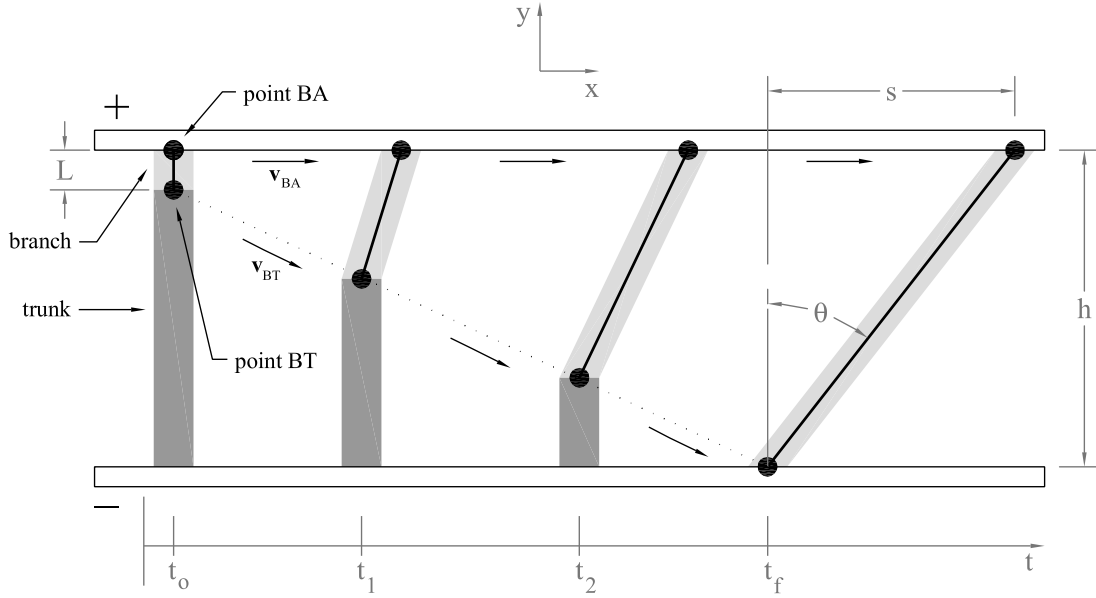


Figure 6.5: Schematic of current sheet canting angle calculation elements.

be governed by plasma pushing; thus, the point BT is assumed to propagate both forward and downward at the Alfvén speed: $\mathbf{v}_{BT} = v_A \hat{x} + v_A \hat{y}$. The point BT has two speed components because the flux tubes that wrap around this point (see frame 3 and 4 of Fig. 6.3) exert both axial and transverse components of magnetic pressure, driving the point both forward and downward. The branching phase is assumed to terminate when the point BT reaches the cathode (indicated by time t_f in the figure). The predicted terminal canting angle (θ) is calculated using the axial separation of the points BA and BT (s in the figure) at time t_f .

Using the definitions of the speeds given above and and Eqn. 6.17 it is easy to show that the predicted final canting angle is

$$\theta = \tan^{-1} \left[\left(\frac{h - L_C}{h} \right) \left(\frac{1 - R_C}{R_C} \right) \right], \quad (6.19)$$

$$R_C = \frac{L_C}{\delta_i} = \sqrt{\frac{4\pi n_i e^2}{m_i c^2}} L_C. \quad (6.20)$$

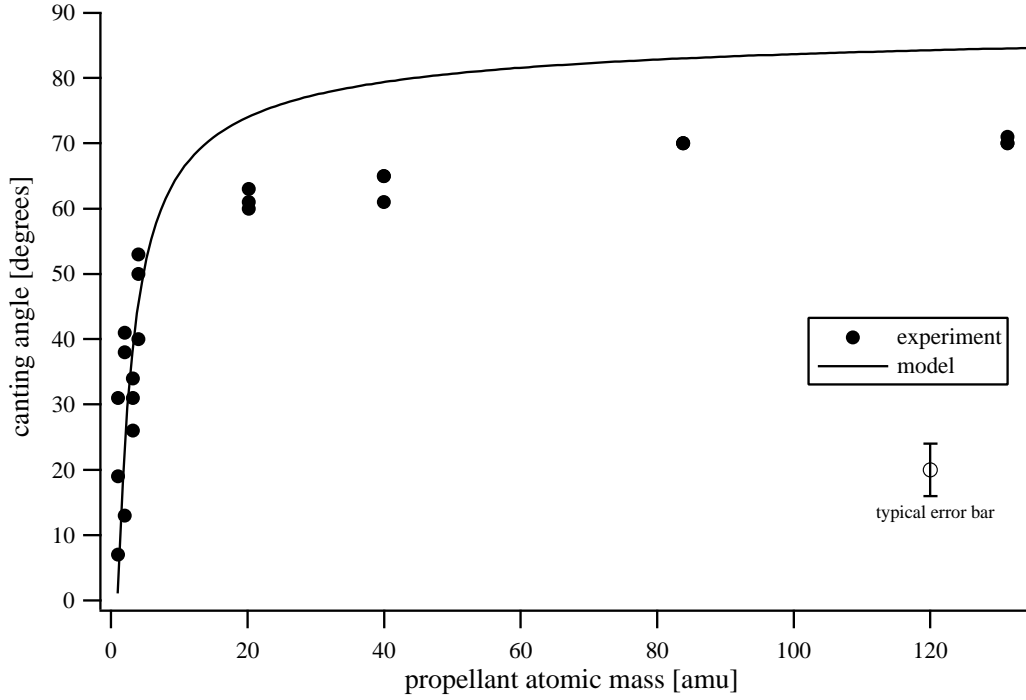


Figure 6.6: Comparison of model and measured current sheet canting angle versus propellant atomic mass.

Equation 6.19 tells us that the canting angle dependence on propellant mass enters through the parameter R_C , which in turn depends on the ion skin depth, which is proportional to the square root of the ion mass. It should be noted that, at least in our analysis, the mass dependence only comes through δ_i , since L_C is related to the diamagnetic drift speed, which is mass-independent. This is important because it allows us to assume a constant value of L_C when plotting the functional dependence θ on m_i ; there are no free parameters in the model.

Using the diamagnetic drift-induced characteristic density gradient L_C (1 mm, from Eqn. 6.12), the typical measured number density ($5 \times 10^{16} \text{ cm}^{-3}$, from Fig. 5.12), we can plot the predicted canting angle as a function of the propellant atomic mass. This curve, along with all of the experimental datum points from Fig. 5.13, are shown in Fig. 6.6. The figure shows that the model captures the general trend of the experimental data; the

model predicts that the canting angle will initially rapidly increase with propellant atomic mass and then taper off toward a more asymptotic trend for higher atomic mass propellants. These are the same trends that are seen in the experimental data.

It is not surprising that the model does not give precise quantitative agreement with the data for the higher atomic mass propellants. The model predicts the “worst case scenario”, or *maximum* expected canting angle, because the simplification in the model that allows the point BA to propagate with velocity v_C along its entire trajectory is probably not the type of behavior realized in the experiment. In the real accelerator the branch anode attachment is likely to transition continuously from the Hall-convective behavior back to plasma pushing – as it picks up speed and the incoming propellant obliterates the anode density gradient. If we were to modify the model to divide the branch trajectory into, say, two parts (half Hall-convective and half plasma pushing), the effect would be to cause the model curve to bend-over more rapidly and come into closer agreement with the data. But, in light of the rather crude order of magnitude estimates used throughout this analysis, further refinement of the model is not warranted. The important point is that the simplest model, which embodies the essence of the proposed physical processes, accurately picks up the trends in the experimental data and gives fairly close quantitative agreement. We shall henceforth refer to the model described above as the “fast field penetration canting model”.

Let us summarize what has been proposed here. Physically, Fruchtmann’s model shows that the Hall effect can lead to an effective mechanism for magnetic field transport when a non-uniformity (i.e., a density gradient) appears in a plasma that is being pushed by the field. This argument is formally derived through the fluid equations. In particular, inclusion of the Hall term in the generalized Ohm’s law leads to a term in the equation for the time-evolution of the magnetic field that allows for the rapid convection of magnetic field through the plasma, without displacement of the ions, with characteristic speed v_C .

This competes with the convection of the magnetic field where the ions are displaced, that is plasma pushing, which has characteristic speed v_A . Consideration of the relative magnitude of each effect reveals that the Hall-convective penetration becomes comparable in magnitude to plasma pushing when a density gradient of scale length comparable to the ion skin depth appears. In our fast field penetration canting model we propose that such a density gradient does arise along the anode in the CSCX accelerator. The variations in the ion skin depths among the different propellants (the ion skin depth is proportional to $\sqrt{m_i}$) leads to different Hall-convective field penetration speeds, and hence different final canting angles, as illustrated in Fig. 6.6.

6.2.5 Snowplow phase

The experimental data show (see Fig. 5.10c) that the canting angle evolves during the first few microseconds of the the discharge, after which the current sheet propagates at a fairly constant angle. During this latter quasi-steady state, plasma pushing, or snowplowing, is expected to be the primary mode of operation.

Figure 6.1c shows that, for higher atomic mass propellants, the measured current sheet speed is substantially higher than the Alfvén speed, which was calculated from measured parameters. The values can be brought into closer agreement if a canting-corrected Alfvén speed is defined:

$$v_A^c = \frac{v_A}{\cos \theta} . \quad (6.21)$$

Physically Eqn. 6.21 is a statement that says since the magnetic pressure force acts normal to the current sheet, it is the *normal* component of the current sheet speed that propagates at the Alfvén speed. Figure 6.1c shows that introducing this correction factor brings the measured speed and calculated Alfvén speed into closer agreement.

An immediate question is “what effect does canting have on the ability of the current

sheet to sweep up and accelerate propellant”? Referring to the electron density data in Fig. 5.12b, we see that the electron density on the anode side is much lower than that on the cathode side (note: both beams were about 5 mm away from each electrode – well outside the electrode Debye sheath regions). This density imbalance may suggest that the effect of canting is to force the plasma entrained by the current sheet toward the cathode (clearly, the force density vector $\mathbf{J} \times \mathbf{B}$ is largely directed toward the cathode) where it stagnates and is then left behind. This picture is supported by the cathode laser beam electron density traces, which show a significant plasma density that persists after the current sheet has passed. Also, the photographs in Fig. 5.4 show a long luminous layer of plasma behind the current sheet. This information indicates that, in addition to causing an off-axis component of thrust, current sheet canting may undermine the effective sweeping up of propellant as the current sheet propagates. Indeed, canted current sheets may act, undesirably, like *real* snowplows – never accumulating but, rather, throwing their load to the side (in our case, underneath) as they pass by.

We can make this assertion a bit more quantitative by considering what the expected electron density at the sampling location should be, and then comparing this value with our measurements. If the current sheet was a perfect propellant sweeper, we would expect the total number of electrons in the current sheet at the sample location to be about the same as the total number of propellant particles that initially filled the volume between the breech and sampling location (this, of course, assumes single ionization). Helium is a good candidate for this analysis, since its high second ionization potential precludes the presence of a significant population of double ions. The interferometric data taken with the upstream probe in configuration 1 should give an adequate representation of the average properties of the current sheet since it was traversed by the plasma midway between the anode and cathode. Let us consider the tests with helium propellant at 75 mTorr ambient fill. Using

the current sheet width data in Fig. C.17b, the electron density data in Fig. 5.12, and the dimensions of the discharge chamber (see Fig. 3.2), the total number of electrons in the current sheet can be estimated:

$$N_e = n_e V_{sheet} \approx (1 \times 10^{16} \text{ cm}^{-3})(1\text{cm})(5\text{cm})(10\text{cm}) = 5 \times 10^{17} \text{ electrons} . \quad (6.22)$$

On the other hand, the total number of neutral propellant particles encountered by the current sheet as it propagated to the sampling location (35 cm downstream of the breech) was

$$N = \frac{pV_{chamber}}{kT} \approx \frac{(10\text{Pa})(0.05\text{m})(0.1\text{m})(0.35\text{m})}{(1.38 \times 10^{-23} \text{ J/KgK})(300\text{K})} = 4 \times 10^{18} \text{ neutrals} . \quad (6.23)$$

Comparing the two figures implies that only about 10% of the propellant was entrained into the current sheet. The rest was presumably convected to the cathode, where it was overrun and left to trail behind the propagating front. This does not mean that the propellant utilization efficiency was only 10%, as the current sheet may have imparted a significant amount of axial momentum to the propellant as it transported it to the cathode; the exact amount of momentum transferred in this process remains an open research question. Although this is an important issue from a propellant utilization efficiency perspective, no attempt is made here to model the process since, as the data indicate (again, see Fig. 5.10c), the process does not drastically alter the canting angle that is established early in the discharge.

The propellant entrainment calculation above neglects the possibility that the current sheet entrains and accelerates a large amount of neutral atoms – atoms that are never ionized yet are convected along with the current sheet. If this was in fact the case, the analysis above would be invalid, since the interferometer is insensitive to the presence of neutrals. Such a scenario could arise if, for example, the ions in the current sheet are tightly collisionally coupled to the neutrals. Theoretically, the presence a prodigious amount of neutral gas in the current sheet is unlikely, since the high measured temperature (~ 2 eV, see section

5.6.2) and low gas density should result in a completely ionized gas[4]. However, complete analysis of the potential for entrainment of neutrals into the current sheet would involve making an estimate of the ionization length and ion-neutral mean free path. These type of calculations are beyond the scope of what we are trying to accomplish here, but should be part of a more comprehensive study on the propellant sweeping characteristics of current sheets. Our purpose here was to show that the electron density data cannot account for all of the propellant, suggesting the possibility that canting is causing it to be driven toward the cathode where it is overrun by the current sheet.

6.3 Correlations with earlier research

It is interesting, in light of the analysis presented in this chapter, to reflect back on the results from earlier researchers, as presented in Chapter 2. It is clear that several of the researchers were trying to draw conclusions from data that were taken while their accelerators were in the branching phase; they did not have the benefit of a protracted current pulse, which exposes the transient nature of the canting process.

Since Johansson[22] (see section 2.1.3) was the only prior researcher to publish a theory for current sheet canting (which we termed the ion conduction current canting model), it is fitting that we should return to consider his conclusions, and compare them with the fast field penetration canting model put forth in the present study. Johansson proposed (see Fig. 2.6) that a portion of the current sheet (of height h_o) will cant in order to direct ions toward the cathode. This type of partitioning of the current sheet into a canted and uncanted section was observed in the CSCX study as well (see, for example, the top-center photograph in Fig. 6.3); however, in the present study, the presence of two distinct regions of the current sheet was found to be the manifestation of a *transient* phenomenon, which we termed branching. In all cases, the structure of the current sheet was found to eventually evolve

into a continuous, straight, canted front. It seems clear that Johansson attempted to draw conclusions from data which showed the presence of both the branch and trunk; evidently he assumed that the features were stable structures. Johansson's theoretical formula for h_o cannot be compared with the CSCX experimental data since h_o is observed to continuously increase, until the canted portion of the current sheet spans the entire inter-electrode gap. The two models share in common the notion that the current sheet cants near the anode. Beyond this the two models diverge. The ion conduction current canting model suggests that the canting of the current sheet near the anode will maintain its general shape as the current sheet propagates whereas the fast field penetration canting model proposes that the distortion of the current sheet near the anode leads to a "runaway" effect wherein the magnetic field propagates ahead of the initial current sheet and forms a straight, canted, current sheet that spans the entire discharge chamber.

The data from the Princeton Z-pinch experiments (see Fig. 2.1) appear to indicate that the current sheets reached the centerline of the accelerator before the branch-trunk interface completed its migration to the cathode. Additionally, the images from Lovberg's rectangular-geometry accelerator study (see Fig. 2.9b) clearly show the bifurcation of the current sheet; however, the electrodes were not long enough for the current sheet to transition into its stable, constant-angle phase. Similarly, MacLelland's images also show current sheets in various stages of branching. The Fig. 2.10(Series 3)b schlieren photograph bears a strong resemblance to some of the intermediate schematics of the current sheet canting model proposed above (see Fig. 6.5).

Lovberg's coaxial geometry accelerator research is insightful because it may indicate a path toward inhibiting current sheet canting. In Lovberg's initial coaxial accelerator work (solid electrodes), polarity-dependent current sheet canting was observed. On the other hand, he did not observe the same effect when he reversed the polarity in his coaxial-

geometry, slotted-outer-electrode accelerator (see Fig. 2.9d.) The reason for the different results between the two experiments may be due to the second experiment's slotted outer electrode and the use of a uniform backfill of propellant surrounding the second accelerator. It is possible that as the formation of a radial density gradient, near the anode, was inhibited by the replenishment of propellant from outside the accelerator – through the slotted outer electrode. The influx of propellant into the depleted region may have suppressed anode starvation and the associated accelerated magnetic field penetration near the anode. This is a revealing, albeit inadvertent, example of how propellant feeding might be used to suppress current sheet canting. When Lovberg's accelerator was operated with the center electrode as the anode, we see the expected behavior (that is, a bullet shaped current sheet). The feature that Lovberg considered anomalous, the planar, non-conducting plasma sheet behind the main front is probably the initiation trunk; as expected near a solid electrode, anode starvation allowed the magnetic field to propagate around the initiation trunk to form the leading branch current sheet. It should be emphasized again that Lovberg's experiments used two different propellant loading techniques (ambient fill and injection), which may in fact have played a role in producing the different results. However, without knowing the details of the initial propellant distribution in each accelerator, it would be difficult to make conclusions regarding the influence of each loading method.

6.4 Concluding remarks on the analysis

This chapter has attempted to characterize the plasma environment in the CSCX accelerator, identify physical mechanisms which could potentially cause current sheet canting and, finally, to implement those mechanisms into a simple canting model, which draws on available experimental data, for comparison with experimental canting-angle data. Before leaving this chapter, a few comments are in order regarding some issues that were not

discussed in the analysis, yet may be relevant.

First, no mention has been made of the experimentally measured variation in canting angle with pressure. The data shows (see Fig. 5.13), for the most part, that the lowest canting angles were attained at the highest pressure levels. Since the canting angle is a function of δ_i and L_C (see equation 6.19), which are in turn related to n_i and ∇n_e , we might consider using the experimental data to investigate the influence of pressure; however, the size of the error bars in the measurements (see, for example, Fig.C.17) precludes a meaningful analysis, and reinforces our rationale for keeping the calculations used in the phenomenological modelling to order-of-magnitude estimates.

Still, some qualitative statements regarding pressure dependence can be made. The lower atomic mass propellants show a wide scatter in canting angle at different pressures. This may be related to contamination. Figure 6.6 shows that, at the low atomic mass limit, the canting angle rapidly increases for small incremental increases in atomic mass. Therefore, we might expect that small amounts of contaminants in the propellant (which might originate from adsorbed gas in the electrodes, or electrode erosion) could slightly increase the effective, or average, atomic mass of the propellant, and lead to large increases in the canting angle. The lower pressure experiments would be more sensitive to contamination (given a constant amount of contaminant material), since the net concentration of contaminants, and hence the effective atomic mass, would be higher than in the higher pressure experiments. This assertion is given credence by the fact that the data show that the highest pressure experiments gave the smallest measured canting angles.

Another factor that has not been discussed is the influence of the rapid current rise (see Fig. 5.1) that occurs during the initiation of the discharge. Indeed, the rise-rate is $\mathcal{O}(10^{11})$ A/s, which qualifies it as a “conspicuous feature” in our problem. We have attempted to model the influence of dI/dt on anode starvation, using the unsteady fluid equations, but

have yet to find a correlation. Nonetheless, it is a topic that merits further investigation.

The purpose of this chapter has been to present a *plausible* explanation for why current sheets cant. The scant amount of data available from the breech region of the accelerator, where the transient canting process takes place, makes it difficult to ascertain that the proposed physical mechanisms are actually at play. It has been tacitly assumed that the measurements taken downstream are representative of the current sheet properties near the breech. Accordingly, emphasis has been put on order-of-magnitude analysis and trends in the data. Furthermore, deeper issues related to the proposed physical canting mechanisms have not been addressed. For example, direct application of Fruchtmann's results to the present problem requires detailed knowledge of, among other factors, the local collisionality, the penetration of the magnetic field into the bounding conductors, and an analytical expression for the density gradient. Clearly, measurements were not made in the CSCX study to quantify these parameters near the breech, in the vicinity of the anode; in actuality, given additional time and resources, it would still be difficult to conceive of measuring these quantities (e.g., measuring density gradients on a sub-millimeter scale). The reader that may be unconvinced by our attempt to make a case for the proposed canting mechanism, using available data, is invited to consider the inverse of what we have done here. That is, to assume that the convective skin effect allows fast magnetic field penetration, and then ask what conditions near the anode must exist to allow the field to rapidly penetrate. First, one must choose a representative estimate for the number density, perhaps based on the initial fill density; having done so, the ion skin depth can be calculated. For the convective skin effect to be activated, a density gradient of scale length comparable to the ion skin depth, by some unspecified mechanism, must somehow form. Carrying out this procedure leads to values of δ_i (and, hence, L_C) that are reasonable, that is, length scales that are much smaller than the accelerator dimensions, and much larger than sheath dimensions,

the electron skin depth, etc.. The point is as follows: there is no *a priori* reason to exclude the convective skin effect as a candidate mechanism for causing current sheet canting.

Furthermore, since the available data from the CSCX study and other researchers do not contradict the proposed phenomenological model, it should be considered a strong candidate, even in the absence of detailed experimental data in the anode region. Prior to developing the fast field penetration canting model, we made many attempts to find revealing trends in the canting data by plotting the datum points as a function of individual and products of characteristic parameters. None of these attempts were successful in capturing the relatively sharp “knee” in the relationship between canting angle and propellant atomic mass. However, the relatively complex relationship predicted by the fast field penetration canting model is able to capture this trend.

Chapter 7

Conclusion

The CSCX study has provided measurements which quantify the degree of current sheet canting under a variety of experimental conditions. Further analysis of the data lead to the conclusion that current sheet canting appears to be a natural consequence of the manner in which current is conducted in pulsed electromagnetic accelerators. It is proposed that depletion of plasma along the anode can lead to a sequence of events that result in a canted current sheet. In the sections which follow, we summarize our major findings, suggest future experiments to address deficiencies in the study, and finally make suggestions for how the insight gained can be practically implemented to improve the performance of pulsed plasma thrusters.

7.1 Summary of findings

The major experimental findings and theoretical conclusions reached in the CSCX study were:

- Current sheet canting was observed in all propellants and pressure levels tested.

- The canting angle was found to depend on the atomic mass of the propellant; lighter atoms were observed to yield less canting (the measured angles ranged from approximately 10° for hydrogen to 70° for xenon). Molecular propellants which contain hydrogen (hydrogen, deuterium, and methane were tested) showed a pronounced reduction in canting at the highest pressure levels.
- Calculations (which make use of measured CSCX current sheet thermodynamic properties) reveal that the diamagnetic drift induced fluid motion may be appreciable in the CSCX accelerator. It is proposed that diamagnetic drift may contribute to plasma depletion in the anode region.
- It is proposed that Hall effect-enhanced penetration of the magnetic field through the tenuous anode plasma causes the current sheet to bifurcate and, ultimately form a canted current sheet.
- A simple model which includes the Hall effect (based on theoretical results from Fruchtman[45]) yields qualitative agreement with the measured dependence of canting angle versus propellant atomic mass.
- Current sheet canting may negatively impact the ability of current sheets to sweep up propellant. A rough calculation that made use of the measured electron density of a helium current sheet indicated that only about 10% of the propellant was entrained within the sheet.
- It is proposed that the life of a current sheet has three main phases:
 1. **Initiation phase** – thinning of the current sheet near the anode, possibly due to diamagnetic drift, causes anode starvation and allows the magnetic field (through Hall effect-enhanced field transport) to rapidly propagate along the

anode, faster than the rest of the current sheet.

2. **Branching phase** – a canted current front (branch) emerges from the top of the initiation trunk; the branch-trunk interface recedes down the trunk at the Alfvén speed (v_A), while the branch-anode interface propagates ahead at the (faster) Hall-convective speed (v_C), until the branch contacts the cathode.
3. **Snowplow phase** – After the transient branching phase, a single, canted, planar current sheet propagates at a fairly constant angle (θ), pushing plasma with an axial speed approximately equal to $v_A / \cos \theta$. The $\mathbf{J} \times \mathbf{B}$ force density pumps propellant preferentially toward the cathode where it may stagnate and accumulate, and ultimately get left behind the propagating current sheet.

7.2 Future work

The present study made detailed measurements to quantify the degree of current sheet canting under a variety of experimental conditions; however, some questions still remain. The following course of action is proposed to build upon the experimental work presented here and to prove some of the theoretical assertions made in the previous chapter.

Since the onset of canting has been proposed to occur at the breech, detailed mapping of the current, magnetic field, and electron density in that region should be revealing. Ideally, a 2-d interferometric imaging system, in conjunction with an array of magnetic field probes, would be used to obtain a highly resolved set of data for the evolution of the current sheet plasma and magnetic fields, near the breech of the accelerator.

Since current sheet canting appears to negatively affect the current sheet's ability to entrain propellant, a study which makes an accurate accounting of the total amount of propellant contained in the current sheet, as well as quantifying the amount of leakage, would

be beneficial. The desired measurement could be accomplished using an interferometer aligned in configuration 2 (see Fig. 4.6) but with perhaps four or more beams, to determine the spatial distribution of electron density in the current sheet. The device could be positioned at several different axial locations to gain an understanding of the rate at which plasma “leaks” from the current sheet near the cathode. The use of pressure probes could also provide valuable data in mapping the distribution of the propellant both before and after the current sheet has passed.

A performance related experiment should be conducted in order to determine if current sheet canting actually impacts the performance of a pulsed plasma thruster. A simple experiment would involve measuring the impulse bit of a coaxial gas-fed pulsed plasma thruster operated in both positive and negative polarities.

7.3 How to build a better thruster

It is fitting to conclude this thesis by returning to the primary role of the work, as stated in the Introduction – to provide insight on how to build better pulsed plasma thrusters.

The data collected in this study show that the most direct way to inhibit current sheet canting is to use low atomic mass propellants at high pressure. In this study hydrogen, deuterium, and methane showed markedly lower canting at higher pressures. However, hydrogen is not an ideal PPT propellant, due to the difficulty of handling cryogenic propellants on a spacecraft. To practically exploit the benefits of low current sheet canting which results from the use of hydrogen at high pressure, we sought alternative propellants which contain a significant amount of hydrogen in their molecular structure. Alkanes, with their $C_N H_{2N+2}$ structure, seemed like a natural choice. Methane was tested as part of the interferometric study and was found to have the same reduced canting behavior (at higher pressures) as hydrogen. Further tests are needed on longer-chain hydrocarbons. If butane,

for example, is found to exhibit similar behavior, it will be an appealing GFPPT propellant on two levels. In addition to the aforementioned canting benefits, butane can be stored as a liquid under relatively low pressure, at room temperature; therefore, a butane propellant system will have a much smaller specific volume (smaller fuel tank and feed system) than a high pressure gas system.

Thruster designs should also strive to prevent diamagnetic drift-induced anode starvation. The most obvious way to accomplish this would be to somehow load the propellant preferentially along the anode. This might be accomplished by having an array of propellant injectors distributed axially along the anode, rather than the typical back-plate injection scheme. Alternatively, a segmented electrode (anode), such as the one used in Lovberg's study (see Fig. 2.9c), could be used. Gas could be injected into a shroud that encloses the electrodes, approximating the ambient fill technique used in Lovberg's device.

In coaxial accelerators a simple design rule can immediately be stated: the outer electrode should always be the anode. In the coaxial geometry, the $1/r^2$ variation in magnetic pressure predisposes the current sheet to run faster along the inner electrode; by making the inner electrode the anode, this undesirable situation would only be amplified because of the natural tendency of the current sheet to move faster along the anode. But, if the outer electrode is made to be the anode, some antagonism between the two effects might be established wherein the non-uniform magnetic pressure effect could be counteracted by the tendency of the current sheet to move faster along the anode – leading to a non-canted current sheet. The current measurements of Keck shown in Fig. 2.3b clearly display this type of behavior.

The discussion above, and indeed this entire thesis, has addressed the behavior of “classical” pulsed plasma thrusters – thrusters which use diffuse distributions of low pressure propellant and current levels on the order of 10-100 kA. Both the experimental investiga-

tions and accompanying preparation of this thesis have strongly shaped our views on the prospects for pulsed plasma thrusters as practical space propulsion devices. Clearly we must move away from the type of current sheet behavior reported in this work. Since current sheet canting apparently results from particle-kinetic effects, the most direct way of alleviating the problematic behavior is to use higher density propellant loading schemes – that is, to create plasmas in the PPTs that have more fluid-like characteristics. A practical solution would be to inject liquid propellant into thrusters; the droplets could be vaporized, ionized, and accelerated as a dense “slug” of plasma. In addition to reducing current sheet canting, liquid propellant injection could positively impact the dynamic efficiency of the acceleration process, and eliminate the need for ultra-fast gas valves. Of course the increased mass loading would have to be accompanied by higher current levels (500 kA-1 MA) to provide a sufficient amount of force to accelerate the more massive propellant load to high exhaust speed. But, again higher current density should help to achieve higher efficiency in the acceleration process[4]. In summary, it is our opinion that the next step in the development of PPTs should not be to continue studying accelerators that operate in the plasma regime of the CSCX experiment but, rather, we should pursue the development of thrusters that operate at approximately an order of magnitude higher plasma density and current level.

Appendix A

DESIGN and CONSTRUCTION DETAILS

This appendix provides design and construction details for several pieces of experimental hardware that were developed specifically for the the current sheet canting experiment.

A.1 Pulse forming networks

Details regarding the design and construction of the pulse forming networks used in CSCX are given below.

A.1.1 Design principles

The PFNs used in the present study are commonly referred to as LC ladder networks or delay lines. The general electrical configuration and theory of operation for this type of PFN is described by Barnett[48]. The task for the present study was to design a PFN which could deliver a rectangular current pulse with adequate current rise rate and duration. Theoretical expressions for estimating these two quantities (for a given physical configuration)

are described below; specific numerical examples for the CSCX PFN's will be given in the proceeding sections.

Analytical derivation of the current rise rate in a simple LRC circuit yields[49]:

$$\frac{dI_o}{dt} \propto \frac{V_o}{L_o} . \quad (\text{A.1})$$

Empirical observations[4] suggest that a current rise rate of at least 10^{11} A/s·cm is necessary to generate a thin current sheet at the lowest inductance point within the accelerator. Equation A.1 indicates that this may be accomplished by using a high bank voltage and low initial inductance. Therefore, for a given maximum capacitor voltage rating, a PFN design should strive to minimize the inductance between the first stage of the PFN and the accelerator (i.e., low inductance transmission lines should be used.)

Since the accelerator used in the present study had rectangular geometry, flat strips of copper bar were used for the transmission lines. The calculation of the inductance per unit length of two parallel plate conductors of arbitrary separation distance is not trivial. Kohlberg *et al.*[40] has solved the problem using conformal mapping techniques; the final result, however, is not in closed form, and must be evaluated numerically; he provides results for several representative plate widths (w) and separation distances (h) by specifying the the result as

$$L' = f_g \mu_o , \quad (\text{A.2})$$

where f_g is a parameter obtained through numerical integration of the governing equations. For the present PFN design purposes, Kohlberg's tabulated values of f_g were plotted and a polynomial curve fit was performed to provide a rough design tool for arbitrary values of h/w . This curve, along with Kohlberg's data, is plotted in figure A.1. It is clear that using the well known one dimensional, or no "fringing" fields, result (which states that in the limit of $h/w \ll 1$, $L' = (h/w)\mu_o$), leads to large errors in the estimation of L' for values of h/w greater than about 0.1.

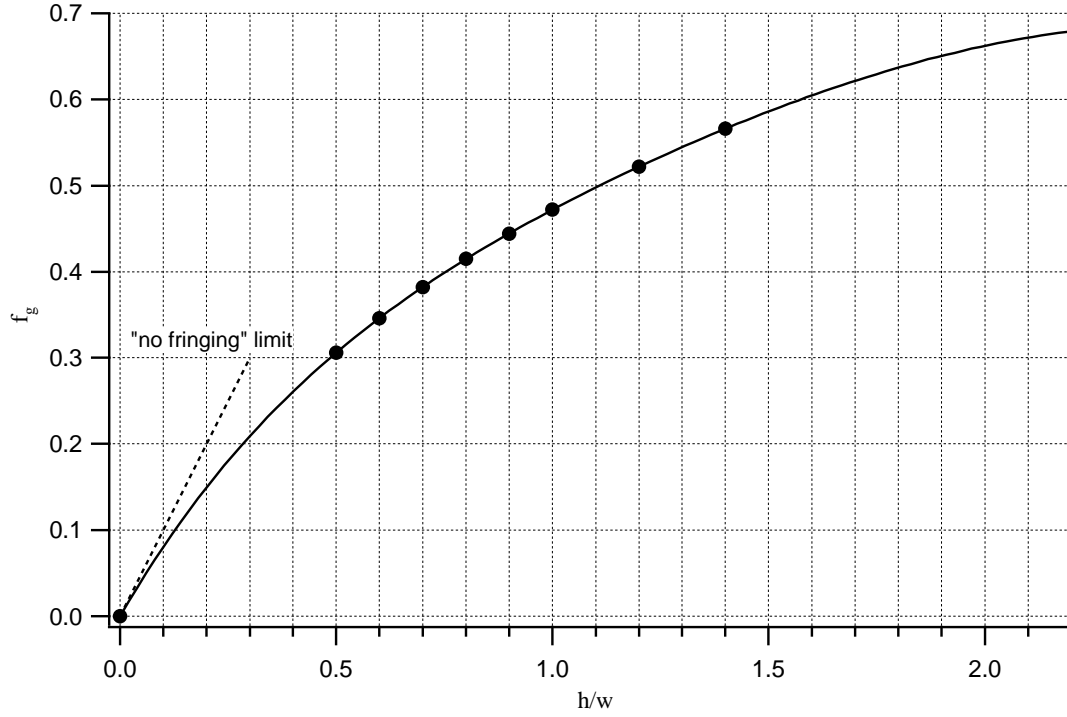


Figure A.1: Curve fit of data (indicated by dots) from Kohlberg *et al.*[40] for estimating the inductance per unit length of two parallel plate conductors.

Using the data and the equations given above, we can calculate L_o for a given transmission line configuration, and estimate dI_o/dt via equation A.1. The second task, indicated above, was to design the PFN to give the desired current pulse duration. It can be shown that the pulse width of an LC ladder network, connected to a matched load, is given by[48]

$$\tau_p = 2n\sqrt{LC} , \quad (\text{A.3})$$

where, n is the number of stages, and L and C are the parallel capacitance and series inductance of each stage, respectively. The required stage inductance can be calculated for a given design pulse width and number of capacitors with known capacitance C . Since both CSCX PFNs used rectangular flat plates for inductors, equation A.2 was used to estimate the physical dimensions of the inductors needed to give the required stage inductance.

A.1.2 Analytical design

The relations given above were used in the preliminary design of the CSCX PFNs; the final designs were developed with the aid of numerical circuit simulations, as described in the next section. This section gives the details of the preliminary designs of the two PFNs.

Both PFNs were required to provide a current pulse of sufficient duration to accelerate the current sheet along the entire length of the accelerator. So, the first step in the design process was to estimate the required pulse width. Review of electromagnetic accelerator literature reveals that typical current sheet sweeping speeds range from 2-3 cm/ μ s. Thus, for a 60 cm long accelerator, a current pulse of approximately 20-30 μ s was needed.

PFN I. Eight 18 μ F (5 kV) capacitors were available for the construction of PFN I. Inserting these values into equation A.3 yields a required stage inductance of $L = 86.8$ nH for a 20 μ s pulse.

PFN II. Ten 10 μ F (10 kV) capacitors were acquired for use in PFN II. Inserting these values into equation A.3 yields a required stage inductance of $L = 100$ nH for a 20 μ s pulse.

A.1.3 Numerical simulations

Modelling the PFN using the ideal relations given above provides a good rough estimate of the necessary electrical component values. However, since a great amount of time and expense is required to construct a PFN, more detailed analysis is warranted. A more rigorous design process includes modelling the non-ideal properties of the electrical components (e.g., a capacitor has, in addition to capacitance, non-negligible resistance and inductance) and modelling the load (which has time-varying electrical properties.) Modelling of the complete networks was accomplished using the Microcap software[50], which is an implementation of the PSPICE numerical circuit simulation code.

Component	Description	Value
<u>PFN I:</u>		
C1-C8	Stage capacitor capacitance	18 μF
L1-L8	Stage capacitor inductance	14 nH
L9-L15	Stage series inductance	60 nH
L16	First stage and parasitic inductance	100 nH
L17	Accelerator (time-varying) inductance	$10 \times t$ mH
R1-R8	Stage capacitor resistance	9 m Ω
R9-R16	Stage series resistance	100 $\mu\Omega$
R17	Accelerator plasma resistance	10 m Ω
S1	Ignitron switch	Perfect switch
<u>PFN II:</u>		
C1-C10	Stage capacitor capacitance	10 μF
L1-L10	Stage capacitor inductance	20 nH
L11-L19	Stage series inductance	100 nH
L20	First stage and parasitic inductance	120 nH
L21	Accelerator (time-varying) inductance	$10 \times t$ mH
R1-R10	Stage capacitor resistance	20 m Ω
R11-R20	Stage series resistance	10 $\mu\Omega$
R21	Accelerator plasma resistance	10 m Ω
S1	Ignitron switch	Perfect switch

Table A.1: PFN I and II numerical simulation elements.

Figure A.2 shows electrical schematics of the components that were input into the Microcap software for PFN I and PFN II. The values of the components illustrated in the schematic are given in table A.1. The indicated values were either taken from published values or estimated. A resistor in series with a time-varying inductor was used to simulate the plasma discharge in the accelerator. The total inductance of the accelerator channel was estimated to be about 180 nH, using the methodology given above. Assuming a sheet

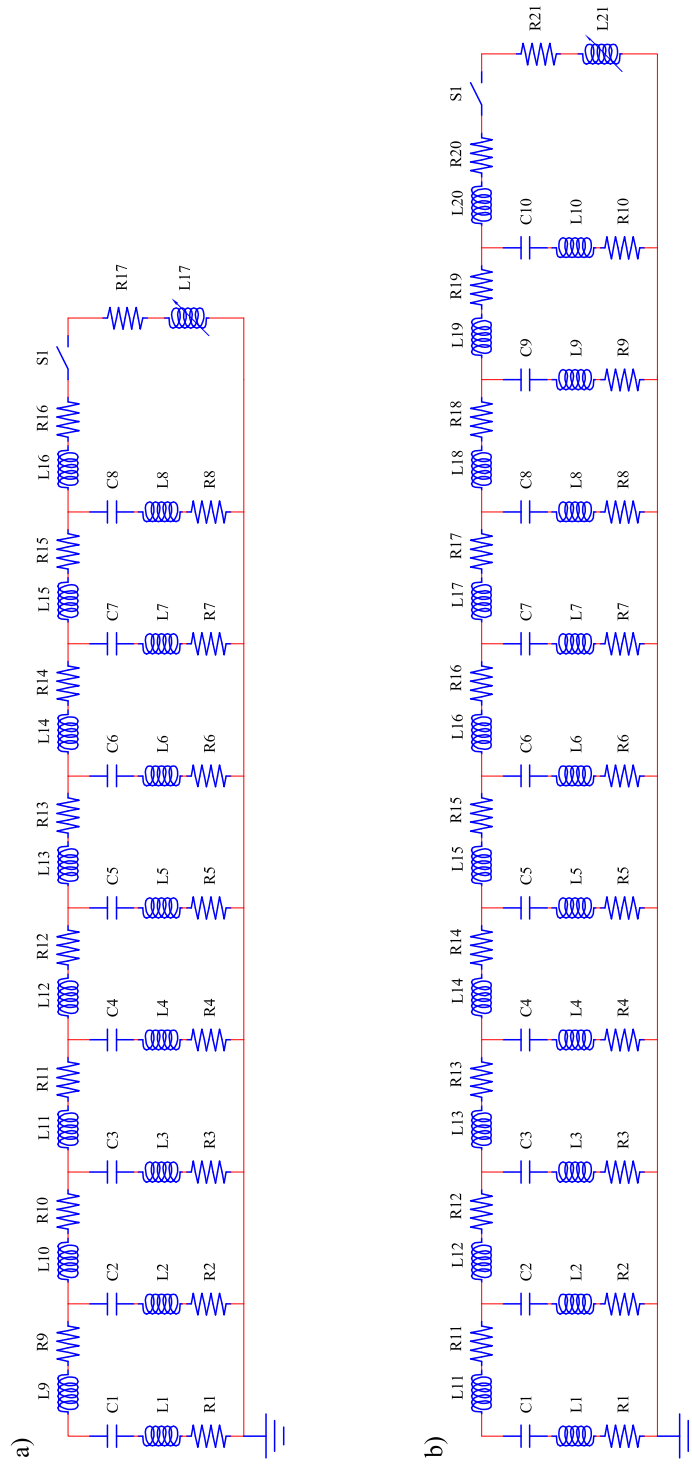


Figure A.2: Electrical schematics of elements used in numerical simulation of a) PFN I and b) PFN II.

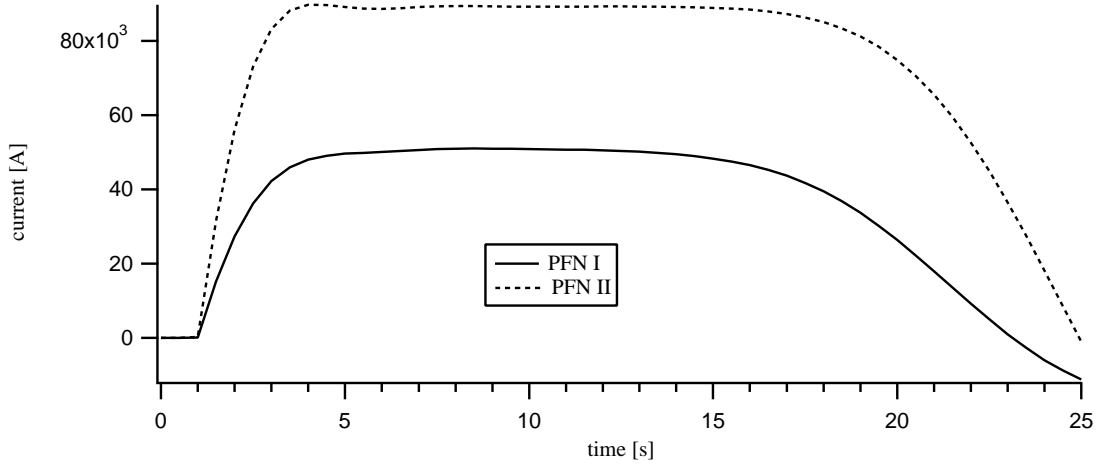


Figure A.3: Predicted total current delivered to accelerator ($V_{PFN I}=5$ kV, $V_{PFN II}=10$ kV.)

propagation speed of $3 \text{ cm}/\mu\text{s}$, the time varying inductance was found to be about 10 mH/s . The characteristic voltage drop in the plasma is likely to be on the order of 10 V . Assuming currents on the order of 10 kA , this implies a plasma ohmic resistance of approximately $10 \text{ m}\Omega$. These estimates for accelerator inductance and resistance were used in both numerical models of PFN I and II.

Figure A.3 shows the results of the simulations. As desired, both curves show a current pulse length of about $25 \mu\text{s}$. The predicted peak current of PFN I is about 50 kA , whereas PFN II, with its higher voltage capability, is predicted to have a maximum current of about 80 kA .

A.1.4 Physical construction

The PFNs were constructed by connecting a line of capacitors with wide copper conductors. The copper strips served as both structural support as well as the inter-stage inductors. By adjusting the spacing between the copper strips which joined the capacitors, the desired inductance was attained. Figure A.4 shows schematics of the two PFN assemblies. Since the capacitors used in PFN I were of the single-ended variety, bending of the copper strips

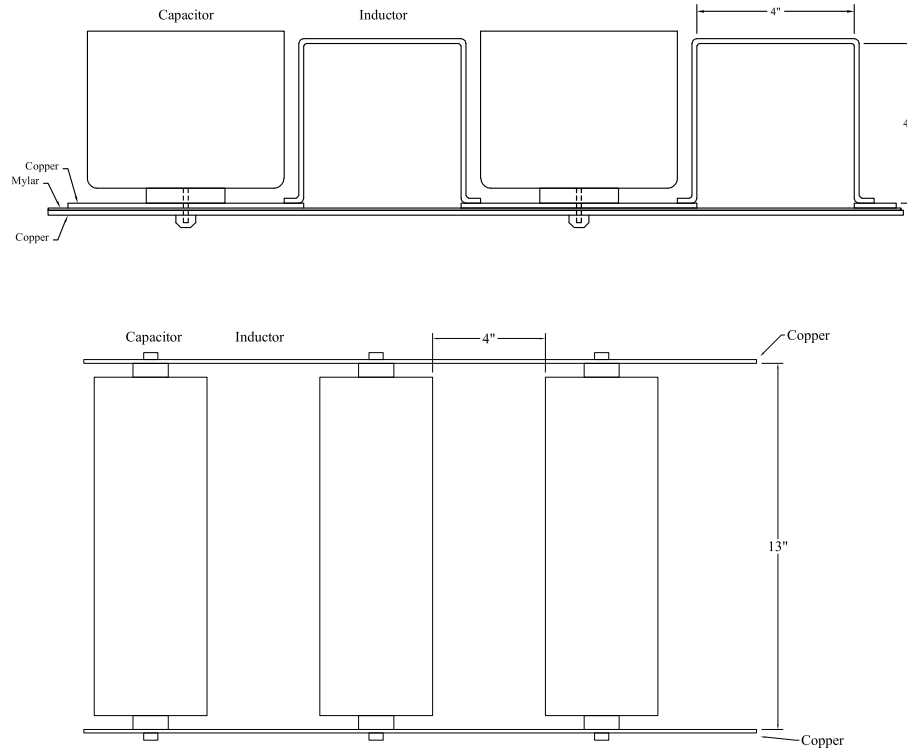


Figure A.4: Schematics of two stages of PFN I (top) and three stages of PFN II (bottom).

was required to produce the inter-stage inductors. PFN II used double-ended capacitors which facilitated much easier construction; the capacitors were simply spaced evenly (to yield the desired stage inductance) along two continuous copper electrodes with no need for bending or attaching multiple sections.

PFN I used $4'' \times 1/8''$ copper sheets throughout. The total length of the PFN was about eight feet; however, to keep the entire assembly in a smaller package, the line was folded in half so that the height of the complete assembly is about four feet. PFN II used $6'' \times 1/8''$ copper sheets. The height of the complete assembly is about seven feet. PFN II was not folded in half because it would have considerably complicated the construction and assembly procedures.

The transmission line used to connect the accelerator to both PFNs was constructed from $4'' \times 1/8''$ rectangular copper sheet. Approximately 2 m long strips were needed to po-

sition the accelerator in the desired position in the chamber and accommodate the switching circuitry between the accelerator and the PFNs. About 20 mils (0.5 mm) of electrical insulation separated the the charged and grounded plates. In this case h/w is small so $f_g \approx h/w$ and $L' = 6.18$ nH/m. Therefore, L_o is approximately 12 nH and, from equation A.1, the initial current rise rate is estimated to be about $0.5\text{-}1 \times 10^{11}$ A/s·cm for bank voltage of 5-10 kV (and a 10 cm wide accelerator channel). This current rise rate is adequate to fulfill the aforementioned requirements.

A.2 Accelerator electrical schematic

Figure A.5 shows an electrical schematic for the CSCX accelerator and power supply. The power was supplied in a pulsed mode from a 5 kJ pulse forming network (PFN II). The bank was charged with a high voltage power supply. The DC charging current was limited by a 100 k Ω series resistance. An approximately 1 mH inductor was placed in series to provide an AC shunt between the PFN and ground connection. In early studies the PFN was found to "pull" the ground potential around during discharge. This was unacceptable, as it caused the diagnostic instruments referenced to the ground connection to behave unpredictably. The introduction of the series inductance eliminated the problem by not allowing the PFN to "talk" to ground at high frequencies.

An ignitron (which was triggered by a krytron-switched high voltage pulse) was used to switch the PFN into the accelerator. A 1 k Ω resistor was placed in parallel at the breech of the accelerator to hold the floating (cathode) electrode at ground potential before the (negatively charged) PFN was discharged.

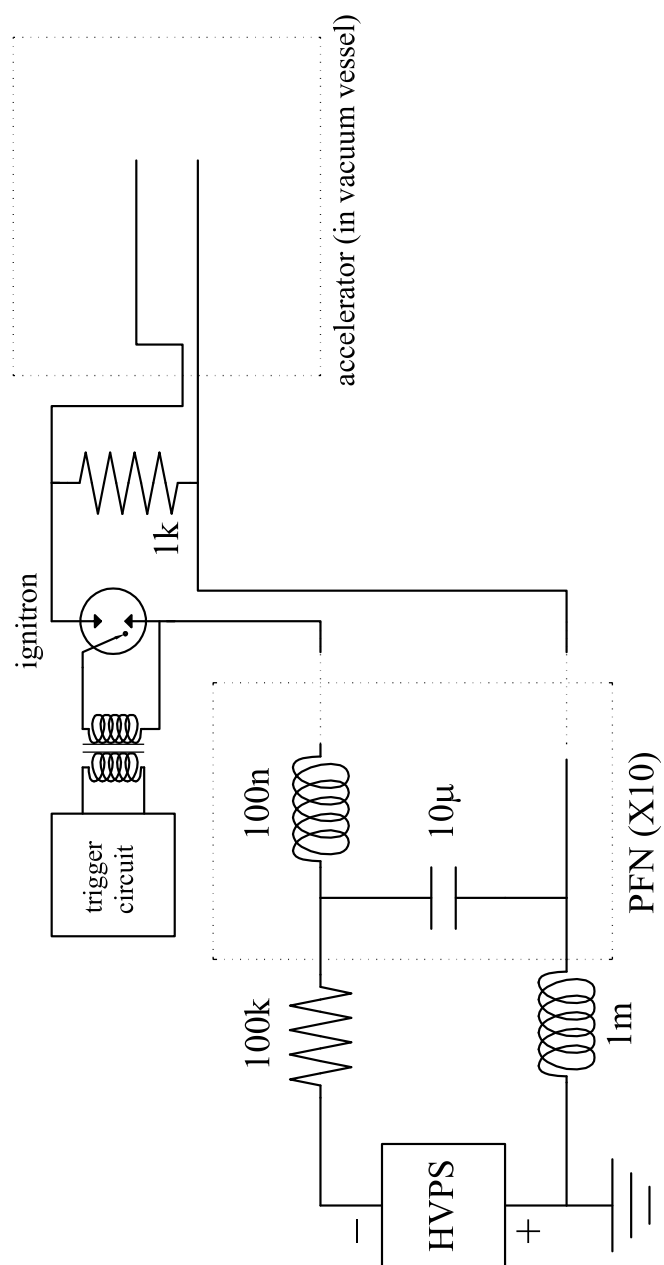


Figure A.5: Electrical schematic of the CSCX accelerator and power supply.

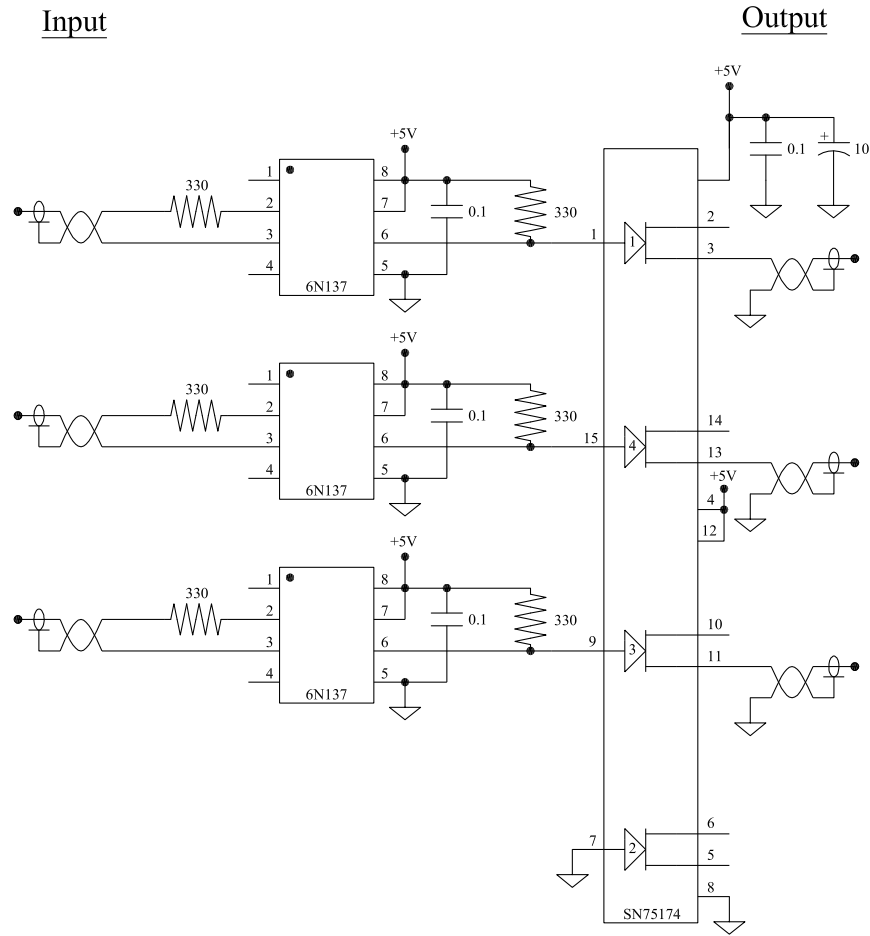


Figure A.6: Electrical schematic of three channels of the optically isolated trigger box.

A.3 Optically isolated trigger box

In order to electrically isolate the various instruments which required trigger signals, a six channel optically coupled trigger box was constructed. The box used six 6N137 optocouplers and two SN75174 TTL line drivers. Three channels of the device are illustrated in figure A.6.

In addition to eliminating cross-talk between the devices, the box provided about 5 kV of high voltage isolation.

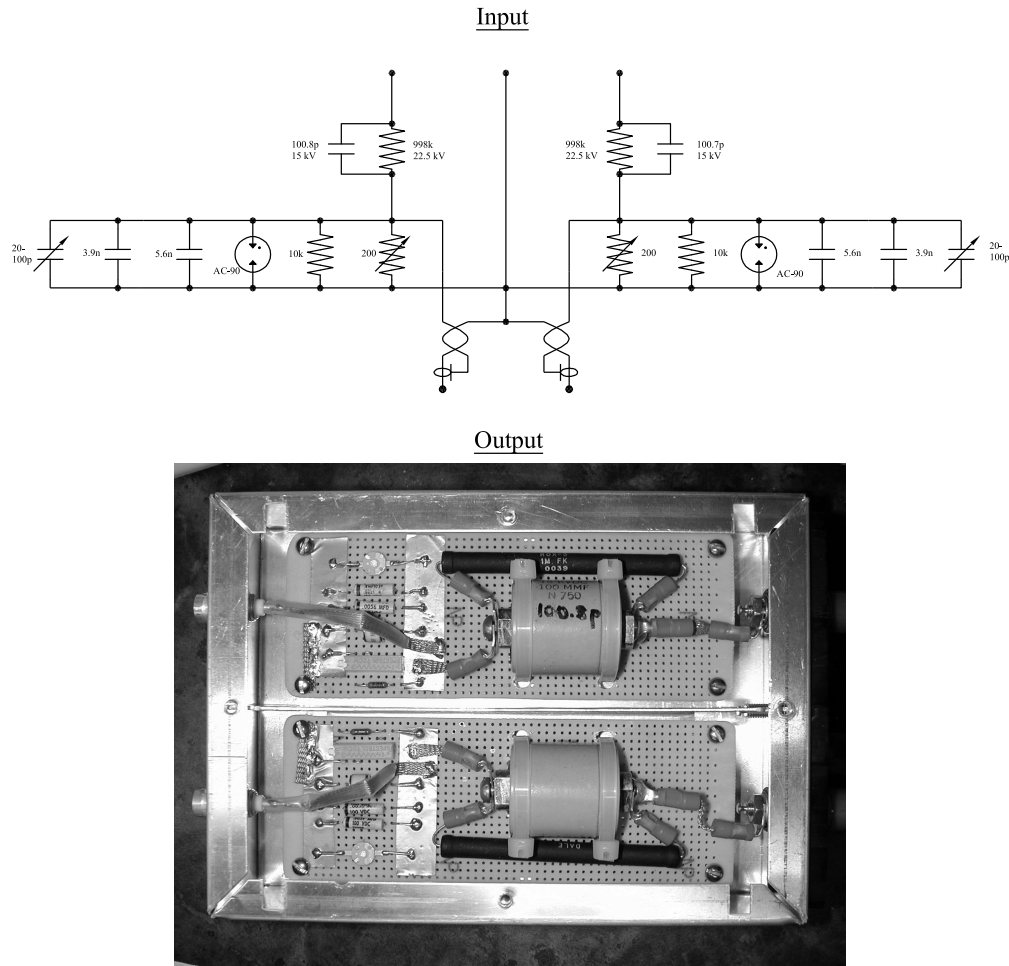


Figure A.7: Electrical schematic and photograph of the differential high-voltage probe.

A.4 Differential high-voltage Probe

Figure A.7 shows the construction details of the differential high-voltage probe used in this study. It consisted of two independent 100:1 compensated voltage dividers. DC compensation was accomplished using a $200\ \Omega$ potentiometer on the low-voltage side of each divider; the dividers were AC compensated using 20-100 pF variable capacitors. The components were mounted in a $4'' \times 3\frac{1}{2}'' \times 2''$ aluminum enclosure. The high-voltage end was filled with acrylic epoxy to inhibit arcing.

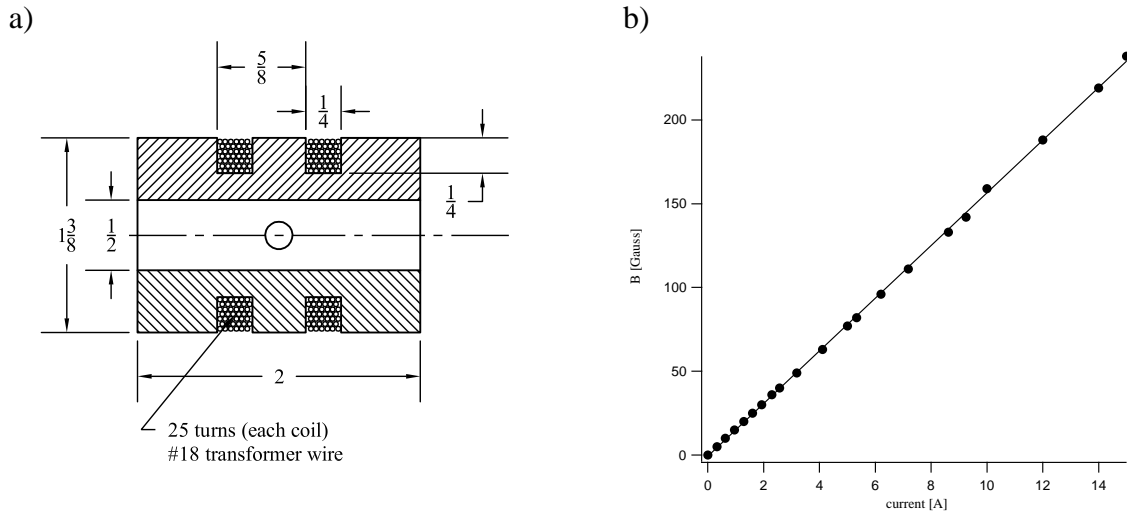


Figure A.8: a) Schematic (cross-section) of calibration Helmholtz coil used in magnetic field calibration; b) measured magnetic field at center of coil as a function of (DC) current.

A.5 Helmholtz coil

A Helmholtz coil was constructed for use as a calibration source for magnetic field probes. The Helmholtz coil is an attractive calibration source because it produces a uniform-field region between its two windings. A schematic of the Helmholtz coil used in the present study is illustrated in Fig. A.8a. The winding body was constructed using a $1\frac{3}{8}$ " polycarbonate cylinder. Fifty turns of #18 copper transformer wire were used in the coil windings. A $\frac{1}{8}$ " hole in the side of the coil was made to allow the b-dot probes to be inserted into the central region of the Helmholtz coil.

The internal magnetic field of the coil was calibrated by passing DC currents at various levels through the coil and recording the resultant magnetic field. The current was measured using a Fluke model 79III digital multimeter and the magnetic field was measured using an Applied Magnetics Laboratory model GM1A Gaussmeter. The recorded (linear) response of the coil is shown in Fig. A.8b; a linear fit to the data yielded a calibrated response of 15.72 Gauss/A.

Appendix B

CALIBRATION

Calibration of each measurement device in the experiment allows us to quantify the complete systematic uncertainty corresponding to the reported data values. The calibration procedures and results for each diagnostic device follow.

B.1 High-voltage probe calibration

The differential high-voltage probe was calibrated to give accurate DC and AC response. DC calibration was accomplished using a DC power supply of known output voltage; the potentiometer on the low-voltage side of each divider (see Fig. A.7) was adjusted to give 100:1 voltage division. AC calibration was carried out to compensate for stray capacitance in the dividers and BNC cables and to assess the frequency response of the probe. The input side of the probe was driven with a square wave; the trim capacitor on the low-voltage side of each divider was adjusted to make the output waveform as square as possible. During this procedure high frequency ringing was observed at the rising and falling edge of the output waveform. Further experimentation using sinusoidal driving of the input side of the probe identified this ringing as a circuit resonance at about 3.5 MHz.

In summary, the calibrated output of the differential probe was $100 \text{ mV/V} \pm 0.1 \text{ mV/V}$ for $\omega \leq 3.5 \text{ MHz}$. The voltage oscillations in the CSCX accelerator were expected to fall below this 3.5 MHz cutoff.

B.2 Spectroscopy calibration

The combination of the collection optics, spectrometer, and detector give us information about the wavelength and intensity of radiation being emitted from the plasma. Inferences about the bulk plasma thermodynamics are then made from these two quantities. It is therefore critical to understand the dispersive characteristics of the system, that is, how the performance of these devices changes with the wavelength and intensity of the incident radiation. Also, it is important to know the ultimate resolution of the system – the smallest variations in wavelength and intensity which can unambiguously be determined. By calibrating the complete system we can measure these quantities and provide error bars for subsequent experimental data.

B.2.1 Spectroscopic system ultimate resolution

The ultimate resolving power (usually defined by the so-called Raleigh Criterion[51]) of the spectroscopic system is limited by its mechanical characteristics. Two factors determine the resolving power of the spectrometer itself – linear dispersion and input slit width.

Linear dispersion, D , is defined as the number of wavelengths (per unit length) projected on the spectrometer exit plane; for a finite sized detector, the linear dispersion tells us the range of wavelengths which can be acquired in a single shot. For a given input slit width, w , the minimum resolvable wavelength variation, $\Delta\lambda$, is

$$\Delta\lambda = Dw . \tag{B.1}$$

The resolving power of a spectroscopic system with a CCD array as the detector is almost always limited by the large size of the CCD pixels (w_p) rather than the dispersive capabilities of the spectrometer. In other words, the smallest attainable value of $\Delta\lambda$ in eqn. B.1 is obtained when $w = w_p$; further reduction in the slit width will not result in better wavelength resolution. Using the values of D and w_p given above, the minimum resolvable wavelength variation for this system is $\Delta\lambda = 0.20 \text{ \AA}$.

B.2.2 Spectrometer input slit

It is important to know the width of the spectrometer entrance slit since, in part, the ultimate resolution of the spectrometer depends on it. The slit width is adjusted using a dial indicator located above the slit. Calibration of the slit involves verifying that the dial setting reflects the actual width of the slit.

The actual width of the slit may be measured using single slit diffraction theory. When parallel, monochromatic light is passed through a narrow slit an interference pattern will appear on a screen placed “downstream” of the slit; the image will consist of alternating light and dark regions. Far away from the slit, the spacing of these fringes is adequately described by far field, or Fraunhofer diffraction theory[52]:

$$I(\theta) = I(0) \left(\frac{\sin \beta}{\beta} \right)^2, \quad (\text{B.2})$$

$$\beta = \frac{kw}{2} \sin \theta, \quad (\text{B.3})$$

where, I is the irradiance, k is the wavenumber of the incident light, w is the slit width, and θ is the angle between the centerline of the slit and any point on the diffraction pattern, in the imaging plane. The irradiance is equal to zero when $\sin \beta = 0$, in which case

$$\beta = \pm\pi, \pm2\pi, \pm3\pi, \dots \quad (\text{B.4})$$

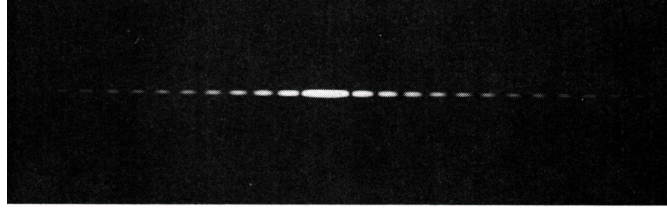


Figure B.1: Diffraction pattern which results from passing monochromatic light through a narrow slit[52].

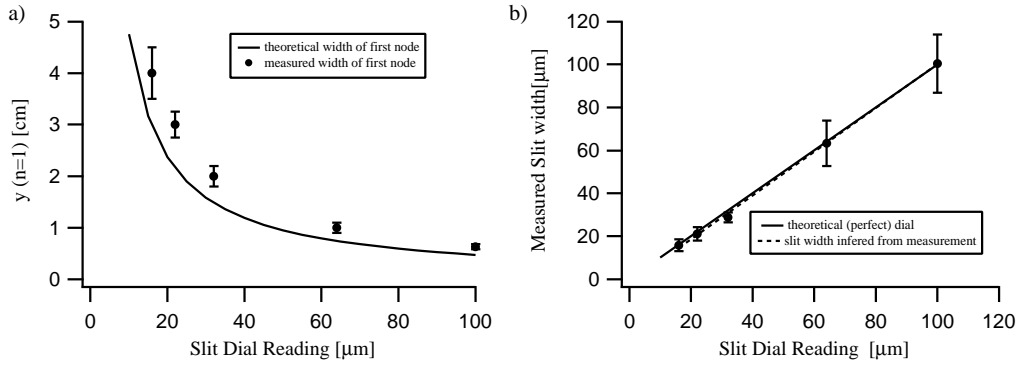


Figure B.2: Theoretical and experimental values for a) width y for $n=1$ node versus slit width, and b) measured slit width versus slit dial setting.

If we define x as the distance to the imaging plane, and y as the distance from the center of the diffraction pattern, in the imaging plane, then equations B.2-B.4 yield

$$y = \frac{x}{\sqrt{\left(\frac{w}{n\lambda}\right)^2 - 1}} \quad (\text{B.5})$$

as the spatial position of the n^{th} node in the diffraction pattern. Figure B.1 shows a typical diffraction pattern which results from passing monochromatic light through a narrow slit.

The entrance slit on the Spex spectrometer was calibrated using a collimated beam from a Uniphase Model 1107P HeNe laser ($\lambda = 6328 \text{ \AA}$). The width of the $n = 1$ node was measured at an image plane distance of $x = 0.5 \text{ m}$. Figure B.2 shows the theoretical and measured values of y and the corresponding values for the calibrated slit width.

B.2.3 Wavelength calibration

In order to unambiguously correlate acquired spectral data with tabular data (i.e., to identify atomic species), it is necessary to calibrate the spectroscopic system for wavelength measurements. Wavelength calibration involves quantifying the linear dispersion and center-shift of the spectrometer. The procedure results in a calibration curve which shows the wavelength range that is spanned by the physical extents of the CCD array as a function of frequency, and the number of pixels (from the center of the CCD array) which the center frequency is shifted due to misalignment of the internal spectrometer optics. The center shift is constant, independent of frequency.

A mercury-argon Geisler tube and a HeNe laser were used in the wavelength calibration. These light sources have very narrow emission lines, allowing each line to be imaged on a single column of pixels.

The procedure used for wavelength calibration was to place the light source at the accelerator position and image it onto the slit of the spectrometer. Several strong transitions were identified which spanned the wavelength range of interest. Each line was imaged onto the first, center, and last columns of the CCD array and the corresponding wavelengths were recorded. Taking the difference of the lowest and highest wavelengths divided by the horizontal number of pixels on the CCD array yields the linear dispersion of the spectrometer. Figure B.3 shows the experimentally measured linear dispersion. The center-shift was found to be sixteen pixels at all wavelengths. The linear fit and center-shift were used in all subsequent data analysis in the data reduction code.

B.2.4 Intensity calibration

Certain physical quantities, such as electron temperature, can be inferred by comparing the relative intensity of spectral lines. It is, therefore, essential to quantify the transmittance

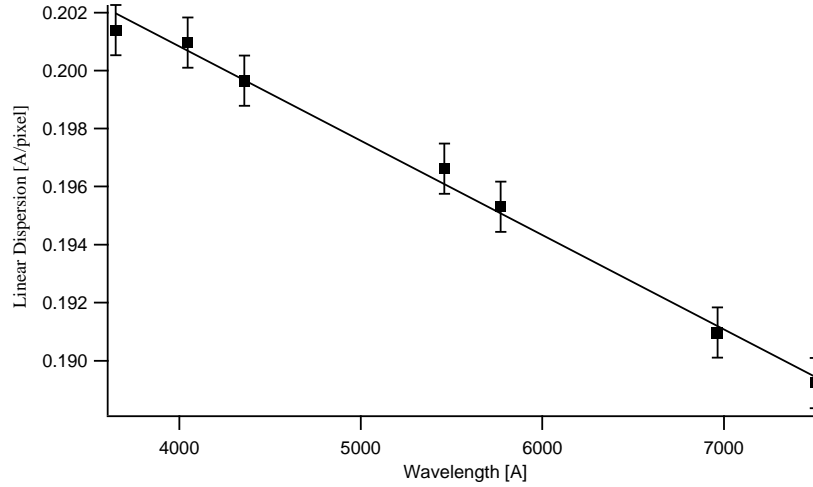


Figure B.3: Measured values and linear fit of linear dispersion of spectrometer.

dispersion for all optical elements in the spectroscopic system.

The procedure used for intensity calibration was to record the response of the complete system to a light source of known output characteristics. An Oriel model 1934 quartz-tungsten-halogen (QTH) broadband source was placed at the accelerator location and imaged onto the entrance slit of the spectrometer. The emission from the source was recorded from 3500 to 8000 Å. The raw data was processed using the data reduction software and the resulting intensity versus wavelength trace was compared with the published emission curve[53], yielding an intensity calibration filter. The intensity filter function is simply the function which results from dividing the function which represents the published data by the experimentally acquired curve. Figure B.4 shows the published curve, the raw data, and the curve which results from applying the intensity calibration filter. This filter was integrated into the data reduction software and applied to all subsequent analysis. It should be emphasized that this calibration is for relative intensity only; no calibration for the absolute intensity response of the system was performed. Figure B.5 shows the calibrated spectrum of the Hg-Ar lamp used in the wavelength calibration. Distinct sets of mercury and argon lines are observed.

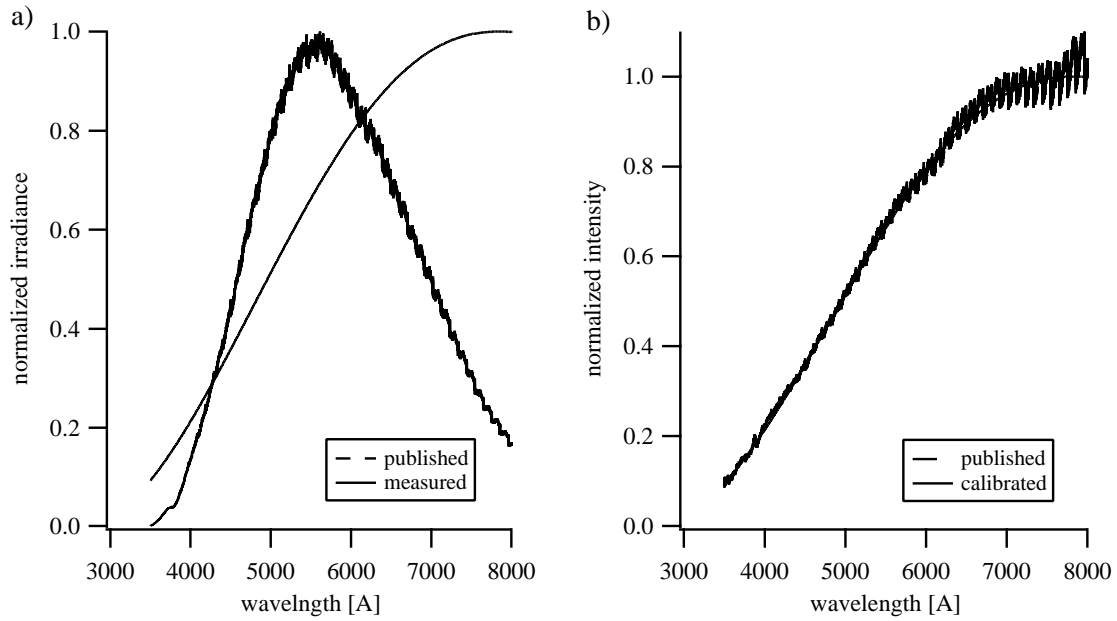


Figure B.4: Intensity calibration data: a) Published and raw data, b) Filtered raw data.

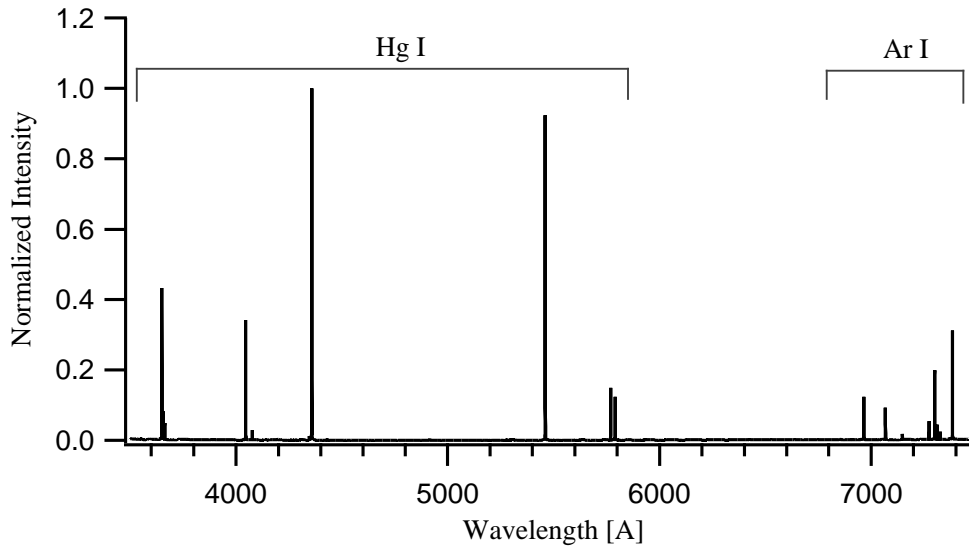


Figure B.5: Calibrated spectrum of Hg-Ar lamp.

B.3 Magnetic field probe calibration

The magnetic field probes were calibrated using the Helmholtz coil described in appendix A.5. The task was to determine $c(\omega)$ as defined in Eq. 4.1.

Calibration was accomplished by recording the probe response to a known magnetic field inside the Helmholtz coil. Current waveforms of various frequencies (0.01-2.0 MHz) were pulsed through the Helmholtz coil by discharging capacitors of various capacitances ($1 \times 10^{-5} - 5 \mu\text{F}$) through the series LC circuit (i. e. , the Helmholtz coil was the inductive element.) An SCR was used to switch the capacitors into the coil. The current through the coil was measured using a Pearson model 410 current monitor. The instantaneous magnetic field at the probe location was calculated by multiplying the measured current by the Helmholtz coil calibration constant given in appendix A.5. The integrated b-dot probe responses were divided by the known instantaneous magnetic field to yield c ; the values of c were found to be constant throughout the frequency range tested (0.01-2.0 MHz). The measured values of c for each probe are given in table B.3(note: 50Ω termination).

probe	set	c [T/V-s]
1	I	9.11 ± 0.01
2	I	7.45 ± 0.01
1	II	7.55 ± 0.01
2	II	8.07 ± 0.03

Table B.1: Calibration constants for b-dot probes.

Appendix C

ADDITIONAL DATA

This appendix presents additional supporting data for Chapter 6: Experimental Results. The purpose of that chapter was to concisely report data directly related to the current sheet canting problem, without cluttering the presentation with page after page of raw data. Here, much of that support data is accumulated; its inclusion is intended to support further research in current sheet physics.

C.1 Circuit Current

The dependence of maximum and average current on propellant mass is more clearly shown by plotting the currents as a function of the total initial propellant in the accelerator discharge chamber; the data in Fig. C.1 show a clear trend in the influence of total propellant mass (the propellant mass density times the discharge chamber volume): for a given pressure, the peak and average currents increase as the atomic mass of the propellant increases and, for a given species, the peak and average currents increase as the pressure increases. Both of these effects are most likely due to the variation of the circuit dynamic impedance.

As was discussed in Chapter 1, the dynamic impedance (i.e., the voltage drop associated

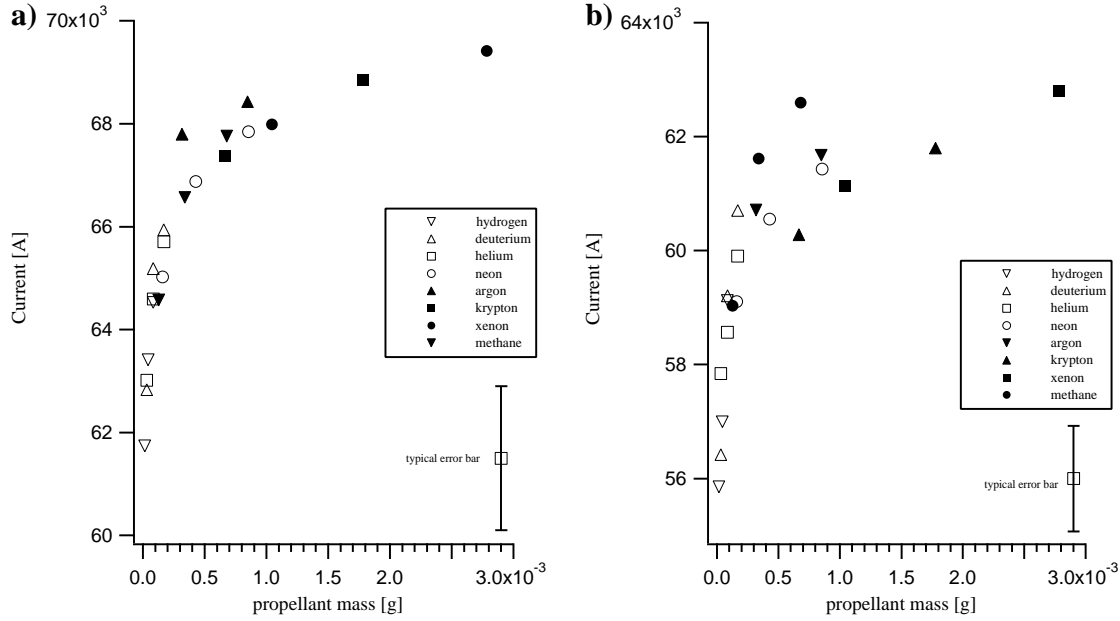


Figure C.1: Influence of propellant species and pressure on a) peak current and b) average current. The current is plotted as a function of the total propellant mass in the discharge chamber prior to firing. These mass loadings correspond to initial pressures of 75, 200, and 400 mTorr (Ar, Kr, and Xe data for 75, 200 mTorr only), $V = 9\text{kV}$.

with IdL/dt as the current sheet moves) is expected to dominate over resistive (Ohmic) losses. Thus, the variation of peak and average currents among the propellants is not due to differences in plasma resistivity but, rather, the variations are most likely due to differences in current sheet propagation speed. A more rapidly accelerating current sheet will present a higher dynamic impedance to the PFN and, hence, will result in a lower peak current than in the case of a more slowly accelerating current sheet. Since the current sheet acceleration is impeded by the inertia of the (stationary) propellant that it sweeps up, we should expect that higher atomic mass propellants (as well as higher gas pressure) will lower current sheet propagation speed and, hence, yield higher peak current. These trends are indeed born out in the data.

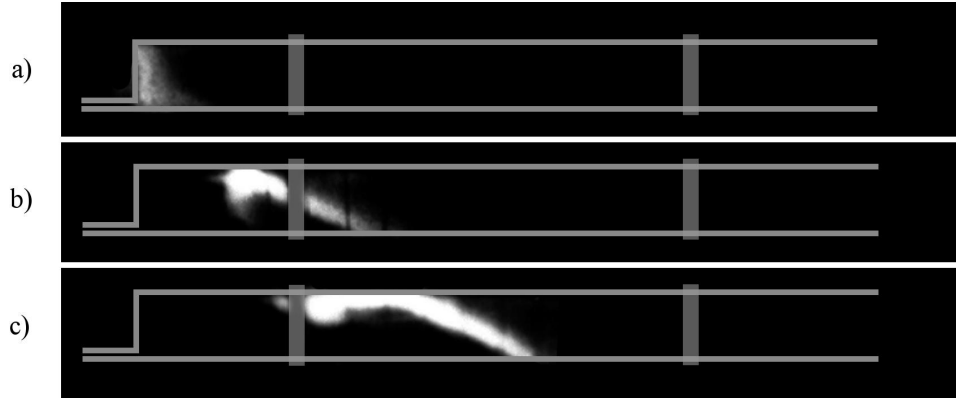


Figure C.2: Photographs showing the influence of changing polarity ($p=100$ mTorr (Argon), $V=4$ kV): a) $t=5\mu s$, b) $t=11\mu s$, c) $t=14\mu s$.

C.2 High-speed photography

Some additional data from the high-speed photography experiment is presented below.

C.2.1 Influence of Polarity

The first operating condition that was changed was the polarity of the electrodes. There was some concern that the asymmetric construction of the back of the accelerator (see Fig. 3.2) was creating a non-uniform magnetic field behind the current sheet, causing it to tilt. If magnetic field asymmetry is the dominant mechanism which drives the canting, reversing the polarity of the electrodes should not affect the structure of the discharge (i.e., the discharge attachment on the top electrode should still lead the attachment point on the bottom electrode). However, as is apparent in Fig. C.2, changing the polarity was found to result in the bottom electrode attachment point leading the top. Gas loading, etc., was identical to the experiment represented in Fig. 5.4. The conclusions which can be drawn are: it is unlikely that aspects peculiar to the construction of the accelerator are responsible for the canting and, comparing Fig. 5.4 and Fig. C.2, the current sheet always cants such that the anode arc attachment point leads the cathode attachment point.

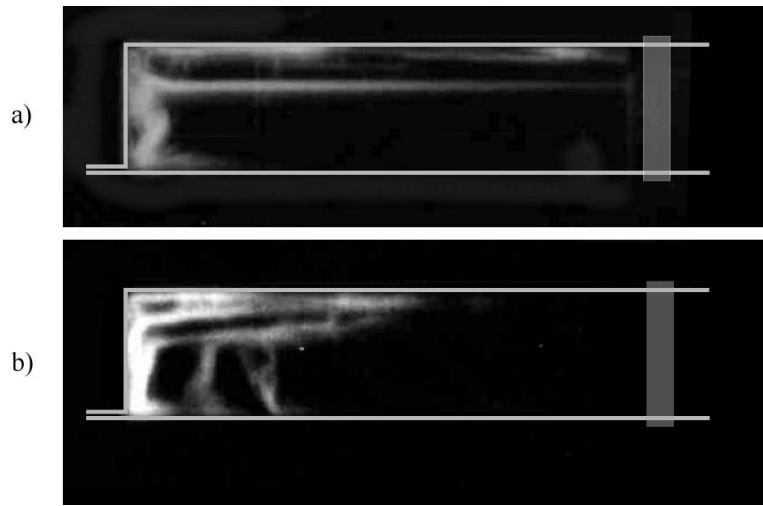


Figure C.3: Two images from the initiation stage (first few hundred nanoseconds) of the discharge ($p=100$ mTorr (Argon), $V=5$ kV).

C.2.2 Influence of Contaminated Electrodes

Early in the CSCX effort the accelerator was removed, cleaned and reassembled. When the accelerator was again fired, the discharge initiation appeared to be quite different from that which was seen in the original accelerator (see figure 5.4.) In the very early stages of the discharge many filamentary structures are visible. Figure C.3 shows two pictures, from separate discharges, during the first several hundred nanoseconds of current flow. Argon (100 mTorr) was used; the bank voltage was set to 5 kV. The lower image was acquired at a slightly later time than the upper image.

It was originally believed that these filamentary structures were breakdown waves, commonly known as streamers. However, these features disappeared after several hundred discharge cycles, leaving us to conclude that the erratic breakdown phenomena were related to electrode surface preparation and conditioning. When the accelerator was reassembled, the electrodes were cleaned with isopropyl alcohol, whereas the accelerator electrodes in the original assembly were cleaned with acetone. It is believed that the isopropyl alcohol created an oxide layer on the copper electrodes, leading to a sporadic breakdown pattern.

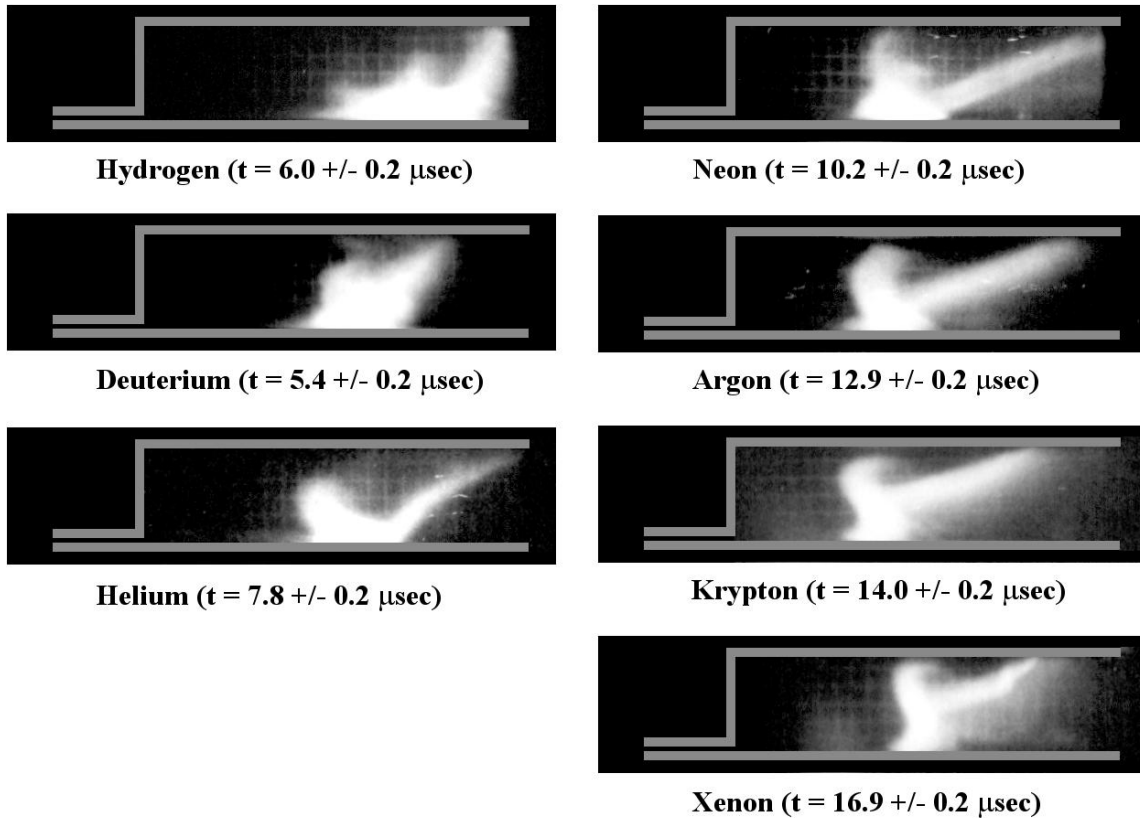


Figure C.4: Breech photographs ($p=75$ mTorr, $V=9$ kV).

After several hundred discharges, this oxide layer presumably vaporized off, leaving clean copper electrodes and allowing normal, sharp, breech-centered breakdown.

C.2.3 Breech Photographs

Figure C.4 shows some additional breech photographs obtained with several different propellants.

C.2.4 Mid-section Photographs

Figure C.5 shows some additional midsection photographs obtained with various propellant/pressure combinations. These photos (and one additional set not shown here) were

used to extract data for Fig. 5.6.

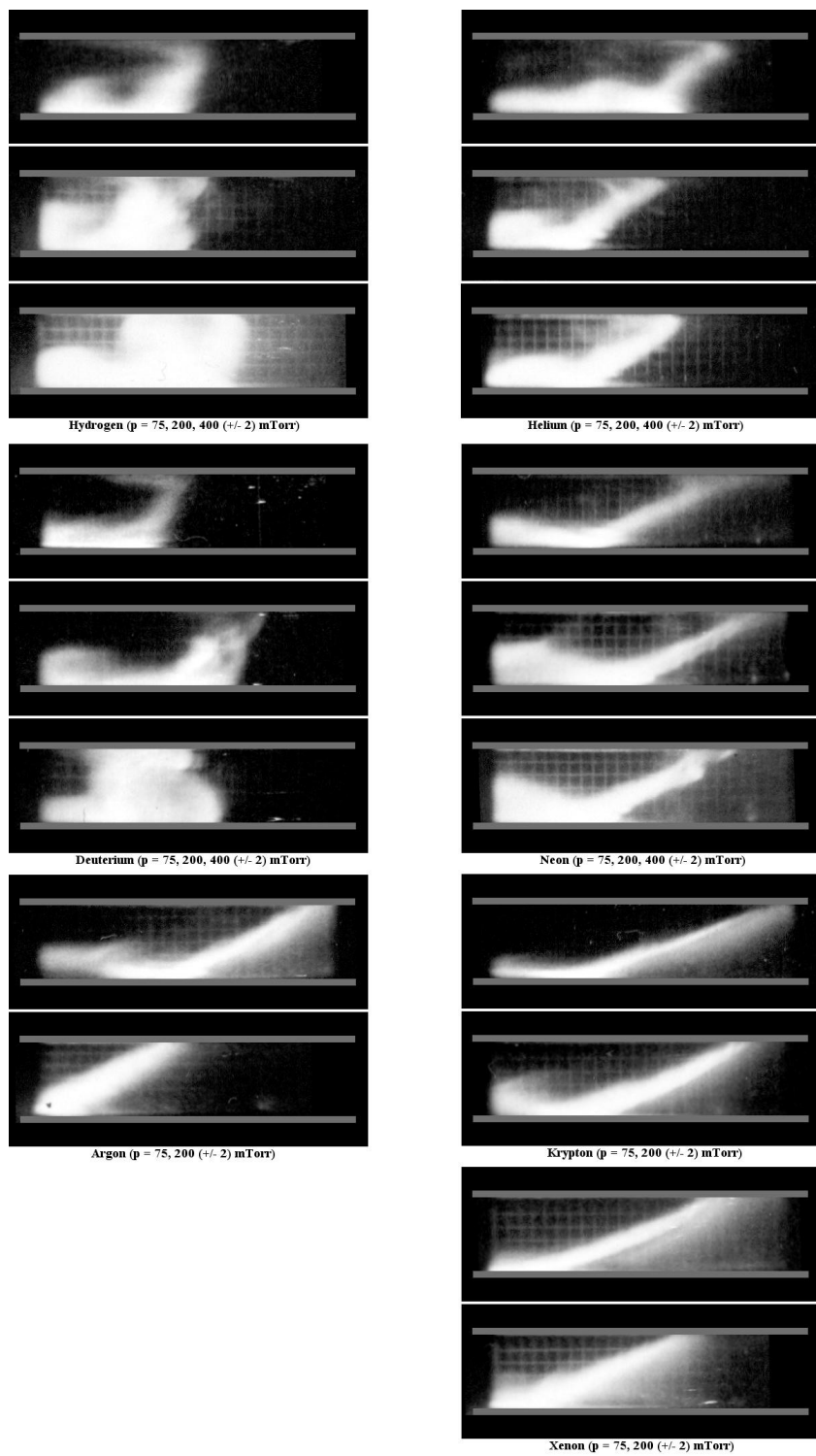


Figure C.5: Mid-section photographs ($V=9$ kV).

C.3 Magnetic field probes

Figures C.6-C.9 give typical magnetic field histories similar to those shown in Fig. 5.8, but for the all of the propellants and pressure levels tested.

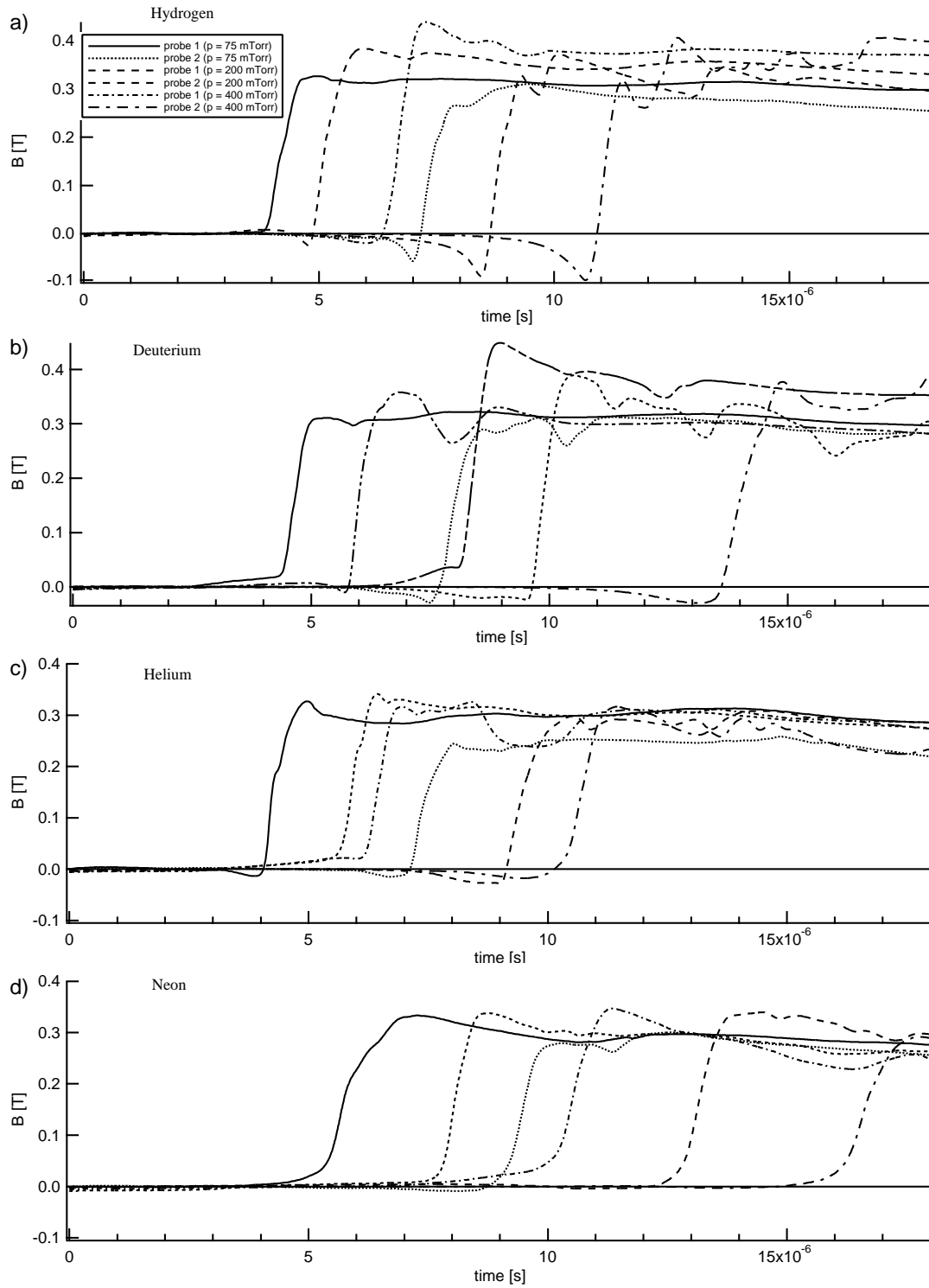


Figure C.6: Magnetic field history for b-dot probes in configuration 1.

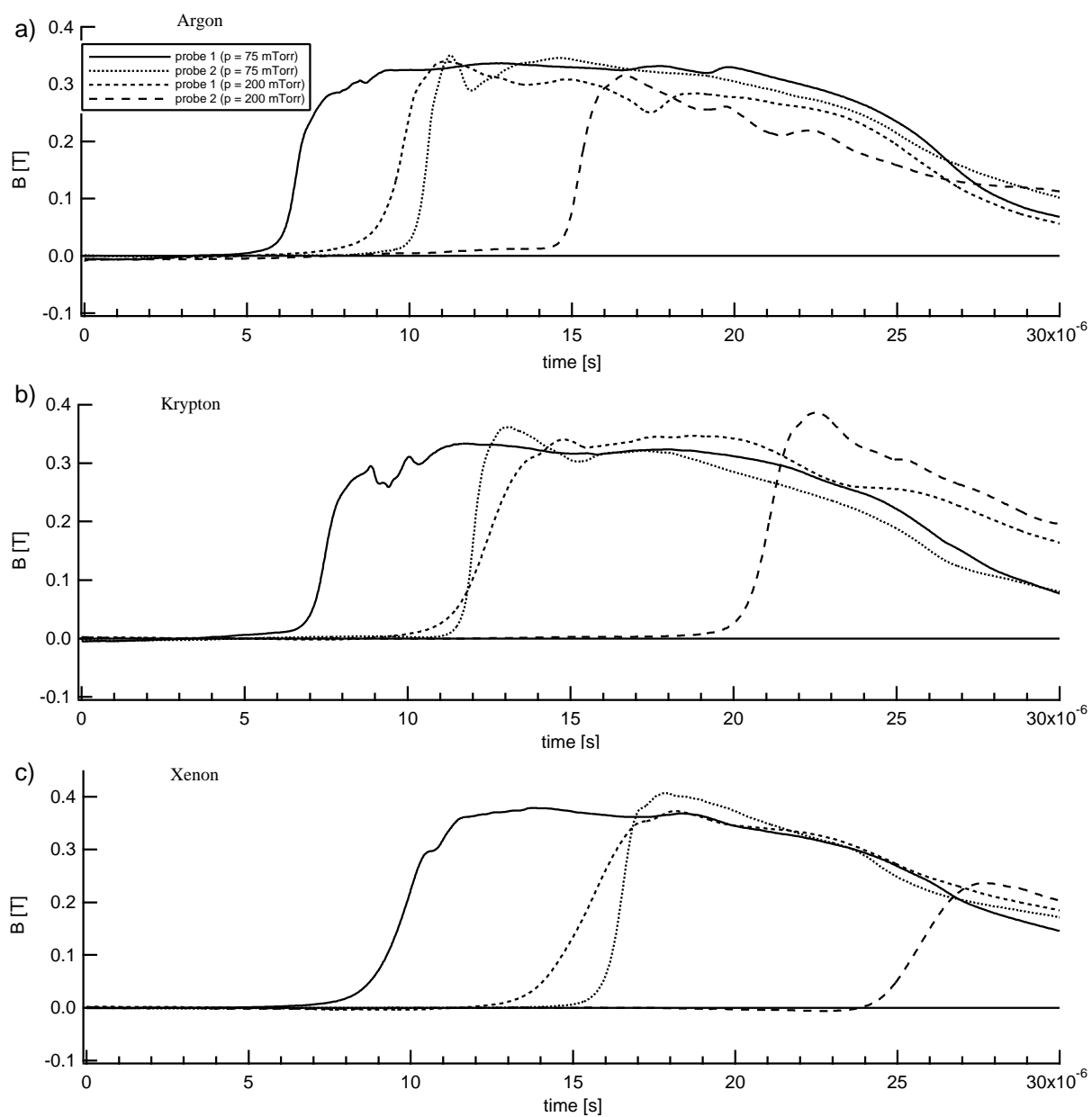


Figure C.7: Magnetic field history for bdot probes in configuration 1.

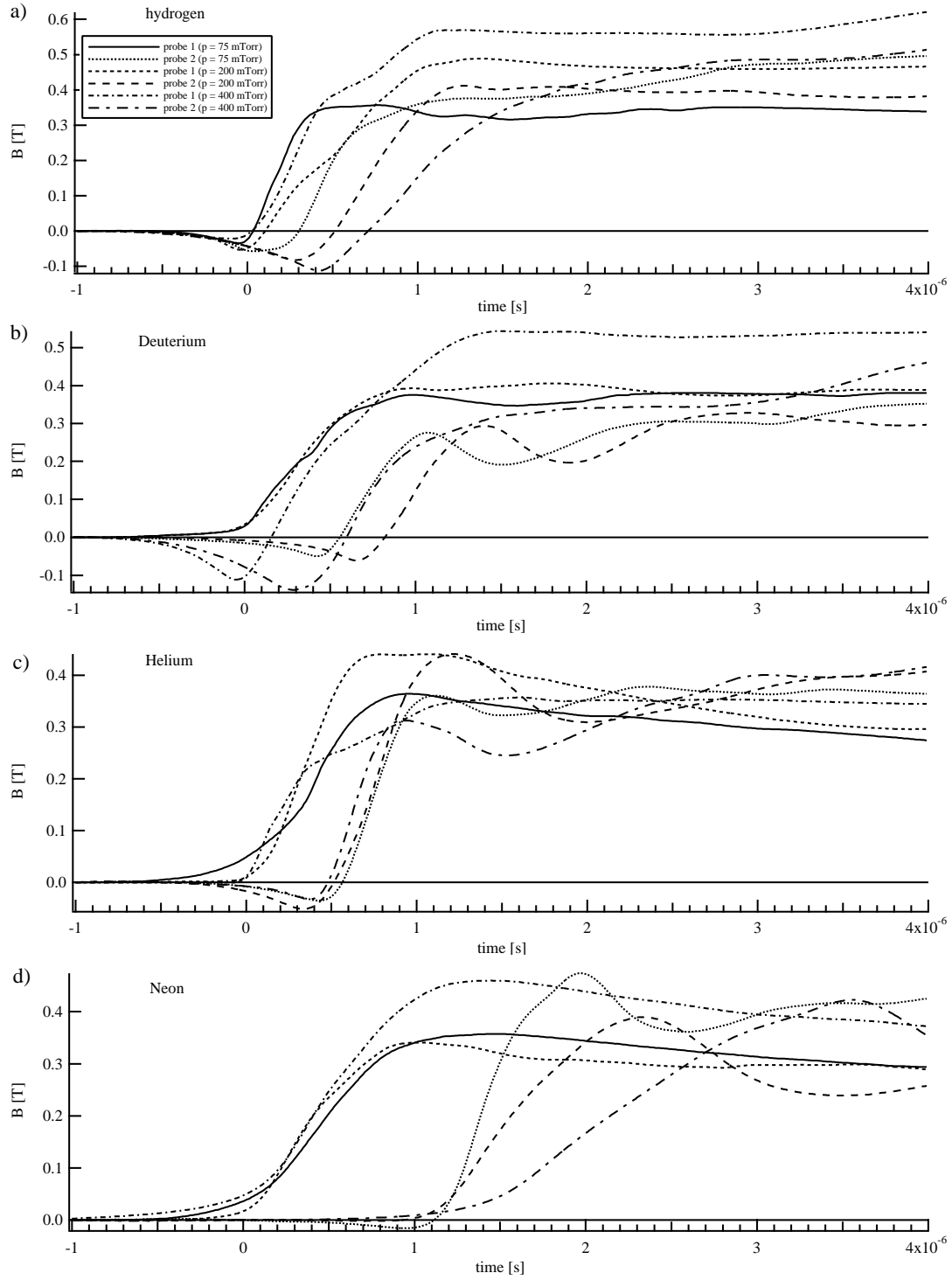


Figure C.8: Magnetic field history for bdot probes in configuration 2.

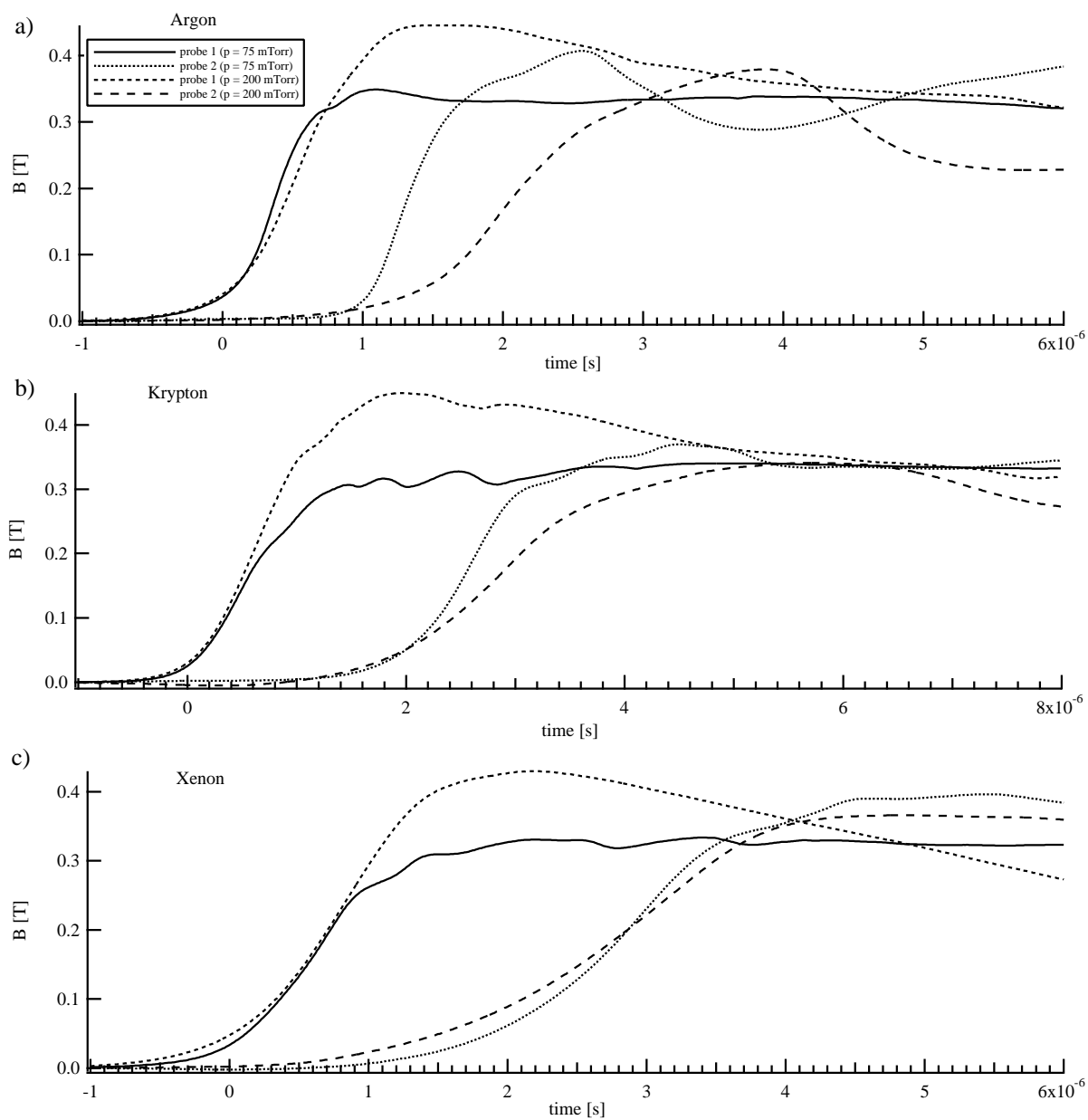


Figure C.9: Magnetic field history for bdot probes in configuration 2.

C.4 Laser interferometry

Figures C.13-C.16 show typical measured electron density profiles (similar to the ones shown in Fig. 5.12a) for all of the propellants and pressure levels tested.

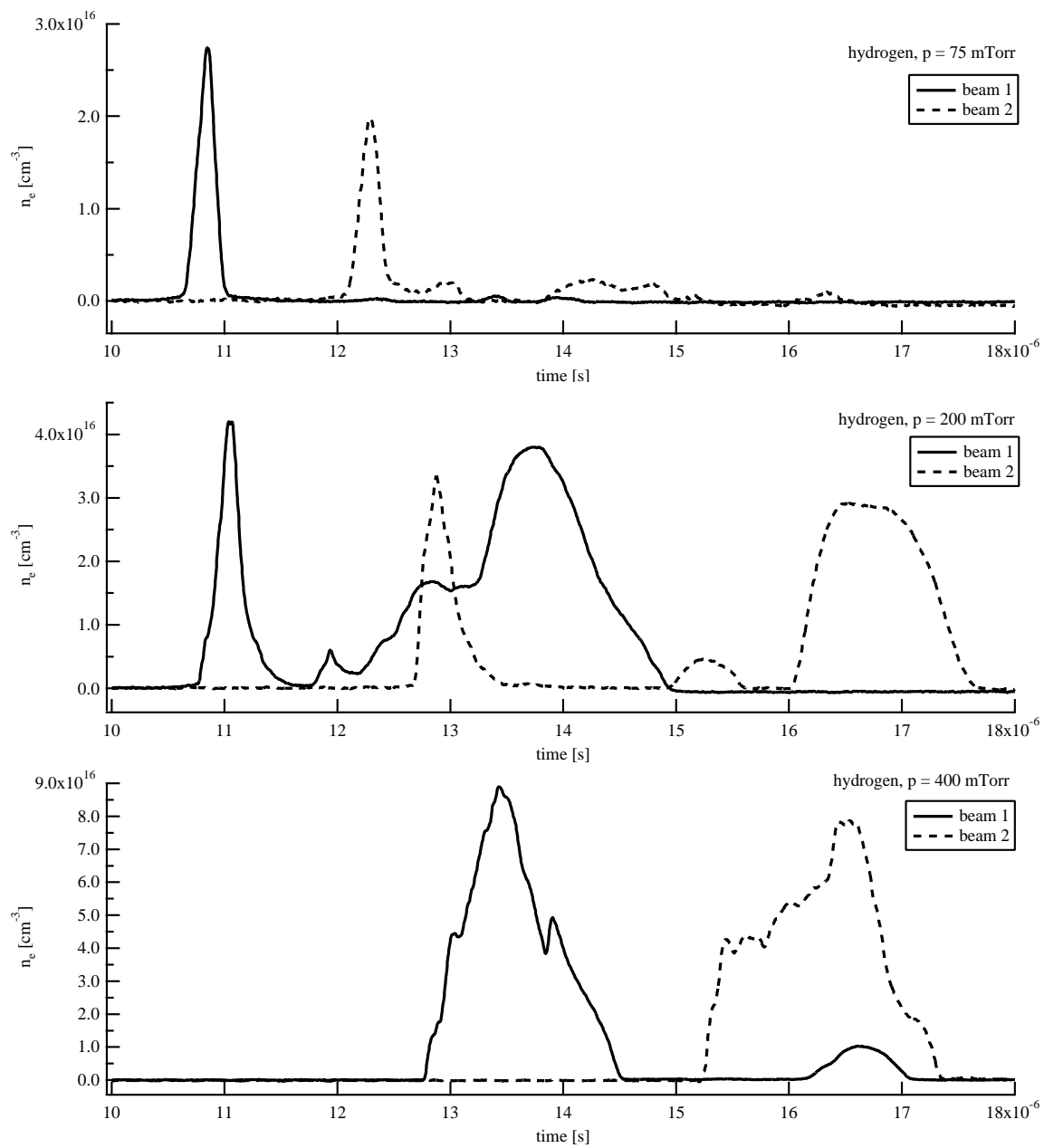


Figure C.10: Electron density histories for hydrogen using interferometer in configuration 1.

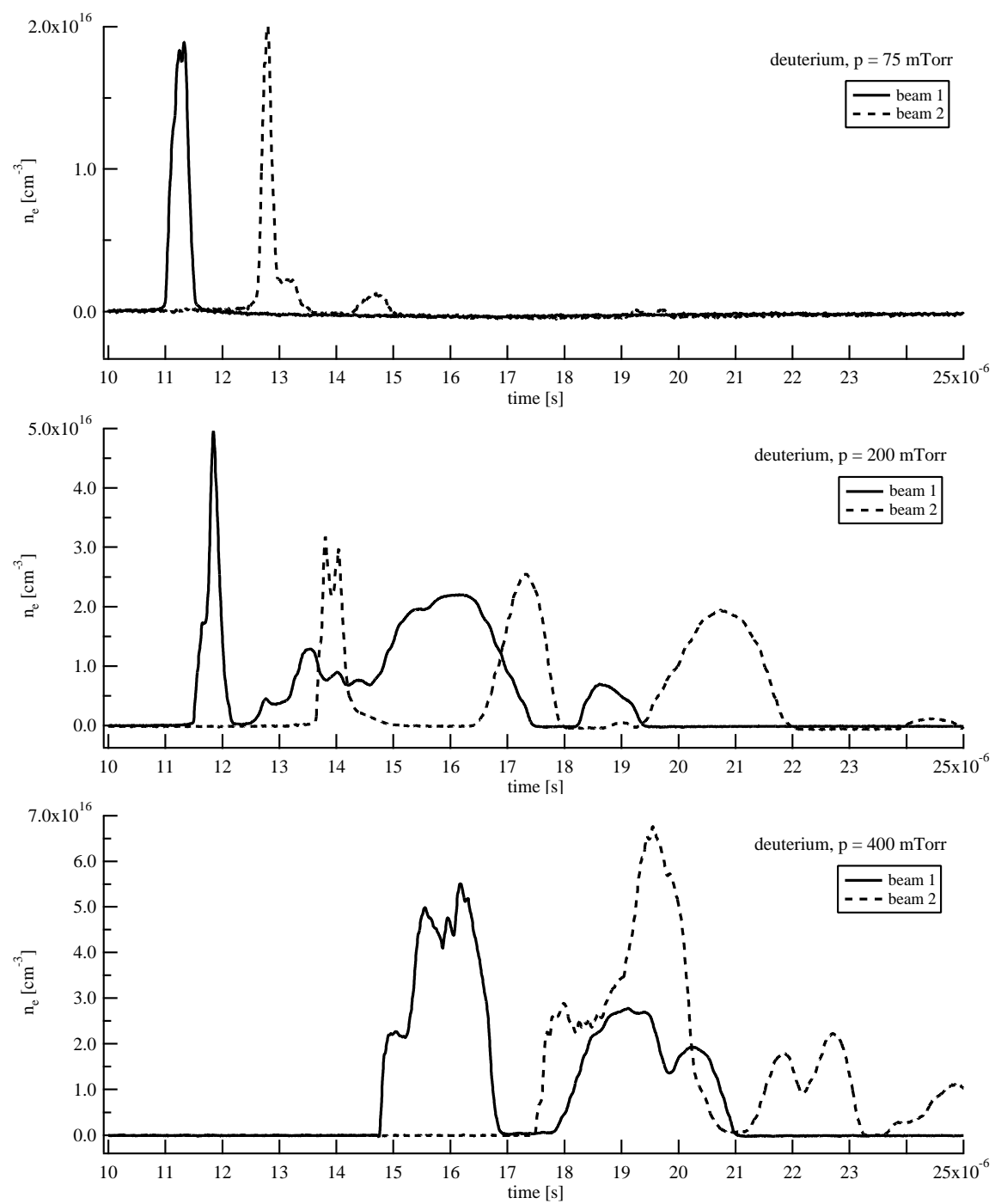


Figure C.11: Electron density histories for deuterium using interferometer in configuration 1.

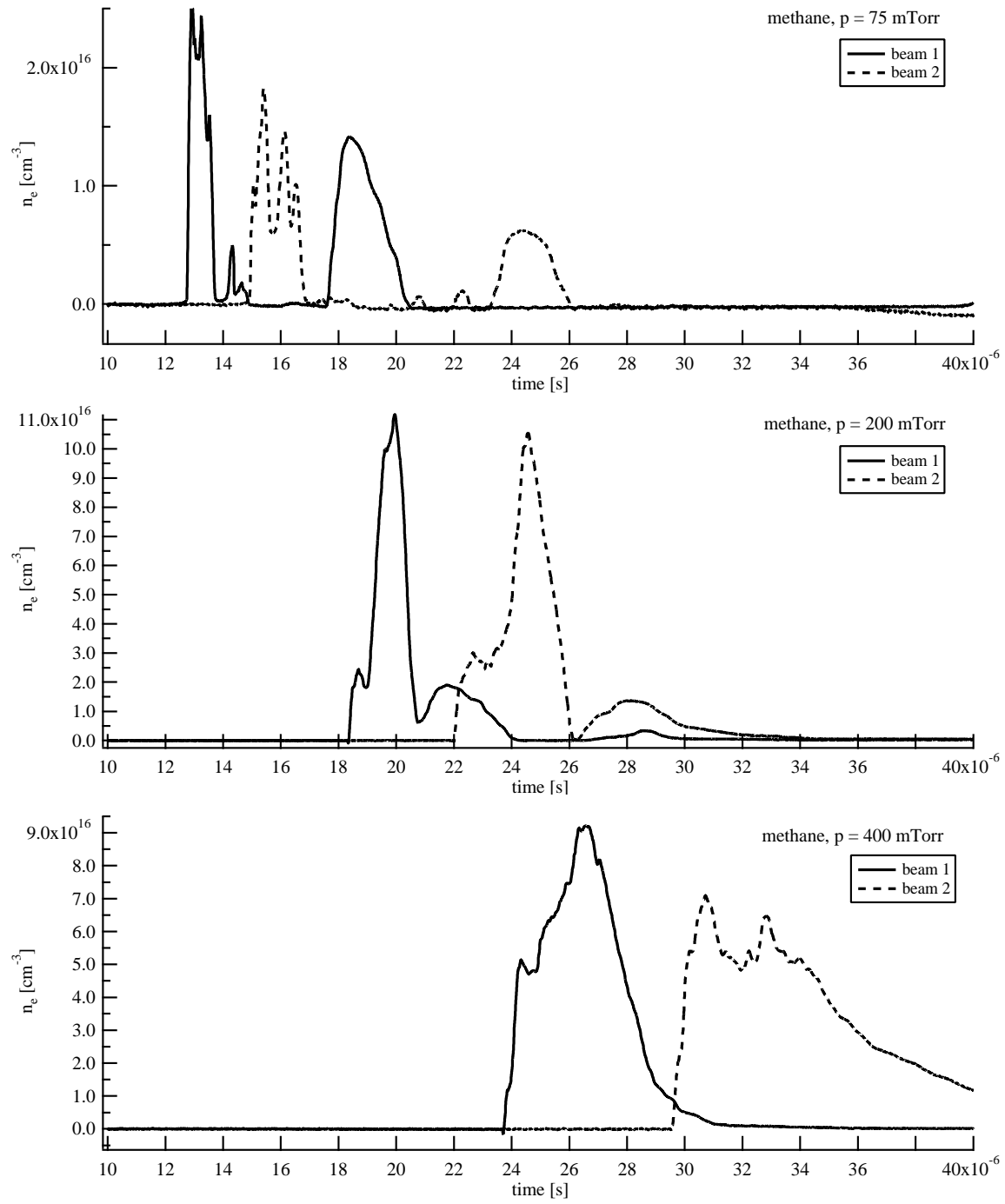


Figure C.12: Electron density histories for methane using interferometer in configuration 1.

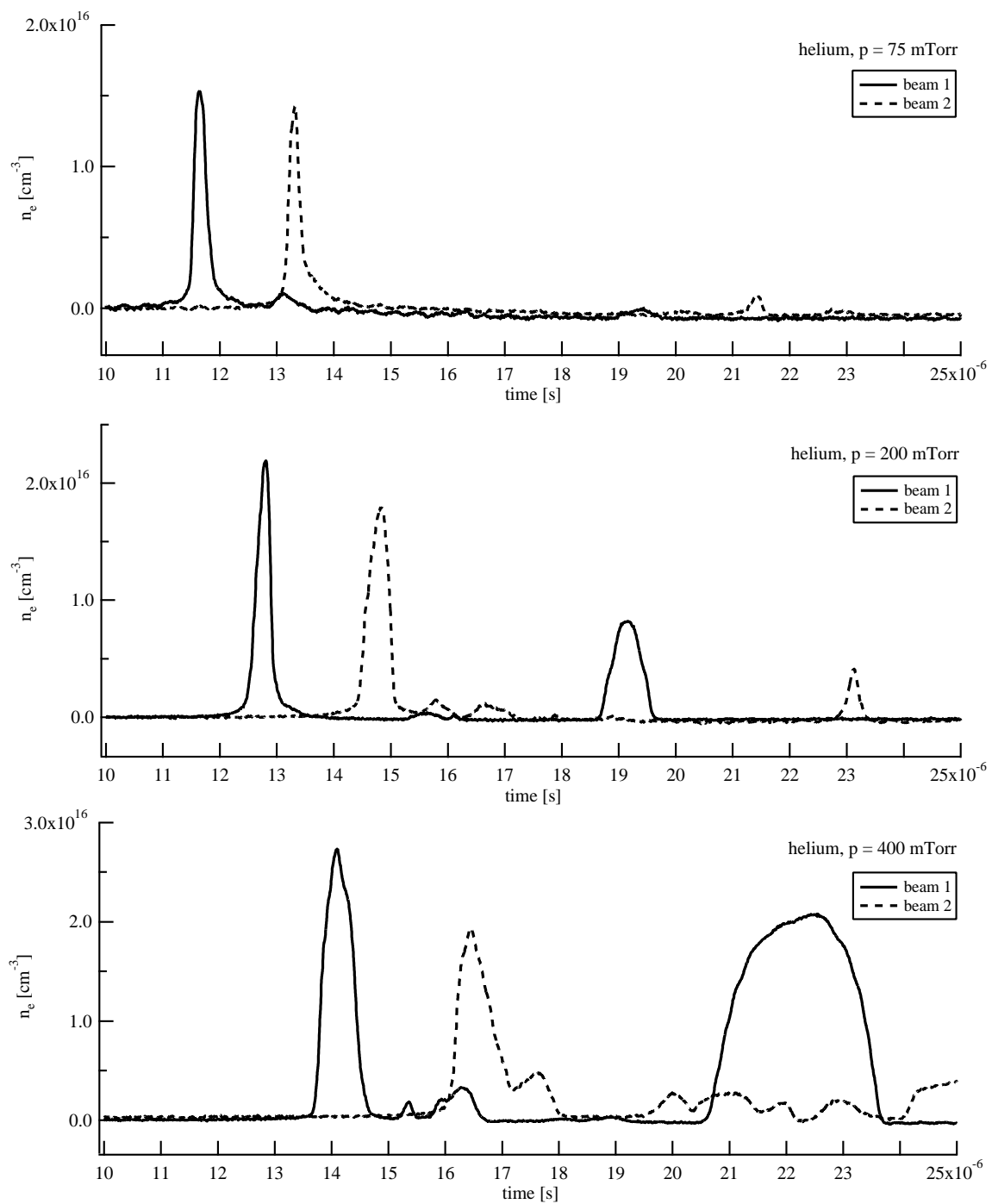


Figure C.13: Electron density histories for helium using interferometer in configuration 1.

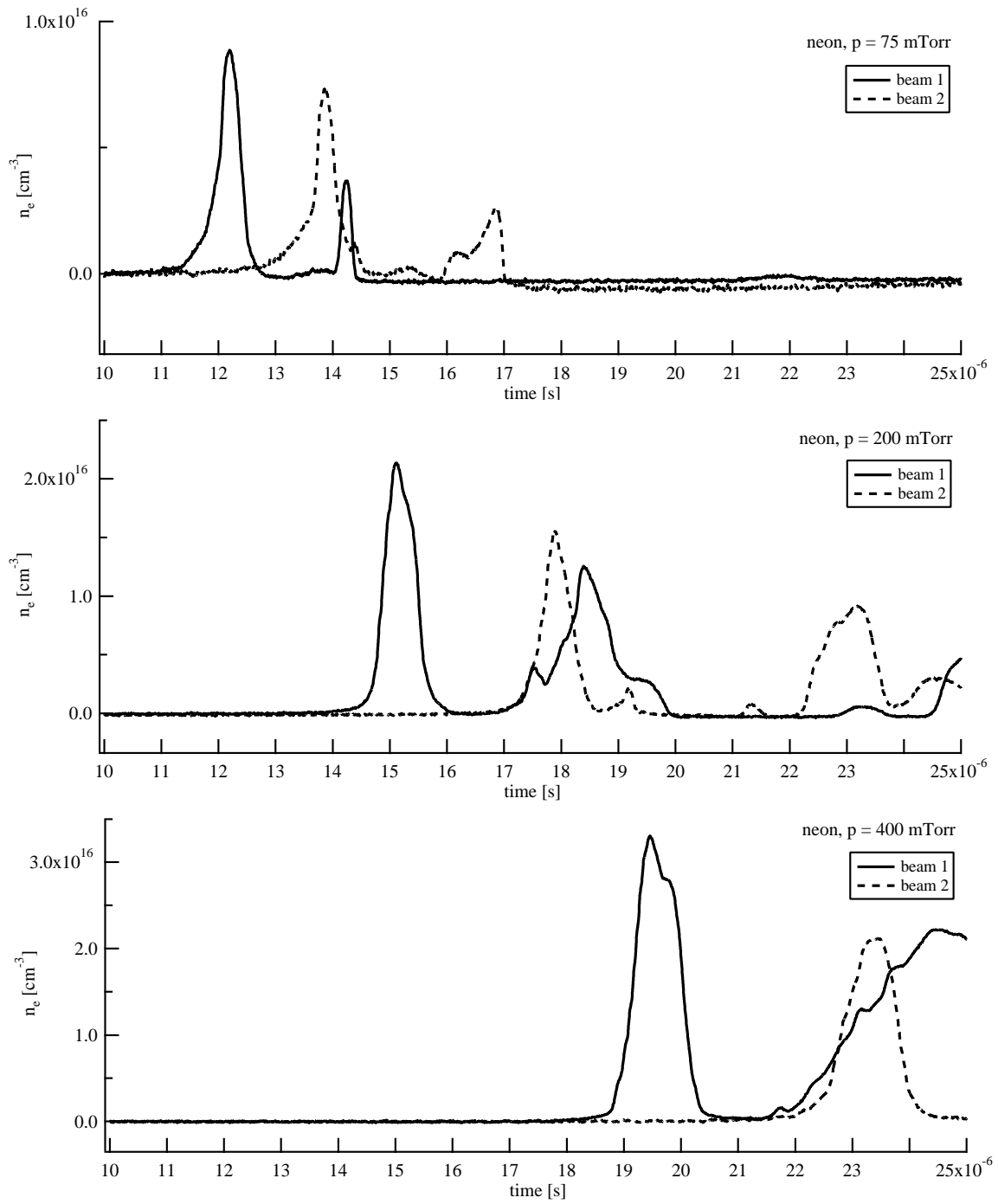


Figure C.14: Electron density histories for neon using interferometer in configuration 1.

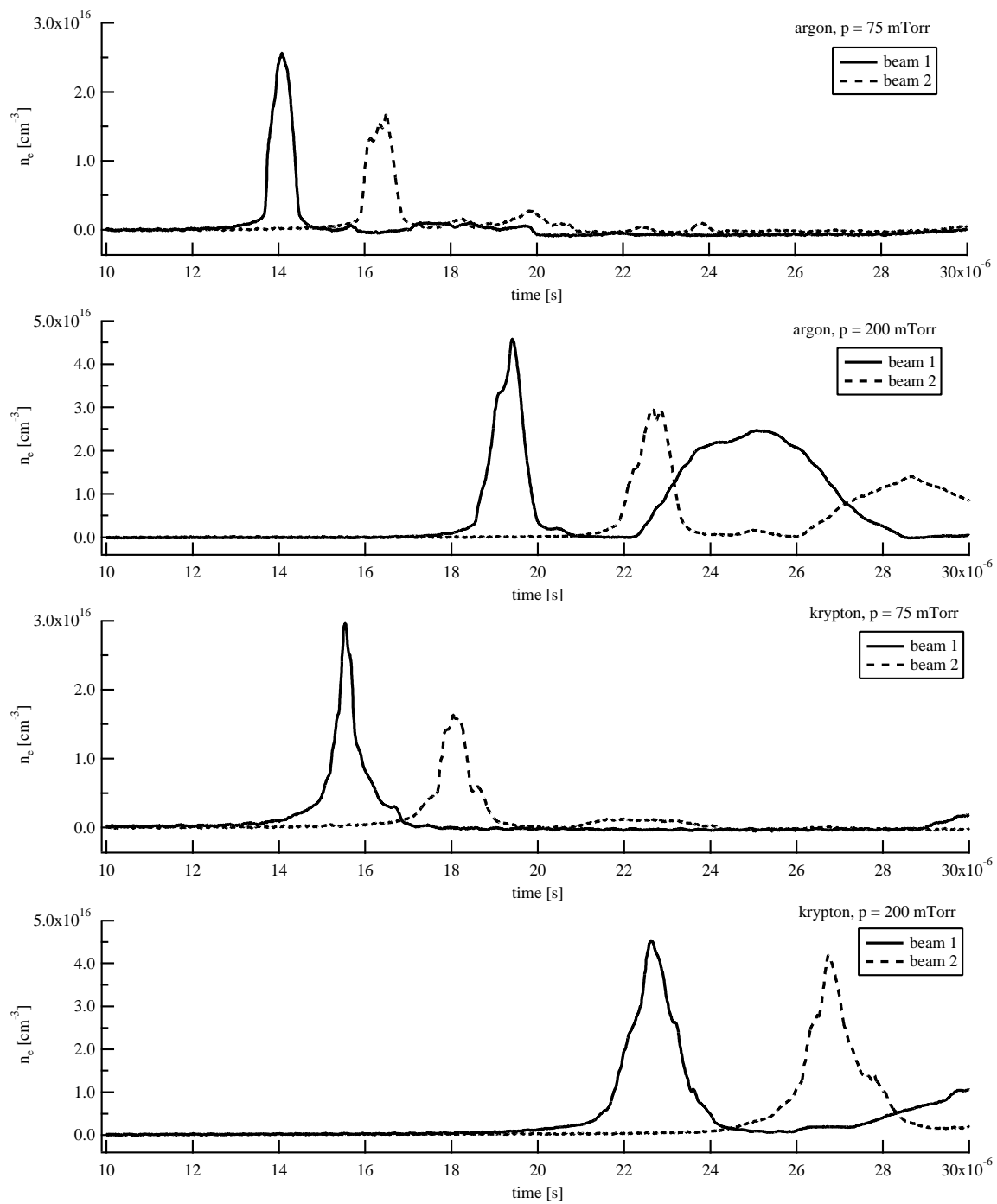


Figure C.15: Electron density histories for argon and krypton using interferometer in configuration 1.

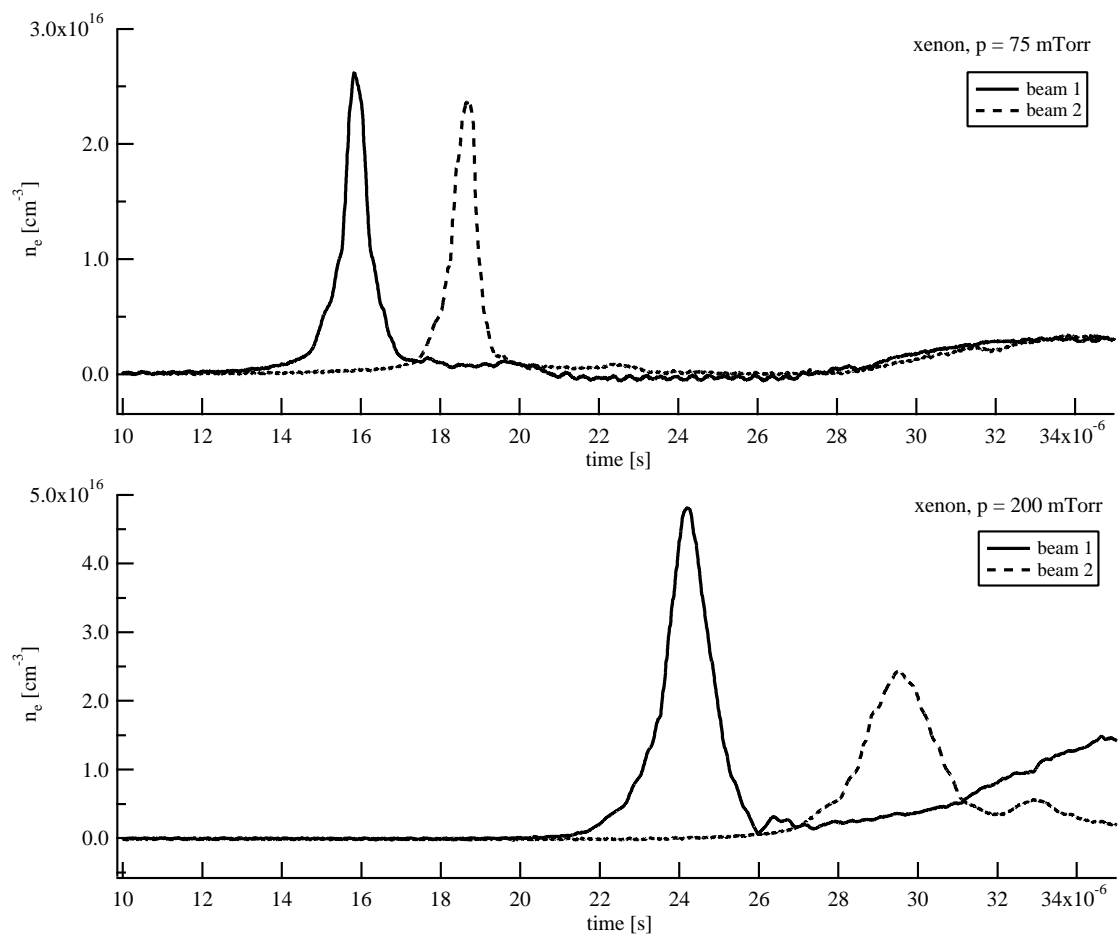


Figure C.16: Electron density histories for xenon using interferometer in configuration 1.

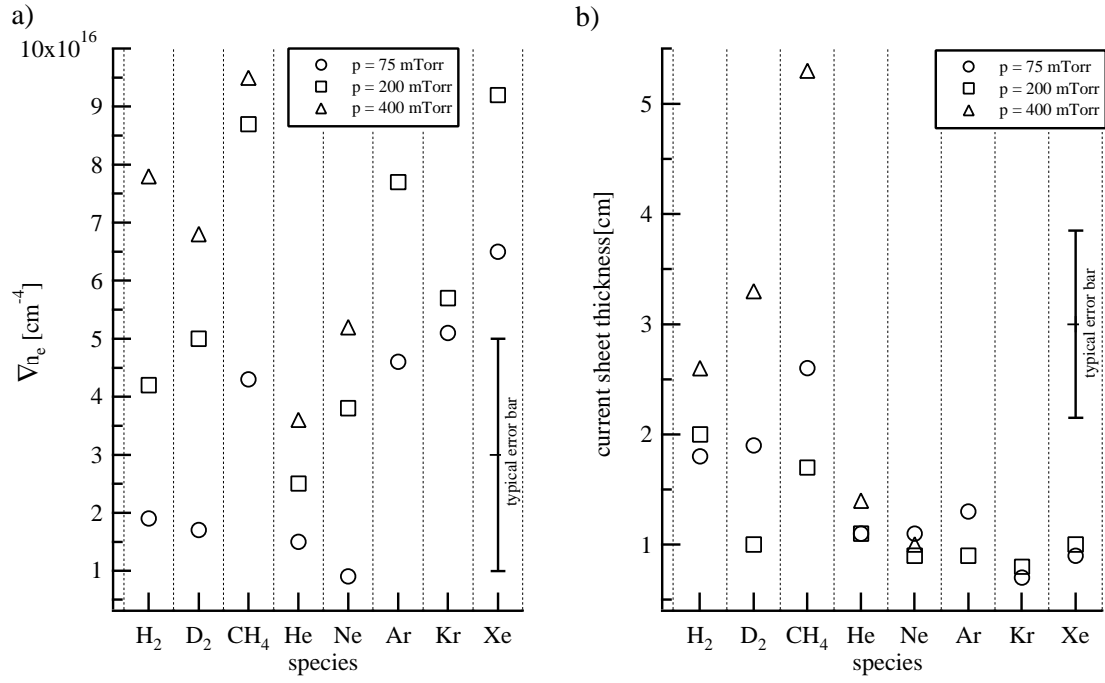


Figure C.17: Interferometric data from upstream laser beam in configuration 1: a) peak electron density gradient, b) current sheet thickness (full width at half maximum electron density).

C.5 Emission Spectroscopy

Figures C.18 and C.19 show the results of the time-integrated emission spectroscopy study. The calibrated intensity of optical emission from the CSCX accelerator between 3500-8500 Å is plotted for hydrogen, helium, neon, argon, krypton and xenon. Dominant lines are tabulated in table C.5 along with the corresponding species which was the source of the radiation.

Table C.5 lists the argon atomic structure data that was used to calculate the electron temperature, as elaborated upon in section 5.6.2.

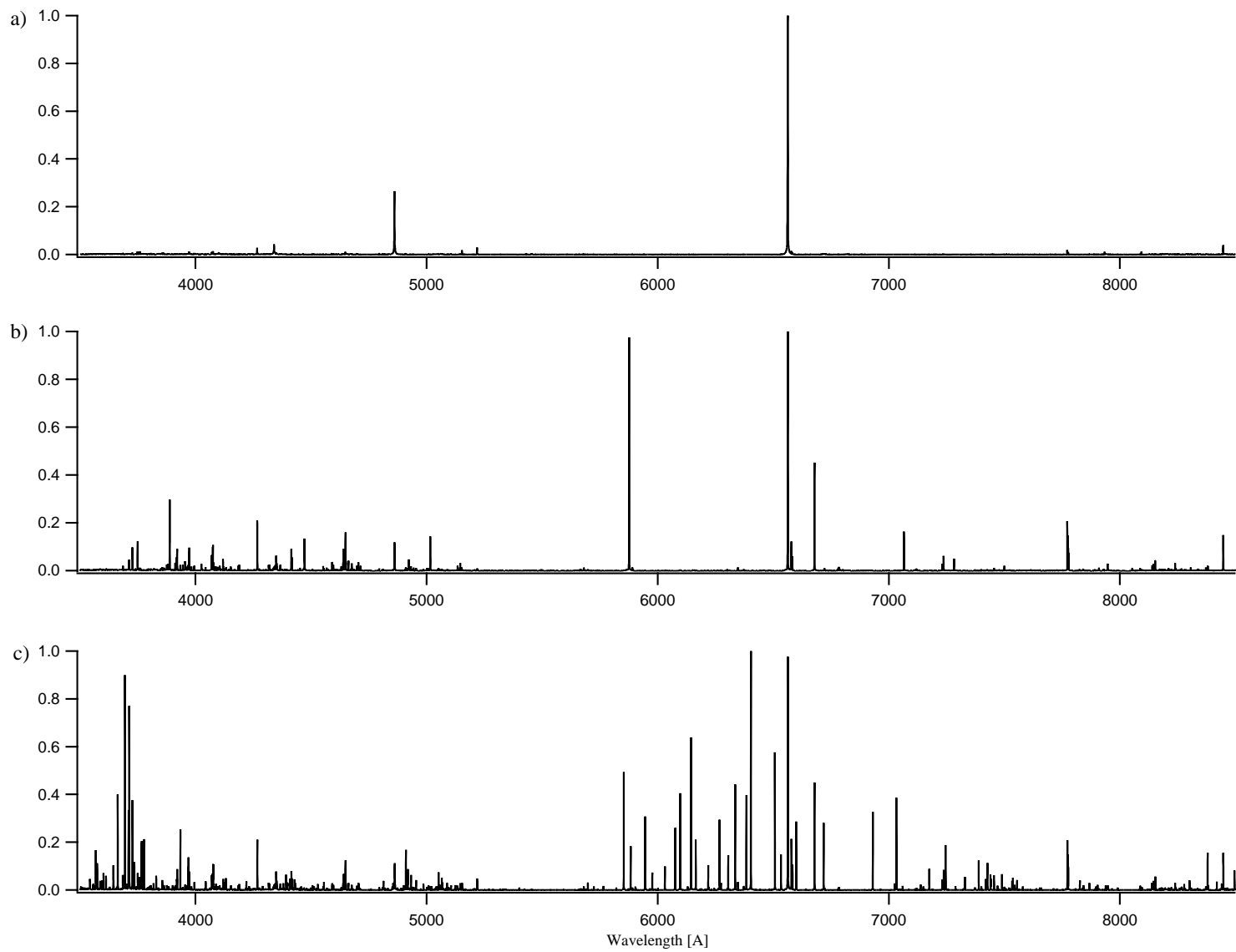


Figure C.18: Survey of spectral lines: a) Hydrogen, b) Helium, c) Neon.

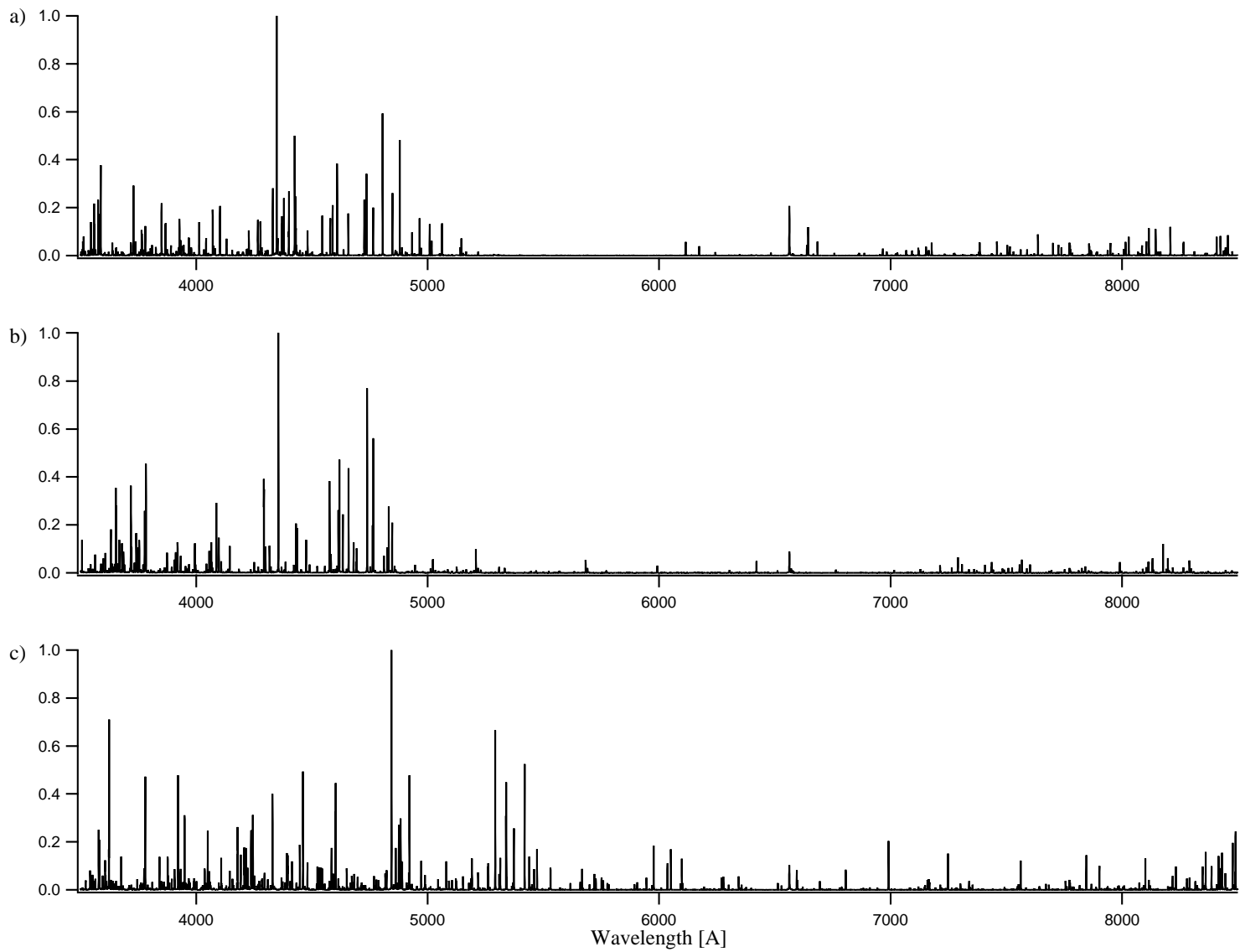


Figure C.19: Survey of spectral lines: a) Argon, b) Krypton, c) Xenon.

species	line [Å]	species	line [Å]	species	line [Å]	species	line [Å]	species	line [Å]	species	line [Å]
hydrogen		Ne I	6096.16	Ar II	4072.39	Kr II	3721.35		3877.10	Xe II	6051.15
H I	4861.33	Ne I	6143.06	Ar II	4103.91	Kr II	3741.64		3922.10	Xe II	6097.59
H I	6562.72	Ne I	6163.59	Ar II	4228.16	Kr II	3744.80		3950.30	H I	6562.72
H I	6562.85	Ne I	6217.28	Ar II	4266.29	Kr II	3754.25		4049.60	Xe II	6990.88
		Ne I	6304.79	Ar II	4266.53	Kr II	3778.09		4108.50		7248.10
helium		Ne I	6334.43	Ar II	4277.53	Kr II	3783.10		4179.10		7562.00
	3479.80	Ne I	6382.99	Ar II	4331.20	Kr II	3920.08	Xe II	4180.10		7845.40
He I	3888.65	Ne I	6402.25	Ar II	4348.06	Kr II	3994.84	Xe II	4193.15		7901.30
	4075.30	Ne I	6506.53	Ar II	4371.33	Kr II	4065.13	Xe II	4208.48		8100.00
	4267.00	Ne I	6532.88	Ar II	4379.67	Kr II	4088.34	Xe II	4209.47	Xe I	8231.64
He I	4471.48	H I	6562.72	Ar II	4400.10	Kr II	4098.73	Xe II	4213.72	Xe II	8347.24
He I	4471.68	H I	6562.85	Ar II	4400.99	Kr II	4145.12	Xe II	4215.60		8360.50
	4648.80	Ne I	6578.28	Ar II	4426.00	Kr II	4292.92	Xe II	4238.25		8385.50
H I	4861.33		6583.10	Ar II	4430.19	Kr II	4300.49		4243.90		8416.60
He I	5015.68	Ne I	6598.95	Ar II	4431.00	Kr II	4317.81	Xe II	4245.38		8431.20
He I	5875.62	Ne I	6678.28	Ar II	4481.81	Kr II	4355.48	Xe II	4330.52		8476.90
He I	5875.97		6717.40	Ar II	4545.05	Kr II	4431.69	Xe II	4393.20		8490.00
H I	6562.72	Ne I	6929.48	Ar II	4579.35	Kr II	4436.81	Xe II	4395.77		
H I	6562.85	Ne I	7032.41	Ar II	4589.90	Kr II	4475.01	Xe II	4448.13		
He I	6577.70	Ne I	7245.18	Ar II	4609.57	Kr II	4577.21	Xe II	4462.19		
He I	6678.15		7389.00	Ar II	4657.90	Kr II	4615.29	Xe II	4480.86		
He I	7065.19		7426.80	Ar II	4726.87	Kr II	4619.17		4523.60		
He I	7065.71		7772.60	Ar II	4735.91	Kr II	4633.89		4584.90		
	7772.00		7774.80	Ar II	4764.87	Kr II	4658.88		4602.50		
	7774.30		7776.00	Ar II	4806.02	Kr II	4680.41		4843.29		
	8446.70		8378.90	Ar II	4847.81	Kr II	4694.36		4861.90		
			8446.90	Ar II	4879.86	Kr II	4739.00		4876.20		
neon				Ar II	4965.08	Kr II	4762.44		4883.10		
Ne II	3568.50	argon		Ar II	5009.33	Kr II	4765.74		4886.90		
Ne II	3574.18	Ar II	3545.85	Ar II	5062.04	Kr II	4825.18		4889.70		
Ne II	3574.61		3558.90	H I	6562.85	Kr II	4832.08		4921.10		
Ne II	3643.93	Ar II	3559.51	Ar II	6643.70	Kr II	4846.61	Xe II	4972.71		
Ne II	3664.07	Ar II	3561.03	Ar II	8115.31	Kr II	5208.32	Xe II	5080.62		
Ne II	3694.21	Ar II	3576.62		8144.60		8176.60	Xe II	5191.37		
Ne II	3709.62	Ar II	3582.36		8208.20			Xe II	5260.44		
Ne II	3713.08	Ar II	3588.44			xenon		Xe II	5261.95		
Ne II	3727.11	Ar II	3729.31	krypton			3579.00	Xe II	5313.87		
	3735.20	Ar II	3765.27		3507.20		3583.10	Xe II	5339.33		
Ne II	3766.26	Ar II	3780.84	Kr II	3631.89		3606.70	Xe II	5372.39		
Ne II	3777.13	Ar II	3850.58	Kr II	3653.93		3622.90	Xe II	5419.15		
Ne I	5852.49	Ar II	3868.53	Kr II	3669.01		3623.90	Xe II	5438.96		
Ne I	5881.90	Ar II	3928.62	Kr I	3679.56		3676.00	Xe II	5472.61		
Ne I	5944.83	Ar II	4013.86	Kr II	3718.02		3780.50	Xe II	5976.46		
Ne I	6074.34	Ar II	4072.01	Kr II	3718.60		3841.50	Xe II	6036.20		

Table C.1: Dominant spectral lines in CSCX discharges.

species	line [Å]	E_m $\times 10^{-18}$ [J]	ω_{mn} $\times 10^{14}$ [s $^{-1}$]	A_{mn} $\times 10^8$ [s $^{-1}$]	g_m
Ar II	3576.62	3.6899	1.335	2.75	8
Ar II	3588.44	3.6793	1.331	3.03	10
Ar II	4348.06	3.1255	1.098	1.24	8
Ar II	4426.00	3.1340	1.079	0.83	6
Ar II	4806.02	3.0820	0.0993	0.78	6
Ar II	4879.86	3.1550	0.0978	0.78	6
Ar II	4904.75	3.3898	0.0973	0.045	8
Ar II	6643.70	3.1255	0.0719	0.167	8

Table C.2: Atomic structure data for argon which was used in the electron temperature analysis[54].

Appendix D

THEORY DETAILS

This appendix provides derivation details for analytical expressions used in various chapters of the thesis.

D.1 Emission spectroscopy electron temperature calculation

For an "optically thin" plasma of depth l along the line of sight, the spectrally integrated emission line intensities are given by[34]

$$\begin{aligned} i_{nm} &= \int I_{nm}(\omega) d\omega \\ &= \frac{\hbar\omega_{mn}}{4\pi} A_{nm} \int_0^l N_m dx \\ &\approx \frac{\hbar\omega_{mn}}{4\pi} A_{nm} N_m l . \end{aligned} \tag{D.1}$$

If LTE prevails, then the population of the m^{th} energy level is given by the Boltzmann distribution:

$$\frac{N_m}{N} = \frac{g_m}{Z_a} \exp(-E_m/kT) , \tag{D.2}$$

where g_m , Z_a , and E_m are the statistical weight, partition function, and energy of the m^{th} energy level of the atom, respectively. Combining equations D.1 and D.2, we find

$$i_{nm} = \frac{\hbar\omega_{mn}A_{nm}Nl g_m}{4\pi Z_a} \exp(-E_m/kT) . \quad (\text{D.3})$$

Rearranging terms we find that the equation can be written in the linear form

$$y = ax + b , \quad (\text{D.4})$$

where,

$$\begin{aligned} y &= \ln \left(\frac{i_{nm}}{\omega_{mn}A_{nm}g_m} \right) \\ a &= -\frac{1}{kT} \\ x &= E_m \\ b &= \ln \left(\frac{\hbar N l}{4\pi Z_a} \right) . \end{aligned} \quad (\text{D.5})$$

Equation D.4 is used to interpret experimental data when the intensities of several lines from a single species are measured. Then, with knowledge of ω_{mn} , A_{nm} , and g_m for each transition, a plot of y versus x is constructed and linear fit of the experimental data is computed. The slope of this line gives the temperature and the y -intercept gives the number density. It should be noted that in order to calculate the number density, an *absolute* measurement of the intensity is required, while calculation of temperature requires only a *relative* measurement of intensity. Since calibration and measurement of absolute intensity is prohibitively difficult (especially for a target plasma that is moving at high speed, such as a propagating current sheet), only temperature measurements are attempted in the present study.

D.2 Laser interferometry electron density calculation

The simplest model of the plasma-EM wave interaction assumes a weak magnetic field and isotropic plasma, in which case it can be shown that[55]

$$n = \sqrt{1 - \frac{\omega_p^2}{\omega^2}} , \quad (\text{D.6})$$

where, ω_p is the plasma frequency and ω is the laser radiation frequency. Additionally, if $\omega_p \ll \omega$, the number density of electrons in terms of the measured phase shift is approximated by

$$n_e = \frac{2cn_c}{\omega l} \Delta\phi , \quad (\text{D.7})$$

where, c is the speed of light in vacuum, l is the physical length of the plasma through which the beam propagates, and n_c is the so-called cutoff density, above which the beam is reflected out of the plasma:

$$n_c \equiv \omega^2 m_e \epsilon_o / e^2 . \quad (\text{D.8})$$

In our particular implementation, equation D.7 reduces to

$$n_e = 2.78 \times 10^{15} \Delta\phi [\text{cm}^{-3}] . \quad (\text{D.9})$$

In the deriving the expressions above it has been tacitly implied that the inter-particle collisions and applied magnetic field do not significantly contribute to the current sheet of index refraction. An expression for the index of refraction which includes these effects is[56]:

$$n = \sqrt{1 - \frac{\omega_p^2}{\omega^2(1 \pm \omega_c/\omega)[1 + i(\nu/\omega)]}} , \quad (\text{D.10})$$

where ω_c is the electron cyclotron frequency and ν is the electron collision frequency. Referring to Fig. 6.1 we find $\omega_c \sim 10^{10}$ Hz and $\nu \sim 10^{11}$ Hz. Hence, since $\omega \sim 10^{14}$ Hz for a HeNe laser, equation D.10 reduces to D.6 – the collisional and magnetic field modifications of the index of refraction are expected to be small in CSCX current sheets.

Lastly, it can be shown that the contribution of bound electrons is expected to be small for a fully ionized plasma such as the CSCX current sheet[56]. In our experiment, if any appreciable concentration of neutral particles were present, we would expect to see them in a dense shock wave ahead of the current sheet. Since neutral atoms give a phase shift opposite to free electrons, the presence of a dense shock wave containing neutrals would result in a negative dip in the electron density just prior to the arrival of the current sheet. No such structure was observed in any of our plots.

D.2.1 Analysis of experimental waveforms

This section describes the procedure used in taking the raw data from the phase detection circuitry and transforming it into electron density profiles such as those shown in Fig. 5.13.

The output from the quadrature phase detection circuitry is two channels per laser beam (or detector) – the instantaneous sine and cosine of the phase. Then, the instantaneous phase angle is given by

$$\phi = \arctan \left(\frac{\sin \phi}{\cos \phi} \right) . \quad (\text{D.11})$$

Figure D.1 shows an example of the construction of an electron density profile from the raw output of the quadrature phase detector. In Fig. D.1a the raw detector sine and cosine signals are plotted. Figure D.1b shows the phase, which results from applying Eq. D.11 to the waveforms in D.1a. The phase ranges between $-\pi \leq \phi \leq \pi$. As the phase changes it discontinuously jumps as it crosses the polar axis ($\phi = \pm\pi$.) Since we are interested in the *total* phase change rather than the *instantaneous* phase angle, the individual segments (which are delineated by the sharp discontinuities) must be "stacked" in a manner that respects the direction of the phase change (i. e. , correctly records whether the phase is increasing or decreasing at the time of the jump.) This is done by noting the slope of

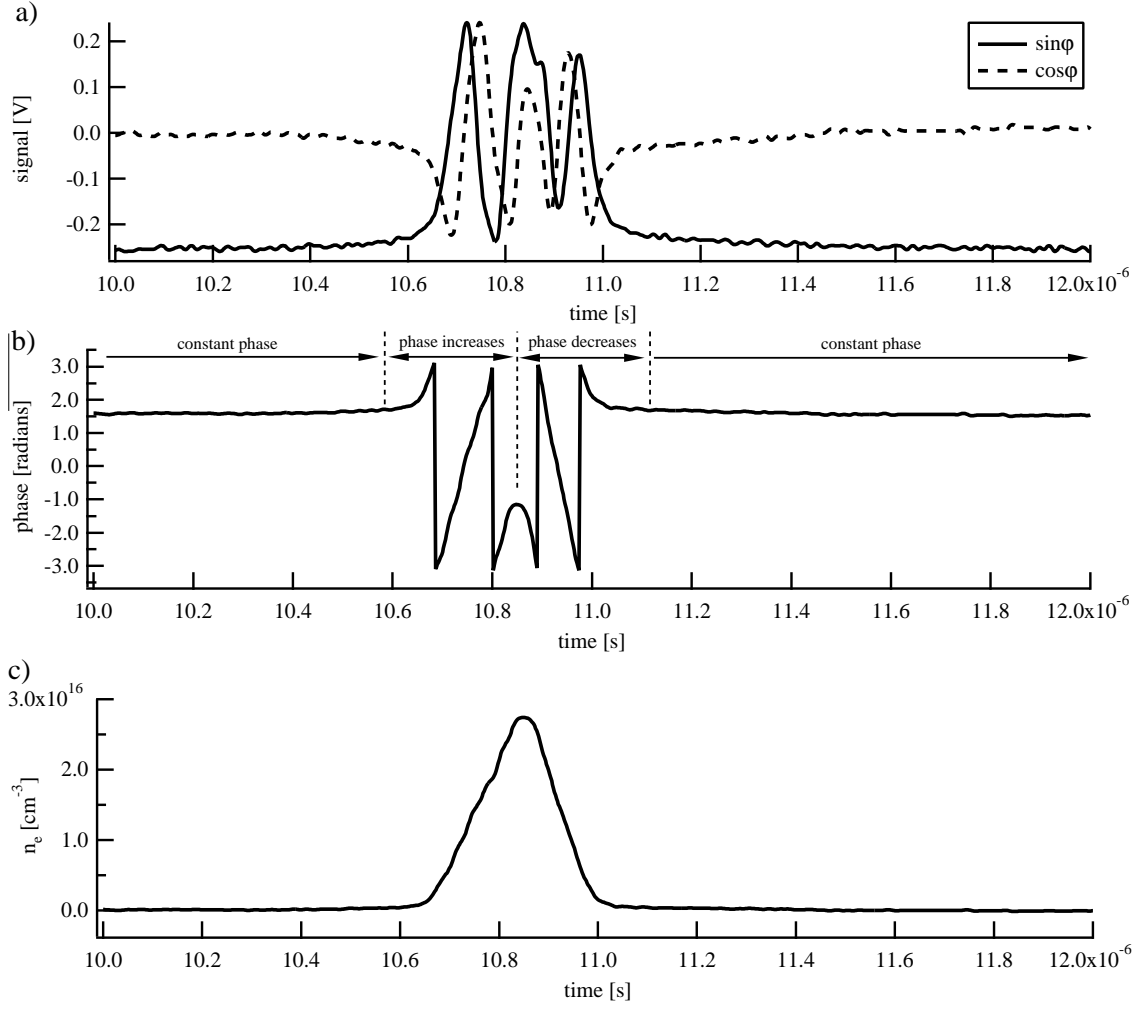


Figure D.1: Construction of an electron density profile from raw phase detector output (hydrogen, $p = 75$ mTorr, configuration 1, upstream beam): a) raw quadrature phase detector output, b) phase and c) electron density.

the phase just before the jump: positive pre-jump slope corresponds to increasing phase, negative pre-jump slope corresponds to decreasing phase. So, returning to Fig. D.1b, we see that the phase vector is initially at some arbitrary initial angle of about $\phi = \pi/2$. As the current sheet approaches the laser beam (at approximately $t = 10.6 \mu\text{s}$), the phase increases and crosses through $\phi = \pi$, whereupon the phase discontinuously jumps to $\phi = -\pi$. Since the slope of the phase was positive, we know that the jump was related to an increase in

phase as it crossed the polar axis. The phase goes through a similar positive-going jump at $t = 10.8 \mu\text{s}$. At approximately $t = 10.85 \mu\text{s}$ the phase reaches its maximum value and begins to decrease. After going through two negative-going phase changes, the phase returns to its original value of about $\phi = \pi/2$; this corresponds to the passing of the current sheet and the return of the optical path length to its original, unperturbed value. When the individual segments are properly stacked and the initial phase is subtracted out (this essentially removes the initial “DC offset”), the resulting waveform can be multiplied by the calibration constant given in Eq. D.9 to yield the desired electron density profile, as shown in Fig. D.1c. The process of performing all of the numerical manipulations of the raw data described above was automated; an Igor Pro[57] macro was written to quickly process the hundreds of experimental data files collected during the study.

Phase error resulting from high-density plasmas

When the electron density gradients are especially steep (as is the case near the cathode in the present study), the phase jumps described in the example above can occur at a rate that is comparable to or greater than the laser modulation frequency. In this case, the detector can completely fail to record one or more of the positive-going phase jumps as the phase vector “winds up.” When the phase vector “unwinds” on the back-side of the current sheet (which usually has less severe density gradients), the number of recorded negative-going phase jumps can be greater than the number of recorded positive-going phase jumps. As a result, when the segments are stacked to construct the total phase change waveform, the post-current-sheet phase will not return to the pre-current-sheet value as described in the example above but, rather, it will relax to a negative value – which is clearly un-physical.

The example illustrated in Fig. D.1 is actually representative of a case where the phase detector was pushed to near its frequency limit (the phase jumps are seen to occur at about

10 MHz in frequency.) When the the laser beam (in the same configuration as in Fig. D.1) was exposed to a hydrogen-plasma current sheet in a $p = 400$ mTorr pre-fill pressure, the phenomenon described in the previous paragraph was observed in many of the recorded shots. This is illustrated in Fig. D.2, where the calculated electron density is seen to (unphysically) go negative after the current sheet has passed. An accurate measurement of the peak electron density is not possible using such waveforms but, one can make a rough accounting of the missed positive phase shifts, assuming there were no concomitant missed negative phase shifts; in this case the corrected peak electron density can be estimated to be

$$n_{e_{max}}^{corrected} \geq n_{e_{max}} + |n_{e_{min}}| . \quad (D.12)$$

There are two ways to work around this problem. First, the "double pass" configuration can be realigned so that the laser passes through the plasma only once, rather than being retro-reflected back through it. Second, the modulation frequency can be increased. In addition to requiring a new Bragg cell and RF power supply, this would involve replacing many of the (frequency sensitive) components in the phase detector as well and, hence, would be rather expensive.

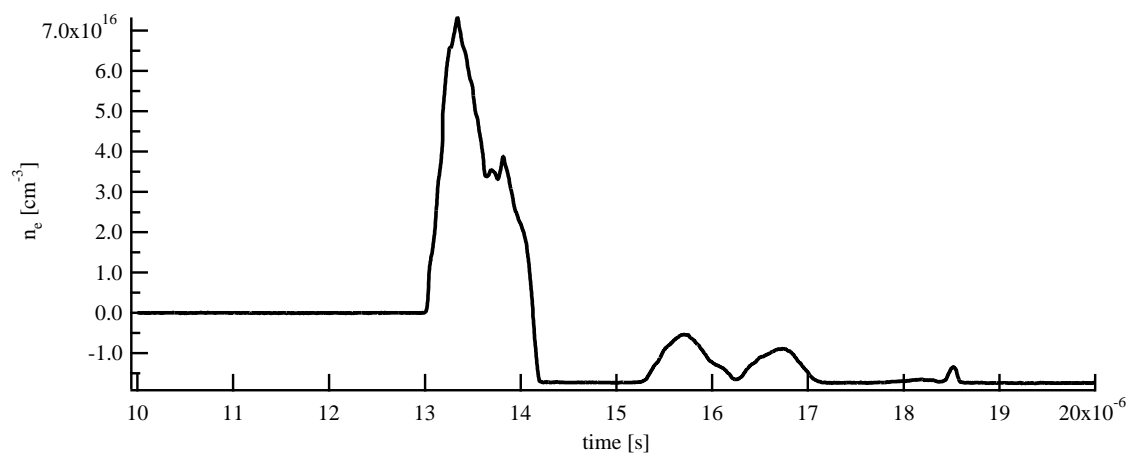


Figure D.2: Example of a case where $d\phi/dt$ exceeded the frequency response of the phase detector(hydrogen, $p = 400$ mTorr, configuration 1, upstream beam.)

Appendix E

UNCERTAINTY ANALYSIS

In any report of experimental error there is a certain degree of subjectivity in the procedure which is used to quantify the uncertainty in a measurement. In the present study most of the experiments can be described as “small sample” experiments, i.e., too few data points were taken to characterize the data as an adequate representation of a continuous distribution and, hence, it is improper to use the usual continuum definitions of uncertainty measures, such as the continuum standard deviation. Therefore, algorithms which account for the finite number of data points must be applied. In order to avoid ambiguity, the sections which follow define the algorithms used in this study to quantify uncertainty. The methods used closely follow those suggested by the ISO standard[58] and which are elaborated upon further by Coleman and Steele[59].

The remainder of this appendix is divided into two major sections. The first defines how the uncertainty in a single *measured* value was calculated. The next section describes the uncertainty in quantities that were *calculated* from multiple, unrelated measurements.

E.1 Definitions

It is useful, in one place, to first define a few terms that will be used in the remainder of this appendix:

Sample (x_i): A single data point taken from the set x .

Sample mean (\bar{x}):

$$\bar{x} = \frac{1}{N} \sum_{i=1}^N x_i . \quad (\text{E.1})$$

Number of Samples (N): The number of samples (data points) in a set.

Degrees of freedom (ν): The number of degrees of freedom in the data set:

$$\nu = N - 1 . \quad (\text{E.2})$$

Sample standard deviation (S_x):

$$S_x = \left[\frac{1}{N-1} \sum_{i=1}^N (x_i - \bar{x})^2 \right]^{1/2} . \quad (\text{E.3})$$

Assume an observable quantity X (temperature, for example) is measured and the data is contained in the set x . To accurately quantify a measured value, the minimum amount of information that can be given when reporting the value of X is: 1) the mean value (i.e., the average of the measured values (\bar{x})), 2) the range over which the reported value may vary (U) (i. e. , the "error bar"), and 3) the degree of confidence that any subsequent measurements will fall within the reported error bar (c). Our task is then, for a given set of data x , to find U for the desired level of confidence c . The results of the experiment are then reported in the form

$$X_c = \bar{x} \pm U . \quad (\text{E.4})$$

E.2 Uncertainty Analysis for a Measured Value

E.2.1 Random Uncertainty

The random uncertainty arises from the natural "spread" in data points which results from the inability to construct a perfectly reproduceable experiment, or from the observation of some intrinsically stochastic physical phenomenon. For a finite set of data points x , the random uncertainty, U_x^R , is defined by

$$U_x^R = tS_x \quad (\text{E.5})$$

The parameter t is tabulated as a function of ν in Table E.1 for a 90% confidence level. The table shows that t , and hence the random uncertainty, decreases as the number of data points increases.

E.2.2 Systematic Uncertainty

The systematic error is the instrumental error associated with the measurement device. This error is *fixed* and can be (at least partially) removed through calibration. Although calibration procedures reduce the systematic error, it cannot be eliminated because of the

Table E.1: Values of the random uncertainty parameter t as a function of ν for a 90% confidence level[59].

ν	t	ν	t	ν	t	ν	t	ν	t	ν	t
1	6.314	7	1.895	13	1.771	19	1.729	25	1.708	40	1.684
2	2.920	8	1.860	14	1.761	20	1.725	26	1.706	60	1.671
3	2.353	9	1.833	15	1.753	21	1.721	27	1.703	120	1.658
4	2.132	10	1.812	16	1.746	22	1.717	28	1.701	∞	1.645
5	2.015	11	1.796	17	1.740	23	1.714	29	1.699		
6	1.943	12	1.782	18	1.734	24	1.711	30	1.697		

intrinsic error associated with the calibration source (i.e., the calibration source comes with its own calibration uncertainty). Two situations arose in the present study with regard to quantifying the systematic uncertainty: 1) we built and calibrated some instruments, and 2) some instruments were purchased and came with calibration (and associated uncertainty) information) from the manufacturer.

In instruments that we calibrated ourselves, we defined the systematic error in the subsequent use of that instrument as the random error which was observed while taking data from a known (calibration) source:

$$U_x^S = tS_x \quad . \quad (\text{E.6})$$

In situations where the instrument was not calibrated as part of this study but, rather, the data calibration data was provided by the instrument's manufacturer, the systematic uncertainty was simply taken as

$$U_x^S = E \quad , \quad (\text{E.7})$$

where E was the published instrumental error.

In the next section we show how the total uncertainties in our measurements were calculated. To do so the number of degrees of freedom in the systematic uncertainty (ν_x^S) must be known. For instruments that we calibrated, the value of ν_x^S is self-evident. However, the appropriate value of ν_x^S to use for systematic error reported by instrument manufacturers is not clear. The *Guide* suggest using the following definition:

$$\nu_x^S \approx \frac{1}{2} \left(\frac{\Delta U_x^S}{U_x^S} \right)^{-2} \quad , \quad (\text{E.8})$$

where $\Delta U_x^S / U_x^S$ is generally specified as a percentage by the manufacturer (e.g., the value indicated by a meter may have an indicated uncertainty of, say, $\pm 10\%$, in which case we take $\Delta U_x^S / U_x^S = 0.1$ and, hence, $\nu_x^S = 50$).

E.2.3 Total Uncertainty

To establish an "error bar" for the reported data, we need to combine the systematic and random uncertainties in some manner. The methodology suggested in the *Guide* is to define the overall or *expanded uncertainty* as

$$U_{\%}^T = t_{\%} \sqrt{(S_x^R)^2 + (S_x^S)^2} , \quad (\text{E.9})$$

where S_x^R is the standard deviation of the random error associated with the measurement of the observable X and S_x^S is the standard deviation of the systematic error of the device used to carry out the measurement. The % subscripts on U^T and t indicate the degree of confidence; for example, if the the degree of confidence is 90%, then in the reporting of data the total uncertainty would be labelled U_{90}^T .

To determine $t_{\%}$ we must use a value of ν that simultaneously reflects the degrees of freedom of both the systematic and random errors. Again, the *Guide* suggests that the effective number of degrees of freedom, ν_x^T , for determining the t value can be approximated by the Welch-Satterthwaite formula:

$$\nu_x^T = \frac{((S_x^R)^2 + (S_x^S)^2)^2}{(S_x^R)^4/\nu_x^R + (S_x^S)^4/\nu_x^S} , \quad (\text{E.10})$$

where ν_x^R is the number of degrees of freedom associated with the random uncertainty and ν_x^S is the number of degrees of freedom associated with the systematic uncertainty.

E.3 Uncertainty Analysis for a Calculated Value

In many cases the physical quantity that we wish to determine in an experiment is not measured directly but, rather, it is *derived* from other measured parameters via a theoretical model. For example, to determine the gas density we might measure the pressure and temperature and then use the ideal gas equation of state to infer the density. The question is

then, from an uncertainty point of view, how do we combine the uncertainty in the temperature and pressure measurements to obtain a measure of the uncertainty in the density?

There are many ways to answer this question; the answer depends on the number of tests conducted, the desired degree of confidence, etc.. In this study the techniques used are applicable to an experiment where a small number of samples were collected (less than ten). The formalism presented in the *Guide*, however, is general, and can be applied to large sample experiments as well.

Consider a derived quantity, r , that is a function of j observables (X_i):

$$r = r(X_1, X_2, \dots, X_j) . \quad (\text{E.11})$$

The overall uncertainty in the value of r is

$$U_r^T = \sqrt{(U_r^R)^2 + (U_r^S)^2} , \quad (\text{E.12})$$

where,

$$U_r^R = t S_r^R = t \left(\sum_{i=1}^j \theta_i^2 (S_{x_i}^R)^2 \right)^{1/2} , \quad (\text{E.13})$$

and

$$U_r^S = t \left(\sum_{i=1}^j \theta_i^2 (S_{x_i}^S)^2 + 2 \sum_{i=1}^{j-1} \sum_{k=i+1}^j \theta_i \theta_k S_{x_i}^S S_{x_k}^S \right) , \quad (\text{E.14})$$

$$\theta_i = \frac{\partial r}{\partial X_i} . \quad (\text{E.15})$$

The second term in Eqn. E.14 is the so-called systematic correlation uncertainty. This type of uncertainty arises when there is a correlation between two of the measurement devices (for example, when two different instruments are calibrated using the same calibration source.) If there is no cross-correlation, then this term may be set to zero. To determine t , the effective degrees of freedom are determined from the following form of the Welch-

Satterthwaite formula:

$$\nu_r^T = \frac{\left\{ \sum_{i=1}^j [(\theta_i S_{x_i}^R)^2 + (\theta_i S_{x_i}^S)^2] \right\}^2}{\sum_{i=1}^j [(\theta_i S_{x_i}^R)^4 / \nu_{x_i}^R + (\theta_i S_{x_i}^S)^4 / \nu_{x_i}^S]} . \quad (\text{E.16})$$

Appendix F

EQUIPMENT SPECIFICATIONS

F.1 Pearson 301X Current Monitor[1]

Output = 0.01 V/A
Max Peak Current = 50 kA
Usable Rise Time = 200 ns
3dB Point (low) = 5 Hz
3dB Point (high) = 2 MHz .

F.2 Tektronix P6015A High Voltage Probe[2]

Attenuation = 1000X
Bandwidth = 75 MHz
Usable Rise Time = 4 ns .

Bibliography

- [1] Pearson Electronics Inc. *www.pearsonelectronics.com*. 2000.
- [2] Tektronix Inc. *www.tek.com*. 2000.
- [3] J. Marshal. Performance of a hydromagnetic plasma gun. *The Physics of Fluids*, 3(1):134–135, January-February 1960.
- [4] R.G. Jahn. *Physics of Electric Propulsion*. McGraw-Hill Book Company, 1968.
- [5] D.R. Keefer and B. Rhodes. Electromagnetic acceleration in pulsed plasma thrusters. In *25th International Electric Propulsion Conference*, Cleveland, OH, August 1997. IEPC 97-035.
- [6] K.A. Polzin, E.Y. Choueiri, P. Gurfil, and N.J. Kasdin. Multiple plasma propulsion options for multiple terrestrial planet finder architectures. *Submitted for publication: Journal of Spacecraft and Rockets*, 2002.
- [7] R.G. Jahn K.E. Clark. Quasi-steady plasma acceleration. In *AIAA 7th Electric Propulsion Conference*, Williamsburg, Virginia, March 3-5 1969. AIAA 69-267.
- [8] P.J. Turchi and R.L. Burton. Pulsed plasma thruster. *J. Propulsion and Power*, 14(5):716–735, Sept.-Oct. 1998.

- [9] J.K. Ziemer, E.A. Cubbin, E.Y. Choueiri, and D. Birx. Performance characterization of a high efficiency gas-fed pulsed plasma thruster. In *33rd Joint Propulsion Conference*, Seattle, Washington, July 6-9 1997. AIAA 97-2925.
- [10] J.K. Ziemer, E.Y. Choueiri, and D. Birx. Is the gas-fed ppt an electromagnetic accelerator? an investigation using measured performance. In *35th AIAA Joint Propulsion Conference*, Los Angeles, CA, June 20-23 1999. AIAA-99-2289.
- [11] J.K. Ziemer and E.Y. Choueiri. Scaling laws for electromagnetic pulsed plasma thrusters. *Plasma Sources Science and Technology*, 10(3):395–405, August 2001.
- [12] J.K. Ziemer. A review of gas-fed pulsed plasma thruster research over the last half-century. EPPDyL internal report, Princeton University, 2000.
- [13] T.E. Markusic and E.Y. Choueiri. Visualization of current sheet canting in a pulsed plasma accelerator. In *26th International Electric Propulsion Conference*, Kitakyushu, Japan, October 17-21 1999. IEPC 99-206.
- [14] L.C. Burkhardt and R.H. Lovberg. Current sheet in a coaxial plasma gun. *The Physics of Fluids*, 5(3):341–347, March 1962.
- [15] R.L. Burton. *Structure of the Current Sheet in a Pinch Discharge*. PhD thesis, Princeton University, 1966.
- [16] R.G. Jahn and K.E. Clark. A large dielectric vacuum facility. *AIAA Journal*, 1966.
- [17] N.A. Black and R.G. Jahn. Dynamic efficiency of pulsed plasma accelerators. *AIAA Journal*, 3(6):1209–1210, June 1965.
- [18] R.G. Jahn, W. Jaskowsky, and R.L. Burton. Ejection of a pinched plasma from an axial orifice. *AIAA Journal*, 3(10):1862–1866, October 1965.

- [19] A.C. Eckbreth. *Current Pattern and Gas Flow Stabilization in Pulsed Plasma Accelerators*. PhD thesis, Princeton University, 1968.
- [20] J.C. Keck. Current distribution in a magnetic annular shock tube. *The Physics of Fluids*, 5:630–632, 1962.
- [21] F.J. Fishman and H. Petschek. Flow model for large radius-ratio magnetic annular shock-tube operation. *The Physics of Fluids*, 5:632–633, 1962.
- [22] R.B. Johansson. Current sheet tilt in a radial magnetic shock tube. *The Physics of Fluids*, 8(5):866–871, 1964.
- [23] W.H. Bostick. Hall currents and vortices in the coaxial plasma accelerator. *The Physics of Fluids*, 6(11), 1963.
- [24] L. Liebing. Motion and structure of a plasma produced in a rail spark gap. *The Physics of Fluids*, 6:1035–1036, 1962.
- [25] R.H. Lovberg. The measurement of plasma density in a rail accelerator by means of schlieren photography. *IEEE Transactions on Nuclear Science*, pages 187–198, January 1964.
- [26] R.H. Lovberg. Schlieren photography of a coaxial accelerator discharge. *The Physics of Fluids*, 8(1), 1965.
- [27] J.R. MacLelland, A.S.V. MacKenzie, and J. Irving. Schlieren photography of rail-tube plasmas. *Research Notes*, pages 1613–1615, April 1966.
- [28] E. Robert and L. Reding. Etude experimentale d’un accélérateur de plasma a électrodes lineaires. *ONRA Report*, 1968.

- [29] R.J. Vondra and K.I. Thomassen. Flight qualified pulsed electric thruster for satellite control. *Journal of Spacecraft and Rockets*, 11(9):613–617, September 1974.
- [30] H.W. Liepmann and A. Roshko. *Elements of Gasdynamics*. John Wiley and Sons, Inc., 1967.
- [31] W.A. Hoskins. Asymmetric discharge patterns in the mpd thruster. Master’s thesis, Princeton University, 1990.
- [32] G. Spanjers. Propellant inenefficiencies in pulsed plasma thrusters. In *6th Aerospace Sciences Meeting*, New York, New York, January 22-24 1998. AIAA 68-85.
- [33] D.R. Lide. *CRC Handbook of Chemistry and Physics, 77th Edition*. CRC Press, 1997.
- [34] H.R. Griem. *Principles of Plasma Spectroscopy*. Cambridge University Press, 1997.
- [35] 2002. Personal correspondance with Prof. Dennis Keefer.
- [36] J.D. Huba. *NRL Plasma Formulary*. Naval Research Laboratory, 1994.
- [37] M. Rosenbluth. Infinite conductivity theory of the pinch. In C.L. Longmire, J.L. Tuck, and W.B. Thompson, editors, *Plasma Physics and Thermonuclear Research*, page 217. Pergamon, 1963.
- [38] R.H. Lovberg. Investigation of current-sheet microstructure. *AIAA Journal*, 4(7), 1966.
- [39] F.F. Chen. *Plasma physics and controlled fusion*. Plenum Press, 1984.
- [40] I. Kohlberg and W.O. Coburn. A solution for the three dimensional rail gun current distribution and electromagnetic fields of a rail launcher. *IEEE Transactions on Magnetics*, 31(1), 1995.

- [41] K.D. Diamant. *The anode fall in a high power pulsed MPD thruster*. PhD thesis, Princeton University, 1996.
- [42] L. Spitzer. *Physics of fully ionized gases*. Interscience Publishers, 1962.
- [43] L.C. Woods. *Principles of Magnetoplasma Dynamics*. Oxford University Press, 1987.
- [44] A. Fruchtman. Penetration and expulsion of magnetic fields in plasmas due to the hall field. *Phys. Fluids B*, 3(8), 1991.
- [45] A. Fruchtman. The snowplow in plasmas of nonuniform density. *Phys. Fluids B*, 4(4), 1992.
- [46] A. Fruchtman and K. Gomberoff. Magnetic field penetration due to the hall field in (almost) collisionless plasmas. *Phys. Fluids B*, 5(7), 1993.
- [47] N.A. Krall and A.W. Trivelpiece. *Principles of Plasma Physics*. San Francisco Press, 1986.
- [48] J.W. Barnett. *Operation of the MPD Thruster with Stepped Current Input*. PhD thesis, Princeton University, 1985.
- [49] P. Horowitz and W. Hill. *The Art of Electronics*. Cambridge University Press, 1989.
- [50] Spectrum Software. *Microcap 5 Users Manual*, 2001.
- [51] W. Demtroder. *Laser Spectroscopy*. Springer-Verlag, 1988.
- [52] E. Hecht. *Optics*. Addison-Wesley, 1998.
- [53] Oriel Inc. *Optics and Light Sources*. Oriel, 1999.
- [54] W.L. Wiese, M.W. Smith, and B.M. Glennon. *Atomic Transition Probabilities Volume II: Sodium through Calcium*. National Bureau of Standards, 1969.

- [55] I.H. Hutchison. *Principles of Plasma Diagnostics*. Cambridge University Press, 1987.
- [56] F.C. Jahoda and G.A. Sawyer. Optical refractivity of plasmas. In R.H. Lovberg and H.R. Griem, editors, *Methods of Experimental Physics, Volume 9 - Part B*, page 1. Academic Press, 1971.
- [57] Wavemetrics Inc. *Igor Pro v.4.0 Users Manual*, 2001.
- [58] International Organization for Standardization. *Guide to the Expression of Uncertainty in Measurement*. ISO, 1995.
- [59] H.W. Coleman and W.G. Steele. *Experimentation and Uncertainty Analysis for Engineers*. John Wiley and Sons, Inc., 1999.